Specific heat measurements using the A.C. technique on the chevrel phase superconductor Pb(_1-x)Gd(_x)Mo(_6)S(_8) in high magnetic fields

Salamat Ali

Specific Heat Measurements Using The A.C. Technique On The Chevrel Phase Superconductor $Pb_{1-x}Gd_xMo_6S_8$ In High Magnetic Fields.

Salamat Ali

University of Durham

A thesis submitted in partial fulfilment of the requirements for the degree of Doctor of Philosophy

Department of Physics, University of Durham

1996

Superconductivity Group
Department of Physics
University of Durham

Supervisor
Dr. D. P. Hampshire

Specific Heat Measurements Using The A.C. Technique On The Chevrel Phase Superconductor $Pb_{1-x}Gd_xMo_6S_8$ In High Magnetic Fields.

Salamat Ali

University of Durham

A thesis submitted in partial fulfilment of the requirements for the degree of Doctor of Philosophy

Department of Physics, University of Durham
1996

Abstract

We have developed a probe to measure specific heat of Gd-doped $PbMo_6S_8$, at low temperatures in high magnetic fields up to 12.5 T using a heat pulse method and an a.c. technique. Comparison between these heat capacity measurements and transport measurements provides critical complimentary information about fundamental thermodynamic properties and granularity in superconductors.

We have used a tiny, robust, highly sensitive and broadly field independent Cernox thermometer (CX-1030), eliminating the use of bulky gas thermometry or capacitance thermometry. The diameter of the probe is 20 mm which facilitates use in our 17 T high field magnet and in free-standing cryostats.

Experiments include accurate measurement of temperature oscillations of 10^{-6} K. The measurements and analysis of the data were made fully computer controlled. Measurements on Cu and NbTi demonstrate we achieved an accuracy of ±0.2 K in temperature and a typical accuracy of ~10% in the specific heat values quoted.

Gd-doped Lead Chevrel phase material $Pb_{1-x}Gd_xMo_6S_8$ has been fabricated in a controlled environment using simple sintering methods and a Hot Isostatic Press (HIP) operating at pressures up to 2000 atmospheres. Cp has been measured and the properties of the materials including $B_{C2}(T)$ have been determined. HIP processing improves the materials, increasing Tc ~ 15 K and $B_{C2}(0)$ ~ 60 T. These values are amongst the best reported values for the Chevrel phase materials to date.

I am personally responsible for taking all the data and its analysis. The modification of the probe were also undertaken by me. The fabrication of the samples was not my work

بسم الله الرحمن الرحيم

قُلْ سِيرُوا فِي الْأَرْضِ فَانظُرُوا كَيْفَ بَدَأَ الْخَلْقَ
ثُمَّ اللَّهُ يُنشِئُ النَّشْأَةَ الْآخِرَةَ إِنَّ اللَّهَ عَلَىٰ كُلِّ شَيْءٍ قَدِيرٌ

صدق الله العظيم

Say: Travel Through The Earth And See How Allah Did Originate Creation; So Will Allah Produce A Later Creation: For Allah Has Power Over All Things.

TMQ 29:20

Copyright

Salamat Ali
Aug. 1996.

Acknowledgement

All praise to **Allah** (God) who provided me the energy, courage, and patience to complete this study and always kept me in the right path. I am particularly thankful to the **Govt. of Pakistan** who sponsored me during my whole tenure in the U.K. The Pakistan High Commission in London, for their full financial support and tackling a lot of unseen jobs.

I am very thankful to my supervisor Dr. Damian P. Hampshire who always encourage and guided me during my difficulties and without his proper instructions I'll be never able to finish this work and inviting us on many Bar-be-Ques. I am thankful to Prof. D. Bloor, and Prof. B.K. Tanner who allowed me to use all the facilities available in the Dept. related to my work.

I am also very thankful to P. A. Russell who drew all the drawings for this theses. I am thankful to the secretarial staff who provided me the assistance and the technical staff who assisted at various stages.

To my various friends, Dr. Luc. L. Lay, Dr. C. Friend, Dr. H. Ramsbottom who helped in computing. Dr. D. Evans, Dr. D.N. Zheng and Dr. N. Cheggour for very useful discussions during the experimentations and writing up. To H. A. Hamid, and I. Daniel, as group fellows and T. Hase, C. Moore, C. Leighton, Horsfal as office fellows and Dr. A. Bashir and Marlene during their stay.

My particular thanks to; Abdul Hamid (Turkish) and Aysha from whom I learned cooking, Brs. Mahdi, Collin, Asif, who continued the study circles from where I learnt a lot about life, Buzied who let me use his flat while away, Ruh-ul-Amin for his nice smile and helping behaviour, Abrar, Abubaker, Amir, Jamil, Hafiz, N. Zaidi, Ghassan, Emmad, M. Gregory, S. Mehta, Peter (Computer man), and a lot of other friends.

On a more personnel note, I wish to express my gratitude to my parents who always remembered me in their prayers, supported and encouraged me. To my wife Umama Ali, daughter Hafsa Ali, and son Mussab Ali, who sacrifice and suffered a lot, faced a lot of problems while I was away and gave me the continuous support and to Younas Ch. for his keen interest in to solve a lot of official matters.

Contents

Variables

A	vector potential of the magnetic field
A	cross-sectional area
a	radius of the wire carrying current I_C
α	suitable constant in the GL-theory
α	Maki's parameter
B	net external field
B_0	constant in field dependence j_C
B_{int}	internal field
B_{ext}	external field
B_C	thermodynamic critical field
B_{C1}	lower critical field
B_{C2}	upper critical field
B_{C3}	surface critical field
B_P	paramagnetic critical field
b	reduced magnetic field
b^*_{C2}	reduced upper critical field
β	slope of the straight line to calculate Debye temperature θ_D
β_M	combined parameter in the Maki's theory
C_P	specific heat at constant pressure in $mJ.mole^{-1}.K^{-1}$
c_p	specific heat at constant pressure in $mJ.gm^{-1}.K^{-1}$
C_V	specific heat at constant volume
C_n	specific heat in the normal state
C_{en}	electronic specific heat in the normal state
C_S	specific heat in the supercondicting state
C_{eS}	electronic specific heat in the superconducting state
C_{el}	electronic contribution to the specific heat
C_m	specific heat of the superconducting mixed state
C_M	magnetic specific heat
C_{ph}	phonons (lattice) contribution to the specific heat

χ	susceptibility
Δ	energy gap
Δ_{00}	energy gap at zero Kelvin
δ	coeffiecient of magnetic specific heat
$D(\omega)$	phonon density of states
e	charge on an electron
e	emmissivity of the material
<E>	average energy per atom
En	quantised energy of the nth harmonic oscillator
E	electric field strength
E_F	Fermi Energy
ξ_{GL}	Ginzburg-Landau coherence length
ξ_0	BCS coherence length
F	Helmholtz free energy
F_n	free energy of the normal state
F_S	free energy of the superconducting state
g	Gibbs free energy
g_n	Gibbs free energy in the normal state
g_S	Gibbs free energy in the superconducting state
γ	Sommerfeld constant
γ_V	volumetric co-efficient of specific heat
u_0H	applied d.c. field
u_0H_{C1}	lower critical field
u_0H_{C2}	upper critical field
$u_0h^*_{C2}$	reduced upper crtical field
h	reduced magnetic field
h	Plank's constant
$\hbar$	Plank's constant /2π
H_u	upper critical field < H_P
H_P	paramagnetic limiting field
I	current
$I_{Thermometer}$	excitation current to CX-1030 thermometer

J	current density
J	angular momentum
J_C	critical current density
J_n	normal state current
J_S	suppercurrent
K	thermal conductivity
κ	thermal conductivity
k	wave vector
k	$(\omega/2n)^{1/2}$
k_F	Fermi wave vector
k_B	Boltzmann's constant
κ_{GL}	Ginzburg-Landau parameter
l	thickness of the sample
L	length of sample
L	latent heat
λ_{GL}	Ginzburg-Landua penetration depth
λ_L	London's penetration depth
λ_{SO}	spin-orbit scattering parameter
m	magnetic moment
m_e	mass of electron
M	magnetisation
M	atomic mass
μ_0	permeabilty of the free space
μ_B	Bohr magnetron
N	number of atoms
N(E)	density of normal states electrons
$n(\epsilon_F)$	density of normal states electrons at the Fermi-energy
$N(E_F)$	density of normal states electrons at the Fermi-energy
n	thermal diffusitivity
n_0	density of superelectrons at 0 K
n_s	fraction of superelectrons
ω	angular frequency

ω_C	cut-off frequency
ω_D	Debye frequency
P	pressure in the system
P_h	heating power
P_0	heat leak to the surrounding
ρ	density
ρ	resistivity
ρ	electric charge density
ϕ	flux
ϕ_0	the flux quantum
ϕ	phase angle
$\psi(r)$	Ginzburg-Landau order parameter
$\psi(x)$	di-gamma function $\{d/dx[\Gamma(x)]\}$
Q	heat added to the system
R	gas constant
R	thermal resisitvity of the heat link
σ	Stefan-Boltzmann constant
S	surface area of the sample
SC	superconductor state
SC	superinsulation shield
S_n	entropy in the normal state
S_S	entropy in the superconducting state
T	temperature
T_{ac}	amplitude of the temperature detected by the LIA
T_{dc}	constant temperature difference between the sample and background
T_C	superconducting transition critical temperature
T_M	magnetic transition critical temperature
T_S	superconducting transition temperature in the magnetic field
t	thickness of the sample
t	reduced temperature
t	time
τ	thermal relaxation time

τ_1	thermal coupling time between the sample and its surroundings
τ_2	inter thermal coupling time (of heater, sample, and thermometer)
τ_{SO}	spin-orbit scattering relaxation time
θ	phase shift
θ_D	Debye temperature
U	internal energy of the sysytem
V	volume of the system
V_0	electron-phonon coupling parmeter
V^{-1}rms	inverse of the root mean square voltage acquired by the LIA
V_m	molar volume of the sample
v	velocity of the elastic waves
v_s	velocity of superelectrons
v_F	Fermi velocity
W	work done by the system
x	amplitude of the harmonic oscillator on either side
z	number of electrons per atom (valency)

CHAPTER 1

SUPERCONDUCTIVITY

1.1. General Introduction

Superconductivity is a strange and remarkable phenomena whereby certain materials when cooled below a certain temperature, called the transition temperature Tc, show a remarkable combination of electric and magnetic properties. Below this temperature the material loses its resistance and excludes the magnetic field. Hg was the first materials observed by Heike Kammerlingh Onnes, in 1911 at Leiden [1] with zero-resistivity. After that a series of material were tested. It was found that Nb has the highest T_C of 9.25 K of elemental superconductors [2] and the lowest T_C is reported in Rh at 0.325×10^{-3} K [2]. Before April. 1986, the highest Tc reported was in Nb_3Ge of 23.2 K [2].

In April 1986, J. Bednorz and K. A. Muller [3] reported a possible Tc of ≈ 30 K in the ceramic Lanthanum-Barium Copper Oxide. In Jan. 1987, Wu et al [4] reported a T_C of 92 K in Yttrium-Barium Copper Oxide. The report of Tc above 90 K initiated a world wide revolution among the technological community since the material can be made superconducting without expensive liquid Helium. During early 1988, Maeda et al.[5] reported a Tc of ≈ 110 K in BiSCCO series. A Tc of 125 K was reported [6] in Tl- series and 133 K in Hg-series [7] at normal pressure and above 150 K [8] with a 150 kbar pressure. There are isolated reports of T_C close to 250 K [9-11] but no general confirmation from other laboratories. The evolution of Tc is shown in the Fig. 1.1. Still the community is waiting for the good news of room temperature superconductivity which may be just around the corner waiting to be discovered.

The chapter consists of ten sections. Section 1.2 gives the basic definition of a superconductor describing the zero resistance and the Meissner effect. Two kind of superconductors type-I and type-II, based upon their behaviour in the magnetic field are described in section 1.3. Some thermal properties are explained in section 1.4. Section

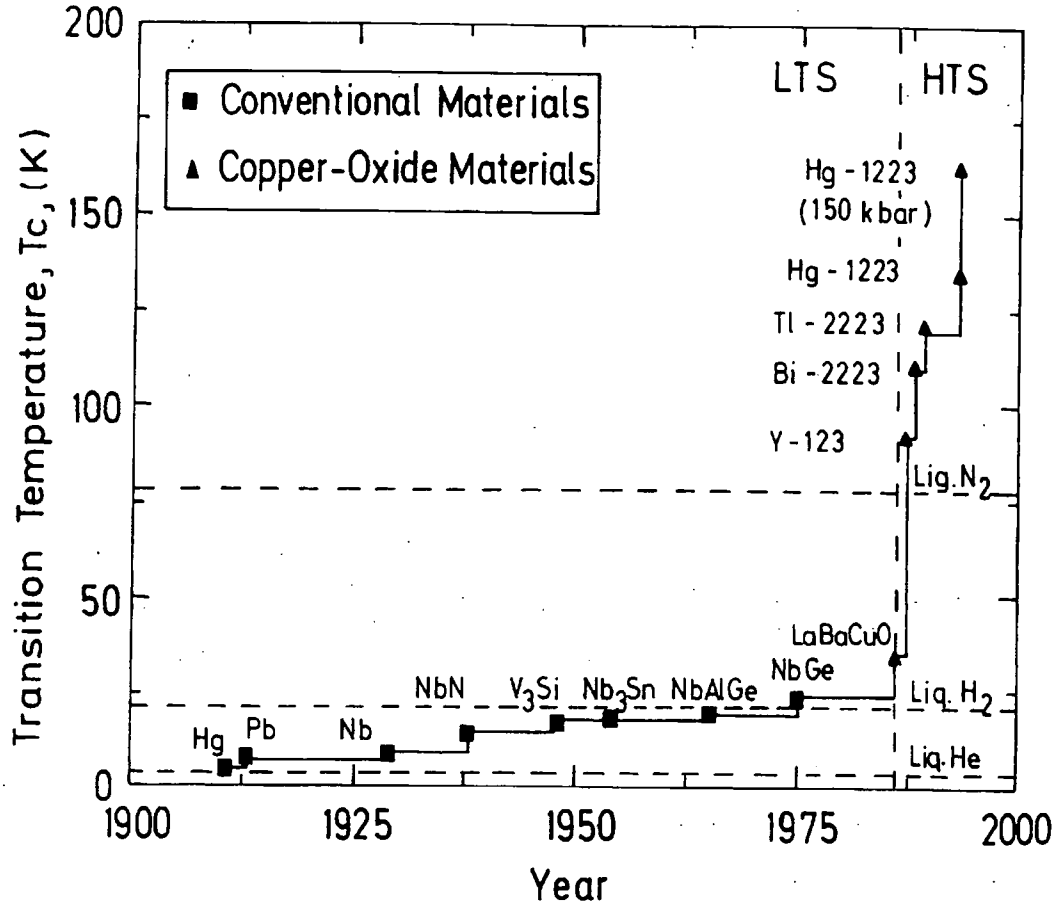

Fig.1.1: The Evolution of the Transition Temperature (1911-93)

1.5 describes the theories of superconductivity including the two fluid model, the London's model, microscopic BCS theory and its main predictions, and the macroscopic GL theory. Section 1.6 explains the different kinds of magnetic materials. In section 1.7 superconducting materials are described. Some small scale and large scale applications of superconductors are described in section 1.8. Since the whole thesis is primarily using ternary superconductors (Chevrel Phases), their preliminary introduction is given in section 1.9. and section 1.10 concludes this chapter.

1.2: Zero-Resistivity and Meissner-Ochsenfeld Effect

All superconductors exhibit zero (d.c) electrical resistivity and pronounced diamagnetic properties below a critical transition temperature T_C. Indeed, persistent or supercurrents in a superconductor have a lower limit of decay time 10^5 years experimentally and beyond 10^{10} years theoretically [2]. This corresponds to a resistivity

which is 20 order of magnitude smaller than that of copper at room temperature.

The abrupt change from normal conductivity to superconductivity occurs at a thermodynamic phase transition. This is determined not only by the temperature, but also by the magnetic field strength H_C applied to the specimen. This was first discovered by Meissner et. al. [13] in 1933 and called Meissner-Ochsenfeld effect or simply the Meissner effect. Alternatively, the superconducting sample will return to its normal state if a magnetic field of greater than that of a critical field H_C is applied. This is contrary to the perfect conductor, where the magnetic flux is trapped in the material. Applying Maxwell's equation, $\nabla \times E = \nabla \times (\rho J) = -dB/dt$, zero resistivity would imply that, $dB/dt = 0$. However, the Meissner effect always occurs whether the sample is cooled in a magnetic field or if the field is applied after cooling below T_C. Therefore, the exclusion of the magnetic field from the material is an intrinsic property of a superconductor. It can therefore be said that the superconducting state is a thermodynamic equilibrium state exhibiting perfect diamagnetism.

The critical current density J_C is defined as the highest amount of electricity that can flow through a superconductor without destroying its superconducting properties. Any greater current than this value will destroy the superconductivity and the material returns to its normal state. It is measured in $A.m^{-2}$. In terms of thermodynamic critical field H_C, the J_C is $2H_C/a$, where a is the radius of the wire carrying current I_C. In reality, the critical current density is usually less than this upper limit.

1.3: Type-I and Type-II Superconductors

Superconductors can be divided into two classes depending on the way in which the transition from the superconducting to the normal state proceeds. Consider a superconductor cooled in zero applied field. On applying a magnetic field, a type I superconductor excludes the flux up to the thermodynamic critical field B_C. Above B_C, the entire sample enters the normal state, the resistance returns and the diamagnetic moments becomes zero i.e. the internal field of the sample B_{int} is equal to the applied field B_{ext}. All superconducting elements (with few exceptions) are considered to be type I superconductors.

For a type-II superconductor, the transition to a completely normal specimen is more gradual. The flux is completely excluded only up to the lower critical field B_{C1},

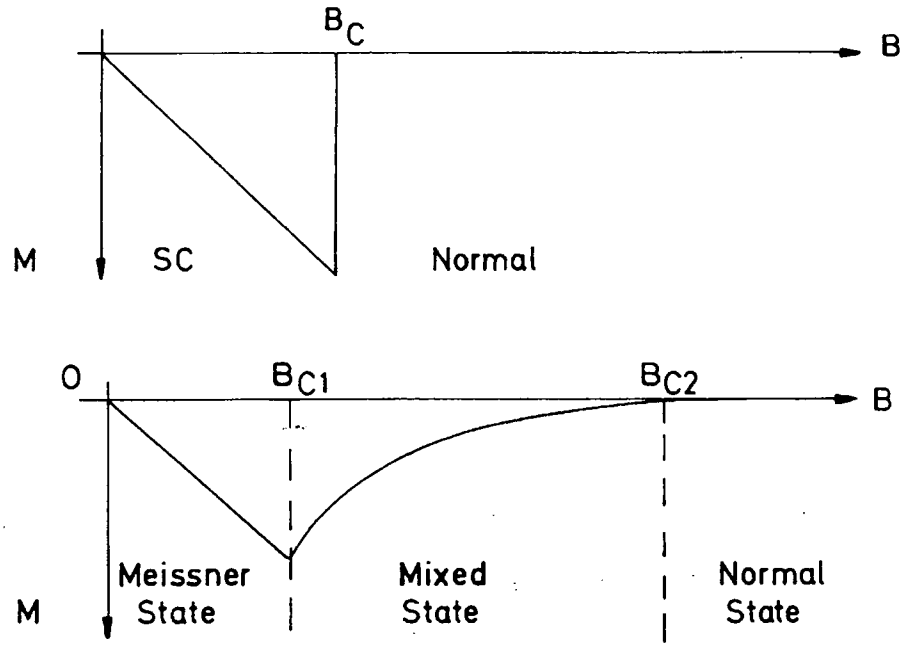

Fig.1.2: The Magnetisation versus applied magnetic field for (a) a type I superconductor, (b) a type II superconductor.

at which point it penetrates in quantised flux lines and the state is called the mixed or vortex state. The superconductivity is only destroyed when the applied field is greater than the upper critical field B_{C2}. All compounds and high temperatures superconductors are type-II superconductors. The magnetisation curves of Type I and Type II superconductors are shown in **Fig.1.2.** All type-I superconductors have a sharp transition at T_C in specific heat measurements while type-II shows a broad transition. Due to their higher B_{C2}, type- II superconductors are used in high field applications.

1.4. Thermal Properties

Gibbs Free Energy

In a fixed magnetic field strength H ($A.m^{-1}$), the thermodynamic potential used to describe an equilibrium state is the Gibbs function g; g = f - BH (f is the free energy, B is the magnetic flux density in Tesla). At a fixed temperature the superconducting-normal transition requires,

$$g_n(T, H_C) = g_S(T, H_C) \qquad (1.1)$$

$$g_n(T, H_C) = g_S(T, H_C) \qquad (1.1)$$

where subscripts n and s denote normal and superconducting states respectively. Noting $B=\mu_0 H$ in the normal state and B = 0 in the superconducting state (i.e. the Meissner effect), and using dg = -SdT - BdH = -BdH (T=constant), it can be shown that,

$$g_n(T, 0) - g_S(T,0) = f_n(T, 0) - f_S(T,0) = \mu_0 H^2_C/2 \qquad (1.2)$$

A system will be most stable if it is in its lowest energy state. As the Gibbs free energy for the superconducting state is less than that of its normal state [14], the superconducting state is the stable state.

Entropy

In all superconductors the entropy decreases markedly on cooling below the Tc. The decrease in entropy between the normal and the superconducting state implies that superconducting state is more ordered than the normal state. Combined with the standard thermodynamic relation, Eq. 1.2 leads to the entropy relation as,

$$S_n - S_S = -\mu_0 H_C \frac{dH_C}{dT} \qquad (1.3)$$

Specific Heat

From the two kinds of the specific heat (lattice specific heat and the electronic specific heat), only the electronic specific heat is playing an active role in the superconducting state as lattice specific heat remains almost constant in normal and superconducting state even in applied magnetic field. The specific heat has a discontinuity or jump at Tc. After that specific heat follows the exponential form instead of the T^3 behaviour. **Fig.1.3.** (See chapter 2 for more details). The above Eq. 1.3 can be written as in terms of specific heat as,

$$C_n - C_S = -\mu_0 T\left(H_C \frac{d^2 H_C}{dT^2} + \left(\frac{dH_C}{dT}\right)^2\right) \qquad (1.4)$$

Equations 1.2-1.4 describes a thermodynamic phase transition along with the superconducting transition. In undergoing this phase transition, normal electrons are condensed into a new state which has lower free energy.

Energy gap.

The first hint of a "forbidden" energy range or energy gap in the superconducting state came from measurements of an exponential specific heat [16,

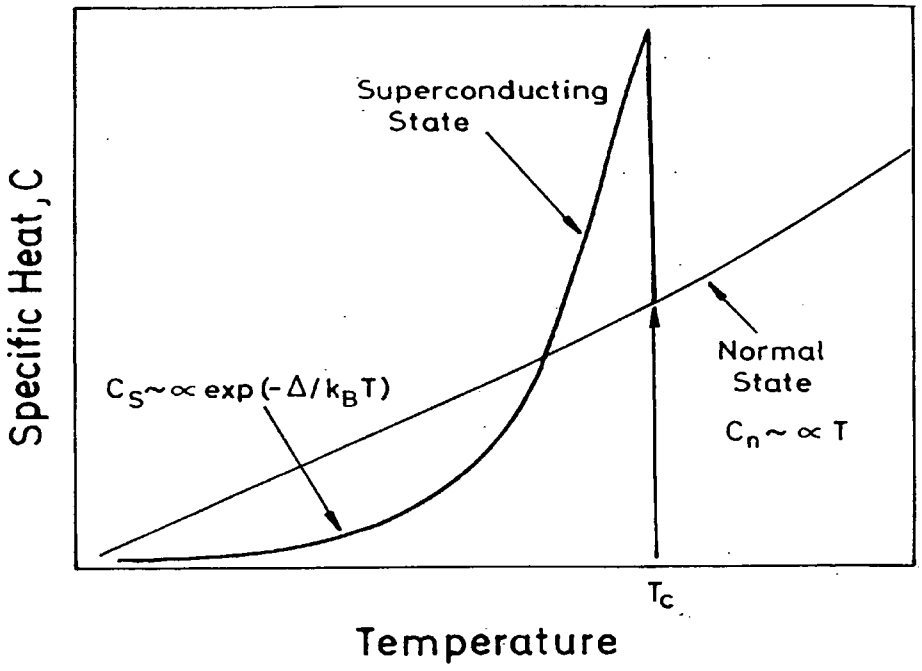

Fig.1.3: The Specific heat of a typical superconductor in its normal and superconducting state.

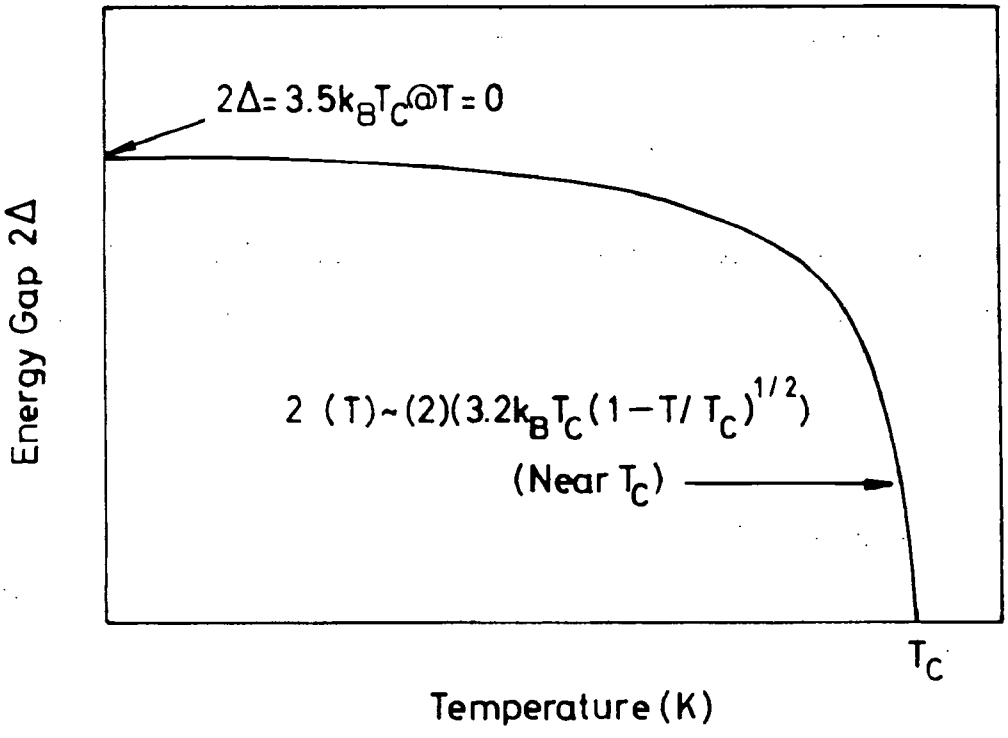

Fig.1.4: The BCS type superconductor energy gap, it is zero at T_c and increases with decrease in temperature, becomes maximum at 0 K.

Corak, 1954]; the presence and magnitude of the gap was confirmed by measurements of electromagnetic absorption. It has totally different origin than that of insulators.

The energy spectrum of Cooper-pair electrons has a gap of $\pm\Delta$ around the Fermi level E_F, that is, a width specified as 2Δ, typically on the order of 10^{-3} eV. The gap reduces to zero as temperature approaches Tc, but is maximum at 0 K [17, J.D. Doss, pp.62]. The demonstration of the energy gap has been shown in Fig. 1.4.

1.5: The Theories of Superconductivity

1.5.1: Two fluid model

Gorter and Casimer [18] proposed two-fluid model in which at Tc there are no superelectrons, all are conduction electrons with a density of $n_n = N/V$, where N is the number of conduction electrons in the sample with volume V. As the sample is cooled down the number of superelectrons n_s start increasing and the number of conduction electrons n_n start decreasing. It implies that, at non-zero temperature, not all conduction electrons participate in the superconducting behaviour and sample is considered to be two-fluid state. The density of superelectrons n_s at any temperature below Tc can be calculated as,

$$n_s = n_0\{1 - t^4\} \qquad (1.5)$$

where n_0 is density of superelectrons at 0 K, and t is T/T_C. If the fraction of superelectrons is $1 - t^4$, the fraction of normal electrons is $1- (1- t^4)$ or simply t^4 for values of $T \leq T_C$ [17]. Fig.1.5. displays the graphical representation of the two fluid model.

1.5.2: The London Model

To explain the superconducting state i.e. zero resistivity and the exclusion of the magnetic field, F. London and H. London in 1935 [19] proposed a theory based on two-fluid model. According to the two-fluid model, the total current flowing in the superconductor is simply, the sum of the superconducting current plus the normal current, $J = J_S + J_n$. The supercurrent is $J_S = n_S e v_S$ and $m_e(dv_S/dt) = eE$, which leads to

$$\frac{\partial J_s}{\partial t} = \frac{n_s e^2}{m_e} E \qquad (1.6)$$

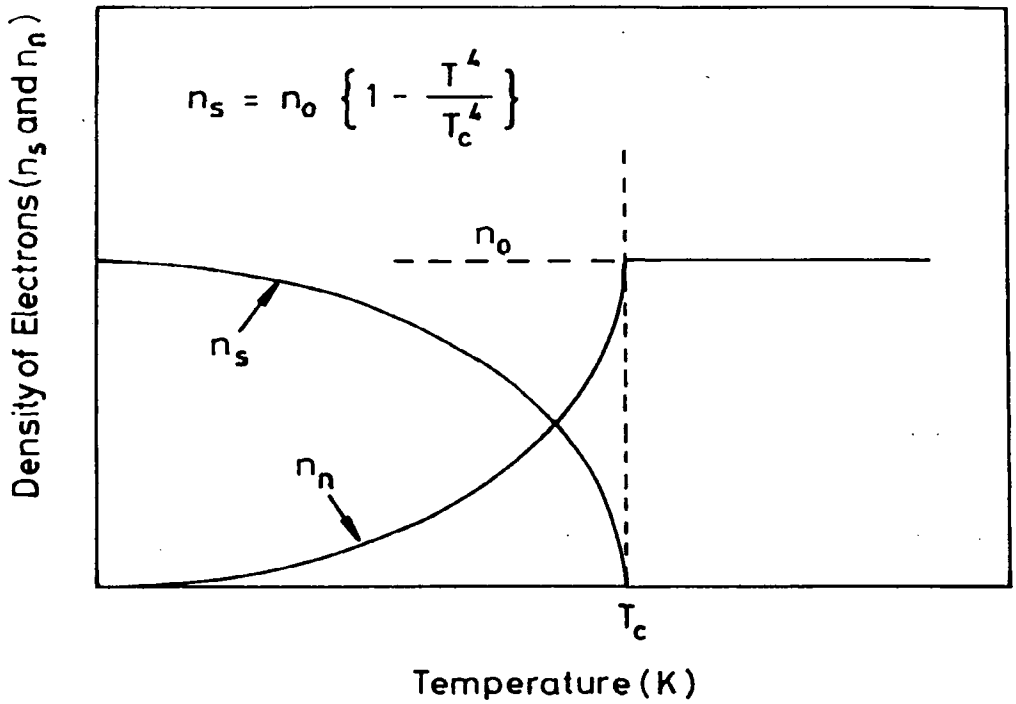

Fig.1.5: In the two fluid model, the density of the paired electrons (n_s) increases as temperature drops below T_c, while the density of the unpaired electrons (n_n) is decrease; the paired electrons provide the supercurrent flow.

(here, m_e is the mass of the electron, v_s is the velocity of the superconducting electrons, e is the charge of the superconductor electrons and E is the electric field strength). Combining Eq. 1.6 with the Maxwell equation, $\nabla \times E = -dB/dt$ and integrating they obtained,

$$\nabla \times J_s = -\frac{n_s e^2}{m_e} B \qquad (1.7)$$

Eq. 1.6 and Eq. 1.7 are the two London equations. Eq. 1.6 describes a conductor with R= 0 and Eq. 1.7 describes the Meissner-Ochsenfeld effect. By applying another Maxwell's equation, $\nabla \times B = \mu_0 J_S$ to Eq. 1.7 and solving for a simple one dimensional case, it can be shown that the parameter λ_L, called the London Penetration Depth, describes the range over which the field extends inside the superconductor and is given by,

$$\lambda_L = \left(\frac{m_e}{\mu_0 n_s e^2}\right)^{\frac{1}{2}} \qquad (1.8)$$

Again applying Maxwell's equation, $\nabla \times B = \mu_0 J_S$ to Eq. 1.7 gives $\nabla B^2 = B/\lambda_L^2$. If this is solved for fields parallel to the surface, then,

$$B(x) = B_0 e^{-\frac{x}{\lambda_L}} \qquad (1.9)$$

i. e. the field decays exponentially in the sample within the London penetration depth.

1.5.3: The Microscopic Theory (BCS)

Although the London equations are able to describe the distribution of currents and fields in superconductors (at low fields), they do not actually explain the Meissner effect and perfect conductivity. The microscopic theory, that resolves the mystery of superconductivity, was given by Bardeen, Cooper, and Schrieffer in 1957 [20], and is referred as BCS theory.

The central point in BCS theory is that the weak attraction between conduction electrons leads to a condensation of electrons into bound pairs. These bound pairs, called **Cooper pairs**, have a lower energy than the original normal electrons [Cooper, 21].

The pairing interaction between electrons occurs because the motion of one electron modifies the vibration of an ion in the lattice of the superconductor. This in turn interacts with a second electron. The total effect is a net attractive force between the electrons. The distance over which the pair is correlated is the BCS coherence length ξ_0. The electrons pairs are considered to be interacting by the exchange of a virtual phonon. Because the pair has a total momentum of zero it cannot be influenced by, say an electric field, without being destroyed (broken apart). The Cooper pairs does not interact with the lattice unless it is subjected to an energy greater than its binding energy. This leads to zero resistance in the superconducting material.

The next section presents the main predictions of the BCS theory.

1)Cooper Pairs:

According to the BCS theory [20], the electrons in a superconductor pair up with one another with opposite momentum and spin (or wave vector $\mathbf{k}\uparrow$ and $-\mathbf{k}\downarrow$). The coherence length ξ_0 of the pairs is given by,

$$\xi_0 = 0.18 \frac{\hbar v_F}{k_B T_C} \qquad (1.10)$$

where v_F is the Fermi velocity. With a net attractive interaction the pairs will condense into the ground state, expressed in terms of the state ($\mathbf{k}\uparrow$, $-\mathbf{k}\downarrow$). In the normal phase all the states are filled up to the Fermi wave vector $\mathbf{k}_F$.

2) Critical Temperature

In the absence of magnetic field, superconducting ordering sets in at a critical temperature given by,

$$k_B T_C = 1.14\,\hbar\omega_C \exp\left(-\frac{1}{N(E_F)\,V_0}\right) \qquad (1.11)$$

where $N(E_F)$ is the density of normal-state electrons at the Fermi energy. The cut-off phonon energy $\hbar\omega_C$ is related to the Debye energy $\hbar\omega_D$, in which $\omega_D \propto M^{-1/2}$, where M is the atomic mass and V_0 is the coupling parameter.

3) Energy Gap:

The attraction between electron pairs, leads to a temperature-dependent energy gap $2\Delta(T)$ in the electron energy spectrum at the Fermi level. The energy gap is a maximum at absolute zero, and it is related to T_C by

$$2\Delta(0) = 3.52\ k_B T_C \qquad (1.12)$$

As temperature is increased, $\Delta(T)$ remains nearly constant up to about 0.5 T_C and then it begins to decrease rapidly, becoming zero at T_C. At temperatures below about 0.5 T_C the energy required to break up a Cooper pair is approximately $2\Delta(0)$ and, therefore, the number of pairs broken up is proportional to $\exp[-2\Delta(0) / k_B T]$. This leads to an exponential temperature variation for the electronic specific heat, a behaviour which is observed in experiments at sufficiently low temperatures [22]. This is shown in Fig.1.4.

4) Ratio between C_{es} and γT_C:

The result for C_{es} (the electronic specific heat in the superconducting state) and γ (the coefficient of electronic specific heat in the normal state, called Sommerfeld constant = C_e/T, where C_e is the electronic specific heat in the normal state) from BCS theory [20] may be approximated over a limited temperature range by;

$$\frac{C_{es}}{\gamma T_C} = a \exp\left(-b\frac{T_C}{T}\right) \qquad (1.13)$$

where a = 8.5, b = 1.44 for $2.5 < T_C/T < 6$, and a = 26, b = 1.62 for $7 < T_C/T < 12$. [2,16,17, 23].

5) Specific heat Jump:

The BCS result for the jump (discontinuity) at Tc in the electronic specific heat is given by

$$\frac{C_{es}(T_C) - \gamma T_C}{\gamma T_C} = 1.43 \qquad (1.14)$$

The agreement of this prediction with experiment is good to about 10% except for the strong-coupling superconductors. [23].

6) Relationship between H_0 , T_C and γ:

BCS theory has also predicted a relationship between the critical field at absolute zero (H_0), the critical temperature (T_C), and the coefficient of electronic specific heat in the normal state (γ) as:

$$\frac{\gamma T_C^2}{\mu_0 H_0^2 V_m} = 2.14 \qquad (1.15)$$

The BCS value for $H_C(T)$ exhibit a negative deviation from a reference parabola with a maximum deviation of almost -4% near $(T/T_C)^2 = 0.5$; the values may be approximated at low temperatures ($T \ll T_C$) by [17,20,23,24],

$$H_C \simeq H_0[1 - 1.07(\frac{T}{T_C})^2] \qquad (1.16)$$

Almost all weak coupled superconductors show the above mentioned properties. But there are other (strong coupled) superconductors which are in disagreement with BCS theory including Hg, Pb, Nb, and many non-elemental superconductors.

1.5.4. The Ginzburg-Landau Theory

The BCS theory provides a successful account of the superconducting properties in cases where the energy gap Δ (or the order parameter as it is alternatively known) is constant in space. However, there are many situations in which the order parameter shows a strong spatial variations. The well known example is the complex magnetic structure of both the, type-I and type-II superconductors, in which there is the co-

existence of the normal and the superconducting regions. In such cases GL-theory is more successful.

According to the theory proposed by Vitaly Ginzburg and Lev Landau in 1950 [25], all the electron pairs are condensed into a macroscopic quantum state with a wave function $\psi(r,\Phi) = |\psi(r)|\, e^{i\Phi}$, ($\Phi$ is the phase) which characterises the degree of superconductivity at a point in a material. It is defined to be zero in a normal region and unity in a fully superconducting region at T = 0. The superelectron density is obtained as,

$$n_s(r) = |\psi(r)|^2 \qquad (1.17)$$

They assumed the transition is of second order and the superconducting free energy in a magnetic field can be expanded in a series of $|\psi|^2$ of the form,

$$F_s = F_n + \alpha|\psi|^2 + \frac{1}{2}\beta|\psi|^4 + \frac{1}{2\mu_0}|B_{ext} - B_i|^2 + \frac{1}{2m_e}|(-i\hbar\nabla - 2eA)\,\psi|^2 \qquad (1.18)$$

The first three terms come from Landau's own theory of the second order transition [23]. F_n is the free energy in the normal state and α, β are suitable coefficients. Close to T_C, a good approximation is made by neglecting terms in higher powers of $|\psi|$. The fourth term gives the energy to change the magnetic field from its external value, B_{ext} to the internal field B_i. The last term is the energy associated with the local variation in the supercurrent and the Cooper pair density (A is the vector potential of the magnetic field). Minimising the free energy with respect to ψ gives,

$$\left[\alpha + \beta|\psi|^2 + \frac{1}{2m_e}(i\hbar\nabla - 2eA)^2\right]\psi = 0 \qquad (1.19)$$

and minimising the free energy with respect to A gives an equation for the supercurrent as,

$$J_s = \frac{e}{2m_e}\left[\frac{\hbar}{i}(\psi^*\nabla\psi - \psi\nabla\psi^*) + 4eA\psi^*\psi\right] \qquad (1.20)$$

The GL coherence length ξ_{GL}, is the distance over which the order parameter decays at a superconducting-normal interface. Empirically, the temperature dependence near T_C is,

$$\xi_{GL} \propto (1-t)^{-1/2} \qquad (1.21)$$

where t is the reduced temperature T/T_C. The GL penetration depth λ_{GL} varies in the same way as λ_L close to T_C. At T_C both λ_{GL} and ξ_{GL} become infinite, the normal vortex

cores expand to fill the entire material and flux penetration is complete. The GL theory can be formulated in terms of Ginzburg-Landau parameter, κ_{GL} as,

$$\kappa_{GL} = \frac{\lambda_{GL}}{\xi_{GL}} \qquad (1.22)$$

Ginzburg and Landau showed that at a superconducting-normal boundary the condition $\kappa_{GL} = 1/\sqrt{2}$ describes the point at which the surface energy goes from positive to negative. Type-I superconductors are characterised by $\kappa_{GL} < 1/\sqrt{2}$ which corresponds to a positive surface energy and type-II superconductors are characterised by $\kappa_{GL} > 1/\sqrt{2}$ which corresponds to a negative surface energy.

By applying appropriate conditions, Abrikosov in 1957 [26] solved the GL equations for a type-II superconductor in fields $B_{C1} < B < B_{C2}$ (mixed state). He showed that a magnetic field penetrates a superconductor as tubes of flux (fluxons), each containing one flux quanta,

$$\phi_0 = \frac{h}{2e} = 2.07 x 10^{-15} \quad wb. \qquad (1.23)$$

Flux quantization was confirmed experimentally by two groups in 1961 [27,28]. Each flux line consists of magnetic flux surrounded by a vortex of superelectrons at a distance of λ_L. The core is in the normal state. When fluxons enter a superconductor they attempt to organise in such a way as to minimise their free energy. This array of fluxons is known as the flux line lattice and usually in a hexagonal (or triangular) configuration in the superconductor. In Fig.1.6 it is shown, how the order parameter is changing [2].

The two critical fields can then be derived as,

$$B_{C2} = \frac{\phi_0}{2\pi\xi^2_{GL}} = \sqrt{2}\kappa_{GL} B_C \qquad (1.24)$$

and

$$B_{C1} \approx \frac{\phi_0}{4\pi\lambda^2_{GL}} \ln \kappa_{GL} \approx \frac{B_C}{\sqrt{2}\kappa_{GL}} \ln \kappa_{Gl} \qquad (1.25)$$

If a field is applied parallel to the surface of the sample, a superconducting region can exist at the surface for fields greater than B_{C2}, up to a field given by,

$$B_{C3} = 1.695\ B_{C2} \qquad (1.26)$$

As the angle of the applied field is changed, B_{C3} reduces to B_{C2} when the field is perpendicular to the surface.

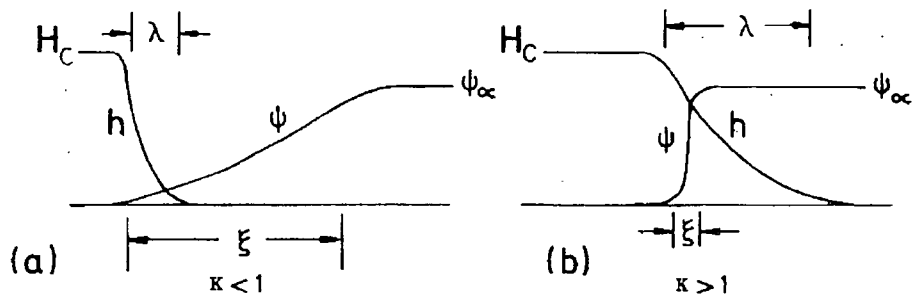

Fig.1.6: Schematic diagrams showing how the local magnetic field and ψ(x) vary with the distance from a normal-superconductor interface. The two cases, (a) and (b), show the GL-parameter much smaller and larger than unity, in indicated [2].

1.6: Magnetism:

Magnetism is a branch of science covering magnetic fields and their effect on materials, due to the unbalanced spin and orbital momentum of electrons in atoms. Whenever an electric current flows a magnetic field is produced; as the orbital motion and the spin of atomic electrons are equivalent to tiny current loops, individual atoms create magnetic fields around them, when their orbital electrons have a net magnetic moment as a result of their angular momentum. The magnetic moment of an atom is the vector sum of the magnetic moments of the orbital motions and the spins of all the electrons in the atom. The fundamental unit of magnetic moment is Bohr magnetron, μ_b. The dipole moment associated with a loop of current I is IA, where A is the area of the loop. The current I of a single electron of charge q, and mass m_q, rotating in a circular orbit of radius r, at angular frequency ω, will give a magnetic dipole moment, m defined as;

$$m = IA = -q(\omega/2\pi).\pi r^2 = -\tfrac{1}{2}(q\omega r^2) \qquad (1.27)$$

The angular momentum $L = m_q\omega r^2$, therefore,

$$m = -(q / 2m_q) L \qquad (1.28)$$

i.e. the angular momentum is quantized in units of $\hbar = (h/2\pi)$, where h is the Planck's constant. The lowest non-zero value for $\mu_b = q\hbar/2m_q = 9.2741\times10^{-24}$ J.T^{-1} $= 5.79\times10^{-5}$ eV.T^{-1}. The *susceptibility* is defined as χ = M/H and *permeability* as μ = B/H, where M is the magnetisation, H, the applied field strength, and B, is the magnetic induction.

All macroscopic magnetic properties of a substance arise from the magnetic moments of its component atoms and molecule. Different materials have different characteristics in an applied magnetic field; there are four major types of the magnetic materials, they are discussed here;

Diamagnetism:

In these materials, M opposes H, the Susceptibility is $\approx -10^{-8}$ $m^3 mol^{-1}$ and relative permeability ≈ 0. Metals such as copper ,silver and gold are diamagnetic. While superconductors are special kind of perfect diamagnetism, with susceptibility -1

Paramagnetic Materials

In these materials spin and magnetic moment have random alignment in the absence of a magnetic field, while the application of a magnetic field will align the spin and magnetic moment in the direction of applied field. Metals such as Al, and most ionic solids are paramagnetic. In these materials susceptibility > +0 and relative permeability ≈ 1.

Ferromagnetic Materials

Spontaneous magnetisation occurs, i.e. M is finite in zero applied field and is not proportional to H. Spin and Moment have one direction alignment, parallel to each other. These materials are characterised by the hysteresis in their magnetization,(M-H) loops. Iron, cobalt, and nickel together with a few rare earth (RE) metals such as gadolinium are Ferro-magnetic. Above a particular temperature called Curie Temperature they lose their behaviour and become simple paramagnetic. Susceptibility = $\lim_{B->0}$ dM/dH and relative permeability $\approx 10^4$.

Antiferromagnetic Materials

In these materials spin and moments are aligned with alternate order of moments, i.e. anti-parallel and cancel each other with 0-magnetisation. This alignment can be observed below Neel's Temperature.

1.7: Superconducting Materials:

Since the discovery of superconductivity in Hg in 1911, hundred of thousands materials have been investigated. Many of them shows superconducting properties. These include elemental, conventional low $T_C < 25$ K and new high T_C, 77 K < T_C< 152 K, and Chevrel phase (CPC) superconductors and Organic superconductors. Some of them are listed in Table 1.1.

Material	T_C (K)	$B_{C2}(0)$ (T)	$B_{C1}(0)$ (mT)	$\Delta C/\gamma T_C$ BCS=1.43	θ_D (K)	$2\Delta(0)/k_B T_C$ BCS=3.52
Hg	4.16	-	41.1	2.37	72	4.6
Pb	7.19	-	80.3	2.71	105	4.5
Nb	9.22	-	206	1.87	277	3.6
NbTi	9.8	17	0.06	2.06	270±20	3.66±0.46**
Nb_3Ge	23.2	38	0.44	2.3	302±3	4.2±0.2
$PbMo_6S_8$	15.3	60	6.4	2.29	411	3.84
Y-123 (‖ ab-plane)	92	670	85	2.1±0.7	440±10	≈ 6
Y-123 (‖ c-axis)		120	25			
Bi-2223(‖ ab-plane)	110	1200	2	0 to 1.84	312±5	6.8
Bi-2223(‖ c-axis)		40	0.2			

Table.1.1: The data in the table has been compiled from refs. 2, 29, 30, 31, 32, 33, and 34; **, Due to different composition.

1.8: Applications

Before the discoveries of HTSC, the superconductors were already in use in industry with some small scale and large scale applications. A leading use of superconductors is to produce high magnetic fields. Magnetic fields exceeding 10 T have been produced in a handful of laboratories. With the discovery of ceramic HTSC, a chance of producing very high magnetic fields is quite feasible but still some technical problems have to be overcome. There are three major parameters by which the superconductor can be characterised, named, T_C, H_{C2}, and J_C. For the commercial use of a material J_C should be in the range of 10^5 amp.cm^{-2} or more. HTSC have T_C and H_{C2}

very high but J_C is not crossing the basic limits. However, all over the world a tremendous effort is being made to overcome this problem..

Zero resistance in superconductors can help in electrical transmission lines where about ≈ > 5 % energy are being dissipated during the transmission. This can be saved using superconductor wires. Due to its of high B_{C2}, the superconductors are currently used in noiseless and high efficient levitation trains. Certainly the industry is looking for the use of superconductor in transmission cables, generators, and energy storage. However, as with any new technology its takes time, same is true for HTSC in large scale applications.

Superconductors are already used in small-scale applications, major use in SQUID (Superconducting Quantum Interference Device, based on two quantum effects, the flux quantization and the Josephson effect in SC) which can detect and measure extremely small currents, voltages and changes in magnetic flux densities of the order of 10^{-9} T to study the human brain activities etc. Progress continues on the development of other building blocks of HTSC circuit technology; multilayers, which are required to produce integrated circuit chips. With a lot of efforts, it is still difficult to predict the future but optimism is there.

1.9: Ternary Superconductors (Chevrel Phases Compounds, CPC)

These ternary superconductors, well known by the name of their founder R. Chevrel [35] in 1971, have a general formula $M_nMo_6X_8$, with M = 3d elements, In, Sn, Pb, alkalines, alkaline-earth, etc; X is either Sulphur, Selenium, or Tellurium, and n is a number less than 4 depending on the element M. In 1972, Matthias et.al. [36] reported that many of these new phases were superconducting with reasonably high transition temperature (e.g. $PbMo_6S_8$: T_C ≈ 15 K). A year latter it was reported by Fischer et. al. [37] that many of these compounds have very high B_{C2}(e.g. ≈ 60 T, in $PbMo_6S_8$) and they became a potential candidate for high field applications beyond 20 T to 40 T at 4.2 K. Since then a large number of investigations have been published showing that most properties of these material are of intermediate nature. (Intermediate in the sense that the properties lie in between the LTSC and HTSC).

If one compares the B_{C2} of $PbMo_6S_8$ with that of NbTi and Nb_3Sn, two technical superconductors, at 4.2 K, B_{C2} is a factor of 2 - 2.5 higher compared to Nb_3Sn and more

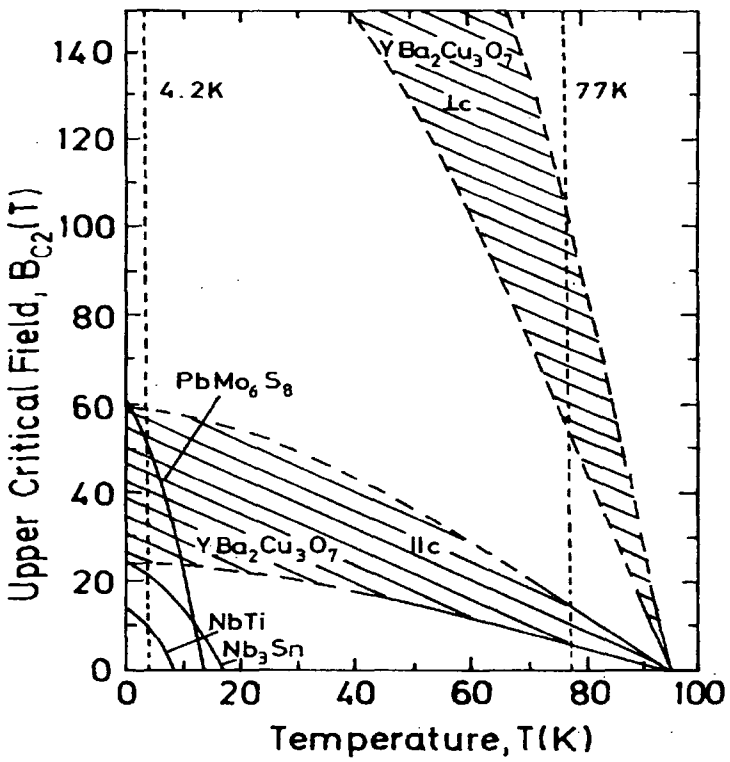

Fig.1.7: The B_{C2} of PMS material compared with LTSC and HTSC.

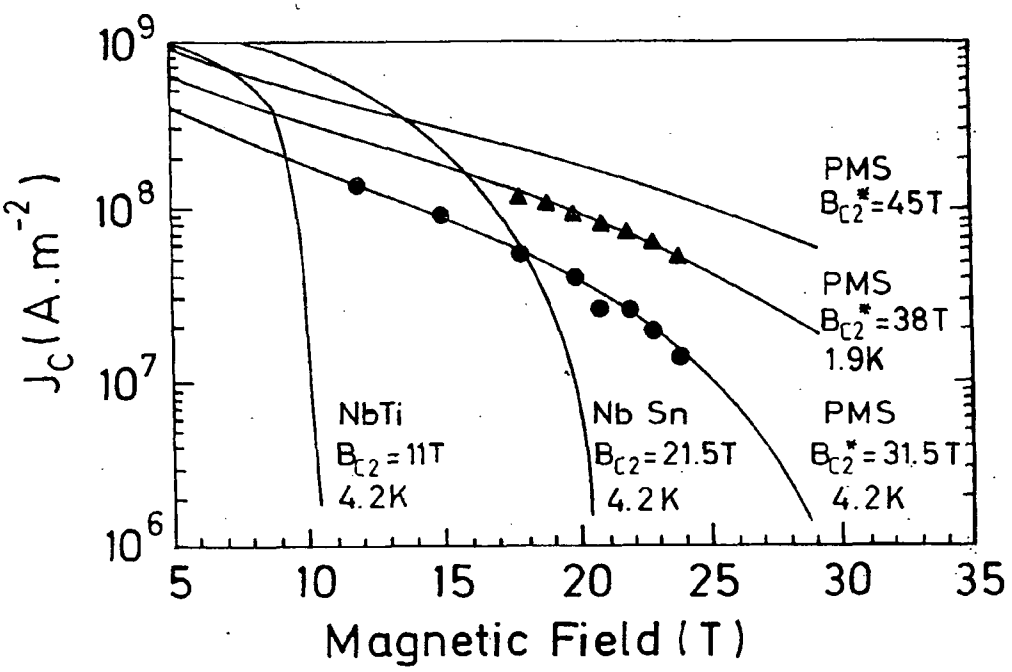

Fig.1.8: The critical current density J_C, of PMS wires, compared with two technically important materials.

than a factor of 4 to NbTi. [38]. In Fig.1.7, the temperature dependence of the upper critical field B_{C2} of $PbMo_6S_8$ has been compared with both LTSC and HTSC. [2,34,38].

Currently, several groups are working in the fabrication of PMS wires and at present, critical current density are of the order of 2 x 10^8 $A.m^{-2}$ under a 20 T magnetic field [39-41]. The transport critical current density J_C, of PMS material fabricated in Geneva using Hot Isostatic Pressure is compared with two low temperature superconductors in the magnetic field is shown in Fig.1.8.

1.10: Concluding Remarks:

This chapter is based on the basic ideas of the superconductivity. The discovery of superconductivity by H. K. Onnes in 1911, opened a door of a totally new field of science. Meissner in 1933 completed the definition of superconductor which distinguished it from the perfect conductors where magnetic flux is trapped but in superconductors the flux is excluded. Using this criteria, superconductors can be divided into two families, elemental type I and complex type II superconductors with high B_{C2}. It is difficult to describe all the thermal properties in this short chapter. Some of them have been discussed, including, Gibbs free energy, which is a parameter to find the stability of the system, the lower the Gibbs free energy, the more stable the system is. The superconducting state has a $\mu_0 H^2_C/2$ less Gibbs free energy as compared to the normal state which demonstrates that the superconducting state is the stable state. It is clear from section 1.4 that superconducting state has lower entropy than the normal state, which points to the superconducting state being highly ordered as compared to the normal state. Similarly, by measuring the specific heat much information can be gathered which will be explained in chapter 2. The energy gap in a superconductor is typically on the order of 10^{-3} eV which has a zero value at T_C and increases as the temperature decreases toward the zero Kelvin, where it has a maximum value. It has a totally different origin with that of an insulator. The first indication of an energy gap in a superconductor came from the specific heat measurements which along with isotope effect gave grounds to Bardeen et.al. (BCS) in 1957 to develop their landmark microscopic BCS theory. Although Gorter et.al. in 1934, using the idea of superfluid helium and applying it to superconductivity, had already given a model of two fluids stating that at T_C there are no superelectrons but as the temperature is decreasing the

amount of superelectrons starts increasing and becomes maximum at 0 K. Nevertheless, the two-fluid model gives a physical basis for understanding superconductivity. The London's brothers tried to explain the phenomena on the basis of two fluid model but were unable to explain the phenomena completely.

As discussed above, the first comprehensive explanation of the mysterious phenomena of superconductivity came after the work of Bardeen, Cooper and Schrieffer, BCS, in 1957, who gave the concept of condensation of electrons into a bound pair called Cooper pairs. They explain, the transition temperature T_C, the energy gap Δ, the electronic specific heat C_{es}, and the jump ratio, $\Delta C/\gamma T$, and gave the successful explanation of the exclusion of the magnetic field from the superconductor, the Meissner effect. The theory deals well with the weak coupled superconductors but for strong coupled and type II superconductors in high fields it is not suitable where one has to consider the GL-theory developed in 1950's.

The superconducting materials are a special case of diamagnetic materials and the ferromagnetic materials can be better understand by considering the domain concept in the materials. The whole thesis is on the Chevrel phase superconductors, which have intermediate properties as compared to the LTSC and ceramic HTSC. Due to the high B_{C2}, and J_C, they are potential candidates for use for commercial purpose to produce a high magnetic field beyond 10 T to 40 T at 4.2 K. The major properties of these materials rely on the third metallic element to be added to the Mo_6S_8 cluster. The small tilting angle of this cluster from 90 degree gives appreciable change in its superconducting properties.

Although with the discovery of HTSC, a revolution occurred as the community found a suitable superconducting material above cheap liquid nitrogen temperature, but one out of three major parameters still needs a lot of work, which makes it difficult to use these materials for large scale applications. However, small scale applications are in use and people are working hard to overcome all the problems encountered in the fabrication process and to better the quality of the materials. Apparently the good news of room temperature superconductivity and overcoming of all the problems is waiting shortly in some corner to come true.

References

1). Onnes, H. K., Physical Laboratory Communication, Leiden University, No. 120b, 122b, and 124c. (1911).

2). Burns, G., in High-Temperature Superconductivity, An Introduction, Academic Press, INC, San Deigo, 1992. pp.1-75.

3). Bednorz, J. G., and K. A. Muller, Z. Phys. B-Condensed Matter, 64 (1986) 189-93.

4). Wu, M. K., J. R. Ashburn, C. J. Torng, P. H. Hor, R. L. Meng, L. Gao, Z. J. Huang, Y. Q. Wang, and C. W. Chu, Phys. Rev. Lett. 58 (1987) 908-10.

5). Maeda, H., Y. Tanaka, M. Fukutomi, and T. Asano, Jap. J. Appl. Phys. 27 (1988) L209-L210.

6). Parkin, S.S.P., V.Y. Lee, E.M. Engler, A.I. Nazzal, T.C. Huang, G. Gorman, R. Savoy, and R. Beyers, Phys. Rev. Lett. 60 (1988) 2539-42.

7). Schilling, A., M. Cantoni, J. D. Guo and H. R. Ott., Nature, 363 (1993) 56-58.

8). Chu, C. W., L. Gao, F. Chen, Z. J. Huang, P. L. Meng, and Y. Y. Xue, Nature, 365 (1993) 323-25.

9). Lagues, M., X. M. Xie, H. Tebbji, X. Z. Xu, V. Mairet, C. Hatterer, C. F. Beuran, C. D. Cavellin, Science, 262 (1993) 1850-52.

10). Tholence, J. L., B. Souletie, O. Laborde, J. J. Capponi, C. Chaillout and M. Marezio, Phys. Lett. A., 184 (1994) 215-17.

11). Levi, B.G., Physics Today, Feb. 1994, 17-18.

12). Ramsbottom, H. D., Thesis, University of Durham, 1996.

13). Meissner, W., and R. Ochsenfeld, Naturwiss, 21 (1933) 787-88.

14). Rose-Inns, A. C., and E. H., Rhoderick, in Introduction to Supperconductivity, 2nd Edition, The Pergamon Press, Oxford, 1978. Chap.4.

15). Kittel, C. in Introduction to Solid State Physics, 6th Edition, John Wiley & Sons Inc, New York, 1986. Chap.12.

16). Corak, W. S., B. B. Goodman, C. B. Satterthwaite, and A. Wexler, Phy. Rev., 96 (1954) 1442-4.

17). Doss, J. D., Engineers Guide to High Temperature Superconductivity, John Wiley & Sons Inc, New York, 1989. Chap.1-4 and Index H.

18).Gorter, C. J., and H. Casimir, Phys. Z.,35 (1934) 963. and Z. Tech. Phys. 15 (1934) 539.

19). London, F. and H., Proc. Roy. Soc. A149 (1935) 71-88.

20). Bardeen, J., L. N. Cooper, and J. R. Schrieffer, Phys. Rev. 108 (1957) 1175-1204.

21). Cooper, L. N., Phys. Rev. 104 (1956) 1189-90.

22). Phillips, N. E., in Critical Reviews in Solid State Sciences (D. E. Schuele, and R. W. Hoffman, Editors), Vol. 2, Chemical Rubber Co., Clevland, OH. 1972, 467-553.

23). Miller, A. P., in Specific Heat of Solids, Editor, C. Y. Ho, Hemisphere Publishing Corporation, New York, 1988, pp. 1-89.

24). Rosenberg, H. M., in The Solid State, 3rd Edition, Oxford Science Publication, Oxford, U. K., 1990.

25). Ginzburg, V. L., and L. D. Landau, Zh. Eksp. Teor. Fiz., 20 (1950) 1064-82.

26). Abrikosov, A. A., Sov. Phys. -JETP, 5 (1957) 1174-82.

27). Deaver, B. S. Jr., and W. M. Fairbank, Phys. Rev. Lett. 7 (1961) 43-46.

28). Doll, R., and M. Nabauer, Phys. Rev. Lett. 7 (1961) 51-52.

29). Colling, E. W. in Applied Superconductivity, Metallurgy, and Physics of Titanium Alloys, Vol. 1, Chap.8,10.

30). Kinoshita, K., Phase Transition, A 23 (1990) 73-

31). Stewart, G. R., L. R. Newkirk and F. A. Valencia, Solid State Comm., 26 (1978) 417-20.

32). Cors, J., D. Cattani, M. Decroux, B. Seeber, and Φ. Fischer, Fruhjahrstagung der S. P. G. 63 (1990) 795-96.

33). Junod, A., in Physical Properties of High Temeprature Superconductors II, Edited by D. M. Ginsberg, World Scientific, Singapore, 1990.

34). For YBCO, Same as reference 2, and for BiSCCO, Matsubara, I., H. Tanigawa, T. Ogura, H. Yamashita, and M. Kinoshita, and T. Kawai, Phys. Rev. B., 45 (1992) 7414-17.

35). Chevrel, R., M. Sergent, and J. Prigent, J. Solid State Chem, 3 (1971) 515-19.

36). Matthias, B. T., M Marezio, E. Corenzwit, A. S. Cooper, and H. E. Barz, Science, 175 (1972) 1465-66.

37). Fischer, Φ., R. Odermatt, G. Bongi, H. Jones, R. Chevrel, and M. Sergent, Phys.Lett. 45A (1973) 87-88. Odermatt, R., Fischer, Φ., H. Jones, and G. Bongi, J. Phys. C: Solid State Phys. 7 (1974) L13-L15.

38). Pena, O., and M. Sergent, Prog. Solid St. Chem. 19 (1989) 165-281.

39). Chevrel, R., M. Sergent, L. Le Lay, J. Padiou, O. Pena, P. Dubots, P. Genevey, M. Couach, and J.-C. Vallier, Revue Phys. Appl. 23 (1988) 1777-1784.

40). Cheggour, N., A. Gupta, M. Decroux, J. A. A. J. Perenboom, P. Langlois, H. Massat, R. Flukiger, and Φ. Fischer, Proc. EUCAS, 1995, Edinburgh.

41). Zheng, D. N., H. D. Ramsbottom, and D. P. Hampshire, Phys. Rev. B, 52 (1995)

CHAPTER 2

RELATED THEORY OF SPECIFIC HEAT OF MATERIALS

2.1: Introduction

The competition between theory and experiment in the study of specific heat has played an important role in understanding the properties of substances in their solid state. The theory which describes thermodynamic phenomena in a solid generally leads to a set of energy levels which the particles of the system can occupy. These energy levels may be inter-related with a particular mode of energy such as the vibrational, electronic, or magnetic energy of the constituent particles. By using some suitable statistics, one can find the average energy of the system from where the relationship to the specific heat of that mode can be determined. But often the observed specific heat consists of more than one mode of energy. In such cases, theory can help in identifying the contributing modes and calculate them and, hence, separate their specific heats [1].

A lot of information about the lattice and electronic properties of the material can be gathered by measuring specific heat [1-4]. As specific heat is a bulk measurement, it can used to check whether the transition that has occurred is complete or due to some minority phase present in the material. The field of measuring specific heat has been developed to such an extent that one can measure the thermodynamic critical field B_{C1} and B_{C2} by applying a magnetic field, the Sommerfeld constant γ, Debye temperature θ, lattice and electronic contribution to specific heat and the energy gap Δ. The adiabatic stability of a material can also be checked on the basis of specific heat, since higher specific heat leads toward a more stable system [5, pp.357]. The field of measuring specific heat is not new but started before 1819 when Dulong and Petit [6] measured thirteen materials and collated their findings in a well-known law that "the specific heat of any material is a constant quantity equal to approximately 24.92 $J.mole^{-1}.K^{-1}$". When it was tested at low temperatures, it was found that the law is only valid at room temperature and above and not for low temperatures. The failure of classical theory to predict the behaviour of specific heat of solids at low temperature led Einstein (1907) [7] and Debye (1912) [8], to use quantum theory to explain low temperature

behaviour of C_V for solids using phonons. The electronic contribution, on the basis of free electron model to specific heat was explained by Sommerfeld (1928) [9].

In thirties Keesom et.al.[10-11] measured the specific heat of superconducting tin and predicted an energy gap in the superconductor which led Bardeen, Cooper, and Schrieffer [12] in 1957 to develop the BCS theory.

The range of topics related to the study of specific heat are very broad because in principle, any thermodynamic quantity can contribute to the specific heat of solids. Therefore, it is difficult to discuss all the topics in this chapter rather I will confine myself to discuss only those topics of specific heat which are related to my work.

The Chapter is divided into two major parts. Part I describes the specific heat of materials in general while Part II explains some properties of the Chevrel phase materials which are the particular focus of this thesis. Part I consists of sections 2.1 - 2.8. Section 2.1, gives some introduction about specific heat. Section 2.2, provides the definition of specific heat and its relation to other thermodynamics quantities. In section 2.3, the theories of lattice (C_{ph}) and electronic specific heat (C_{el}) of normal materials will be discussed. What sort of information one can get by measuring specific heat of superconductors will be addressed in section 2.4. The specific heat of Type-I superconductors will be described in section 2.5. Type-II superconductors are currently used in industry, their theory and specific heat jump will be explained in section 2.6. Specific heat of some magnetic materials will be described in section 2.7. The final section 2.8 of Part I, consists of high field and magnetic studies, where different kinds of materials, evaluation of H_{C2}, and the possibility of co-existence of magnetism and superconductivity at the same time will be studied.

Part II consists of sections 2.9 - 2.11. In section 2.9, synthesis of Chevrel Phase materials (MMo_6S_8) has been provided, section 2.10 gives the structure of Chevrel phases and section 2.11 provided some electronic and magnetic properties of these materials. In section 2.12, the summary of the whole chapter is provided.

2.2: Definition of Specific Heat

The heat capacity of a system of arbitrary mass can be defined as,[1];

$$C = \lim_{\Delta T \to 0} \left(\frac{\Delta Q}{\Delta T}\right) \qquad (2.1)$$

where ΔQ is the amount of heat require to add to the system to raise its temperature by ΔT. The specific heat capacity or, more simply, the specific heat which is independent of mass can be obtained by dividing Eq. (2.1) by the system mass 'm' to yield,

$$c \equiv \frac{C}{m} = \left(\frac{dQ}{dT}\right) \qquad (2.2)$$

where dQ represents a very small amount of heat required to raise the temperature of a unit mass of the system by an amount dT. In general, the heat quantity required, will not only depend upon the temperature of the system but also on the changes that may occur in other physical properties (or state variables) which define the equilibrium state of a thermodynamic system for example pressure P, volume V, and temperature T, where the equation of state has the functional form as f(P,V,T) =0 and involves only three variables.

In most theoretical calculations, the heat capacity is normalised to per mole as this refers to a fixed number of particles. This quantity is also referred in literature as the specific heat. In S-I System, the units are $J.kg^{-1}\text{-}K^{-1}$ for c_p and c_v. The subscripts p and v represents the specific heat at constant pressure and at constant volume respectively.

2.2.1. Specific Heat Relationship to Other Thermodynamics Quantities

The first law of thermodynamics, in its differential form can be written as,

$$dQ = dU + dW \qquad (2.3)$$

where,

dQ= Heat added to a substance

dU = Change in Internal Energy due to applied heat

dW = The work done by the system.

Or

$$\frac{dQ}{dT} = \frac{dU}{dT} + \frac{PdV}{dT} \qquad (2.4)$$

if volume is constant,

$$C_v = \left(\frac{dU}{dT}\right)_v \qquad (2.5)$$

From the second law of thermodynamics,

$$dQ = TdS \tag{2.6}$$

and in terms of entropy,

$$C = T\left(\frac{\partial S}{\partial T}\right) \tag{2.7}$$

The change in internal energy can be written as;

$$dU = TdS - PdV \tag{2.8}$$

Other principle thermodynamics functions are (in differential form):

i): Helmholtz Free Energy,

$$dF = d(U - TS) = -SdT - PdV \tag{2.9}$$

ii): Enthalpy,

$$dH = d(U + PV) = TdS + VdP \tag{2.10}$$

iii): Gibbs Free Energy,

$$dG = d(U - TS + PV) = SdT + VdP \tag{2.11}$$

Entropy can be defined as,

$$S= - (\partial F / \partial T)_v \tag{2.12}$$

and

$$C_v = T\left(\frac{\partial S}{\partial T}\right) = -T\left(\frac{\partial^2 F}{\partial T^2}\right) \tag{2.13}$$

As Cp - Cv $\approx$ 1% close to $\theta_D/3$ and 0.1% at $\theta_D/6$, one can take Cp $\approx$ Cv (for Solids).

2.3: Specific Heat of Normal Materials:

2.3.1: Lattice Specific Heat

All lattice dynamic theories are based upon the harmonic approximation in which each atom is bound to its site by a harmonic force. When a solid is heated, the atoms vibrate about their mean positions like a set of harmonic oscillators with some quantised energy E. This idea explains successfully the lattice specific heat of solids.

In the classical treatment, the Cv due to the lattice vibrations can be obtain by averaging over a Boltzmann distribution. The average energy per atom can be written as [13-16],

$$< E > = \frac{\int_0^\infty \int E\, e^{\frac{-E}{k_B T}} dxdv}{\int_0^\infty \int e^{\frac{-E}{k_B T}} dxdv} \qquad (2.14)$$

where k_B is the Boltzmann constant, x, the amplitude to either side and v, the velocity in one dimension. For a crystal which has N atoms, each is oscillating in three dimensions, the total energy is 3N<E> and Cv can be obtained using Eq. 2.5 as,

$$C_v = (\frac{\partial U}{\partial T})_v = 3Nk_B = 3R \qquad (2.15)$$

At room temperature this result, explains very well the Cv of solids. But at lower temperatures, Cv rapidly falls toward zero which is against the prediction of the classical theory. This can be seen in **Fig. 2.1**. Consequently a new theory was developed to explain the behaviour of Cv at low temperatures.

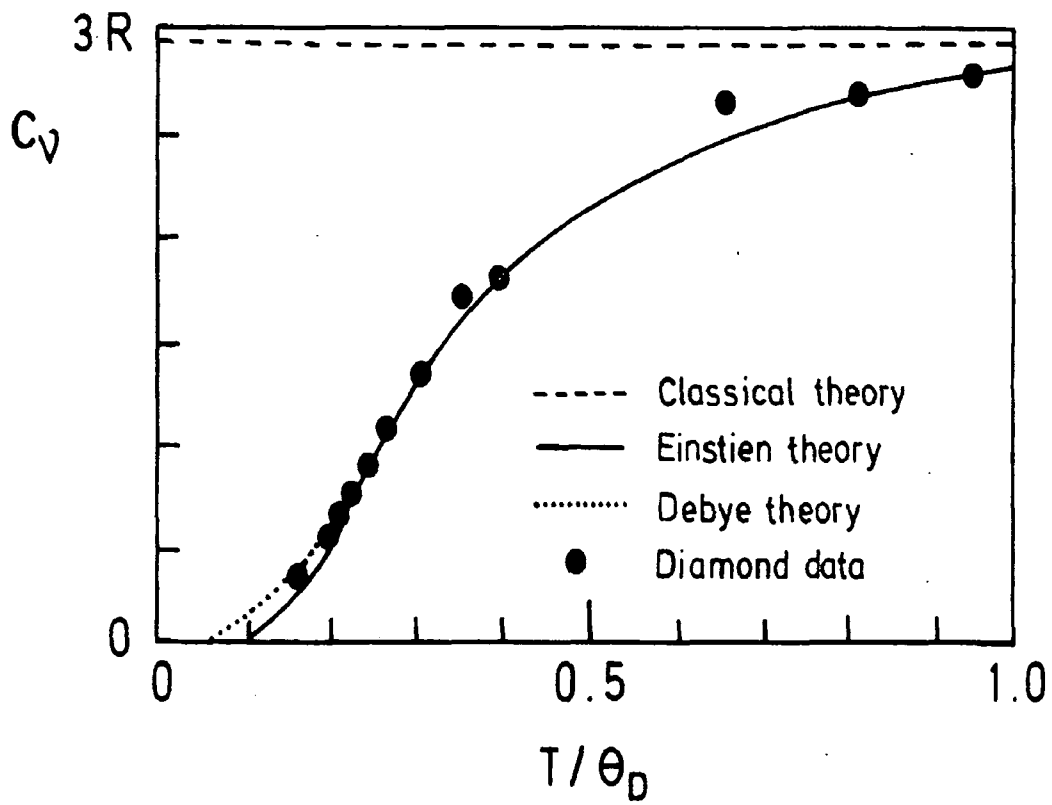

Fig.2.1). The comparison of Heat Capacity of Diamond obtained experimentally to that of obtained by theories. [13]

2.3.2: Einstein Theory of Specific Heat

To explain specific heat at low temperatures, Einstein (1907) [7], used the concept of quantised energy, where every state is discrete given by an energy,

$$E_n = (n + 1/2)\hbar\omega \qquad (2.16)$$

where n =0,1,2, ..., E_n is the energy of the nth state of harmonic oscillator vibrating with an angular frequency ω, $\hbar = h/2\pi = 1.055 \times 10^{-34}$ J.s, with h as Planck's constant. As every atom has a discrete energy E_n, so replacing the integration sign by a summation in Eq. 2.14, one gets,

$$< E > = \frac{\sum_{n=0}^{\infty} E_n \exp(\frac{-E_n}{k_B T})}{\sum_{n=0}^{\infty} \exp(\frac{-E_n}{k_B T})} \qquad (2.17)$$

Putting the value of E_n from Eq. 2.16 in Eq. 2.17 and differentiating it with respect to T, the specific heat becomes,

$$C_v = 3Nk_B \frac{(\frac{\hbar\omega_E}{k_B T})^2 \exp(\frac{\hbar\omega_E}{k_B T})}{[\exp(\frac{\hbar\omega}{k_B T})-1]^2} \qquad (2.18)$$

where ω_E is called Einstein angular frequency, (an adjustable parameter, that is, different for different solids).

2.3.3: Debye theory (1912) of specific heat

The Einstein theory gave us an improved fit to the heat capacity but at low temperature, this fit dropped-off faster than observed experimentally. This fit also led to a thermal conductivity of the wrong magnitude and temperature dependence. This drawback can be removed by considering that all the atoms in a solid do not vibrate independently at the same frequency, but that the crystal lattice as a whole possesses well-defined normal modes. Debye [8] used this concept and proved that a crystal with N lattice points can be excited in at most 3N acoustic vibrational modes.

Instead of an assembly of 3N oscillators all of frequency ω_E we consider a distribution of normal modes of which the number with frequencies between ω and $\omega+$ $d\omega$ is given by $D(\omega)d\omega$[13-16,18], where

$$\int_0^{\omega_D} D(\omega)\, d(\omega) = 3N \tag{2.19}$$

and ω_D, the Debye frequency, is the maximum frequency that can be excited and $D(\omega)$, known as the phonon density of states given by,

$$D(\omega) = 3V\omega_D^2/(2\pi^2 v^3) \tag{2.20}$$

where 'V' is the sample volume and 'v' is the velocity of elastic waves.

The mean thermal energy <E> of the lattice vibrations, can be determined, using the Bose-Einstein distribution for $n(\omega)$ so that:

$$\langle E \rangle = \int_0^{\omega_D} D(\omega)\, n(\omega)\hbar\omega\, d(\omega) \tag{2.21}$$

$$= \frac{3Vh}{2\pi^2 v^3}\int_0^{\omega_D} \frac{\omega^3}{\exp(\frac{\hbar\omega}{k_B T})-1} d\omega \tag{2.22}$$

substituting $V/v^3 = 3N\, 2\pi^2/\omega_D^3$ and $x = \hbar\omega/k_B T$, and a characteristic temperature $\theta_D = \hbar\omega/k_B$ (called Debye temperature) in Eq. 2.22, Cv becomes,

$$C_v = 9Nk_B(\frac{T}{\theta_D})^3\int_0^{\frac{\theta_D}{T}} \frac{x^4 e^x}{(e^x-1)^2} dx \tag{2.23}$$

To check the validity of Eq.(2.23), it can be compared with experimental results. But one must know the Debye temperature θ_D. The Debye temperature can be chosen, from Eq. 2.23, in such a way that when this value is substituted into Eq. (2.23), yields the best fit over the whole temperature range.

Mathematically it can be deduced using Eqs. (2.19) and Eq. (2.20),

$$\Theta_D = \frac{\hbar}{k_B}\left(6\pi^2 v^3 \frac{N}{V}\right)^{1/3} \tag{2.24}$$

where 'v' is an average velocity over all polarizations and mode directions. In determination of Cv, one often finds that the contribution of transverse modes is more than that of the longitudinal mode, due to its lower velocities. Similarly, materials with strong interaction forces and light atoms such as diamond and sapphire have relatively high θ_D, whereas soft materials with low acoustic velocities have smaller values.

It is clear from Eq. (2.23), that if Cv is plotted versus a reduced temperature T/θ_D, the Debye plot, then the curves obtained for all substances should collapse onto each other, that is, there is a universal curve for specific heat. Such a curve is shown

in **Fig. (2.2)** [13,14].

At high temperatures, when 'x' is small, the integral in Eq. (2.23), reduces to x^2dx and hence the energy becomes 3RT and on differentiating with respect to T, it yields the Dulong-Petit value i.e. 3R, for specific heat.

At low temperatures, when 'x' is large, i.e., $T << \theta_D$, we can take the limits of integration as zero and infinity. The integral then has the value $\pi^4/15$. Then [15],

$$C_v = 1941\left(\frac{T}{\theta_D}\right)^3 \quad J K^{-1} mol^{-1} \tag{2.25}$$

This is well-known Debye T^3 law. Thus at low T, the specific heat should decrease as T^3. A calculation shows that the cubic dependence should begin at temperature below $\theta_D/10$ and, the T^3 variation of the specific heat at very low temperatures is experimentally verified.

As Debye theory is strewn with approximations, it achieves greater validity at lower and high temperatures but serious error can occur at intermediate temperatures

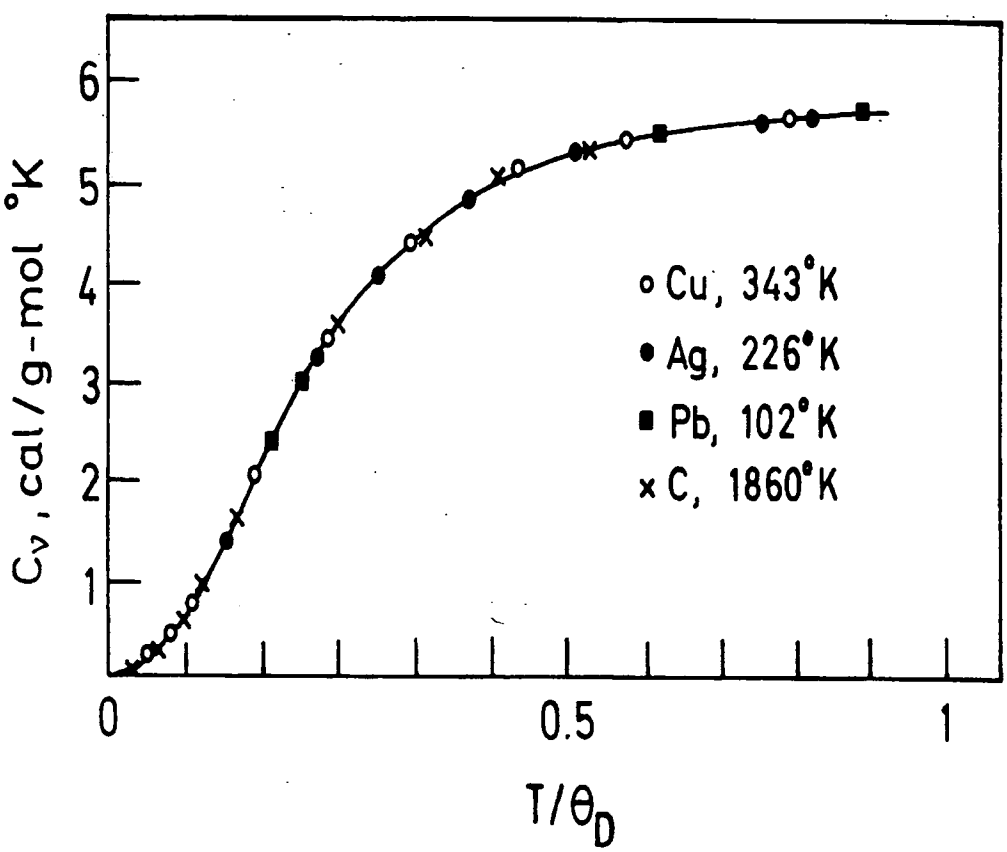

Fig.2.2). Specific heat versus reduced temperature for four substances verifying the universal curve for specific heat [14].

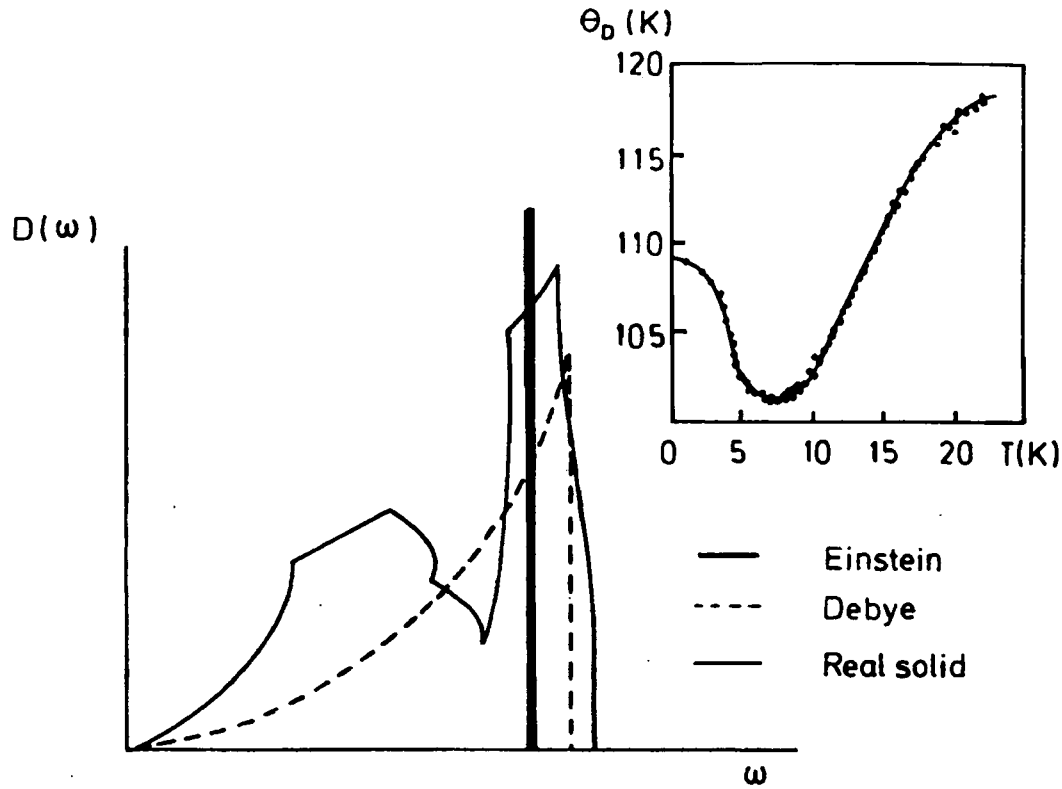

Fig.2.3: The Phonons density of states D(ω) used in the Einstein and Debye theories, compared with that of a typical real solid. The inset shows the variation in the Debye temperature θ_D, of Indium, due to the influence of the extra modes. [13,17].

due to the over simplification of the density of states D(ω). This is shown in **Fig. (2.3)** [17]. The slight deviations from T^3 that do exist are commonly represented as avariation of θ_D with temperature.

2.3.4: Electronic Specific Heat

The conduction electrons in a normal metal are regarded as a highly degenerate Fermi gas obeying Fermi-Dirac statistics. The Pauli exclusion principle leads to the Fermi-Dirac distribution given by [1],

$$f(\varepsilon) = \frac{1}{\exp(\frac{\varepsilon-\varepsilon_F}{k_B T})+1} \qquad (2.26)$$

where f(ϵ) gives the probability that an electron has an energy 'ϵ' at a temperature T, and 'ϵ_F', represents the Fermi Energy. The Fermi temperature can be evaluated as,

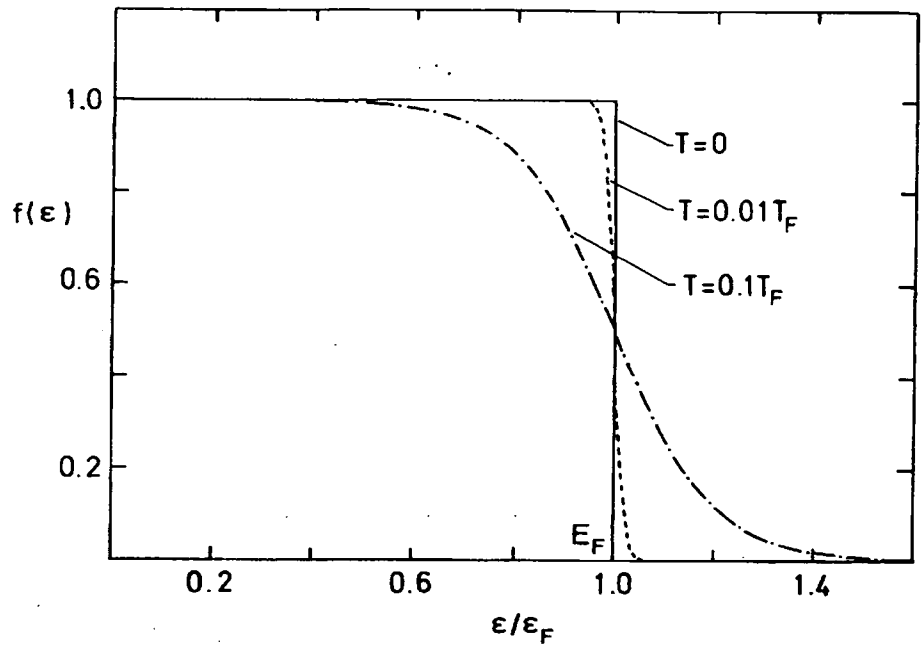

Fig.2.4: Variation of the Fermi-Dirac function (Eq. 2.26) as a function of energy for various temperatures. [1].

$$T_F = \epsilon_F/k_B \approx (10^4 - 10^5\,K) \text{ in metals.}$$

Ground and higher temperature occupation values are described in **Fig. 2.4.**

At room temperature, Electronic specific heat $C_e \approx 2RT/T_F = 10^{-2}R$ or approximately 1% of the lattice contribution.

At low temperatures, $T <<< T_F$ and [15],

$$C_e = \frac{\pi^2}{3} n(\varepsilon_F) k_B^2 T \equiv \gamma T \tag{2.27}$$

where $n(\epsilon_F)$ is the density of states of the electrons at Fermi level given by,

$$n(\varepsilon_F) = \frac{m}{\pi\hbar^2}\left[\frac{3zN_A V_m^2}{\pi}\right]^{\frac{1}{3}} \tag{2.28}$$

where, 'm' is the mass of the electron, $z = N_A/N$ is the number of conduction electron per atom (valency) ratio and V_M is the molar volume.

2.3.5: Experimental Specific Heat at Low Temperatures

The total specific heat in graphical form, at constant volume in the liquid

helium temperature range (~2-10 K) is shown in **Fig.2.5a**. This representation can be written as in mathematical form,

$$C = \gamma T + \beta T^3 \qquad (2.29)$$

where the γ is the Sommerfeld constant defined by Eq. 2.27 and β is defined by Eq. 2.25. The electronic term is linear in T and is dominant at low temperature, while β is dominant at higher temperatures. It is convenient to exhibit the experimental values of C as a Debye plot of $C\,T^{-1}$ verses T^2 which gives a straight line (shown in **Fig.2.5b**), yielding values for the slope β (hence, θ_D) and intercept γ [15] which is proportional to the electronic density of states at the Fermi level (Eq. 2.27).

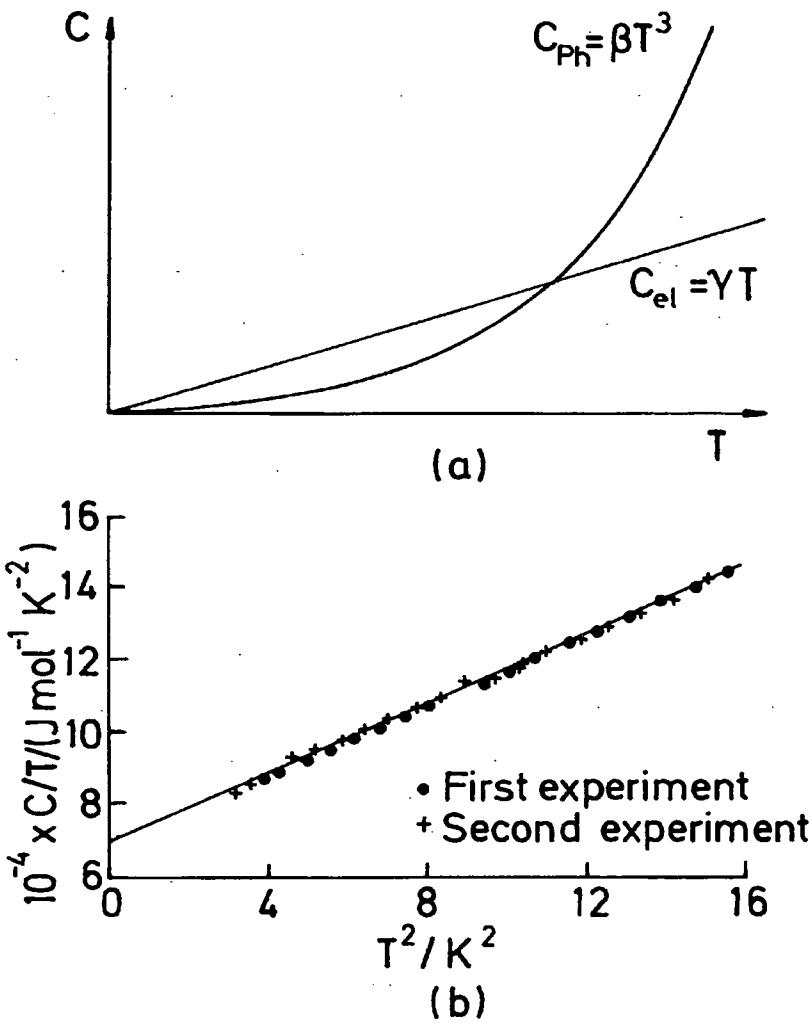

Fig.2.5: The Specific Heat of metals at low temperatures. (a) In the Helium region, the electronic contribution C_{el} can dominate that of the lattice, C_{ph} (b). A plot of C/T against T^2 for copper, showing the very good linear relationship which is obtained [15].

2.4: Specific Heat of Superconductors

The preceding general discussion of low-temperature specific heat naturally leads to a consideration of its use in experimental investigations of the superconducting transition. A typical specific heat curve for Type-I superconductor is shown in **Fig. 1.3**. Calorimetry, a particularly powerful tool in this regard, possesses numerous advantages: [19-22,37]

1) As a bulk-property measurement technique it is superior to electrical resistivity for the study of multiphase or otherwise inhomogeneous samples;

2) The specific heat result yields not only T_C but also two other important solid-state parameters, γ and θ_D;

3) If the transition, for one reason or another is sharp but incomplete, the relative magnitude of the specific heat jump at T_C, viz., $\Delta C/\gamma T_C$, in comparison to some expected value (such as the BCS value, 1.43, or perhaps some more appropriate experimentally calibrated ratio) yields a measure of the fraction of the specimen that participates in the observed transition;

4) If on the other hand the transition is broad, a knowledge of the form of the unrounded specific heat temperature dependence below T_C enables one to derive a transition temperature distribution function related to the metallurgical condition of the sample. In the following sections the specific heat of type-I and type-II superconductors is presented.

2.5: Specific Heat of Type-I Superconductors

Most of the thermal properties of type-I superconductors have been derived from classic thermodynamics and from the Bardeen-Cooper-Schrieffer (BCS) theory;[12]. The corresponding theoretical results have been already discussed in section 1.5. The effect on specific heat of type-I superconductors of magnetic field will be described.

2.5.1: First-order and second-order transition

In the most simple approximation, we assume that the Gibbs free energy G_n of the normal phase is independent of the applied field. When a field is applied to a Type-I superconductor which is in superconducting state, it will induce a magnetization (magnetic moment per unit volume) of magnitude $M = -H$ because of the perfect diamagnetism. In this case, the Gibbs free energy will be different from that of its

normal state energy G_n and that of its superconducting state (in 0-field), See section 1.3.

In terms of specific heat $C_p = T(\partial S/\partial T)_p$, the difference in specific heats of the two states may be expressed in molar form, (Eq.1.4),

$$C_n - C_s = -\mu_0 T\left[H_C\frac{\partial^2 H_C}{\partial T^2} + \left[\frac{\partial H_C}{\partial T}\right]^2\right]V_m \qquad (2.30)$$

In the absence of a magnetic field, when a sample is heated, the transition from superconducting to normal state takes place at T_C with no change in entropy as the superconducting state is more ordered than the normal state therefore $S_S \leq S_n$ but with a discontinuity in specific heat given by,

$$(C_n - C_s)_{T_C} = -\mu_0 T_C\left[\frac{\partial H_C}{\partial T}\right]^2 V_m \qquad (2.31)$$

If the heating is performed in a constant applied field of magnitude H, then the transition from the superconducting state takes place at a temperature $T_1 < T_C$ such that $H_C(T_1) = H$; this results in a sudden increase in entropy (Eq.1.3) and the absorption of a latent heat given by

$$L = -\mu_0 T H_C\frac{\partial H_C}{\partial T}V_m \qquad (2.32)$$

Thus, the transition implied by these relations is first order in a magnetic field and second order in the absence of a magnetic field [1, 23, 24].

2.5.2: Comparison between Theory and Experiment

The comparison between the predictions of theory and the experimental values of specific heat, can be undertaken by separating the observed specific heat into electronic and lattice contributions using Eq. 2.29, as:

$$C = \gamma T + C_{ln} \qquad (2.33)$$

and for the superconducting state,

$$C = C_{eS} + C_{lS} \qquad (2.34)$$

Where C_{eS} is the electronic specific heat in the superconducting state, and C_{ln} and C_{lS} are the lattice specific heat in the normal and superconducting states respectively. The specific heat of the electrons in the superconducting state does not follow the T^3 law, but follows an exponential behaviour. This exponential behaviour can be destroyed by applying a magnetic field greater than H_C and the material returns to its normal state

even below T_C (Fig.1.13 of ref 1. pp.47). The analysis is simplified by the assumption that $C_{ln} = C_{ls}$. This leads to the relation,

$$C_{eS} = C_S - C_{ln} \qquad (2.35)$$

At sufficiently low temperatures, C_{eS} can be obtained as a function of temperature from the observed values of C_S , since C_{ln} can be calculated using Eq. (2.24).

Although deviations of C_{es} from a T^3-law had been observed earlier, until 1954 the measurement techniques were not sufficiently developed to reveal an exponential temperature dependence of C_{es} at the very lowest temperatures [25,26]. An exponential variation suggested the existence of an energy gap in the electron excitation spectrum, since the number of electrons excited across such a gap would vary exponentially with temperature.

The observation of isotope effect ($T_C \sim \propto M^{-1/2}$) in 1950 suggested a fundamental connection between the electrons in the superconducting state and the phonons of the lattice, since phonon frequency is also approximately proportional to $M^{-1/2}$.

These empirical observations provided important information for the microscopic mechanism of superconductivity and ultimately led to the formulation of the quantum theory of superconductivity by Bardeen et. al. [12] discussed in chapter 1.

2.5.3: Critical Field $H_C(0)$ and Lower Critical Field $H_{C1}(0)$

The thermodynamic critical field $H_C(0)$ for type-I superconductor can be calculated [2, pp.492] making the use of volumetric coefficient of specific heat γ_v ($J.m^{-3}.K^{-2}$) as;

$$H_C(0) = 7.65 \times 10^{-4} \times (\gamma_v)^{1/2} T_C. \qquad (2.36)$$

The lower critical field $H_{C1}(0)$ for type-II superconductor can be estimated using the following relation [2, pp.520];

$$H_{C1}(0) = \frac{\ln[0.902 H_{C2}(0)/H_C(0)]}{[1.276 \times H_{C2}(0)/H_C(0)]} \qquad (2.37)$$

where, $H_{C2}(0)$ is the upper critical field described in detail in the coming sections.

2.6): Specific Heat of Type II Superconductors

2.6.1). GLAG Theory:

The GLAG theory is extensively used for analysing superconductors in a

magnetic field because of the spatial inhomogeneities that occur due to penetration and the intermediate state in type I superconductors, and the mixed state in type-II superconductors. This was developed by Ginsburg and Landau [27] as is described in chapter 1, Abrikosov [28,29] and Gor'kov [30,31], who were all Russian scientists working in early and late 1950's. According to the GLAG theory, there is no entropy change during either transition, that is, between the superconducting (Meissner) state and mixed states or between the mixed and normal states. In the whole process no latent heat is involved, therefore both transitions are of the second order. It may be shown [1,20,24] that such transitions have a jump in the specific heat given by, from Meissner state to Mixed state,

$$C_s - C_m = T_1\left(\frac{dH_{C1}}{dT}\right)^2\left[\left(\frac{\partial M_s}{\partial H}\right)_T - \left(\frac{\partial M_m}{\partial H}\right)_T\right]V_m \qquad (2.38)$$

and from Mixed state to Normal state,

$$C_m - C_n = T_2\left(\frac{dH_{c2}}{dT}\right)^2\left[\left(\frac{\partial M_m}{\partial H}\right)_T - \left(\frac{\partial M_n}{\partial H}\right)_T\right]V_m \qquad (2.39)$$

where the subscripts s, m, and n refer to the superconducting (Meissner), mixed and normal states, respectively, and T_1 and T_2 are the temperatures at which the superconducting-to-mixed and the mixed-to-normal transitions occur, H_{C1} and H_{C2} are the thermodynamic critical fields for type-II superconductors. The nature of the specific heat discontinuities can be understand by considering a typical example.

When the specific heat measurements are performed in a constant applied field H as a function of increasing temperature, it will give a straight line parallel to the temperature axis (x-axis) in the H-T plane as shown in **Fig. 2.6**. We may expect to observe two changes in the specific heat, first at T_1 and then at T_2. At temperature T_1, $H = H_{C1}(T_1)$ and the sample passes a transition from the Meissner state to the mixed state. Using the Abrikosov [28-29] model, the slope of the magnetisation curve in the mixed state ($\partial M_m/\partial H$) becomes infinite at H_{C1}, from which it can be shown that at T_1 the entropy is continuous but has an infinite temperature derivative in the mixed state. Eq. (2.38) suggests that a singularity in specific heat will appear at T_1, yielding a 'λ-like anomaly due to the lack of discontinuity in the entropy. The sharp peak observed at T_1 in **Fig.2.6** is consistent with such an anomaly. Thus the transition from Meissner to mixed state is a second order transition even in a applied field as no latent heat is

involved. At T_2 the sample is passing from the mixed to the normal state. Unusual behaviour may also be expected at T_2 where $H = H_{C2}(T_2)$. From **Fig.1.2**, it can be seen that if H_{C2} is approached from below and above, $\partial M_m/\partial H > 0$, and $\partial M_n/\partial H = 0$, respectively and there would be no sudden increase in entropy as the entropy is rising from the mixed to normal state. Thus Eq. (2.39) indicates that there will be a sudden drop in specific heat at T_2 as the specimen undergoes a transition from the mixed to the normal state. Such a drop is indeed observed at T_2 in **Fig.2.6.** Also the appearance of the specific heat versus temperature curve for a type II superconductor is dependent on the strength of the applied field relative to $H_{C1}(0)$ and $H_{C2}(0)$.

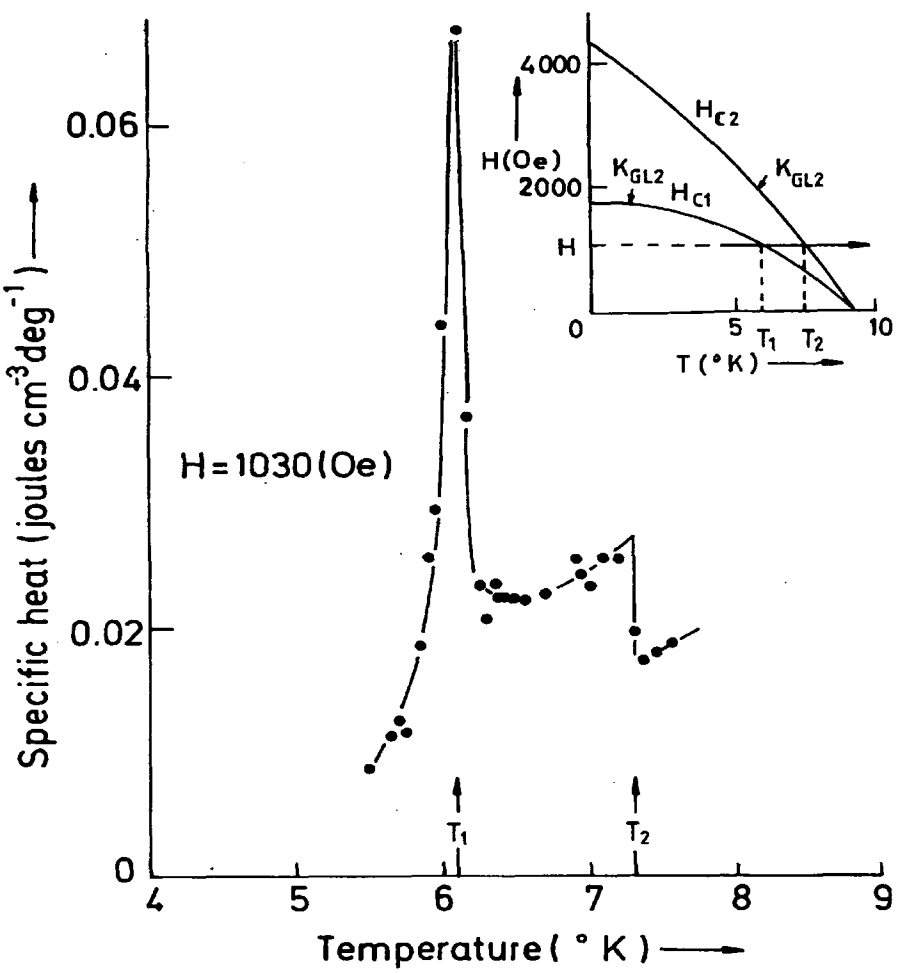

Fig.2.6). Specific heat of Type-II superconductor (Nb) measured in a constant applied magnetic field. Inset: Schematic representation of $H_{C2}(T)$ versus T for two values of the Ginzburg- Landau parameter κ_{GL}, indicating separate transitions into the mixed state during cooling in applied field H_a at $T_S = T_1$ & T_2, respectively [1,20,37].

2.6.2): The Electronic Specific Heat in the Mixed State:

The electronic specific heat of a superconductor in the mixed state can be related to the normal state specific heat in terms of the second derivative with respect to temperature of the molar or unit-volume Gibbs free energy differences between those states. According to Maki [32-35], for example, in unit volume terms, only in the regimes (i) just below H_{C2}, and (ii) just above H_{C1},

$$C_{em}^{v} - C_{en}^{v} = -T\frac{\partial^2}{\partial T^2}(g_m - g_n) \tag{2.40}$$

Maki's work was followed by Van Vijfeijken [36], considering the Gibbs free energy density, whose calculations are valid over the entire mixed state region except near the $H_{C2}(T)$ curve. That phenomenological expression is [36, Eq.3.90],

$$C_{em}^{v} = \gamma_v T - \frac{H_{C0}T}{2\pi T_C^2}\left[\frac{\sqrt{2}\kappa H_{C0} - H_a}{\sqrt{2}\kappa - \ln\kappa(\sqrt{2}\kappa)^{-1}}\right] + \frac{3H_{C0}^2 T}{2\pi T_C^2}\left[\frac{\sqrt{2}\kappa}{\sqrt{2}\kappa - \ln\kappa(\sqrt{2}\kappa)^{-1}}\right]t^2 \tag{2.41}$$

where C^{v}_{em} is electronic specific heat per unit volume in the mixed state, γ_v is electronic specific heat coefficient per unit volume, κ is the Ginzburg-Landau parameter, H_{C0} is the thermodynamic bulk critical field at T = 0, H_a is the applied field and the reduced temperature $t = T/T_C$. Eq. 2.41 has the form,

$$C_{em} = (A_1 + A_2 + A_3 H_a)T + BT^3 \tag{2.42}$$

which is similar to the Eq. 2.29. It means mixed state specific heat data should also lie on a straight line in zero field when plotted C_{em}/T versus T^2 and the y-intercept A_1+A_2 and the slope B can be evaluated. The constants A_1, A_2 and A_3 can be determined from the Eq. 2.41. The comparison between theory (Eq.2.41) and experiment was done by Vijfeijken [36] using experimental data of Ferreira et.al. [38] on Nb and pointed that this rule works rather well y-intercepts are some 30 % higher than the predicted value by Eq. 2.41.

2.6.3): Height of the Specific Heat Jump:

The height of the specific heat jump at some temperature T_S, in a magnetic field, H_a can be obtained by subtracting the specific heat in the normal state from that of specific heat of the mixed state as [37],

$$\Delta C\,(T_S) = C_{em}(T_S) - C_n(T_S) = C_{em}(T_S) - \gamma T_S \tag{2.43}$$

After substituting ,

$$H_a = H_{C2}(T_S) = H_{C2}(0)[1 - t^2] \cong \sqrt{2}\,\kappa_{GL}\, H_C(T_S) \cong \sqrt{2}\,\kappa_{GL}\, H_C(0)[1-t^2] \qquad (2.44)$$

in Eq.2.41, leads to,

$$C_{em}^{v} = \gamma_v T - \frac{H_{C0}T}{2\pi T_C^2}\left[\frac{\sqrt{2}\kappa H_{C0} - \sqrt{2}\kappa H_{C0}[1-t^2]}{\sqrt{2}\kappa - \ln\kappa(\sqrt{2}\kappa)^{-1}}\right] + \frac{3H_{C0}^2 T}{2\pi T_C^2}\left[\frac{\sqrt{2}\kappa}{\sqrt{2}\kappa - \ln\kappa(\sqrt{2}\kappa)^{-1}}\right] t^2 \qquad (2.45)$$

$$C_{em}^{v} = \gamma_v T - \frac{H_{C0}^2 T}{2\pi T_C^2}\left[\frac{\sqrt{2}\kappa}{\sqrt{2}\kappa - \ln\kappa(\sqrt{2}\kappa)^{-1}}\right] t^2 + \frac{3H_{C0}^2 T}{2\pi T_C^2}\left[\frac{\sqrt{2}\kappa}{\sqrt{2}\kappa - \ln\kappa(\sqrt{2}\kappa)^{-1}}\right] t^2 \qquad (2.46)$$

$$C_{em}^{v} = \gamma_v T + \frac{2H_{C0}^2 T}{2\pi T_C^2}\left[\frac{\sqrt{2}\kappa}{\sqrt{2}\kappa - \ln\kappa(\sqrt{2}\kappa)^{-1}}\right] t^2 \qquad (2.47)$$

After substituting Eq. 2.47 into Eq. 2.43, and $t = T_S/T_C$, leads to,

$$\frac{\Delta C(T_S)}{\gamma T_S} = \frac{2H_{C0}^2}{\gamma 2\pi T_C^2}\left[\frac{\sqrt{2}\kappa}{\sqrt{2}\kappa - \ln\kappa(\sqrt{2}\kappa)^{-1}}\right]\left(\frac{T_S}{T_C}\right)^2 \qquad (2.48)$$

taking $\kappa \equiv \kappa_{GL}$

which is well-known, the Gorter-Casimir relative jump height at T_C, viz., $\Delta C/\gamma T_C = 2$. It follows from Eq. 2.48, that the height of the jump $\Delta C(T_S)$, varies as $T^3{}_S$; also, the normalized relative jump height can be expressed in the form,

$$\frac{\Delta C(T_S)/\gamma T_S}{\Delta C(T_C)/\gamma T_C} = \left(\frac{T_S}{T_C}\right)^2 \equiv t_S^2 \qquad (2.49)$$

Many peoples [38-39] have investigated the jump in Nb, and found the relative height of the jump is consistent with Eq. 2.49, within the experimental errors over the entire temperature range.

2.6.4: Rounded Calorimetric Transitions into the Mixed State

It is described in section 2.6.3, that after the application of magnetic field H_a, the superconducting transition occurs at a temperature T_S lower than the T_C which is given by Eq. 2.44, [See section, 2.6.3]. Thus T_S depends on H_{C2}, which in turn depends on the Ginzburg-Landau parameter κ_{GL}. But if one considers 'clean' and 'dirty' limit in the mixed state, then ,[37]

$$\kappa_{GL} = \kappa^{C}{}_{GL} + \kappa^{d}{}_{GL} \qquad (2.50)$$

$$= \kappa^{c}_{GL} + 7.49 \times 10^{3} \gamma^{1/2} \rho_{n} \qquad (2.51)$$

where κ^{c}_{GL} and κ^{d}_{GL} are the GL-parameter in clean and dirty limit respectively and ρ_n is the normal state residual resistivity. If one is taking Eq.2.44 and Eq. 2.50 together, it revealed that T_S responds to variations of T_C at constant H_{C2}, as well as to variations of H_{C2}, κ_{GL} and ρ_n at fixed T_C. Therefore, in the mixed state, the rounding of the transition (distribution in T_S) is mainly due to the impurities and deformation in the sample and is not restricted by the size of the sample.

2.6.5. The Paramagnetic Mixed State:

If Gibbs Free Energy 'G' is field dependent in a system, then one has to include the paramagnetism of the conduction electrons and equilibrium, along with H_{C2} has to be re-evaluated. Pauli paramagnetic limitation (PPL) was proposed by Clogston [40] and Chandrasekhar [41] independently and the theory was developed by Maki [32-35] and Werthamer, Helfond, and Hohenberg, WHH [42-44] who extended the solution of the linearised Gor'kov [30-31] equations for the upper critical field H_{C2} of a bulk type-II superconductors to include the effects of Pauli spin paramagnetism and spin-orbit impurity scattering. A schematic diagram of normal- and superconducting- state free energies versus applied field using WHH theory is shown in **Fig.2.7.**

The reduction of the upper critical field below its ideal value H^{*}_{C2} (upper critical field in the absence of paramagnetic limitation at 0 K), as a consequence of the presence of a finite H_{P0} (paramagnetically limited upper critical field at 0 K) has been described by the Maki parameter α as,

$$\alpha = \sqrt{2}\frac{H^{*}_{C2}}{H_{P0}} \qquad (2.52)$$

which can also be calculated from the normal state resistivity ρ_n (Ω-m) and volumetric specific heat coefficient γ_v ($J.m^{-3}.K^{-2}$), using the following relation [50] as ;

$$\alpha = 2.35 \times 10^{3} \gamma_{v} \rho_{n} \qquad (2.53)$$

It can be concluded from Eq. 2.52, that if one removes the PPL, then $\alpha \rightarrow 0$ [37, pp. 526]. The actual field H_{C2} can be increased to some higher field closer to H^{*}_{C2} by introducing a spin orbit scattering (SOS) frequency parameter λ_{SO} in the WHH theory and by a combined parameter β_M in the Maki's theory,

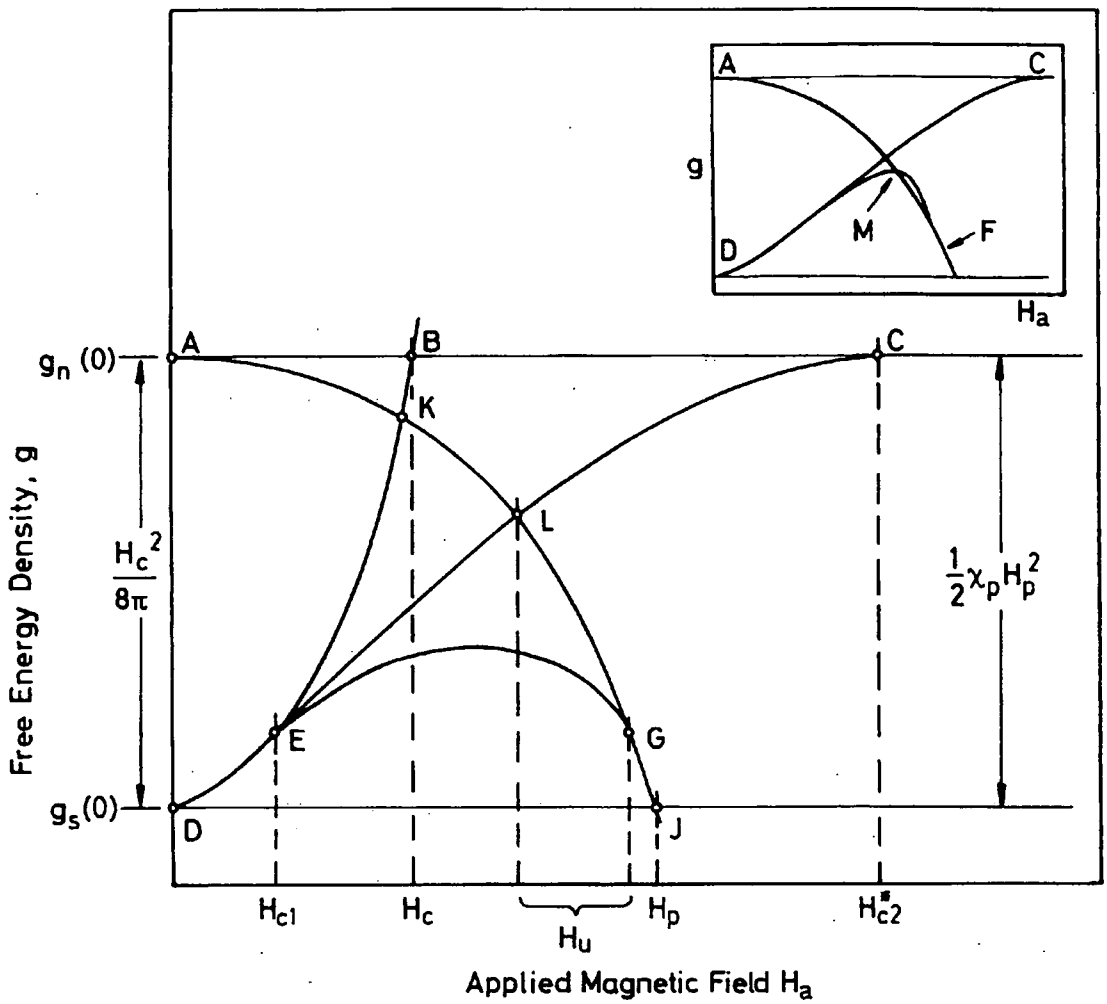

Fig.2.7: Schematic diagram of normal-state and superconducting-state free energies versus applied magnetic field, H_a. An arbitrary temperature $0 < T < T_C$ is assumed. The normal state in the absence of Pauli spin paramagnetism is represented by AC and its continuation; that in the presence of spin paramagnetism, of susceptibility χ_p, by the parabola AJ. The field-ignoring superconducting state is represented by DJ and its continuation; the point J defines the Clogston-Chanrasekhar paramagnetically limited first-order critical field, H_p. The parabola DB represents the response of a type-I superconductor to H_a, with point B itself at the thermodynamic critical field, H_C. The magnetisation of a GLAG (nonparamagnetic) type-II superconductor is represented by DEC with lower critical field, H_{C1}, and upper critical field H^*_{C2}, at E and C, respectively. The inclusion of spin in the normal state leads to a first-order transition at an upper critical field corresponding to L. The further inclusion of spin in the superconducting state can lead to a second-order transition at an upper critical field corresponding to G. Both these upper critical fields, designated H_u in the figure, are lower than H^*_{C2}. The inset suggests that within the context of paramagnetic theory it is also possible to have a first-order s/n transition (at M) followed by a second-order transition at F with a metastable state lying between the two - after Werthamer et .al [37,44].

$$\beta_M^2 \equiv \alpha^2(\frac{3\Delta_{00}}{\hbar})\,\tau_{SO} = 1.11\frac{\alpha^2}{\lambda_{SO}} \qquad (2.54)$$

where Δ_{00} = Energy gap at zero Kelvin (=3.53 $k_B T_C$), τ_{SO} = Spin-orbit scattering relaxation time and,

$$\lambda_{SO} = 2\hbar / 3\pi k_B T_C \tau_{SO} \qquad (2.55)$$

It is clear that as $\lambda_{SO} \to \infty$, $H_{C2} \to H^*_{C2}$, with the vanishing of the paramagnetic difference between the mixed and the normal states. Clearly the condition $\alpha \to 0$ is operationally equivalent to, (physically different) $\lambda_{SO} \to \infty$, which means that by doping heavy element one can increase the frequency of SOS which leads to an increase in H_{C2}.

But early experimental values of the critical field of Ti-alloys as shown in **Fig. 2.8,** [45-47] exceeded theoretical values even with λ_{SO} set equal to ∞, and incidently then went beyond the range of WHH theory itself, which required $\tau_{SO} >> \tau_{tr}$ [37]. However, Schopohl et. al. [48], shows that WHH theory with some corrections is still valid even when spin-orbit scattering is the dominant scattering mechanism.

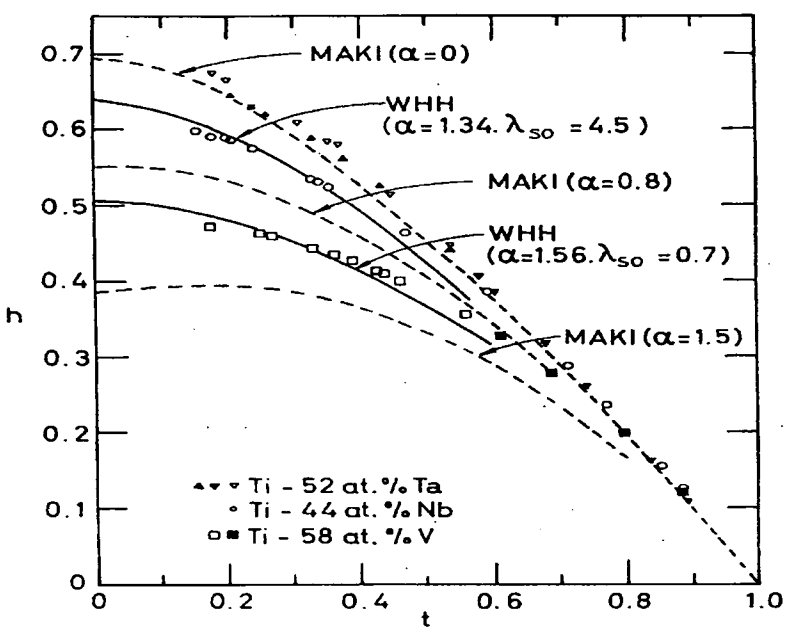

Fig.2.8: Variation of the reduced field h = H_{C2}/H_0 with reduced temperature t. Data points for t > 0.9 have been omitted. The dashed curves are taken from Maki's theory with λ_{SO} =0. The solid curves are from the WHH theory [Neuringer and Shapira, 45].

2.6.6. Pauli Paramagnetic Limiting

If the applied field is zero, there is a difference in the free energy of the superconducting and normal state. That difference is given by $\mu_0 H^2_C$, which vanishes at $H_a = H^*_{C2}$ as result of a quadratic field-induced increase in $g_s(H_a)$ [37,44]. The destruction of superconductivity by a magnetic field results from the pair breaking nature of the interaction of the field with both the conduction-electron orbits and the spins. The interaction [Fischer, 1990, 49] of the field with the conduction-electron spins, the Zeeman terms, leads, when treated alone, to a first-order transition at the paramagnetic limit H_{PO} [40-41], given by,

$$\mu_0 H_{P0} = 1.84\ Tc\ \ [Tesla] \qquad (2.56)$$

The above result is accepted as the pure "Paramagnetic limit" (pure in the sense that it determines the critical field in the absence of any other effect), which is illustrated in **Fig. 2.7.** {37. pp. 528}.

Furthermore, spin-orbit scattering will reduce the paramagnetic pair breaking and thus enhance the paramagnetic limit. In the limit of strong spin-orbit scattering ($\lambda_{SO}>>1$) the paramagnetic critical field becomes, [50];

$$H_P = 1.33\ \sqrt{\lambda_{SO}}\ H_{P0} \qquad (2.57)$$

In a real superconductor, both orbital and paramagnetic effects have to be taken into account when describing the critical field.

2.6.7: Evaluation of upper critical field H_{C2}

The upper critical field of a superconductor in the dirty limit ($\xi_0/l >> 1$) has been calculated by several groups [51-61]. Using the notation of WHH [44] who discovered the following expression for $H_{C2}(T)$ for a superconductor in the dirty limit,

$$\ln\left(\frac{1}{t}\right) = \left(\frac{1}{2}+\frac{i\lambda_{SO}}{4\gamma}\right)\psi\left(\frac{1}{2}+\frac{h+\frac{\lambda_{SO}}{2}+i\gamma}{2t}\right)+\left(\frac{1}{2}-\frac{i\lambda_{SO}}{4\gamma}\right)\psi\left(\frac{1}{2}+\frac{h+\frac{\lambda_{SO}}{2}-i\gamma}{2t}\right)-\psi\left(\frac{1}{2}\right) \qquad (2.58)$$

where $\psi(x)$ representing the di-gamma function given by; d/dx log [$\Gamma(x)$], where $\Gamma(x)$ is the gamma function, $t=T/T_C$, $h= 0.281\ H_{C2}(T)/H^*_{C2}(T)$, $\gamma = (\alpha^2 h^2 - \lambda^2_{SO}/4)^{1/2}$, α is the Maki parameter defined in Eq. 2.52-2.53 and $H^*_{C2}(0)$ is the orbital critical field at T=0 (as discussed above). In order to demonstrate the influence of λ_{SO} on the form of H_{C2} we show in **Fig.2.9a,** [50, pp.16] the reduced critical field $h_{C2}(t)$ for $\alpha = 3$ versus

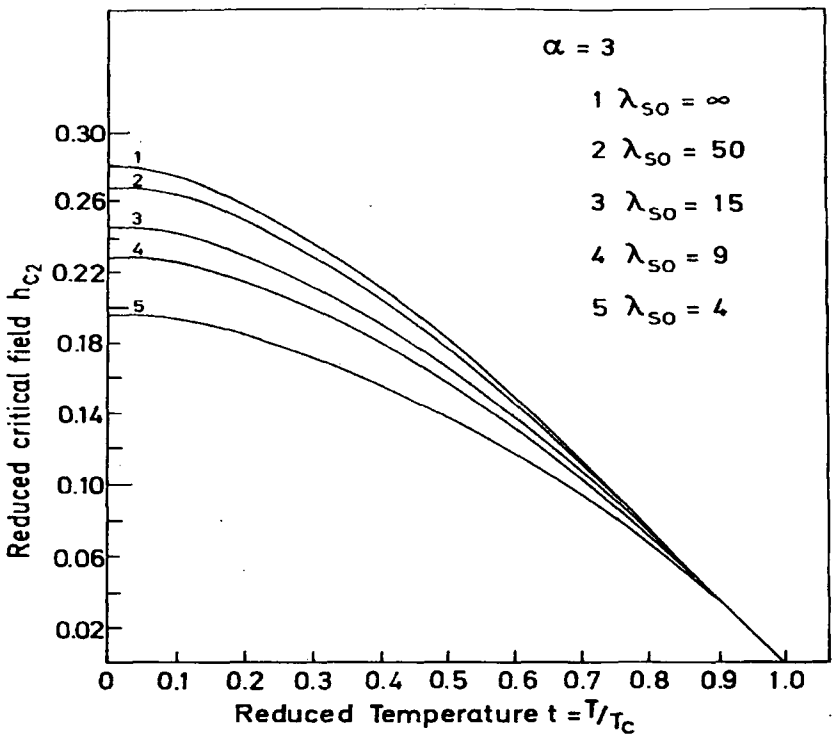

Fig.2.9a). Reduced critical fields h_{C2} for α = 3 and various λ_{SO} values. [50,55].

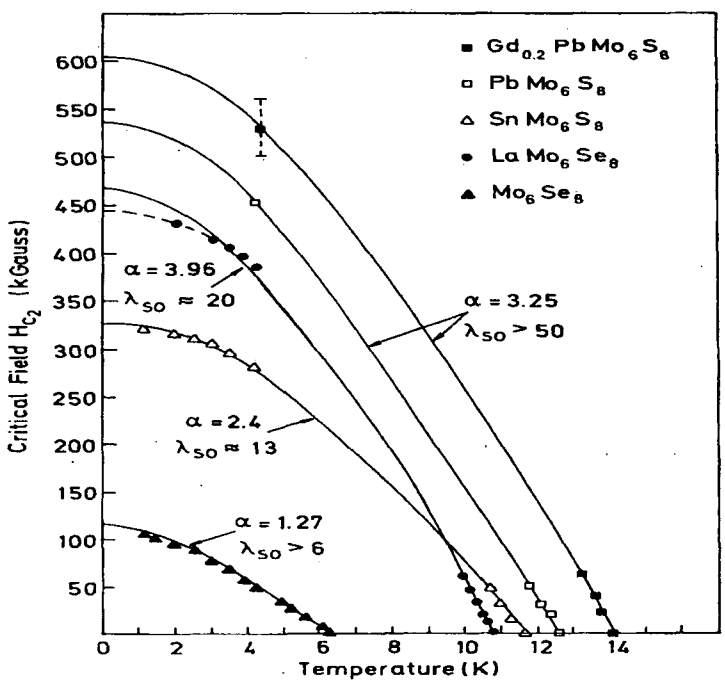

Fig.2.9b). Upper critical field H_{C2} versus temperature for several MMo_6X_8 compounds [50].

reduced temperature t = T/T_C, and for low values of λ_{SO} the form is completely different from that obtained for large λ_{SO}-values. The limit $\lambda_{SO} \rightarrow \infty$ gives the universal curve, determined by [50-53];

$$\ln\left(\frac{1}{t}\right) = \psi\left(\frac{1}{2}+\frac{h}{2t}\right) - \psi\left(\frac{1}{2}\right) \qquad (2.59)$$

Which is the temperature dependence of the orbital critical field $H^*_{C2}(T)$. In the case of $\lambda_{SO}>>1$ we may write a simplified equation for $H_{C2}(T)$ in terms of $H^*_{C2}(T)$[50,52,53];

$$H_{C2}(T) = H^*_{C2}(T) - 0.22\frac{\alpha}{\tau_{SO}T_C}H^2_{C2}(T) \qquad (2.60)$$

The second term on right hand side of Eq.2.60 is necessary to take into account the contribution of the interaction of the conduction electron spins with the external field. **Fig. 2.9b,** shows the critical field versus temperature for many compounds of the type MMo_6X_8, where M stands for metal, X = Chalcogen. The solid lines are calculated from Eq.2.58 using the values of λ_{SO} and α shown.

It can be concluded from Eq. 2.60 that the paramagnetic correction is especially important in high fields, i.e. for $T << T_C$, **Fig.2.8,** [45, fig.2] but that it disappears in the limit $T \rightarrow T_C$. In particular we have from Eq. 2.60;

$$\left(\frac{dH_{C2}}{dT}\right)_{Tc} = \left(\frac{dH^*_{C2}}{dT}\right)_{Tc} \qquad (2.61)$$

since the both slope are equal at T_C, which implies that the influence of the paramagnetic interaction will start well below Tc.

Using Resistivity Data

Using normal state resistivity ρ_n (Ω-m) data and volumetric coefficient of specific heat γ_v ($J.m^{-3}.K^{-2}$) for any superconductor, $H_{C2}(0)$ can be calculated as [2, pp. 517];

$$H_{C2}(0) = 3.1 \times 10^3 \times \gamma_v \rho_n T_C \qquad (2.62)$$

2.6.8. Calorimetric determination of $H_{C2}(T)$

For most of the studies, it is convenient to compare the experimental results with theoretical predictions of the WHH theory for a "dirty" type II superconductor [32-35, 42-44,54]. For no Pauli paramagnetic limiting (PPL), the upper critical field at 0 K, $H^*_{C2}(0)$ is given by,

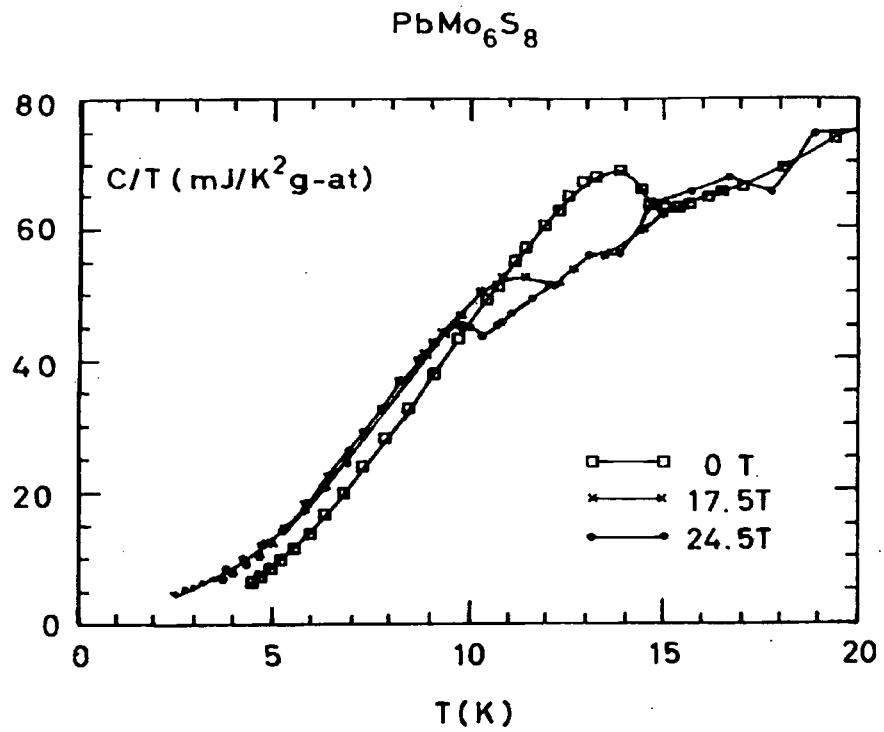

Fig.2.10a). Specific heat of $PbMo_6S_8$ in magnetic field [86].

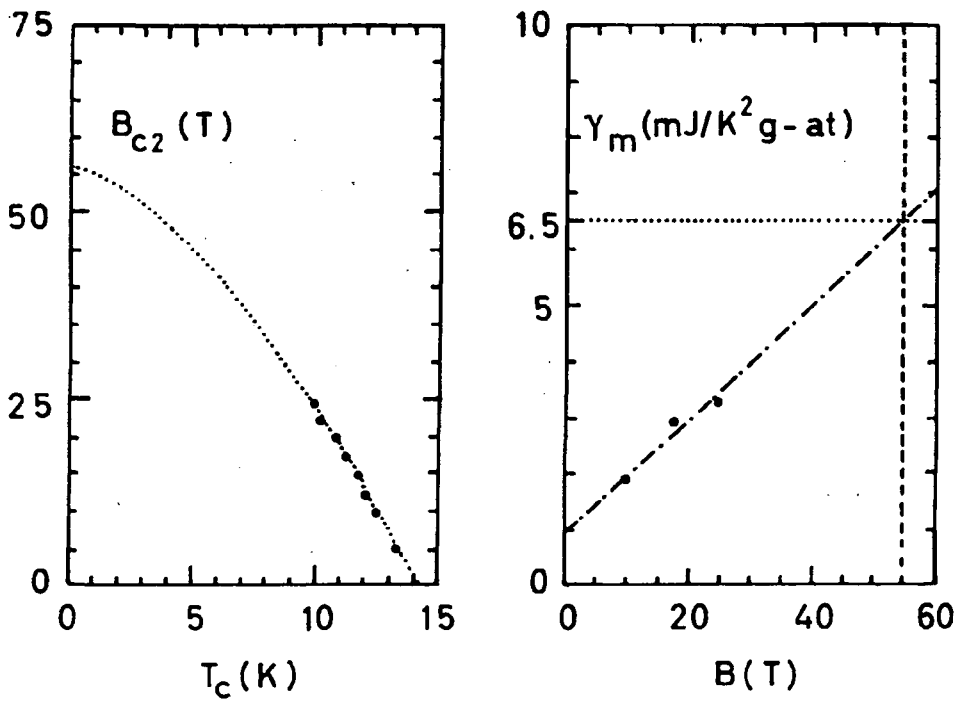

Fig.2.10b). Applied field versus critical temperature, using the data of Fig.2.12a, the dashed line is drawn as guide to the eye. [86].

$$H^{*}_{C2}(0) = -AT_C\left(\frac{dH_{C2}}{dT}\right)_{T=Tc} \qquad (2.63)$$

where Tc and $[dH_{C2}/dT]$ are measured quantities and A varies between 0.693 (for the dirty limit) and 0.726 (for the clean limit) [44,53-54, 85].

$H_{C2}(T)$ can be determined using the specific heat data. A typical example of a superconductor in magnetic field is shown in **Fig. 2.10a,** where, the data of $PbMo_6S_8$ in magnetic field is plotted. The suppression of the specific heat jump in field, will give the initial slope $[dH_{C2}/dT]_{T=Tc}$, from where $H^{*}_{C2}(0)$ can be calculated using Eq. (2.63). $H_{C2}(T)$ of $PbMo_6S_8$ has been calculated using the data of **Fig. 2.10a** which is shown in **Fig.2.10b** [86].

2.7: Specific Heat of Magnetic Materials:

The various forms of the magnetic materials are the result of the electronic spin configurations as explained in section 1.6. Here we'll give some idea about the specific heat of the magnetic materials. In the magnetic materials above their transition temperature T_M most of the metals like Al and ionic solids are paramagnetic. Below this temperature T_M, the material is magnetically ordered. This temperature has different name for different magnetic ordering, i.e., Curie temperature for the ferromagnetic materials and Neel's temperature for Anti-ferromagnetic materials. Thus, the thermal energy required to raise the temperature above this temperature T_M, may include a temperature-dependent magnetic contribution, which is expected to be observed in the specific heat.

2.7.1: Cp of Ferromagnetic Materials

The low temperature specific heat of a metallic ferromagnetic materials consists of three major terms and can be written as, [1]

$$Cp = \gamma T + \beta T^3 + \delta T^{3/2} \qquad (2.64)$$

where γT, the electronic contribution, βT^3, the phonons contribution, and the magnetic contribution is denoted by $\delta T^{3/2}$. The δ is the y-intercept of a graph between $Cp.T^{-3/2}$ and $T^{3/2}$. But, it is difficult to measure the magnetic contribution, as it is screened by the conduction electrons and lattice vibrations. However, very close to the magnetic transition temperature T_M (Curie temperature), a λ-type anomaly can be observed. This

points to an order-to-disorder transition accompanied by rapid changes in a number of thermophysical properties. The magnetic specific heat of Fe, Ni, and Co is displayed in the **Fig. 2.11a**. [63, pp. 49]. The Curie temperatures T_M (and other phase transitions), are visible.

2.7.2: Cp of Anti-ferromagnetic Materials

The low temperature specific heat of an anti-ferromagnetic material can be described by the following way,[1]

$$Cp = \gamma T + \beta T^3 + \delta' T^3 \qquad (2.65)$$

Eq. 2.65 described the total specific heat in the usual way. Only δ' term has been included for an anti-ferromagnetic materials. Which can be measured by plotting a graph between Cp/T vs. T^2. However, T^3-law for magnetic specific heat in these materials is of the same form as the T^3-law for lattice specific heat at low temperatures. This makes it virtually impossible to know the magnetic contribution in the total specific heat in these metallic anti-ferromagnetic materials. However, very close to the magnetic transition temperature, these materials also show a λ-type anomaly. This λ-type singularity is a characteristic of second-order phase transition. This behaviour can be seen in **Fig. 2.11b**, where C/R (gas constant) is plotted against T [64] for $TbPO_4$, which is an anti-ferromagnetic material.

2.7.3: The effect of Magnetic Field on the Cp of Magnetic Materials.

To demonstrate the effect of the magnetic field on the λ-type anomaly, Cp vs T at high temperature for a single crystal Ni [Connelly et.al.1971, 65] is displayed in **Fig.2.12a**. It is noted that the application of the magnetic field reduces the anomaly height and broadens it while the transition temperature is slightly increasing for high fields. Similarly the effect of the magnetic field on an antiferromagnetic material ($CeAl_2$), [Bredl,et.al,1978, 66] is shown in **Fig.2.12b.** It is shown that the application of the magnetic field, is decreases the anomaly height and smears it. In this system, the magnetic transition temperature is also decreasing.

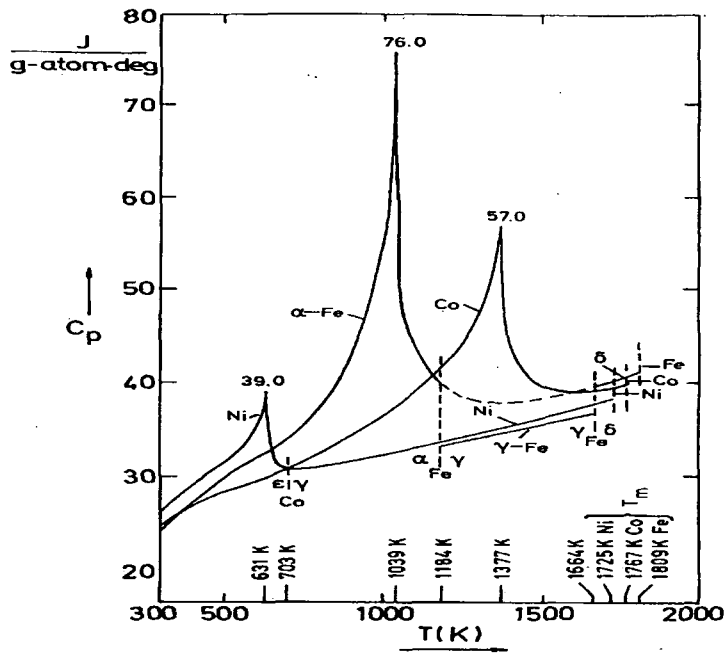

Fig.2.11a). The Specific heats Iron, Cobalt, and Nickel, (all are well-known ferromagnetic materials. C_M has been calculated after subtracting the electronic and lattice contribution [63].

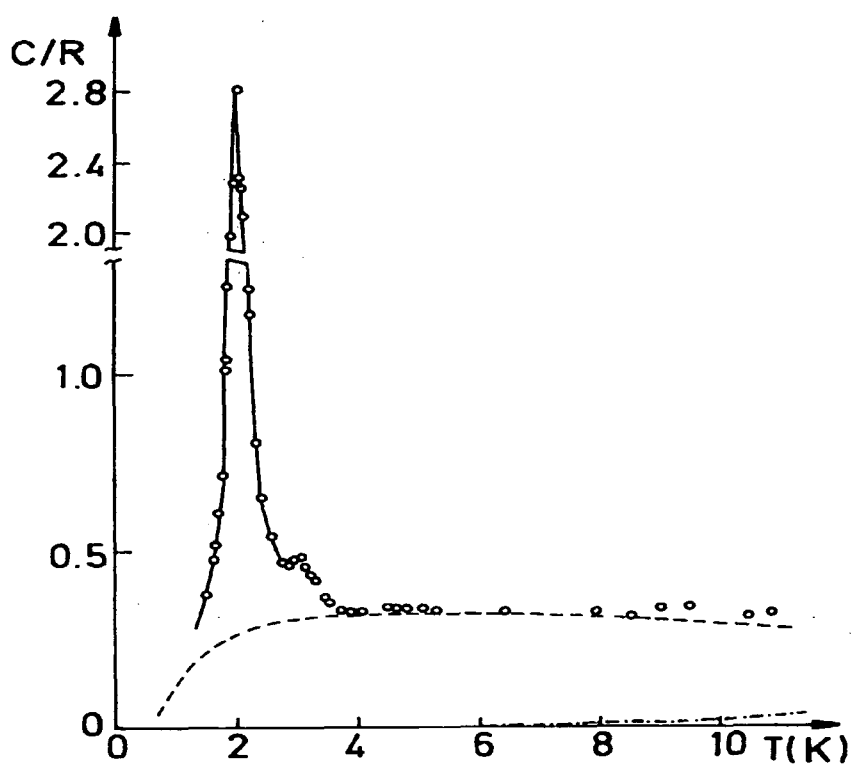

Fig.2.11b). Cp/R vs. T of an antiferromagnetic material. ($TbPO_4$) [64].

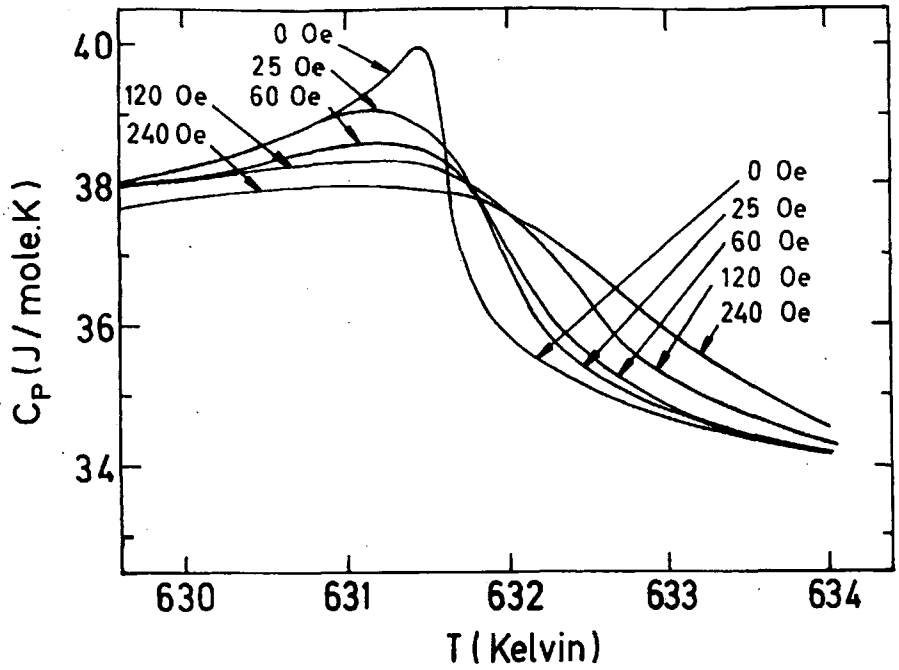

Fig. 2.12a). The Specific heat C/T vs. T of single crystal Ni, a ferromagnetic material, in the applied magnetic fields. Note that, after the application of the field, the height of the λ-type anomaly is reduced and smear out, While the transition temperature is slightly increased [65]

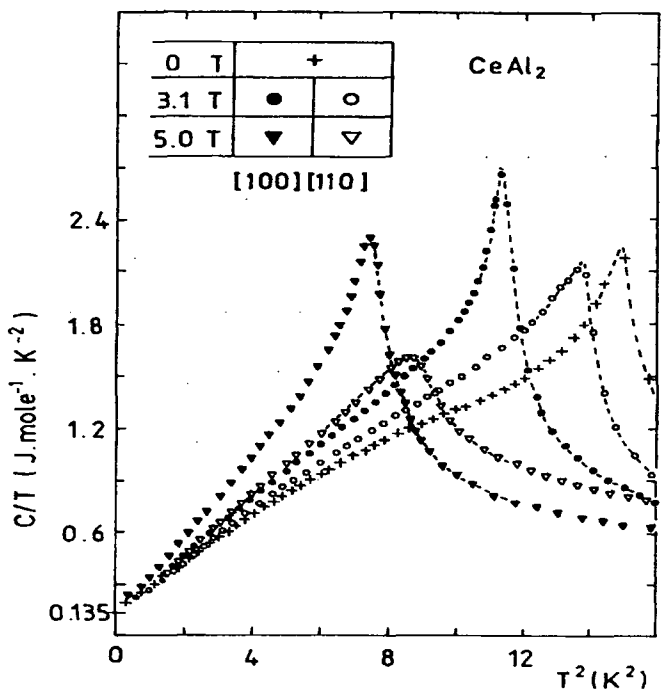

Fig. 2.12b). Low-temperature specific heat C/T vs. T^2 for $CeAl_2$, an antiferromagnetic material, in applied magnetic fields. Note that, after the application of the field, the height of the λ-type anomaly and the transition temperature are reducing [66].

2.7.4: Neutron/Susceptibility measurements on magnetic materials:

Magnetic materials have a sharp anomaly in specific heat measurements when reaching their transition temperatures, say at Neel's or Curie's temperature. But this confuses the issue of what class of material is under investigation. That can be found after performing neutron diffraction experiments or measuring the susceptibility. The difference between anti-ferromagnetic and ferromagnetic is profound, anti-ferromagnetic materials do not have any sharp anomaly in susceptibility measurements, while ferromagnetic materials do show an anomaly at the transition temperature, which makes it easy to find the order of the magnetic material [16]. Another profound difference between these two types of materials emerges after the application of the magnetic field. When a magnetic field is applied to an anti-ferromagnetic material, the height of the anomaly is reduced and the magnetic transition temperature decreases for higher fields, whereas for ferro-magnetic materials, a magnetic field will reduce the height of the anomaly but the transition temperature starts increases slightly.

2.8: Co-existence of Superconductivity and Magnetism:

Apparently magnetism and superconductivity have the opposite nature and co-existence of these two in the same material at the same time have confused many peoples. Ginzburg in 1957 [67], first discussed the possible reason for co-existence of superconductivity and magnetism. Matthias et al.[68-69] experimentally addressed this question for the first time in 1958 by introducing magnetic impurities in the superconductors. But the investigations were made difficult by the absence of materials where the phenomena could be properly studied. The discovery in the mid-seventies of the ternary superconductors containing a regular lattice of magnetic ions, like (RE)Mo_6S_8 [70-72, 78-80], (RE)Mo_6Se_8 [73-75,78-80] and (RE)Rh_4B_4 [76-80] changed this situation (RE stands for rare-earth metals).

The essential property of these compounds is that the magnetic 4f-electrons are just sufficiently weakly coupled [49] to the conduction electrons so that magnetism and superconductivity can coexist to a certain extent, although sufficiently strongly coupled that rather dramatic effects occur in the interplay of the two phenomena. Whereas the rule is normally that the two phenomena couple too strongly, the discovery of the new oxide-superconductors [81-82] have given us the example of the (RE)-$Ba_2Cu_3O_7$

compounds, where the two phenomena coexist with practically no coupling at all.

Using the solution of Eq. 2.59, one can write an equation for the critical field $H_{C2}(T)$ in terms of the orbital critical field H^*_{C2} as [50, 61] ,

$$H_{C2}(T) = H^*_{C2}(T) - M(H_{C2},T) - 3.56\lambda_m H^*_{C2}(0) - 0.22\frac{\alpha}{\tau_{SO}T_{C0}}[H_{C2}(T) + M(H_{C2},T) + H_J(H_{C2},T)]^2 \quad (2.66)$$

where $M(H_{C2},T)$ is the magnetisation, λ_m is magnetic scattering and H_J is the effective exchange field.

2.8.1: Ferromagnetism and Superconductivity:

In the case where both the scattering and the polarization effects can be neglected (i.e. very weak exchange interaction), Eq.2.66 leads to [49,61];

$$H_{C2}(T) = H^*_{C2}(T) - M(H_{C2},T) \quad (2.67)$$

Eq. 2.67 suggests that superconductivity will be destroyed whenever the magnetization exceeds the orbital critical field. Thus, as a result of ferromagnetic order, if the magnetisation increases abruptly, one expects that the critical field decreases abruptly and superconductivity may possibly disappear altogether. However, in type-II superconductors it is rather plausible that $H^*_{C2} > M_0$ (M_0= saturation magnetisation) and thus this electromagnetic interaction between the magnetic moments and the Cooper pairs does not necessarily exclude coexistence.

If the electromagnetic and the scattering term are neglected, in Eq. 2.66, in such cases, the critical field is given by,[49-50]

$$H_{C2}(T) = H^*_{C2}(T) - 0.22\frac{\alpha}{\tau_{SO}T_C}[H_{C2}(T) + M(H_{C2},T) + H_J(H_{C2},T)]^2 \quad (2.68)$$

Most of the ternary superconductors have $H_{C2}(0)$ and $M(H_{C2},T)$ of the order of 1 T or less, while H_J is the several tens of Tesla, so that we can write Eq. 2.68 in terms of Magnetisation M (since H_J is proportional to M) as,

$$H_{C2}(T) = H^*_{C2}(T) - AM^2(H_{C2}, T) \quad (2.69)$$

This Eq. is similar to Eq. (2.67). The only difference is that the term subtracted from H^*_{C2} in Eq. (2.69) may become much larger than the one in Eq.(2.67). This is the term which in most ferromagnetic materials makes a coexistence with superconductivity impossible.

2.8.2: Paramagnetism and Superconductivity:

In a paramagnetic material, the field and temperature dependence of the magnetisation may result in a very unusual temperature dependence of $H_{C2}(T)$. As close to T_C, the second term in Eq. 2.69 is very small, but as T decreases and the critical field increases, the second term rapidly grows and finally dominates, so that the critical fields determined by the condition that the second term does not become too large. This leads to a rounded peak in $H_{C2}(T)$ curve and, thus decrease of H_{C2} at low temperatures. In the ternary superconductors, several examples of this behaviour have been found. **Fig. 2.13,** shows the example of some $(RE)Mo_6S_8$ superconductors [80]. The round maximum is not related to magnetic ordering but rather to the gradual polarization of the spins by the external field. The minimum at low temperature reflects an antiferromagnetic ordering. The full line is the theoretical curve using Eq. 9 in ref.[49].

2.8.3: Anti-Ferromagnetism and Superconductivity:

In an anti-ferromagnetic material the possibility of coexistence of antiferromagnetic and superconductivity was first considered theoretically by Baltensperger and Strassler (1963) [83]. They showed that coexistence is possible, but that the superconducting state would be modified by the antiferromagnetism [87]. Today, a number of compounds have been found where the two phenomena coexist. Such a behaviour, for an antiferromagnetic-superconductor is shown in the graphs of $H_{C2}(T)$ vs. T in **Fig.2.13.**

Low temperature specific heat measurements have been carried out for several of ternary antiferromagnetic superconductors [74-75,77-78]. As can be seen from **Fig.2.14**, a pronounced lambda type anomaly was found at the magnetic phase transition of the material, $GdMo_6S_6$, where the specific heat of a nonmagnetic material ($Lu_{1.2}Mo_6S_6$) is compared. For the Gd compounds it was found that the entropy was roughly equal to the Hunds-rule value, i.e. R ln(2J+1). However, for the other RE the entropy is lower, illustrating the importance of crystal field. In most of these investigations other anomalies are found in the temperature range between 1 and 10 K. So far one has not been able to connect these with other properties of the Chevrel phases, and no satisfactory explanation has been found. In view of the difficulty of making very pure material, it is not excluded that these anomalies are connected with impurity phases.

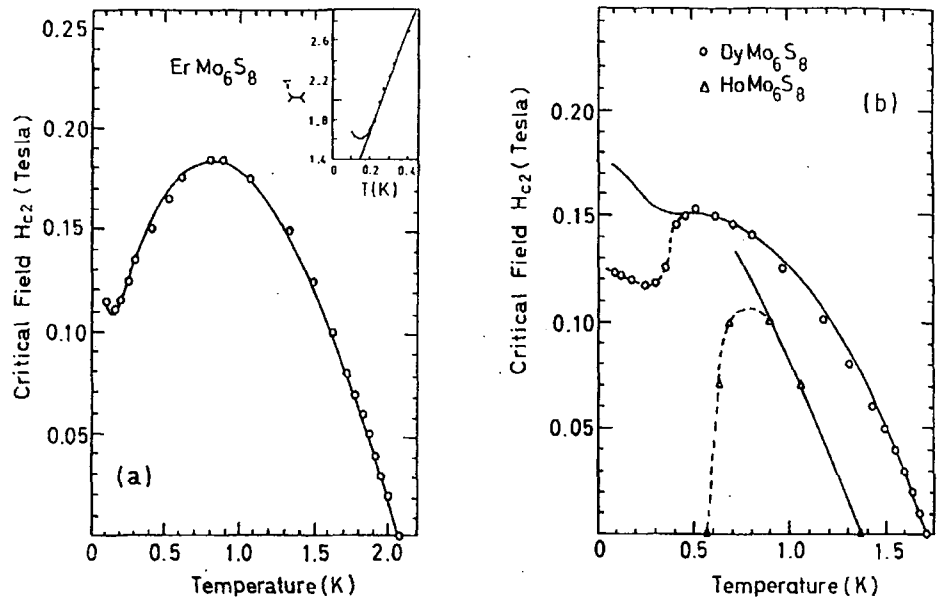

Fig.2.13). Upper critical field for some antiferromagnetic superconductors $REMo_6S_8$ (RE = Er, Dy) and a ferromagnetic superconductor $HoMo_6S_8$ [80].

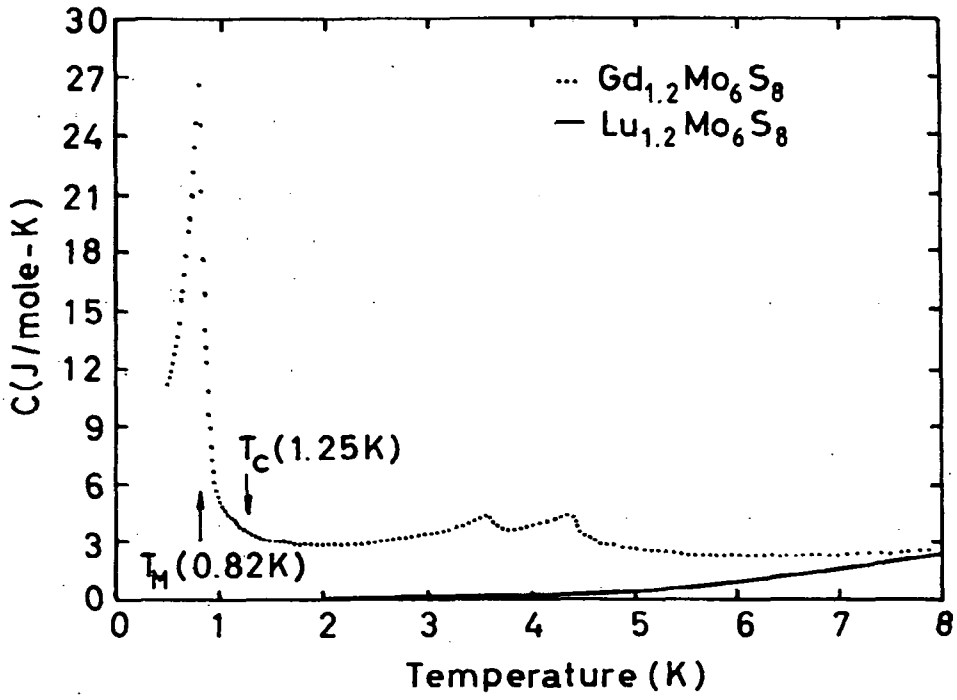

Fig.2.14). The heat capacity versus temperature for $Gd_{1.2}Mo_6S_8$. T_C denotes the onset temperature for superconductivity as inferred by from the corresponding χ_{ac} data while T_M denotes the temperature of the peak of the specific heat anomaly. Also shown is the heat capacity of the isostructural nonmagnetic $Lu_{1.2}Mo_6S_8$.[72].

Part II

2.9: Synthesis of Chevrel Phases:

As stated in chapter 1, Lead Chevrel phase material is a potential candidate for the next generation to be used in industrial application. Its careful and proper sample preparation are very necessary to study the stoichiometry of the compounds and to investigate the intrinsic properties related to their crystal structure. Very dense and homogeneous samples are essential to investigate the transport properties and achieve very narrow superconducting transitions. For this purpose many different techniques have been used to get pure Chevrel phase compounds. To fabricate bulk and single crystal materials, different techniques are used. Some of them are described below;

2.9.1: Bulk Materials

The bulk materials can be fabricated using the, Solid State Reaction Process, Hot Pressing, and Hot Isostatic Press. They are described below;

Solid State Reaction Process

The Chevrel phase compounds can be synthesised by the solid state reaction technique. In this method, the starting materials, RE (rare earth), Mo and X are mixed together in an inert and sealed quartz crucible. An intermediate synthesis can include synthesizing molybdenum chalcogenides and RE-sulphide or selinides. A single phase sample can be achieved by one or two annealing reactions at a temperature ranging between 1000^0 C and 1200^0 C. However, the compounds prepared by this method are slightly Oxygen contaminated due to the quartz tube. This contamination effects the T_c and other superconducting properties. [88] (Hinks, 1983).

Hot Pressing:

To get rid of the porosity and have a good connectivity between the grains, Hot Pressing is used. In this method, the sintered powders are hot pressed by applying a uni-direction pressure at 1400^0 C for several hours in pressure of 1.7-3 kbar using a graphite matrix [90, Meul, 1982]. The hot pressed, high density samples are cut into different shapes of samples for transport properties measurements. In his way the grain

size is 1 μm, which is smaller than melted or single-crystal samples. These samples have high specific resistance as compared to melted materials. But they can be used in the experiments where single crystals are needed but are difficult to synthesise due to the decomposition effects.

Hot Isostatic Press:

This method is currently used in Durham University to get rid of the porosity, to get a better connectivity between the grain boundaries and dense material. Since the sample is fabricated in the controlled environment, contamination can be minimised. This method will be explained in detail in Chapter 7 and 8. Here only the basic principle is described. In this method, the sample (wrapped in Mo) in the Hot Isostatic Press (HIP) unit is squashed from all sides with the Argon pressure surrounding the sample present in the HIP unit. The temperature of the vessel can be increased to 2000 ^{0}C with 2000 kbar pressure.

2.9.2: Single Crystals

Melting Process:

Although the high vapour pressure of Chalcogen materials make it difficult to melt these materials in the open air without losing something or without contamination. The contamination can be made negligible if a large pressure of some inert gas is applied around the sample. The best results have been obtained in the system of $Cu_nMo_6S_8$ and $EuMo_6S_8$ which melt congruently. Grains of the order of several cubic millimetres have been produced by this method. [89, Flukiger and Baillif, 1982]. However it is difficult to get pure $PbMo_6S_8$ by this method.

Crystal Growth:

Many single crystals of Chevrel phases have been achieved by transporting halogen gas around the crucible. Good single crystals of the order of 1 x 1 x 1 mm^3 of almost all the Chevrel phase compounds can also be obtained by using an off-stoichiometry starting product and hold it at a temperature of 1600^0 C in a sealed molybdenum crucible [91, Horyn, 1989].

2.9.3: Thin Films:

Thin films are very suitable material to investigate the intrinsic transport properties of the Chevrel phase materials specially the critical current density. Due to their geometry thin films are potential candidate for the applications.

Thin films of MMo_6S_8 (M= Pb, Sn, Ag, or Cu) can be obtained by co-evaporation method [92, Webb, 1985] or d.c. sputtering process [93, Woolam, 1982]. Sputtering takes place on the target with the material of MMo_6S_8, or a suitable amount of MoS_2, molybdenum and M elements. For $Cu_xMo_6S_8$ the co-evaporation of molybdenum and copper in the presence of a hot sulphur vapour (H_2S or sulphur) gives interesting results. As sapphire has almost same thermal expansion as the Chevrel phases, the best results can be obtained using sapphire as a substrate. In situ preparation of lead Chevrel phase thin-films has always failed due to high vapour pressure of lead above 800^0 C. However, good $PbMo_6S_8$ films have been produced by post annealing the films under a lead atmosphere.

2.10.: Crystal Structure of Chevrel Phases:

The structure of almost all the Chalcogen Chevrel phases is in the sequence of layers -S-S-M-S-S-M- [94, Matthias,1972] where M is a transition metal. The metal-to-metal interaction between the layers is weak and the compounds have a pseudo two-dimensional network of metal atoms. Up to now about 160 compounds are found to be the same structure with the a basic building block of Mo_6X_8 unit shown in **Fig.2.15b.** This unit appears as a pseudocube with one chalcogen at each corner and one molybdenum located almost in the centre of each face. The basic structure of the Chevrel phases is made from the stacking of these Mo_6X_8 units in an almost cubic unit cell as shown in **Fig.2.15a.** Along the cube axis there is a free space either around the central atom or between the adjacent planes of the Mo_6X_8 unit.

There are two types of structure in Chevrel phase materials, depending upon the third element added to the cluster of Mo_6S_8 [95]. If the added element is a lighter one, say Cu, then it will tend to occupy the space on the edges of the large cube, while the heavy atoms like a rare-earth, Pb or Sn, have a tendency to occupy the corners of the

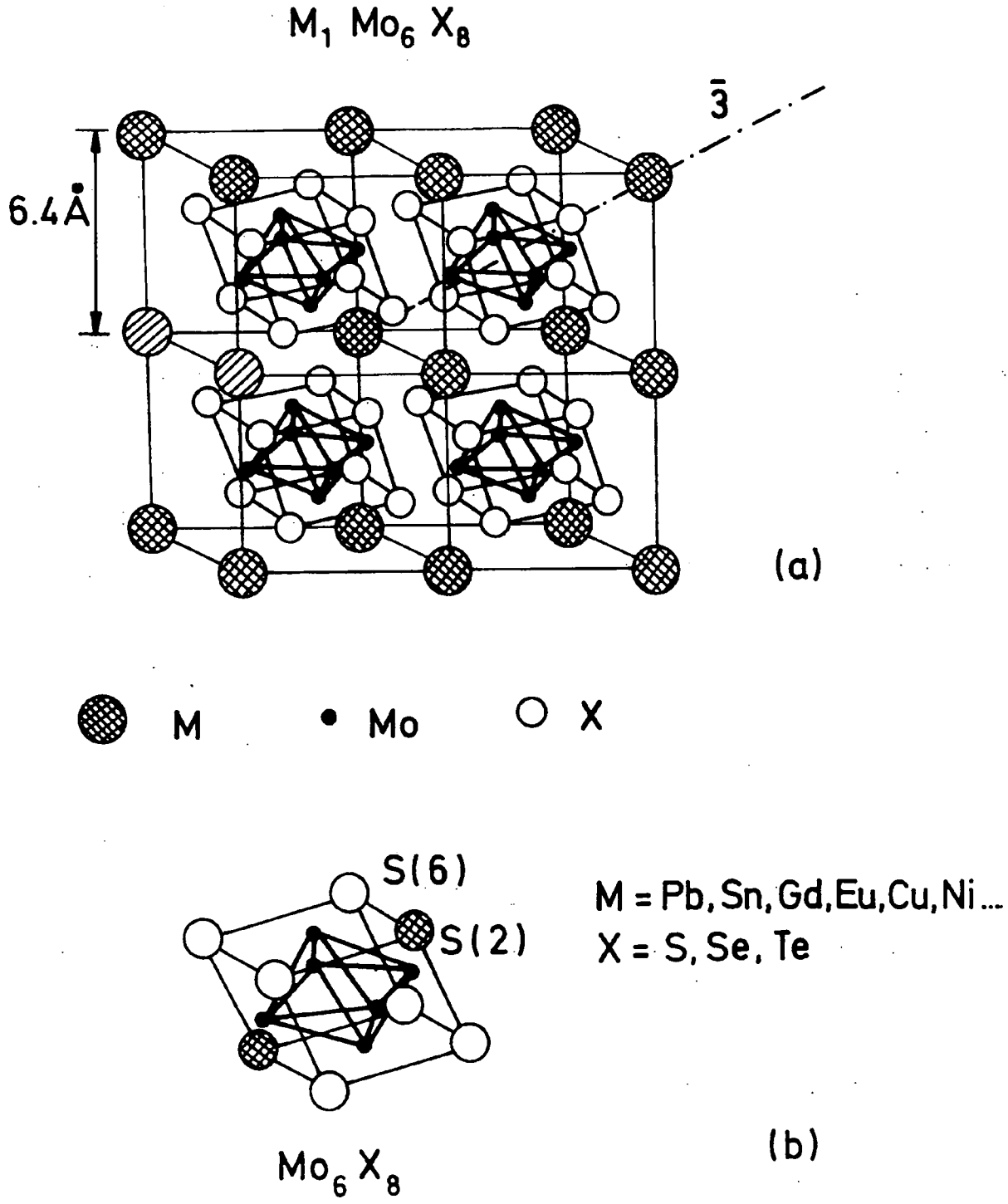

Fig.2.15. (a): The crystal structure of Chevrel phase materials. (b): One building block of the crystal structure.

large cube. Since we are mainly concerned with the doping of Pb to the Mo_6S_8 cluster, one can consider the simplification that there is no rhombohedral distortion to the cubes. In actual practice, the rhombohedral angles α vary from 88.9 to 89.8 for the systems like $PbMo_6S_8$, whereas for calculation purpose people use 90.0. [96, Maple and Fischer, pp174]. It is noted that T_C is a very sensitive parameter to the variation in the angle α which is difficult to explain.

The most interesting physical properties are believed to be evolved from the octahedra cluster of Mo_6S_8 which is closely packed with ~ 74% of packing ratio since the arrangements of the atoms is similar to that of the fcc lattice, while the whole volume is not closely packed with only about 42% packing ratio [96]. The Pb atom occupies a relatively large volume between the octahedra. The closest neighbours to this atom are the S atoms in the corners of the octahedra adjacent to the Pb site. These S sites are called the S_2 while the other six S sites are called the S_6 sites as pointed in the **Fig.2.15b**. Among the 15 atoms per cell, there are 4 inequivalent potential sites, one with Pb, one for Mo, and two for S atoms as stated above. The distance between two Pb atoms is usually 6.4 Å, which is shown in **Fig.2.15a**.

2.11: The Electronic and Magnetic Properties:

The most physical properties of these ternary materials depend on the third element to be added to the Mo_6S_8 cluster which stabilises the crystal structure. This effect is due to the transfer of valence electrons to the electronic deficient cluster, which stabilises the crystal structure [97,98] and modifies the other physical properties such as T_C. A simple calculation shows that every Mo atom yields a 3.66 valence electrons in $PbMo_6S_8$ (T_C ~ 15 K) and 3.83 electrons in $LaMo_6S_8$ (T_C ~ 6 K) [96].

The crystal structure and the band calculations [96] for the ternary Chevrel phase material show that, these materials can be considered as a molecular compounds of three distinct networks;

a); a network consists of Mo-clusters, responsible for the superconducting properties.

b); a network formed by the chalcogens, which gives the intercluster bondings and forms the channels to develop the three dimensions in space.

c); a network constitute by the M^+ atoms inside the chalcogen channel.

The main magnetic properties of these compounds are based upon the nature of the M^{+} ions. So, if M is diamagnetic (e.g. Cu^{+} or Pb^{++}), the compounds show a temperature independent paramagnetic behaviour [99,100], because the diamagnetic contributions from the closed electron shells and the paramagnetic contribution due to the orbital motion of the valence electrons partially cancel each other, whereas the addition of magnetic ions (Fe^{++}, RE^{+++}) gives a Curie-Weiss behaviour over a wide temperature range [101,102]. The susceptibility and the specific heat measurements show that the electronic density of states per atom is about 2-3 times lower than that of A15 compounds such as Nb_3Sn etc.

2.12: Summary:

In this chapter theoretical considerations have been addressed which will be needed to explain the behaviour of low temperature superconductors, particularly $PbMo_6S_8$ and $Pb_{1-x}Gd_xMo_6S_8$, which are considered in this thesis. The definition of specific heat in SI units, the theory of specific heat considering first the approach adopted by Einstein with constant angular frequency, its drawbacks and then the final form of Debye's theory of specific heat have been discussed. Although Debye theory is in good agreement with experimental observations at very low and high temperatures, it has a slight deviation in the intermediate temperature range which is due to the over simplification of a linear dispersion relation to describe all vibration modes.

The electronic specific heat has been discussed using Fermi-Dirac statistics. As electronic specific heat is $\approx 1\%$ of the lattice contribution at room temperature, so it can be ignored at that temperature, but it becomes quite significant at very low and very high temperatures. Experimentally, the specific heat can be separated in a lattice and a electronic contribution using a Debye plot where Cp/T versus T^2 gives a straight line and the slope of this straight line gives the lattice contribution and y-intercept represent the electronic contribution.

The Cp of type-I superconductors in the light of classical thermodynamics and the BCS theory has been discussed. It is evident that the discontinuity in the specific heat in the absence of a magnetic field is a second order phase transition as there is no latent heat involved, but it is a first order phase transition in the presence of magnetic field. Superconductivity can be destroyed if the applied field is higher than H_C.

The specific heat of Type-II superconductors has been discussed in the light of GLAG theory, which is most extensively used for type-II superconductors in magnetic fields. As there is no change in entropy during the transition from superconducting to mixed state or mixed state to normal state and no latent heat is involved, it is second order phase transition, both in the absence, and in the presence of magnetic field [1, pp. 51, 20, pp.200]. Electronic specific heat of type II superconductors can be explained on the basis of Gibbs free energy. Furthermore, the height of the jump gives considerable information concerning the material's homogeneity or inhomogeneity.

High field and magnetic studies have been discussed in the light of WHH theory. To get a realistic description of the thermodynamic critical field H_{c2} it is necessary to take into account both the orbital and paramagnetic effect of the external field, as well as non-magnetic and spin-orbit scattering. The effect of the non-magnetic scattering is to reduce the effective coherence length and thus decrease the effect of the orbital part of the magnetic field, whereas the spin-orbit interaction increases the limit to break the Cooper-pairs, thus increasing the paramagnetic limit Hp. The critical field H_{c2} can be calculated using the specific heat measurements. The breakdown of PPL in high H_{c2} materials can be switched to WHH theory where spin-orbit scattering plays an important role. Although WHH theory is in good agreement with that of experimental values, it still has some limitations in the range of very low temperatures and at high applied fields.

For magnetic materials, above the transition temperature, the materials behave like an ordinary material. Below this temperature, the material is magnetically ordered. However, at the transition temperature, a λ-type anomaly is discovered, which has a different origin compared to a superconductor. This λ-type anomaly is present in both ferro- as well anti-ferromagnetic materials. The magnetic specific heat C_M is difficult to measure due to the presence of electronic and lattice contribution. However, it can be estimated after subtracting these contributions from the total specific heat or comparing the specific heat of a non-magnetic material with that of the magnetic material in the same temperature range.

The co-existence of superconductivity and magnetism in the same material at the same time is unusual. Yet in some superconductors both can exist at the same time. It can be explained on the basis of the exchange interaction between the conduction

electrons and the localized magnetic moments. The discovery of High Temperature Super-Conductors (HTSC) has demonstrated that the two phenomena can exist together with practically no coupling at all.

For our study, emphasis will be placed on the PMS class of materials as they have the potential to be used in industrial applications to produce magnetic fields beyond 20 T to 40 T. It is necessary to fabricate the required material in its suitable proportions and understand its crystal structure. The big problems of fabricating Chevrel phase materials are, the contamination during the fabrication process, granularity, and porosity. The basic and applied science of these materials will be addressed in the coming chapters.

References to Chapter 2:

1).Miller,A. P., in Specific Heat of Solids, edited by C.Y. Ho, (Authored by Ared Cezairliyan), Hemisphere Publishing Corporation, 1988, pp.1-89.

2). Collings, E. W., in Applied Superconductivity, Metallurgy, and Physics of Titanium Alloys, Vol. 1. Plenum Press, New York, 1986, Chap. 10. pp. 383-84.

3). Phillips, N. E., R. A. Fisher, and J. E. Gordon, (The Specific Heat of High-Temperature Superconductors), in Progress in Low Temperature Physics, Vol. XIII, Edited by D.F. Brewer, Elsevier Science Publishers B. V., 1992. pp.267-357.

4). Stewart, G. R., Rev. Sci. Instrum. 54 (1983), 1-11.

5). Sheahen, T. P., in "Introduction to High-Temperature Superconductivity", Plenum Press, New York, 1994. pp.349-72.

6). Dulong, P.L. and A.T. Petit., Annales de Chimie et de Physique, 10 (1819) 395-413.

7). Einstein, A., Ann. Physik, 22 (1907) 180-90.

8). Debye, P., Ann. Physik, 39 (1912) 789-839.

9). Sommerfeld, A., Z. Phys., 47 (1928) 1-32.

10). Keesom, W.H., and J. A. Kok, Communication No. 221e, Kamerlingh Onnes-Laboratory at Leiden, (1932) 743-48.

11). Keesom, W.H., and P.H. Van Laer, Physica, 5 (1938), 193-201.

12). Bardeen, J., L.N. Cooper, and J.R. Schrieffer, Phys. Rev., 108 (1957) 1175-1204.

13). P.V.E. McClintock and J.K. Wigmore, Low Temperature Physics: An Introduction for Scientists and Engineers, Blackie & Son Ltd, Glasgow, 1992.

14). M.A. Omar, Elementary Solid State Physics, Addison-Wesley Publishing Company, Reading, 1975.

15). H.M. Rosenberg, The Solid State, 3rd Edition, Oxford Science Publications, 1990.

16).Gopal, E.S.R.,Specific Heats at Low Temperatures, HeyWood Books, London, 1966

17). J.R. Clement and E.H. Quinnel, Phys. Rev. 92 (1953) 258.

18). N.E. Phillips, in Critical Reviews in Solid State Sciences (D.E. Schuele, and R.W. Hoffman, Editors), Vol. 2, Chemical Rubber Co., Clevland, OH, 467-553, 1972.

19). J.D. Doss, Engineers Guide to High-Temperature Superconductivity, John Wiley & Sons, Inc. New York, 1989, pp. 63.

20). A.C. Rose-Innes and E. H. Rhoderick, Introduction to Superconductivity, Second Edition, Pergmon Press Ltd., Oxford. 1978.

21). Kittel, C., Introduction to Solid State Physics, Sixth Edition, John Wiley & Sons, Inc. New York, 1986, pp. 317-58.

22). A. Junod, in Physical Properties of High Temperature Superconductors II, Edited by D.M. Ginsberg, World Scientific, Singapore, 1990.

23). Pippard, A.B., The Elements of Classical Thermodynamics, University Press, Cambridge, England, 1957, pp. 112-135.

24). R. D. Parks (Editor), Superconductivity, Vol. 2. Chap.14.15, Marcel Dekker, Inc., NewYork. N.Y.

25). W. S. Corak., B.B. Goodman, C.B. Satterthwaite, and A. Wexler, Phys Rev., 96 (1954) 1442-4.

26). Burns, G., in High Temperature Superconductivity An Introduction, Academic Press, Ltd., London, 1992. Chap. 2, (pp. 9-54).

27). V. L. Ginsburg, and L.D. Landau, Zh. Eksp. Teor. Fiz., 20 (1950) 1064-82

28). A. A. Abrikosov, Sov. Phys. -JETP, 5 (1957) 1174-82

29). A. A. Abrikosov, J. Phys. Chem. Solids, 2 (1957) 199-208.

30). L. P. Gor'kov, Sov. Phys. -JETP 10 (1960) 593-9

31). L. P. Gor'kov, Sov. Phys. -JETP 10 (1960) 998-1004.

32). K. Maki, Physics, 1 (1964) 21-30.

33). K. Maki, Physics, 1 (1964) 127-43.

34). K. Maki, Physics, 1 (1964) 201-02.

35). K. Maki, Phys. Rev. A, 139 (1965) A702.

36). A.G. Van Vijfeijken, Phillips Research Report, Suppl. No.8 (1968) 1-114.

37). E.W. Collings, Applied Superconductivity, Metallugy, and Physics of Titanium Alloys, Volume 1. Chap. 8,10 -15,17.

38).Ferreira Da Silva J.,N.W.J.Van Duykeren, and Z. Dokoupil, Physica 32 (1966) 1253

39). R.B. Zubeck, T.W. Barbee, Jr., T.H.Geballe, F.Chilton, J. Appl.Phys. 50 (1979) 6423-36.

40). A.M. Clogston, Phys. Rev. Lett. 9 (1962) 266-67.

41). B.S. Ckandrasekhar, App. Phys. Lett. 1 (1962) 7-8.

as a result of ferromagnetic order,42). E. Helfand and N.R. Werthamer, Phys. Rev. Lett. 13 (1964) 686-88.

43). E. Helfand and N.R. Werthamer, Phys. Rev. 147 (1966) 288-94.

44). N.R. Werthamer,E. Helfand and P.C. Hohenberg, Phys. Rev. 147 (1966) 295-302 (WHH).

45). L. J. Neuringer and Y. Shapira, Phys. Rev. Lett. 17 (1966) 81-84.

46). Crow, J. E., R. P. Guertin, and R. D. Parks, Phys. Rev. Lett. 19 (1967), 77-81.

47). Orlando, T. P. and M. R. Beasley, Phys. Rev. Lett. 46 (1980) 1598-1601.

48). Schopohl, N., and K. Scharnberg, Physica 107B (1981) 293-94.

49). Φ. Fischer, Ferromagnetic Materials, Vol. 5, Edited by K. H. J. Buschow and E. P. Wohlfarth, Elsevier Science Publishers B.V., 1990. pp.465-576.

50). Φ. Fischer, Appl. Phys. 16 (1978) 1 - 28.

51). For a general discussion see, for instance, St. James, Sarma and Thomas: Type II Superconductivity, Pregamon Press, Oxford. 1969.

52). Fischer, Φ., Helv. Phys. Acta, 45 (1972) 329-397.

53). Decroux, M., Φ. Fischer, C. Rossel, B. Lachal, R. Baillif, R. Chevrel, and M. Sergent, in Ternary Superconductors, (Proceedings of the International Conference on Ternary Superconductors, 1980, Lake Geneva, Wisconsin, U. S. A.) edited by G. K. Shenoy, B. D Dunlap and F. Y. Fradin, Elsevier, North Holland, New York. pp. 65-68.

54). Odermatt, R., Φ. Fischer, H. Jones and G. Bongi, J. Phys. C: Solid State Phys., 7 (1974) L13-L15.

55). Fischer, Φ., H. Jones, G. Bongi, M. Sergent, and R. Chevrel, J. Phys. C: Solid State Phys., 7 (1974) L450-L453.

56). Fischer, Φ., M. Decroux, S. Roth, R. Chevrel, and M. Sergent J. Phys. C: Solid State Phys., 8 (1975) L474-L477.

57). Cors, J., Thesis. No. 2456, University of Geneva (1990).

58). Cors, J., D. Cattani, M. Decroux, A., Stettler and Φ. Fischer, Physica B., 165 &166 (1990) 1521-22.

59). Foner, S., E. J. Mcniff Jr., and E. J. Alexander, Phys. Lett. 49A (1974) 269-270.

60). Foner, S., in Superconductivity in d- and f- Band Metals. Edited by D.H. Douglass, Plenum Press. New York and London (1976), pp.161-174.

61). M. Decroux, and Φ. Fischer, in Superconductivity in Ternary Compounds II, 1982, Topics in Current Physics 34, eds. M.B. Maple and Φ. Fischer (Springer, Berlin) p.57.

62). Fischer, Φ., M. Decroux, and R. Chevrel, in Superconductivity in d- and f- Band Metals. Edited by D.H. Douglass, Plenum Press. New York and London. (1976).

pp.175-87.

63). Wohlfarth, E.P., in Ferromagnetic Materials, Vol. 1, edited by E. P. Wohlfarth, North-Holland Publishing Company, 1980, pp. 49-50.

64). Wuchner, W., J. Mag. and Mag. Mat.; 2 (1976) 203-206

65). Connelly, D.L., J.S. Loomis, and D.E. Mapother, Phys. Rev. B., 3 (1971) 924-34.

66). Bredl, C. D., and F. Steglich, J. Mag. and Mag. Mat.; 7 (1978) 286-89.

67). V.L.Ginzburg, Sov. Phys. -JETP, 4 (1957) 153-160.

68). B.T. Matthias, H.Suhl and E. Corenzwit, Phys. Rev. Lett. 1 (1958) 92-94.

69). B.T. Matthias, H.Suhl and E. Corenzwit, Phys. Rev. Lett. 1 (1958) 449-50.

70).Φ. Fischer, A. Treyvaud, R. Chevrel and M. Sergent, Solid State Commun.17 (1975) 721-24.

71). M. Ishikawa, and Φ. Fischer, Solid State Commun. 24 (1977) 747-51.

72).Woolf, L. D., M. Tovar, H. C. Hamaker and M. B. Maple, Phys. Lett., 74A (1979) 363-66

73). R.N. Shelton, R.W. McCallum and H. Adrian, Phys. Lett. A, 56 (1976) 213-14.

74). R.W. McCallum, D.C. Johnston, R.N. Shelton, W.A. Fertig and M.B. Maple, Solid State Commun. 24 (1977) 501-05.

75). M.B. Maple, L.D. Woolf, C.F. Majkrzak, G. Shirane, W. Thomlinson and D.E. Moncton, Phys. Lett. 77A (1980) 487-89.

76). Woolf, L. D., D. C. Johnston, H .B. MacKay, R. W. McCallum, and M. B. Maple, J. Low Temp. Phys. 35 (1979), 651-69.

77). N.E. Alekseevskii, G. Wolf. V.N. Narozhnyi, A.S. Rudenko, and H. Hohlfeld, Sov. Phys. -JETP 62 (1985) 617-20.

78). R.W. McCallum, Ph.D. Thesis, 1977, University of California, San Diego.

79). Machida, K., Appl. Phys. A 35 (1984) 193-217.

80). O. Pena and M. Sergent, Prog. Solid St. Chem., 19 (1989) 165-281.

81). J.G. Bednorz, K.A. Muller, Z. Phys. B, 64 (1986) 189-93.

82). M.K. Wu, J.R. Ashburn, C.J. Torng, P.H. Hor, R.L. Meng, L. Gao, E.J. Huang, Y.Q. Wang, and C.W. Chu, Phys. Rev. Lett. 58 (1987) 908-10.

83). W. Baltensperger, and S. Strässler, Phys. Kondens. Mater. 1 (1963) 20-26.

84). T.W. Barbee Jr., Phys. Status Solidi, 31 (1969) 535-544.

85). R.A. Brand, in Low Temperature Physics,- LT14, (Proc. 14th Int. Conf. Otaniema,

Finland, Aug. 1975), ed. by M. Krusius and M. Vuorio, Elsevier North Holland, New York, 1975, pp. 485-488.

86). van der Meulen, H. P., J. A. A. J. Perenboom, T. T. J. M. Berendschot, J. Cors, M. Decroux, Φ. Fischer, Physica B, 211 (1995) 269-271.

87). L.N. Bulaevskii, A.I. Buzdin, M.L. Kulic, and S.V. Panjukov, Advances in Physics, 34 (1985) 175-261

88). Hinks, D. G., J. D. Jorgensen, H. C. Li, Phys. Rev. Lett. 51 (1983) 1911-14.

89). Flukiger, R, R. Baillif, in Superconductivity in Ternary Compounds I, edited by Φ. Fischer and M. B. Maple, Springer-Verlag, Berlin, Vol. 32, 1982 pp.113-41.

90). Meul, H. W., M. Decroux, R. Odermatt, R. Noer, Φ. Fischer: Phys. Rev. B., 26 (1982) 6431-37.

91). Horyn R., O. Pena, and C. Geantet, Supercond. Sci. Technol. 2 (1989) 71-90.

92). Webb, R. J., A. M. Goldman, -J. Vac. Sci., Technol., A, 3 (1985) 1907.

93). Woolam, J. A., S. A. Alterovitz, H-L. Luo, in Superconductivity in Ternary Compounds I, edited by Φ. Fischer and M. B. Maple, Springer-Verlag, Berlin, Vol. 32, 1982 pp.143-64.

94). Matthias, B.T., M. Marezio, E. Corenzwit, A.S. Cooper, and H. E. Barz, Science, 175 (1972) 1465-66.

95). Marezio, M., P. D. Dernier, J. P. Remeika, E. Corenzwit, B. T. Matthias: Mat. Res. Bull. 8 (1973) 657.

96). Freeman, A. J., and T. Jarlborg, in Superconductivity in Ternary Compounds II, Vol. 34, edited by M. B. Maple and Φ. Fischer, Springer-Verlag, Berlin Heidelberg, 1982, pp.167-200.

97). Sergent, M., Φ. Fischer, M. Decroux, C. Perrin, and R. Chevrel, J. Solid State Chem. 22 (1977) 87-93.

98). Yvon, K., A. Paoli, Solid State Comm., 24 (1977) 41-45

99). Shelton, R. N., in Superconductivity in d- and f-band metals. Edited by D. H. Douglass, Plenum Press, New York, 1976. pp.137-160.

100). Morton, N., J. G. Booth, C. F. Woodhead, J. Less Common Met., 34 (1974) 125-

101). Johnston, D. C., R. N. Shelton: J. Low Temp. Phys., 26 (1977) 561-

102). Pelizzone, M., A. Treyvaud, P. Spitzli, Φ. Fischer, J. Low Temp. Phys., 29 (1977) 453-65.

CHAPTER 3

REVIEW OF TECHNIQUES TO MEASURE SPECIFIC HEAT

3.1. Introduction:

There are many techniques by which one can measure specific heat of a material. Some techniques are more useful for bulk samples, some for very small samples, and some are more suitable for thin films. Similarly some techniques give better results when used at higher temperatures, some are suitable at intermediate temperatures, and some are best for low temperatures and ultra low temperatures. Differences include design and construction of instrumentation and the thermometry.

There are four major established techniques in use at present within the research groups all over the world, they are, Heat Pulse Method, Thermal Relaxation Technique, Differential Calorimetry, and Steady State A.C. Technique. The advantages and disadvantages of each will be discussed in this chapter.

The chapter consists of eight sections. Section 3.2 outlines the factors which effect the design of an experiment. In section 3.3, the heat pulse method has been discussed. Section 3.4 describes the thermal relaxation technique. In section 3.5 differential calorimetry is discussed and section 3.6 consists of the a.c. technique. In section 3.7, specific heat measurements in high magnetic fields have been described and the summary is outlined in section 3.8.

How can the specific heat be measured experimentally? In the next section the discussion about the established calorimetry is presented.

3.2: Established Calorimetry

The calorimeter is an instrument in which heat exchanges in a system can be measured. The essential requirements are, the calorimeter, which consists of a sample, a resistor, and a thermometer [1]. In development of a technique to measure specific heat one has to keep in mind that it should be robust, easy to use, and may have to be equally useful valid in high magnetic fields, where the dimensions of the probe becomes a crucial factor. The thermometry used, should be highly sensitive. High

resolution and precise instruments are needed for the data acquisition. The method chosen for the measurement of specific heat depends on the consideration of many factors as follows:

1). The temperature range of interest.

2). The size (especially thickness), thermal time constant and thermal conductivity of the sample available.

3). The magnitude of the total specific heat relative to the effect under investigation.

4). The desired accuracy and the resolution.

The basic requirements for the heat capacity measurements are shown in Fig. 3.1. In the figure, S, sample; H, sample heater; Th_1, to sense the sample temperature and Th_2, to sense and control the background temperature; K_{ext} is the thermal impedance between the sample and the heat sink acting as a background; K_{Th}, is the thermal impedance between the sample and the thermometer; and K_H is the thermal impedance between the sample and the sample heater. The arrows show the heat leak due to the radiation during the course of the measurements. From many established

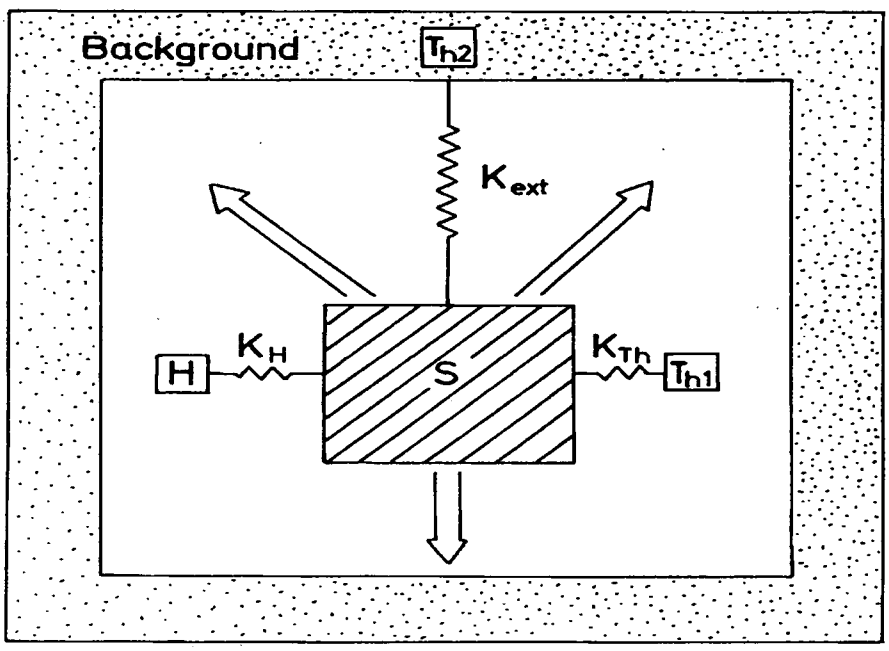

Fig.3.1: Schematic arrangement for heat capacity measurements. S, sample; H, heater; Th_1 and Th_2 are the sample and background heater respectively; K_{ext}, thermal impedance between the sample and the background; K_H and K_{Th} are the thermal impedance between the sample and the sample heater or sample thermometer respectively. Arrows shows the radiation from the sample.

calorimetry techniques, only four major techniques are being discussed below taking into account the factors stated above:

3.3: Heat Pulse Method

The heat pulse method is a traditional technique for measuring Cp. The basic principle to measure specific heat is, adding some heat ΔQ to the sample and measuring the corresponding rise in temperature ΔT. There are different techniques for adding heat and measuring ΔT. Usually, after the pulse, the temperature of the system is allowed to decay freely [1].

The idea of using electrical energy as the heat input and measuring corresponding rise in temperature was first introduced by Gaede in 1902 [2] and further development was done by Nernst in 1910 [3] and Eucken in 1909 [4]. The modern adiabatic vacuum calorimeter is based on their ideas [5]. The adiabatic method was further developed by Southard and Andrew [6] for very low temperature calorimetry.

The basic requirements for this technique are [5]:

1). The sample should be in thermal equilibrium with its surroundings at the beginning of the measurement.

2). The sample should be isolated from its surroundings during the measurement as much as possible.

3). Adding heat energy to the sample.

4). Accurate thermometry.

When a heat pulse is applied to the sample it raises the temperature. This rise in the sample's temperature is sensed by a very sensitive thermometer mounted on the other side of the sample. The heat leak due to conduction, convection and radiation are kept as low as possible. Heat leak due to conduction can be minimised, if not eliminated, by using thin wires, (high thermal resistance), and keeping the sample as isolated as completely as possible from its surrounding using adiabatic shields. Convection can be reduced by having a high vacuum inside the probe and the radiation, using super-insulation and adiabatic shields. In the whole course of measurements the background temperature is kept very stable. Fig.3.1 shows the simple system of this kind of experiment.

Specific heat has been measured and described using heat pulse method by many research groups [7-15] with slight modifications. For an ideal system where there is no heat leak and the sample has infinite thermal conductivity and the heater, thermometer and the connecting wires have zero heat capacity.

3.3.1. Heat Pulse for K = ∞: (Ideal Case);

We assume: the sample is perfectly isolated from its surrounding and has infinite thermal conductivity; the intra-sample time constant is shorter than the external time constant of the heat leak and the thermometer and heater have negligible heat capacity. Let the background temperature of the system be T_0 and the time of the heat pulse Δt is greater than the intra-sample time constant. Under these conditions, when a heat pulse is applied to the system, there is no heat leak and all the heat is stored in the sample and the sample's temperature will rise from T_0 to $T_0 + \Delta T$. Mathematically, [14],

Applied Power = Power recieved in the sample,

$$I^2R = m\, C_p\, (\Delta T/\Delta t) \qquad (3.1)$$

or in the limiting case,

$$C_p = \frac{I^2 R \Delta t}{m \Delta T} \qquad (3.2)$$

Where,

Cp = Specific heat of the specimen ($J.gm^{-1}.K^{-1}$).

I = Current through the specimen in Amp.

R = Resistance of the sample heater,

m = Mass of the specimen in grams.

ΔT = Rise in the temperature due to the addition of heat.

Advantages of this method are,

1). It is a traditional and well established method.

2). It can be used at any temperature, e.g. at very high, intermediate, low temperatures and with some modification, at ultra low temperatures.

3). This is very accurate and gives precise measurement (0.001%).

4). Can be used for the samples with very low thermal conductivity.

Disadvantages of this method are,

1). In this method, only point to point measurements are possible, which is time consuming.

2). In the phase transition measurements, in the vicinity of T_C, peak may be missed.

3). Only large samples can be measured. It is not suitable for very small samples e.g. single crystals.

4). To get the correct specific heat, the addenda contribution need to be subtracted.

5). To inject heat into the sample, heat switches are required.

6). To keep isolation of the sample from its surrounding and maintaining the adiabatic conditions during the measurements, need to control on thermal exchange gas and a high vacuum inside the calorimeter is required.

Note: This method is discussed in detail in chapter 4 of this thesis.

3.4: Thermal Relaxation Technique:

This method was introduced by Bachmann et. al. [16] in 1972 in the temperature range of 1-35 K for very small samples. Schutz [17] and Sellers [18] extended the measurements to below 1 K. Djureck and Baturic [19] have extended the method toward intermediate temperatures and Junod [20] toward high temperatures. This method can be used to measure heat capacity of very small samples. The schematic and the principal of this method is shown in Fig.3.2. The heat leak through the thermal link, the heat capacity of the sample can be compensated for. All the applied heat pulse is not stored in the sample but some of the heat will leak through wires and through the exchange gas, even during the time of pulse as shown in Fig. 3.2. Taking this heat leak into consideration, to a first approximation, Eq.3.1 can be rewritten as, [14];

Applied Power = Power recieved in the sample + Power losses from the system (3.3)

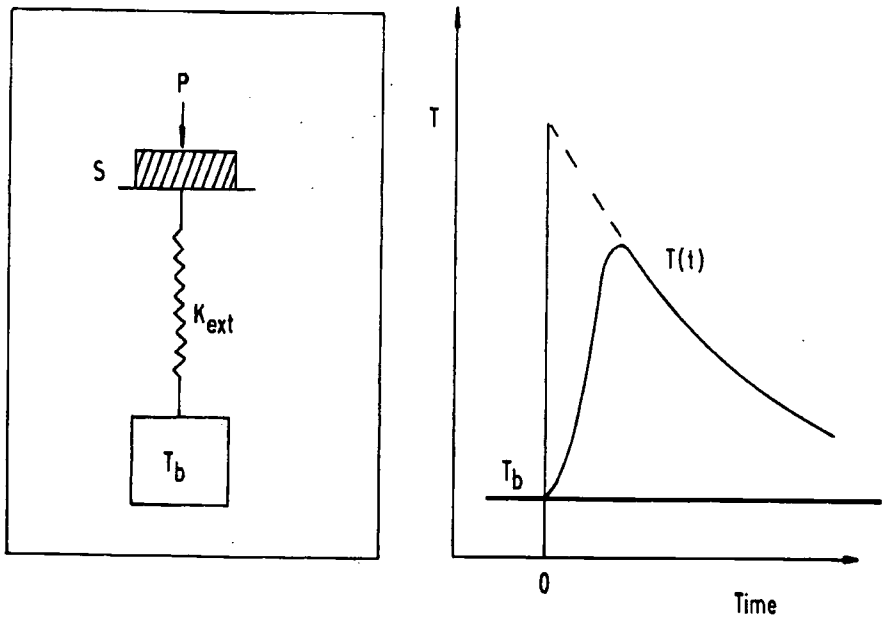

Fig.3.2: Principle of non-adiabatic calorimetry. A schematic arrangement for the thermal relaxation-time method. S, represents sample, sample heater, and the sample thermometer; T_b, constant temperature block; /\/\/\, thermal link; P, heating power. When the heater power is switched-off, the system is allowed to decay freely towards its initial temperature T_b, w.r.t. time [28].

After the pulse, the sample is decaying freely, then Eq. 3.3 can be written as

$$\dot{Q} = - C_p m \left(\frac{dT}{dt}\right) \qquad (3.4)$$

where $\dot{Q}$ is the total power loss from the system. The heat is leaking into its surrounding by conduction, convection and radiation. One needs to develop a relationship where all these types of heat leak are addressed. Due to the high vacuum inside the probe, the heat leak due to convection can be ignored.

Let us consider the heat leak due to conduction only. Let us suppose A, is the cross-sectional area of the thermal link, L, the length of the link, and K, the thermal conductivity. Let T_1 be the sample temperature, and the surrounding or background temperature is taken to be T_0. If T is the temperature of the sample at any time t, then the rate at which heat flows by conduction down the thermal link is given by the expression:

$$\dot{Q} = -KA\frac{\Delta T}{L} \qquad (3.5)$$

where, $\Delta T = T_1 - T_0$ comparing Eq.(3.5) with that of Eq.(3.4), ignoring the finite thermal conductivity of the sample for the time being, the heat flow due to thermal conduction down to the thermal link can be written as [15],

$$\frac{dT}{dt}C_p = -KA\frac{[T_1 - T_0]}{L} \qquad (3.6)$$

The rate at which heat is transferred away from the sample through thermal radiation is given by the Stefan-Boltzmann law:

$$\dot{Q}_1 = -eS\sigma[T_1^4 - T_0^4] \qquad (3.7)$$

e = emissivity of material

S = surface area of sample

σ = Stefan-Boltzmann constant

Make substitution $T_1 = T_0 + \Delta T$, in Eq. 3.7 gives:

$$\dot{Q}_1 = -eS\sigma[(T_0+\Delta T)^4 - T_0^4] \qquad (3.8)$$

On simplification and taking only leading terms, gives,

$$\dot{Q}_1 = -eS\sigma[4T_0^3\Delta T] \qquad (3.9)$$

Substituting $\Delta T = T - T_0$, (as $T_1 = T$), in Eq. (3.9) and simplifying, one gets:

$$\frac{dQ_1}{dt} = -eS\sigma 4T_0^3[(T - T_0] \qquad (3.10)$$

Comparing this with Eq. (3.4), one gets,

$$\frac{dT}{dt} = \frac{-eS\sigma}{C_p}4T_0^3[T - T_0] \qquad (3.11)$$

Since the total heat loss is the combined effect of the heat loss due to thermal conduction and heat loss due to thermal radiation, so combining the expression of thermal radiation Eq.3.11 with that of thermal conduction Eq. 3.6, gives:

$$\frac{dT}{dt} = -\frac{1}{C_p}\left[\frac{KA}{L} + eS\sigma 4T_0^3\right][T - T_0] \qquad (3.12)$$

Integrating both sides with respect to time t, gives:

$$\int \frac{dT}{[T - T_0]} = -\frac{1}{C_p}\left[\frac{KA}{L} + eS\sigma 4T_0^3\right]\int dt \qquad (3.13)$$

simplification, gives:

$$[T - T_0] = B \exp^{-\frac{1}{C_p}\left[\frac{KA}{L} + eS\sigma 4T_0^3\right]t} \qquad (3.14)$$

where B = integration constant.

With the initial conditions

$T = T_1$ when $t = 0$

and $T = T_0$ when $t = \infty$

then Eq.(3.14) becomes:

$$[T - T_0] = [T_1 - T_0] \exp^{-Gt} \qquad (3.15)$$

where

$$G = \frac{1}{C_p}\left[\frac{KA}{L} + eS\sigma 4T_0^3\right] \qquad (3.16)$$

writing $T - T_0 = \Delta T$, and $T_1 - T_0 = \Delta T_{max}$ in Eq. (3.15), one gets,

$$\Delta T = [\Delta T_{max}] \exp^{-Gt} \qquad (3.17)$$

Taking natural log of both sides gives,

$$\ln \Delta T = \ln [\Delta T_{max}] - Gt \qquad (3.18)$$

Differentiating Eq.(3.18), gives,

$$\frac{\partial}{\partial t} \ln dT = -G \qquad (3.19)$$

where G is inversely proportional to the decay time τ (τ is the characteristic time in which system come to its initial temperature after the heat pulse). It is found experimentally that most of the heat leakage is due to conduction, so ignoring the

radiation term in Eq. (3.16), Eq. (3.19) becomes,

$$\frac{\partial}{\partial t}\ln dT = -\frac{1}{C_p}\frac{KA}{L} \tag{3.20}$$

The value of C_p can be calculated from Eq. (3.20), as,

$$C_p = -\frac{KA}{L}\left[\frac{1}{\frac{\partial}{\partial t}\ln dT}\right] \tag{3.21}$$

Hence the heat capacity of any material can be calculated using Eq.3.21, where thermal conductivity K, cross-sectional area A, and the length L, of the thermal link are constant quantities.

This demonstrates that the heat leak wires should be of small diameter with almost zero heat capacity. If the thermal conductance of the sample is high but less than that of heat leak wires, T(t) must be represented with more complicated form of exponential decay with different time constants [23]. Let $\tau_1 >> \tau_2$ be the thermal coupling time between the sample and its surroundings and τ_2 is the inter thermal coupling time between the heater, sample and the thermometer, then the decay curve can be described by Eq. 3.17 [23],

$$T - T_0 = A_1 \exp(-t/\tau_1) + A_2 \exp(-t/\tau_2) \tag{3.24}$$

where A_1 and A_2 are integration constants can be obtained by setting t = 0, gives

$$A_1 + A_2 = \Delta T \tag{3.25}$$

where the ratio τ_2/τ_1 is of the order of 10^{-2} or even smaller then Eq. 3.24 is a reasonable approximation. But if one is working close to the phase transition of the sample, where the heat capacity changes very quickly then the cooling curve can be represented by more complicated way and one has to consider the full decay equation as [22],

$$\frac{dT/dt}{(T-T_0)} = -\frac{K}{C(T)} \tag{3.26}$$

which means very close to the transition temperature dT/dt and T must be known. Which is difficult to know and is a basic limitation of this method. However, this method can be used for accurate absolute heat capacity measurement away from the phase transition (to ~2%) and can be used to calibrate the data acquired by other

methods. This method is very sensitive and using this method the addenda correction can be made small.

In the limit of very low K, the thermal relaxation method can be used in parallel with the adiabatic method, where ΔT is small enough that τ does not vary appreciably between T_0 and $T_0 + \Delta T$. The difficulty with this method is to measure τ and the base line for T_0 accurately. This is addressed in chapter 4.

3.4.1: Sweep Method:

In the sweep method, mainly two methods are used. In the first method, the power is continuously injected into the sample and at a steady state, the power is switched off and the sample is decaying freely to its initial temperature. In the second method, the power is injected continuously during the course of heating as well as cooling. The sample and sample holder are kept in thermal equilibrium, as both drift slowly in temperature, when the power is applied or removed. Suppose C_S is the heat capacity of the sample and C_A is the heat capacity of the addenda, then the heat applied can be written as;

$$(C_S + C_A) = \frac{dQ}{dT} \qquad (3.27)$$

where dQ/dT is the heat flux into or out of the sample assembly. If P_i is the heat applied by the sample heater and P_0 is the heat (conduction) leak through the thermal link, ignoring the radiation, from the sample, then Eq. 3.27 can be written as;

$$(C_S + C_A) = (P_i - P_0)\frac{dt}{dT} \qquad (3.28)$$

It is clear that heat capacity of any material can be calculated using Eq.3.28, if heat flow into the sample and the cooling rate are known. To monitor heat leak during the experiment is quite difficult. This can be done by measuring the sample equilibrium temperature for different power settings of the heater and calibrating the heat leak. But this process is time consuming. This difficulty can be overcome by eliminating the term P_0 from Eq. 3.28 by combining the heating and cooling curves. [Riegel and Weber, 25]. There are two ways to add heat, applying heat continuously with a constant heater power during the heating cycles, and switch off the heater power during the cooling cycle. In the other method, the heating power is not switched off during

the cooling curve, rather it is adjusted in such a way that the rate of heating and cooling cycle remains constant [26]. This method is explained as the accuracy of the former method deteriorates outside some optimum range, so many cycles need to cover a large temperature range. But in the second method, dT/dt can be kept constant over a wide temperature range.

For an actual heat leak P_0 from the sample, let $P_0 + P_e$ as the calibrated heat leak with an error term P_e, then the equation of the calorimeter can be written as,

$$C = \frac{(P_h - P_0)}{(dT/dt)_h} = \frac{(P_c - P_0)}{(dT/dt)_c} \qquad (3.29)$$

where the subscript h and c are for heating and cooling cycles. Let K be the drive power during the heating and cooling run, then;

$$P_h = P_0 + P_e + K \qquad (3.30)$$

$$P_c = P_0 + P_e - K \qquad (3.31)$$

Putting the values of P_h and P_c from Eqs. 3.30 and 3.31 into Eq. 3.29, one gets,

$$C\left[\left(\frac{dT}{dt}\right)_h - \left(\frac{dT}{dt}\right)_c\right] = 2K \qquad (3.32)$$

or

$$C = \frac{2K}{\left[\left(\frac{dT}{dt}\right)_h - \left(\frac{dT}{dt}\right)_c\right]} \qquad (3.33)$$

One can define the heat capacity, to be calculated from the heating or cooling curve alone, as C_h and C_c:

$$C_h = \frac{K}{(dT/dt)_h} \qquad (3.34)$$

$$C_c = \frac{K}{(dT/dt)_c} \qquad (3.35)$$

The above condition could be fulfilled only, if error due to miscalibraton $P_e = 0$. However, inserting these values into Eq. 3.33, one can find the heat capacity of the sample and sample assembly as;

$$C = \frac{2C_hC_c}{(C_c - C_h)} \qquad (3.36)$$

It is clear from these formulae, that heat capacity can be measured knowing only the

heating and cooling rate. From Eq. 3.35, the systematic errors due to the heat leak miscalibration can be corrected.

The advantages of this method are, no other parameter is involved to calculate the heat capacity, only one needs to know the heating and cooling rate. It can be used over a wide temperature range. The accuracy of these measurements is 0.6% [Henry, 26]. The problem with this method is, it takes a very long time, the correction to heat leak can be miscalculated leading to a big error and the whole system (sample, sample assembly) should be in total thermal equilibrium.

3.5: Differential Calorimetry

In differential calorimetry two or more than two samples can be measured simultaneously. One sample is kept as a reference sample and the other as the sample. Using this technique very minute changes can be detected in the sample with respect to the reference sample. This technique was introduced by Shinozaki et. al., [27]. They measured electronic specific heat simultaneously of three samples, one of pure metal and two alloys of that metal and got 1% accuracy in the range of 2-4 K. Many research groups [28-37], have made developments in this technique using the same basic idea.

In Fig. 3.3 [28], 'S' is the sample to be measured with respect to a reference sample S_r. There are two heaters H_S and H_r, and two thermometers Th_S and Th_r, for sample and reference sample respectively. A thermocouple measures the temperature difference between the sample and reference. The same amount of heat is provided to both heaters, and the corresponding changes in temperature are monitored by the thermometers. From the rise in temperature, one can determine the heat capacity of the sample and reference. More importantly when the heat pulses Q_S and Q_r are applied to the heaters H_S and H_r, they will generate a temperature difference of $\delta T = \Delta T_s - \Delta T_r$ where ΔT_s and ΔT_r are the change in temperature of sample and the reference respectively. This temperature difference δT can be measured correctly using the thermocouple and used to calculate the heat capacity of the sample.

Let us suppose the heat capacity of sample be $C_p(s)$ and of the reference sample be $C_p(r)$. Then the ratio between these two heat capacities can be written as [28],

$$\frac{C_p(s)}{C_p(r)} = \frac{(\Delta Q_s/\Delta T_s)}{(\Delta Q_r/\Delta T_r)} \qquad (3.37)$$

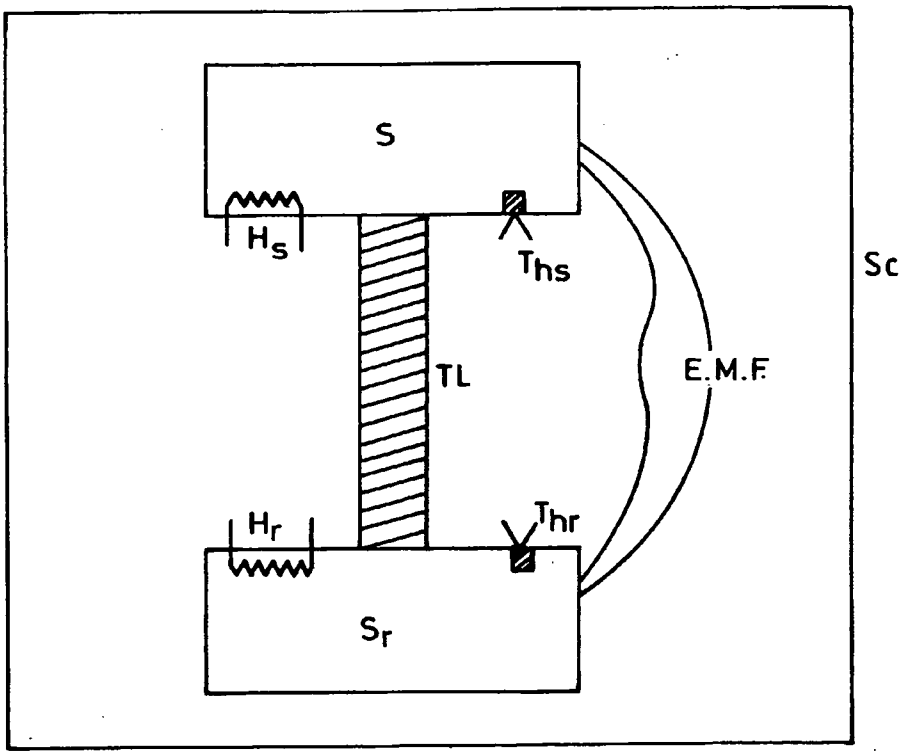

Fig.3.3: A schematic diagram of the differential scanning calorimeter apparatus. S and S_r are sample and reference sample; H_s and H_r are the sample and the reference heater; Th_s and Th_r are the sample and the reference sample thermometer respectively, TL, the thermal link between the sample and the reference sample; E.M.F., the thermocouple, and SC is the superinsulation shield [28].

$$\approx \left(\frac{\Delta Q_s}{\Delta Q_r}\right)(1+\delta T/\Delta T_s) \qquad \text{for } \Delta T_s \approx \Delta T_r \tag{3.38}$$

As this technique gives the relative heat capacities, it is clear that the ratio of C_p is less temperature dependent than the specific heat itself, this increases the relative sensitivity of the measurement, which is a big advantage of this technique.

This technique works well if the inner thermal relaxation times of the samples are equal or nearly equal [35]. If not, then one has to consider the effect of inner thermal times or use some other way to overcome this problem. Marx, in 1978 [35], introduced a similar technique with some modifications. He used two samples connected by a 'thermal weak link' and applying the alternate heat pulses into the samples which causes heat flow in the opposite directions across the thermal weak link. In this way a temperature difference across the thermal link is generated which is

amplified and measured by a pile of several thermocouples distributed along this thermal weak link. The detected temperature variations are inversely proportional to the heat capacity of the two samples. By this way the problem of inner thermal relaxation time can be overcome. Loram [36] also developed a technique similar to Marx [35], but using steady current in the respective heaters, and measuring the ΔT in the heaters by detecting the thermal E.M.F. in the thermocouple piles, and balancing the heater current with a very sensitive Wheatstone bridge. He claimed a very high resolution of $1:10^6$ and an accuracy of $1:10^3$ for C_p in the temperature range of 1.5 K to 300 K. The major advantages of this technique are,

1). The whole experimental set-up is commercially available.

2). The technique has high accuracy and resolution [36].

3). Using this technique a small sample can be measured.

4). In this technique, it is very easy to load the samples, speedy measurements, can be made and it is easy to analyse the data.

5). All thermometers can be calibrated at the same time.

6). It can be used from 1.5 K to 300 K or higher temperature [36].

Some disadvantages are,

1). Due to bigger size of the probe and the differential technique, it is difficult to use in very high fields (bore of the field).

2). If small samples are to be measured, due to their low heat capacity, the fractional errors are large.

3). The drift in thermal E.M.F. causes problems.

4). Due to the use of thermocouple, sensitivity is decreased below 10 K.

5). It is insensitive to the errors in calibration of thermometers.

6). Strong coupling between the heater and samples are required, as the thermal time constant is 2 sec. at 3 K and 20 sec. or more at 300 K.

7). It has a high accuracy of ±1%., but it is difficult with the present instrumentation to get an accuracy of ±0.05-0.2% as is possible with traditional techniques.

8). Differential scanning calorimetry is not as accurate as the adiabatic calorimetry.

9). When the shape of the transition is under investigation, it does not detect

all the phases present in the material if a material has more than one phase [37].

3.6: Steady State A.C. Calorimetry

As remarked by Clement et. al [38] and in private by many other calorimetrists, the traditional techniques have many complications. Although one can get a very high accuracy of 0.001% using traditional techniques, the transient nature of the measurements, the noisy environment, the requirement of thermal isolation of the sample from its surroundings, the use of exchange gases and heat switches and the requirements of using a big sample size to minimize the effect of stray heat leaks, make it difficult to investigate the heat capacity of a material thoroughly using traditional techniques.

All these complications can be overcome using a steady state a.c. technique. This superb technique was introduced by Corbino et.al (39) in 1910. He used incandescent lamps as samples and obtained the temperature oscillations by measuring the oscillations of the electrical resistance at high temperatures. This technique was further developed by, Sullivan and Seidal [40-41], in 1966. They measured specific heat of superconductors at very low temperatures using steady state alternating current for very small samples using the second harmonic method. Handler et. al.[42] measured specific heat at very high temperatures, using the a.c. technique. This is very powerful technique to measure extremely small variations in C_p. It has a lot of other advantages over traditional techniques, which is why many scientists prefer to use it [42-54].

The basic principle and the schematic diagram for this method are shown in Fig. 3.4. When an a.c. current of frequency ω is passed through a sample, its temperature oscillates at twice the frequency of the current. That temperature oscillation is detected by a thermometer on the other side of the sample. In practice, a sinusoidal power $P(\omega)$ of fixed frequency ω is applied to the sample which is connected to the thermometer and the voltage detected by the thermometer is fed into the signal-averaging instrument (usually a Lock-in Amplifier). The a.c. voltage is converted into the temperature ΔT_{ac} and using a first-order approximation, we find [28,40]:

$$\Delta T_{ac} = P(\omega)\ (\omega C)^{-1} \qquad (3.39)$$

Hence measuring the amplitude of the temperature oscillations gives directly measurement of the reciprocal of heat capacity Cp of the sample.

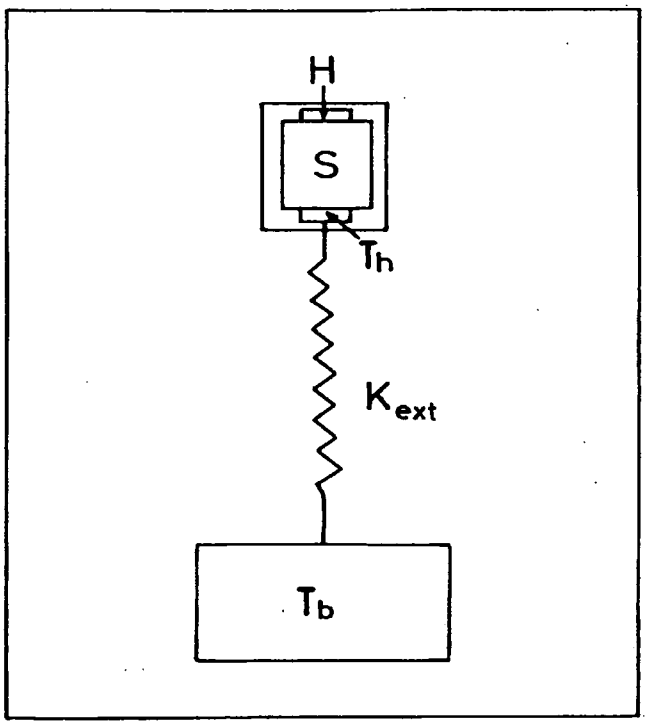

Fig.3.4: A schematic arrangement for the a.c. technique. S, the sample, H, the sample heater and Th, the sample thermometer; T_b, constant temperature block; _/\/_, thermal link; K_{ext}, the thermal impedance between the sample assembly and the background block.

This method is contrary to the adiabatic calorimetry where one has to wait a long time for the sample temperature to come to equilibrium. Hence in this method there is no need to wait for equilibrium of the external time constant τ_1, provided the internal relaxation time $\tau_2 = C/K$, (K is internal thermal conductivity) is short enough. This internal time τ_2 is very important factor. The whole system assembly (heater, sample and thermometer) must obtain thermal equilibrium in a time shorter than the inverse of the applied frequency ω otherwise one will never get the required accuracy. To get 1% accuracy the following condition must hold [28,40-41],

$$\tau_1\omega/10 > 1 > 10\tau_2\omega \qquad (3.40)$$

For simplification, many factors have been ignored in the Eq.3.40. To describe this method in detail, two cases are being discussed as follows:

3.6.1: Sample with infinite thermal conductivity

Let us consider the system shown in Fig. 3.4. It is assumed that the heater,

thermometer, and the sample each have infinite thermal conductivity and they are strongly coupled with each other. The whole sample assembly is coupled to a thermal link which has zero heat capacity. If the sample is heated by a power P(t) then Newton's Law of cooling will give the temperature difference $\Delta T(t)$ between the sample and the reservoir (background) [22] as,

$$C\Delta\dot{T}(t) = P(t) - K\Delta T(t), \tag{3.41}$$

The $\Delta T(t)$ can be obtained using a lock-in-amplifier at the second harmonic when the oscillatory power $P(t) = P_0\cos^2\omega t$. After solving equation 3.41 for the steady state, the solution can be written as [22],

$$\Delta T \approx \frac{P_0}{2K} + \frac{P_0}{4\omega C}\cos(2\omega t - \phi) \tag{3.42}$$

$$= \Delta T_{dc} + \Delta T_{ac}\cos(2\omega t - \phi) \tag{3.43}$$

where ΔT_{dc} represents the constant temperature difference between the sample and the background, ΔT_{ac} is the amplitude of the temperature detected by the lock-in-amplifier due to the oscillatory heater power P(t), and ϕ is the phase shift ($\tan\phi = 2\omega\tau$, $\phi = \pi/2$).

On the other hand if the sample has low thermal conductivity, then the whole sample cannot be heated uniformly, and there will always be a temperature gradient in the sample. To overcome this situation one has to take into account the thickness and low thermal diffusivity. In the next section, a real system using the a.c. technique to measure the heat capacity is discussed.

3.6.2: Sample with finite thermal conductivity:

Following Sullivan and Seidal [40-41] for a finite thermal link between the sample and the bath:

$$T_{ac} = -f_1\frac{R}{(A^* - RC^*)} \tag{3.44}$$

where R = thermal resistivity of the heat link, and the constants are defined by Carslaw [50],

$$\left.\begin{aligned} A^* &= \cosh kl(1+i), \quad \text{and} \\ C^* &= -\kappa k(1+i)\sinh kl(1+i), \end{aligned}\right\} \tag{3.45}$$

The thermal diffusivity n of a material is related to the thermal conductivity κ

($W.cm^{-1}.K^{-1}$) its density ρ ($gm.cm^{-3}$) and its specific heat C ($J.gm^{-1}.K^{-1}$) by a relation, $n = \kappa / \rho C$ ($cm^2.sec^{-1}$). The constant k is defined by, $(\omega/2n)^{1/2}$, l is the thickness of the sample and $i = \sqrt{-1}$. The sinusoidal heat flux through area a and thickness l can be written as, [40-41]

$$f_1 = \dot{q}(0,t) = (\frac{\dot{Q}}{2a})e^{i\omega t} \tag{3.46}$$

For a finite thermal link between the sample and the bath and a sample with infinite thermal conductivity (representing the copper sample),

$$T_{ac} = f_1\left[-\frac{R}{RC^*_h - A^*_h(1+i\omega\frac{RC}{A_r})}\right] \tag{3.47}$$

where Eqs.3.44 and Eq.3.47 are consistent with Eq. 3.39 in the limit that R tends infinity.

Following Sullivan and Seidal and modifying Eq.(3.43), for the case, if the phase shift is not equal to -90^0 which is changing with temperature, then one can write [51];

$$C = \frac{\sqrt{2}\left(\frac{V^2_{rms}}{R_H}\right)}{8\pi f}.\frac{I_{Thermometer}}{V_{rms}(LIA)}.\frac{\partial R_{Th}}{\partial T}.Z \tag{3.48}$$

where

$$Z = kl\left[\frac{2}{(\cos^2 kl \sinh^2 kl + \sin^2 kl \cosh^2 kl)}\right]^{\frac{1}{2}} \tag{3.49}$$

where R_H is the resistance of the sample heater, $\partial R_{Th}/\partial T$ is the slope of the thermometer, V_{rms} is the root mean square value of the sinusoidal input and V_{rms}(LIA) is the root mean square value of the signal detected by the thermometer and measured by the Lock-In Amplifier. $I_{Thermometer}$ is the biased current to the thermometer, k is defined above as $(\omega/2n)^{1/2}$, and l is the thickness of the sample.

To determine kl, the phase shift analysis can be used as,

$$\tan\delta\theta = \frac{-1\left[1 + (\frac{\tan kl}{\tanh kl}\right]}{\left[1-\frac{(\tan kl}{\tanh kl})\right]} \tag{3.50}$$

$\delta\theta$ is the phase shift observed. Z can be measured using Eq.(3.49). Hence using Eq.

(3.48), the heat capacity of any material which has low thermal conductivity can be determined at any temperature.

This method has many advantages, some of them are listed below,

1). The sample is coupled to the bath (heat reservoir) with a thermal link.

2). It is a steady state measurement.

3). Continuous read out of the heat capacity and computer control is easy.

4). Very small samples of the order of 0.1 mg can be measured.

4). Extremely small changes in heat capacities can be detected.

5). To control the sample and the background temperature, there is no need to use heat switches or transfer of gas.

6). This method can be used for, amorphous superconductors [47], liquids [48] and needle shaped specimens [49], at any temperatures.

7). There is no need to generate a very high vacuum in the chamber but on the contrary, can be used at high pressures [52].

8). It is equally applicable in high magnetic fields. [54-60].

There are some disadvantages of this technique,

1). In this technique, the addenda contribution is large.

2). For a sample with poor thermal conductivity, there might be a temperature gradient inside the sample, which needs to be accounted for.

The addenda contribution can be minimised by using chopped modulated light (pulses) incident on the front face of the sample (S.E.Inderhees) [54] and measuring the voltage generated by a thermocouple on the other side of the sample. No physical heater needs to be mounted on the sample.

3.7: Cp measurements of Superconductors in high magnetic fields:

The field of specific heat measurements of superconductors in magnetic fields originated in 1932, when Kessom and Kok [53] while measuring the specific heat of tin accidentally obtained a point in specific heat measurements due to a magnetic field higher than the H_C of tin. Since this discovery many people have measured the specific heat in very high magnetic fields [54-60]. When a magnetic field is applied to a superconductor, the jump height and transition temperature reduce, and if the applied field is higher than the H_C or H_{C2} the superconductor transforms into normal material

and obeys the T^3 law. [see e.g. chapter 2 and 6]. However, measuring the specific heat in a high magnetic field can be problematic. Two major problems which occur are, first, to measure the correct temperature and variations in the sample specific heat, as all the thermometers (except gas thermometer) are affected by the magnetic field and the second is generating a very high d.c. field. Both of these problems can invalidate research findings. To control the background temperature, a field independent capacitor thermometer [61] or bulky gas thermometer is therefore required. Yet the drawback of using capacitance thermometers is that they are not reproducible and sensitive enough to take accurate readings. This problem can be overcome by using a small resistance temperature sensor, diode sensor, or thermocouple for the sample temperature, which can be calibrated using the International Temperature Scale of 1990, according to the field. The other problem is, to generate high d.c. magnetic fields. High field superconductor materials can be used to generate high fields up to 21 Tesla, and after that level, a Hybrid magnet (33 T) can be used, though this introduces considerable problems of noise and vibration. To investigate the properties of superconductors with very high H_{C2}, one hence has to use pulsed magnetic fields. In a pulsed magnetic field, the system equilibrium is crucial, if thermal equilibrium is not achieved, the observed values are too low. So when measuring specific heat in high magnetic fields, one has to be aware of such problems.

3.8: Summary

A wealth of information about the properties of the materials can be gathered by measuring the specific heat. Specific heat data can be used to determine various thermodynamic quantities and to reveal and characterise phase transitions. Significant advances have been made since the time of Nernst [3]. For example, automation by computer control is the most important development in this field in recent years. In established calorimetry, a precise and accurate measurement to 0.001% is now available with the aid of heat pulse method. Though the precision drops dramatically for very small temperature increments. However, this method has been used [22,28] successfully for high resolution at very low temperatures. Heat losses can be minimised if not eliminated by using superinsulation shields, and very thin and high thermal impedance connecting wires. The correct ΔT can be measured by extrapolating the decay curve

back to zero time and applying Eq. 3.18 as described in section 3.4. Digital instrumentation can also be used to get precise data. However, this is a time consuming method and documenting exact point to point data points, close to the transition temperature, peak in specific heat measurements, may result in some data being missed. This problem can be solved, using a long duration of pulse (step method), and using equation 3.20. Unfortunately, this is not suitable for very small samples.

The thermal relaxation method is complementary to the heat pulse method. A thermal heat link is introduced between the sample and the background temperature to measure the decay curve, from where the heat capacity can be calculated. This is a high resolution measurement and is accurate to 1% if certain conditions are met. Using this method very small samples at very low and at high temperatures can be measured. There is no need to use an adiabatic shield to control the heat leak. The difficulty in this method however, is to measure the decay time τ accurately, and then to analyse the data especially close to the phase transition, where the dT/dt is changing rapidly and consequently difficult to measure. For a comparison with other techniques, see **Table 3.1.** However most of these problems can be overcome by using the sweep method. Where one needs to know only the rate of heating and the rate of cooling.

Using differential calorimetry, the specific heat of two or more samples can be measured simultaneously. One sample is kept as a reference sample and the other/s is measured for changes which occur due to temperature scanning or magnetic field variants. This method has a very high resolution, and accuracy if certain conditions are satisfied, see **Table 3.1.** This method can also be used for small samples. Speedy measurements and easy analysis of the data, make it suitable to measure specific heat between the range of 1.5 K to 300 K [Loram,36]. However, due to the large dimension of the probe, it is difficult to use this method for high magnetic fields where the diameter of the probe is a crucial factor. For smaller samples fractional errors are large, and thermocouple sensitivity below 10 K is low. Occasionally, differential calorimetry is misleading in detecting all the phases present in the material. Using this method 1% accuracy can be achieved.

Steady state A.C. Calorimetry is an excellent method for undertaking research. In this method an a.c. power, of particular frequency, is applied to the sample, and the temperature oscillations are measured at double that of the applied frequency. This

Method	Definition	Time Constant	Typical sample size (g)	Conditions for 1% accuracy
Nernst-method[28] (Heat Pulse)	$Cp=\Delta Q/\Delta T$	$\tau_1 >>$ minutes	> 0.2	$10\tau_1 > t_H > 5\tau_2$
Bachmann et.al.[28] (Relaxation time)	$Cp \propto \kappa_1\tau_1$	$\tau_1 > 5\tau_2$	0.01 -1	$\tau_1 >> \tau_2$
Shinozaki et. al. (Differential Calor)	$Cp_{(s)}=Cp_{(r)}$ $\Delta Q_{(s)}/\Delta Q_{(r)}$	$\tau_1 > 10\tau_2$	0.01 -1	$\tau_1 >> \tau_2$
Sullivan et. al.[28] (AC. Method)	$Cp \propto 1/\Delta T_{ac}$	τ_1 short	0.001 - 0.1	$(\omega\tau_1/10) > 1 > \omega\tau_2$

Table: 3.1: Comparison of some methods to measure small samples heat capacities. Cp is the heat capacity of the material, ΔQ, the heat input, ΔT is the temperature increment due to the heat, τ_1 and τ_2 are the external (sample to the surrounding) and internal (between heater, sample and the thermometer) time constants respectively, τ_H is the heating time, s and r represent the sample and the reference sample, ω is the angular frequency of the applied power, ΔT_{ac} is the root mean square value of the temperature increment due to the alternating power.

method can be used to measure extremely small (< 0.1 mg) samples at ultra-low or at high temperatures. Further, there is no need to use high vacuum and exchange gas switches. This is a very sensitive method, and extremely small changes in heat capacity can be measured if certain conditions are met. See **Table 3.1**. It is equally applicable to use this method in very high magnetic fields, and in very noisy environments. Yet if the sample has poor thermal conductivity, and the phase shift is not -90^0 then a modification in the data analysis needs to be introduced using equation 3.48-3.50. The addenda contribution can be large in this method. This can be minimised using chopped incident light pulses on the sample.

Virtually all of the techniques discussed above can be used in the magnetic fields. However, major problems remain in the development of suitable thermometry and in the generation of high magnetic fields. The thermometry problem in high magnetic fields could be overcome by using a new, commercially developed, field independent thermometer by "Lakeshore Measurement and Control Technologies "[61] and high magnetic fields can be generated up to 23 T using low temperature

superconductors, this can be enhanced to 34 T using hybrid technology. There is still more development needed to produce the very high magnetic fields which are required, especially for the high temperature superconductors.

In Durham, we are mainly concerned with the specific heat measurements in the temperature regime of 4 - 20 K on low thermal conductivity superconducting materials in high magnetic fields. We therefore need to choose a method which can fulfill these requirements. As discussed earlier, differential calorimetry has excellent accuracy and resolution but limitations of sensitivity of thermocouple below 10 K, and its bulky dimensions make it difficult to use in our 40 mm high field superconducting bore. The thermal relaxation techniques main disadvantage is that close to the transition temperature it is difficult to calculate dT/dt, which is used to calculate heat capacity.

As discussed above the heat pulse method is very accurate and precise method to measure heat capacity so it is used to check the accuracy and precision of the experiment and to calibrate the data acquired by the a.c. technique. The a.c. technique is being used to measure very small variations in the specific heat as this method is very sensitive in detecting even small changes such as 10^{-6} K by using a Lock-in Amplifier (LIA) and equally applicable in high magnetic fields using a field independent thermometer. This technique can be used at extremely low temperatures for extremely small samples as discussed above. A low thermal conductivity materials can be investigated using the analysis discussed in section 3.7. It is clear that the use of heat pulse method and a.c. technique to study the Chevrel phase materials in the range of 4 -20 K is the best option to minimise ambiguity. Using computer control, very precise and accurate data have been acquired which will be discussed in the following chapters.

References:

A). H. P. Method:

1). Sprackling, M., in Thermal Physics, Macmillan Education LTD. Houndmills, Basingstoke, Hampshire RG21 2XS, 1991, pp. 156-64.

2). Gaede, V. W, Physik Z. 4 (1902) 105.

3). Nernst W., Chem. Abstr. 4 (1910) 2396-98. Sitzber. kgl. preuss. Akad. Wiss., 12,13 (1910) 261-82.

4). Eucken V. A., Physik Z, 10 (1909) 586.

5). E.F. Westrum Jr. G.T. Furukawa and J.P. McCullough, in Experimental Thermodynamics Vol. 1, edited by J.P. McCullough, and D.W. Scott. Butterworth, London, 1968, pp.135-214.

6). J.C. Southard and D.H. Andrews, J. Franklin Inst. 209 (1930) 349.

7). Morin, F.J., and J.P. Maita, Phys. Rev. 129 (1963) 1115-1120.

8). Rapp, R. E., M. L. Siqueira, R. J. Viana, and L. C. Norte, Rev. Sci. Instrum. 63 (1992) 5390-93.

9). Albert, H. B., Rev. Sci. Instrum. 43 (1972) 766-774.

10). Kleinclauss, J., R. Mainard and H. Fousse, J. Phys. E, 10 (1977), 485-489.

11). Dixit, R.N., S.M. Pattalwar, S.Y. Shete, and B.K. Basu, Rev. Sci. Instrum. 60 (1989) 1351-1352.

12). D. L. Martin, Rev. Sci. Instrum. 58 (1987) 639-646.

13). Jirmanus, M., H. H. Sample, and L. J. Neuringer, Journal of Low Temp. Phys., 20 (1975) 229-40.

14). Cezairliyan, A., (Pulse Calorimetry), in Specific Heat of Solids, Edited by C. Y. Ho, Hemisphere Publishing Corporation, New York, 1988. pp. 323-53.

15). Fagaly, R. L., and R. G. Bohn, Rev. Sci. Instrum., 48 (1977) 1502-04.

B): Thermal Relaxation Method:

16). R. Bachmann, F.J. DiSalvo Jr., T.H. Geballe, R.L. Greene, R.E. Howard, C.N. King, H.C. Kirsch, K.N. Lee, R.E. Schwall, H.-U. Thomas, and R.B. Zubeck, Rev. Sci. Instrum. 43 (1972) 205.

17). Schutz, R.J., Rev. Sci. Instrum. 45 (1974) 548-551.

18). Sellers, G. J., and A.C. Anderson, Rev. Sci. Instrum., 45 (1974), 1256-1259.

19). Djurek, D., and Baturic-Rubcic, J., J. Phys. E, 5 (1972) 424- .

20). Junod, A., J. Phys. E: Sci. Instrum., 12 (1979), 945-952.

21). Schwall, R.E., R.E. Howard, and G.R. Stewart, Rev. Sci. Instrum. 46 (1975) 1054-1059.

22). Bednarz, G., B. Miller, M.A. White, Rev. Sci. Instrum. 63 (1992), 3944-52.

23). Shepherd, J.P. Rev. Sci. Instrum. 56 (1985), 273-77.

24). Stewart. G. R. Rev. Sci. Instrum. 54 (1983), 1-11.

25). Riegel and Weber, see, Henry Report for reference.

26). Henry Report, see DPH for reference,

C). Differential Calorimetry:

27). Shinozaki. S.S, and A. Arrot., Phys. Rev. 152 (1966), 611-22.

28). Gmelin, E., Thermochimica Acta, 29 (1979), 1-39.

29). Watson, E. S., M. J. O'Neill, J. Justin, and N. Brenner, Analytical Chem., 36 (1964), 1233-45.

30). Mraw, S.C., in Specific Heat of Solids, Edited by C.Y.Ho., Hemisphere Publishing Corporation, New York, 1988, pp. 395-435.

31). Montgomery, H., G.P. Pells, and E.M. Wray., Proc. Roy. Soc. A301 (1967), 261-84.

32). Bevk, J. and T.B. Massalski, Phys. Rev. B., 5 (1972), 4678-83.

33). Buckingham, M.J., C. Edwards, and J.A. Lipa., Rev. Sci. Instrum. 44 (1973), 1167-72.

34). Martin, D.L., in Specific Heat of Solids, Edited by C.Y.Ho., Hemisphere Publishing Corporation, New York, 1988, pp. 113-52.

35). Marx P. Rev. Phys. appl., 13 (1978), 298-303.

36). Loram, J.W., J. Phys. E., Sci. Instrum., 16 (1983), 367-76.

37). White, M.A., Thermochimica Acta, 74 (1984), 55-62.

D). A.C. Method:

38). Clement, J. R. and E. H. Quinnell, Phys. Rev. 92 (1953), 258-67.

39). Corbino, O. M., Phys. Z. 11 (1910), 413.

40).(a)Sullivan P.F., and G. Seidel, Ann. Acad. Sci. Fennicae, Ser. A., VI, 210 (1966), 58-62.(b) Phys. Letters, 25A (1967), 229-230. (c) Phys. Rev. 173 (1968), 679-685.

41). Sullivan, P. Thesis, Brown University, Providence, Rhode Island, U.S.A.

42). Handler P., D.E. Mapother, and M. Rayl, Phys. Rev. Lett. 19 (1967), 356-358.

43). Varchenko, A.A.,and Ya. A., Kraftmakher, Phys. Stat. Sol. (a) 20 (1973), 387-393.

44). Ya. A., Kraftmakher, High Temp.-High Pressures, 5 (1973), 433-454.

45). Ya. A., Kraftmakher, in Specific Heat of Solids, Edited by C.Y.Ho., Hemisphere Publishing Corporation, New York, 1988, pp. 299-321.

46). Garland, C. W., Thermochimica Acta, 88 (1985), 127-142.

47). Zally, G.D., and J. M. Mochel, Phys. Rev. B. 6 (1972), 4142-4150.

48). Imaizumi, S., K. Suzuki., and I. Hatta, Rev. Sci. Instrum. 54 (1983), 1180-85.

49). Ivanda, M., and D. Djurek, J. Phys. E: Sci. Instrum. 22 (1989), 988-992.

50). Carslaw, H. S. and J .C. Jaeger, in Conduction of Heat in Solids, Oxford University Press, London, 1959, 2nd Edition, pp. 110ff.

51). Full details of these Equations are being given in Appendix I of this thesis.

52). Baloga, J.D., and C.W. Garland, Rev. Sci. Instrum. 48 (1977), 105-110.

E).Cp. in Magnetic Fields:

53). Keesom, and J.A. Kok, Akademie der Wetenschappen, Leiden, University , Physical Lab. Commun. 35 (1932), 743-748.

54). Inderhees, S.E., M.B. Salamon, J.P.Rice, and D.M. Ginsberg, Phys. Rev. B. 47 (1993), 1053-1063.

55). Schmiedeshoff, G.M., N.A. Fortune, J.S. Brooks, and G.R. Stewart., Rev. Sci. Instrum. 58 (1987), 1743-45.

56). Orlando, T.P., E.J. McNiff, Jr., S. Foner, and M.R. Beasley, Phys. Rev. B., 19 (1979) 4545-61.

57). Khlopkin, M.N., Sov. Phys. JETP., 63 (1986), 164-168.

58). Foner, S., in Superconductivity in d- and f- band Metals, edited by, D.H. Douglass, Plenum Press, New York, 1976.

59). Junod, A., E. Bonjour, R. Calemczuk, J.Y. Henry, J. Muller, G. Triscone and J.C. Vallier, Physica C., 211 (1993) 304-318.

60). Janod, E, C Marcenat, C. Barabuc, A. Junod, R. Calemczuk, G. Deutscher and J.Y. Henry, Physica C., 235-240 (1994), 1763-1764.

61).Temperature Measurement and Control, Product Catalog by LakeShore Cryotronics Inc, 1995, part 1.

CHAPTER 4
HEAT PULSE METHOD

4.1: Introduction:

The heat pulse method is a traditional and well established technique to measure heat capacity of a sample. In this chapter, the Durham Specific Heat Probe, its design, use, and accuracy, in heat pulse measurements will be addressed.

This chapter consists of 10 sections, as follows: Section 4.2 deals with the principle of operation. Section 4.3, is devoted to external circuitry used in this experiment. Section 4.4 describe the probe design, where physical and mechanical description and thermal requirements to build a specific heat probe are explained. Section 4.5, describes how the sample is mounted. In Section 4.6, development of the appropriate thermometry is explained. In section 4.7, calibration of the instruments and the devices is discussed. Section 4.8 consists of the experimental results acquired using the heat pulse technique in 0-field, and section 4.9 is involved with the high magnetic field measurements. Sections, 4.10 includes the discussion, advantages and the disadvantages, and accuracy, in the light of the data acquired and section 4.11, concludes this chapter.

4.2: Principle of Operation:

The principle of operation of quasi-adiabatic heat pulse method is, by adding heat of short duration of pulse of known current I and time Δt to the system and noting the changes occurred in the system. The heat pulse raises the temperature of the sample. The temperature of the sample is allowed to decay freely. During the decay, ΔV is recorded. The recorded voltage has an exponential decay. Taking the natural log of ΔV gives a straight line which is extrapolated back to zero (i.e. when the heat pulse has been started) using Eq. 3.18. In this way Cp can be measured.

4.3: External Circuitry:

The external circuitry of the experimental set up of the system is shown in Fig.4.1. It consists of many devices and instruments. A Farnell power supply is used to supply the current to the heater on the sample. The amount of current and time of the pulse is controlled by a computerised switch and recorded by a Keithley [1] 196 DVM acting as an ammeter. The Cernox-1030 thermometer is biased with a

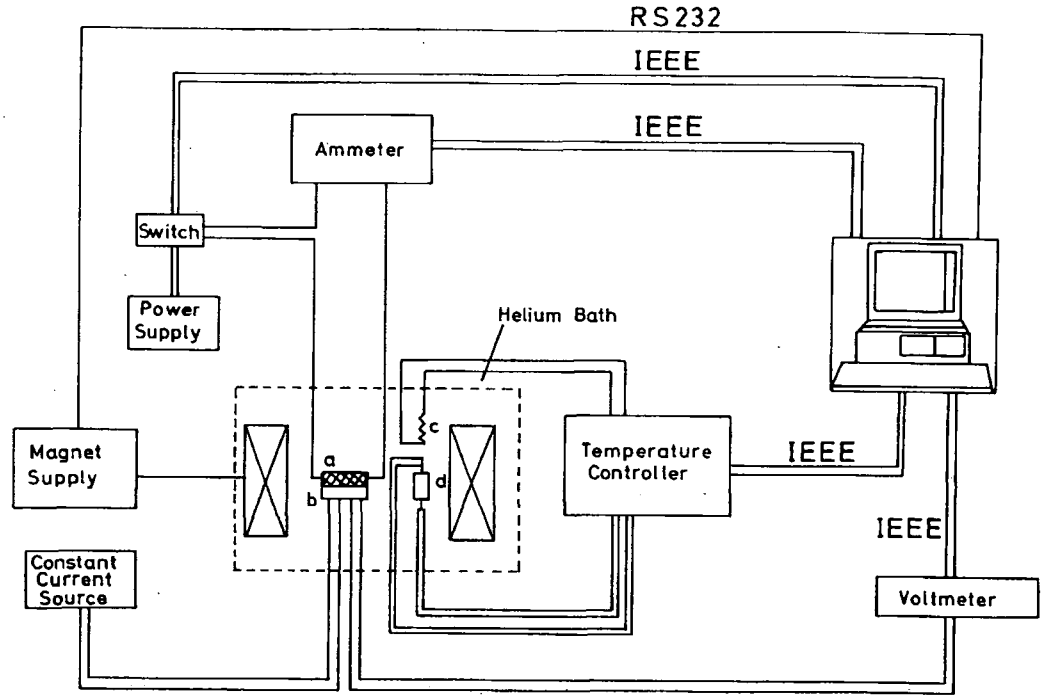

Fig.4.1. A schematic of the experimental Set up. In the Fig. 'a' stands for the sample and the sample heater, 'b' denotes the CX-1030 thermometer, 'c' is background heater, and 'd' the RhFe-thermometer.

Lakeshore constant current source.

To measure the signal and the variation due to the heat pulse a Keithley 2000 DVM is used as a voltmeter. The background temperature of the system is controlled by a Lakeshore Temperature Controller DRC-91CA. If the measurements needed to be made in high magnetic field, a Superconducting Magnet and Cryostat [2] can be used which is able to provide a field of 15/17 Tesla at 4.2 K / 2 K. This is operated by an Oxford IPS120-10 Power Supply. The Computer has control on all these instruments. All these instruments except magnet power supply, are connected to an 386-IBM Computer with a series combination of IEEE interface cables. The magnet power supply is connected with computer by RS-232 cable. The ASYST language developed by the Keithley Instruments [1] is used for computer control. The good interactive, real time, and graphical displays on screen, make ASYST a powerful language to control the instruments. In this way, the whole experiment can be monitored with very high resolution and the accuracy.

The 8-wire high magnetic shield cable is used to reduce the magnetic field induced errors. At the bottom end of the probe, PTFE-enamel wires are used. Every pair

of PTFE-wires is twisted to reduce the noise in the system.

4.4: The Probe Design:

In this section the description of Durham specific heat probe, the factors on which the probe design is based are discussed in detail;

4.4.1: Physical and Mechanical Description:

The overview of the Durham Specific Heat Probe is shown in Fig. 4.2. The probe has a total length of 1590 mm with outer diameter of 19 mm. The head of the probe is made of brass with its outer diameter of 90 mm and a length of 80 mm. The brass head has two 10-pin connector terminals for the sample/ thermometry leads and a vacuum pump connector for controlling the pressure inside the probe. The upper outer jacket of the probe can be separated from its lower outer jacket at a distance of 70 mm from the bottom end of the brass head, and during the experiment, is sealed, using vacuum fitting (O-ring and a clamp). The inner pumping tube has a diameter of 9 mm for the thermometry/sample leads and has 10 Copper spacers mounted on it to make a good thermal link with the outer jacket. The inner pumping tube finishes at the bottom end of the probe at Steel spacers, which connect the top end to the bottom end of the probe.

The bottom end of the probe is shown in Fig. 4.3. The bottom end is mainly made of Copper which is connected to top end (steel spacer) with the aid of Tufnol support struts. Tufnol is used to minimise the heat leak to the outer environment from the bottom end. The terminal block support has two opposed flat regions for terminal connectors. These terminal connectors are used to prevent the thermal voltages developing across the terminals of the circuitry and easy access to the circuit. Next to the terminal block support is the Cu-block, which is the most important part of the system and acts as heat sink which provides an environment connected thermally to sample chamber. Almost half of the background heater is mounted on this part on the space provided of the Cu-block and the other part is mounted on the demountable Cu-Can. The RhFe-thermometer is also mounted in the copper block in a cavity and is used to control the temperature of the Cu-block. The bottom end of the Cu-block has two steel rods to support the sample. Inside the Sample Chamber is the CX-1030 thermometer and the strain gauge which are mounted on the sample. This system is supported by dental floss which is attached to the steel rods with brass screws.

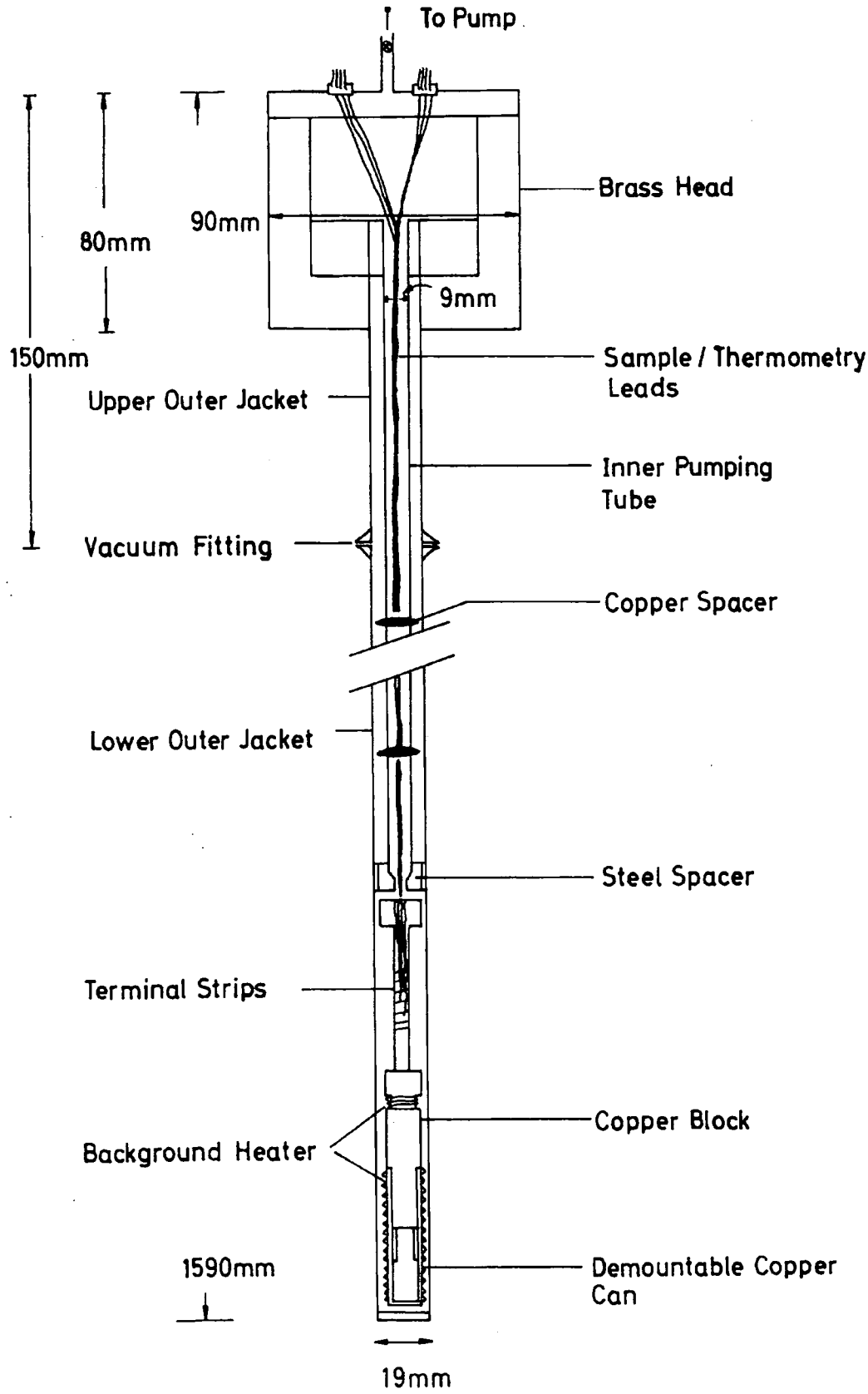

Fig.4.2. Overview of the Durham Specific Heat Probe.

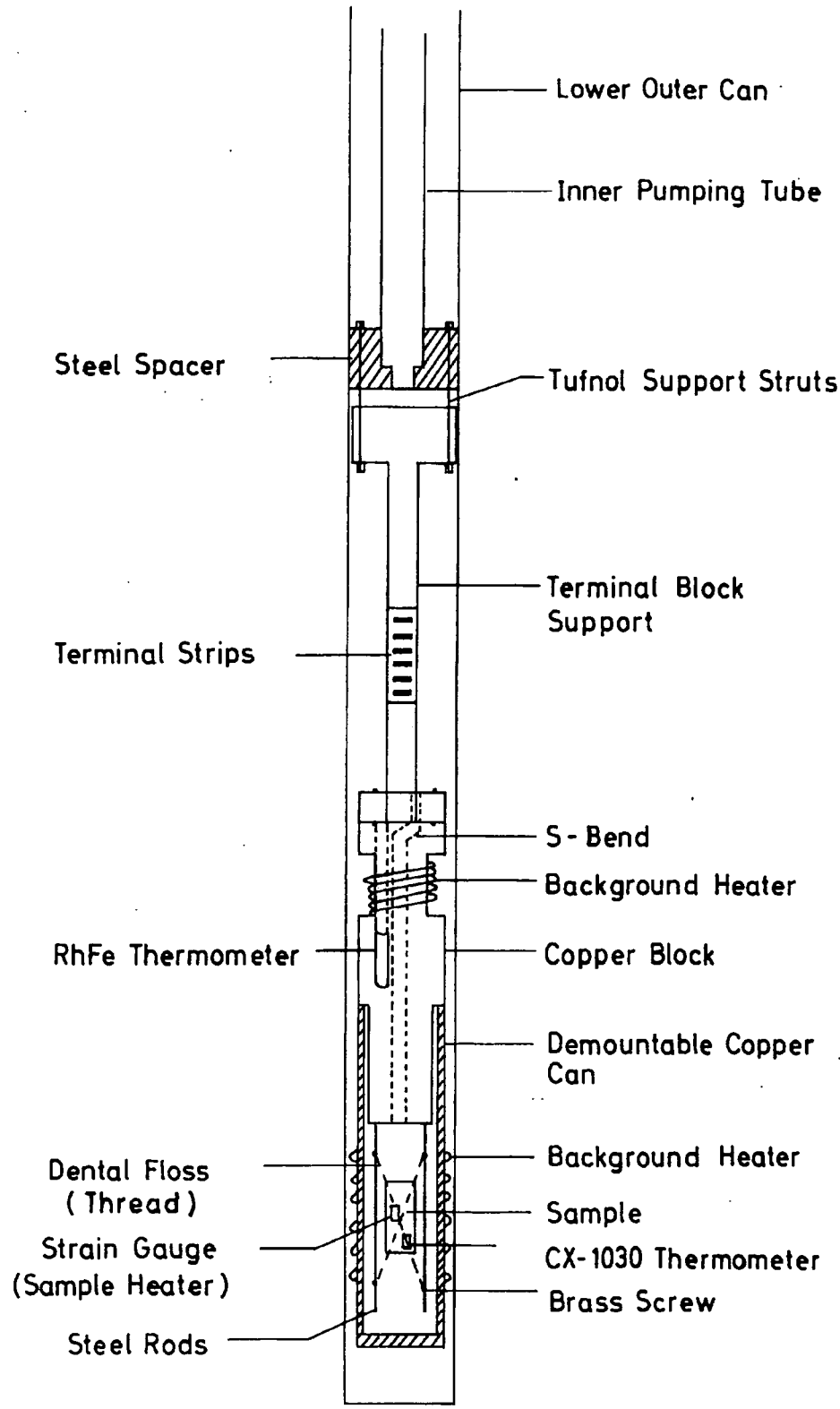

Fig. 4.3. The Bottom end of the Durham Specific Heat Probe.

4.4.2: Thermal requirements:

To meet the thermal requirements, important factors include how to control the background and the sample temperature and how to minimise the heat leak. The background temperature is controlled by a Lakeshore DRC-91CA Temperature Controller with the help of a 4029-RhFe-Thermometer and a background heater made of Constantan alloy wire of SWG-36. The sample temperature is controlled and sensed by a CX-1030 thermometer from Lakeshore Cryogenics. The CX-1030 thermometer has very short dimensions of [3], 3.2 mm x 1.9 mm base x 1 mm high, with a mass ≈ 40 mg, which make it possible to mount very small samples to it. A strain gauge WK-06-062AP-350 from Micro-Measurements Division [4] is used after cutting into a suitable size of 5 mm x 2.5 mm x 0.05 mm and mass of 3.19 mg to use with the small samples as the sample heater.

To minimise the heat conduction down to the leads, thin high thermal impedance wires has been used. Only two of the four terminals of the sample heater (strain gauge) are used to minimise the cross-sectional area for thermal conduction. The leads are flat with thickness of 0.06 mm and 0.14 mm width and made of Beryllium Copper. The sapphire base of CX-1030 thermometer made it useful for achieving equilibrium given its 15 milli sec. at 4.2 K and 0.25 sec. at 77.25 K thermal response time. Two non-magnetic connecting leads of phosphor-bronze with 0.2 mm diameter each are soldered to the sensor [3] to connect it with other circuitry. An S-bend hole in the main copper block reduces the radiation. The 3-turns of super-insulation of Aluminium foil round the bottom end of the probe maintain the adiabatic behaviour and reduce liquid helium consumption.

A pressure of typically 10^{-3} mbar at the warm end is maintained to reduce conduction and convection. With the conditions discussed above, it is quite possible to get good accuracy in a large temperature range of 4.2 K to 300 K.

4.5: Sample Mounting:

To mount the sample properly is crucial. In the heat pulse method, large samples of almost any geometry or dimension can be used. To mount the sensor and heater on opposite sides of the sample, General Electric-Varnish (G.E. Varnish) supplied by Oxford Instruments, is used. It can provide a thin layer helps to reduce intra-sample time and enhanced the thermal contact. After mounting the sample, it is tightly bound by the dental floss and allowed to dry for a minimum of two hours at room

temperature. After drying, the two leads of sample heater are soldered with the enamel-insulated Constantan wires. The soldered contacts are wrapped with the cigarette paper to eliminate short-circuiting between two terminals of the heater. The whole sample assembly is tightened by two crosses of Dental floss, with the aid of brass screws on the steel rods, on both sides of the sample assembly to eliminate the vibrations in the system and keep the sample fixed. The demountable copper can is mounted on the copper block. The part of the background heater on the demountable Cu-can is connected electrically to the other part of the background heater and the soldered parts are covered with cigarette paper to eliminate short circuiting. All connections on the terminal strips are checked thoroughly with a DVM.

In mounting samples, Tweezers, a very useful instrument for holding the thermometer/ strain gauge to the sample while the GE-Varnish dries, Acetone and Safe-Buds are good for dissolving the GE-Varnish and can be used to demount the sample and cleaning the surfaces of sample, CX-1030 thermometer and Heater.

4.6. Development of Appropriate Thermometry:

To sense the sample temperature, a very sensitive sensor is required which should be field independent and of suitable size to mount on even very small samples. Prior to selecting CX-1030 thermometer, a large variety of heat sensors were tested and rejected due to one or another reason. They are discussed below;

Type T Thermocouple:

First of all, a Type T thermocouple was tested. Its calibration is shown in Figs.4.4. The Cu-results obtained using this thermocouple are compared with literature and shown in Fig. 4.5. These specific heat results differ by 20% from the literature. The thermocouple's small area make it suitable to reduce the addenda contribution and minimise the radiation losses but due to poor reproducibility of results, its low sensitivity at liquid helium temperature [1], and the large heat leak from its leads, we considered it unsuitable to use in the experiment.

Thin Film RhFe- Thermometer.

Thin film RhFe-resistance thermometer was tried. It is good due to its small size and positive temperature coefficient but not suitable due to its low sensitivity at liquid helium temperature, the fragile nature of the wires and strong magnetic field

dependence.

DT-450 Thermometer.

The DT-450 thermometer is quite suitable at all temperatures due to its high sensitivity particularly at liquid helium temperature. Its calibration is shown in Fig.4.6. The specific heat results obtained using DT-450 thermometer has a very close agreement with that of literature [5], typically ~ 3% as shown later in this chapter. However the big drawback of DT-450 thermometer was its strong magnetic field dependence.

Cernox (CX-1030) Thermometer.

All the above sensors were investigated to find a suitable sensor to use in our experimental set-up but all were rejected due to one or another reason. We found CX-1030 thermometer quite suitable for our measurements. It has a very high sensitivity at liquid helium temperature, short thermal response time, a robust design, long life over a large number of cycles, small size, and above all its weak magnetic field dependence make it most suitable for use in our measurements. CX-1030 thermometer eliminates the need of a capacitor thermometer to be used in the experiment to control the background temperature of the system. It is used to read the sample temperature and can be used to read the true temperature, in a magnetic field, of its surroundings in zero-and in high magnetic fields.

Calibration:

To control the background temperature of the system, a RhFe-4029 thermometer purchased from the Oxford Instrument is used. A 0-field commercial calibration was provided with this thermometer which was checked and extended with another similar RhFe-Thermometer. The results are shown in Figs.4.7. The high field calibration made in Durham using a capacitor thermometer is shown in Fig.4.8. Similarly the calibration of CX-1030 thermometer was completed in 0- and high fields are shown in Figs. 4.9-4.10 [6]. The results shown in Fig.4.11, demonstrated that the CX-1030 thermometer has a very small magnetic field induced errors of 200 mK at 15 T.

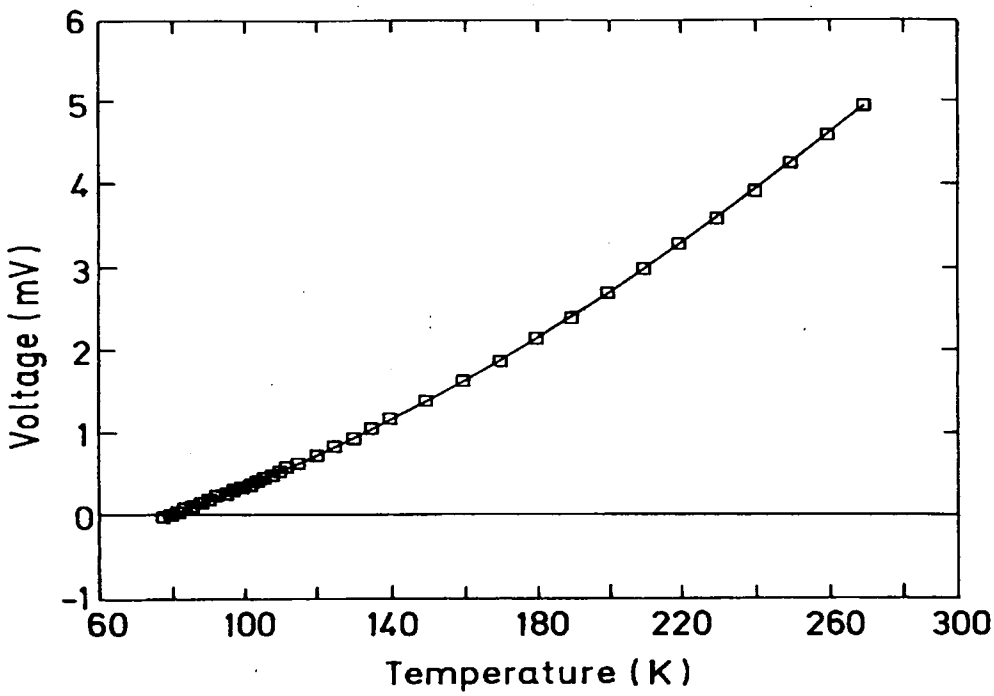

Fig.4.4. Calibration of Type-T (Copper-Constantan) Thermocouple as a function of Temperature.

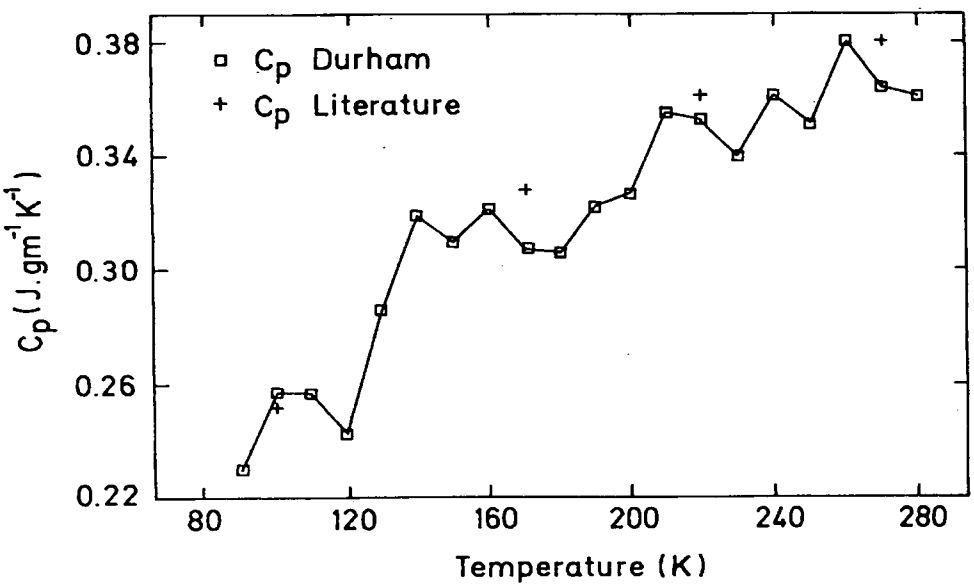

Fig.4.5. Specific Heat Capacity of Cu using Type-T Thermocouple. Durham Results are compared with literature [5].

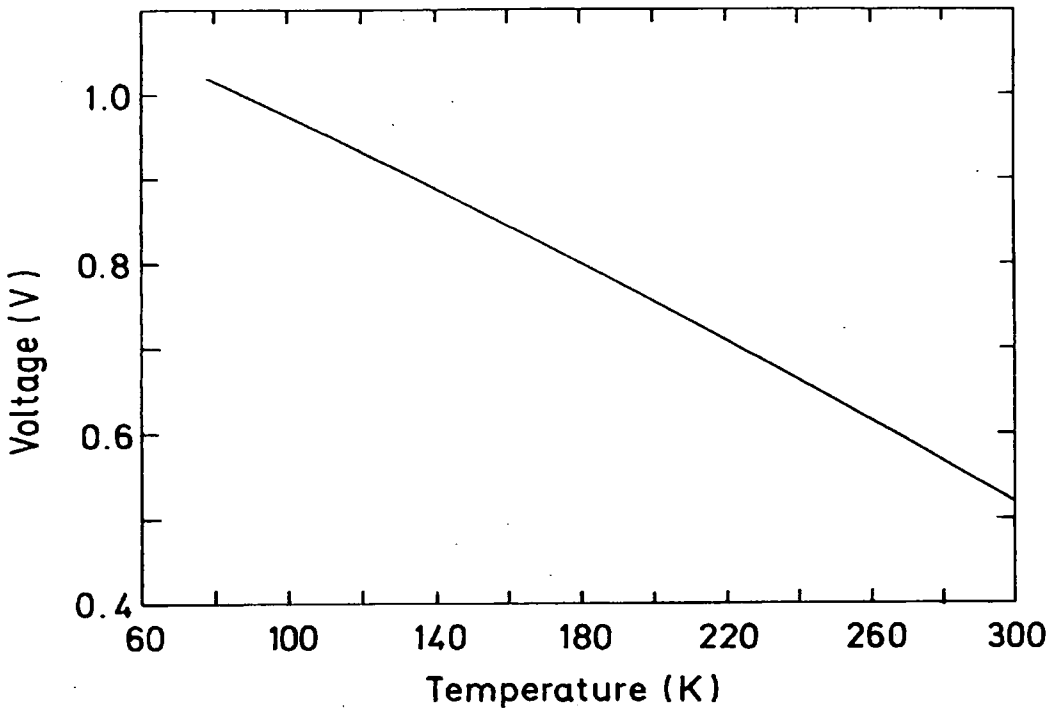

Fig.4.6. Calibration of DT-450 Thermometer as a function of Temperature.

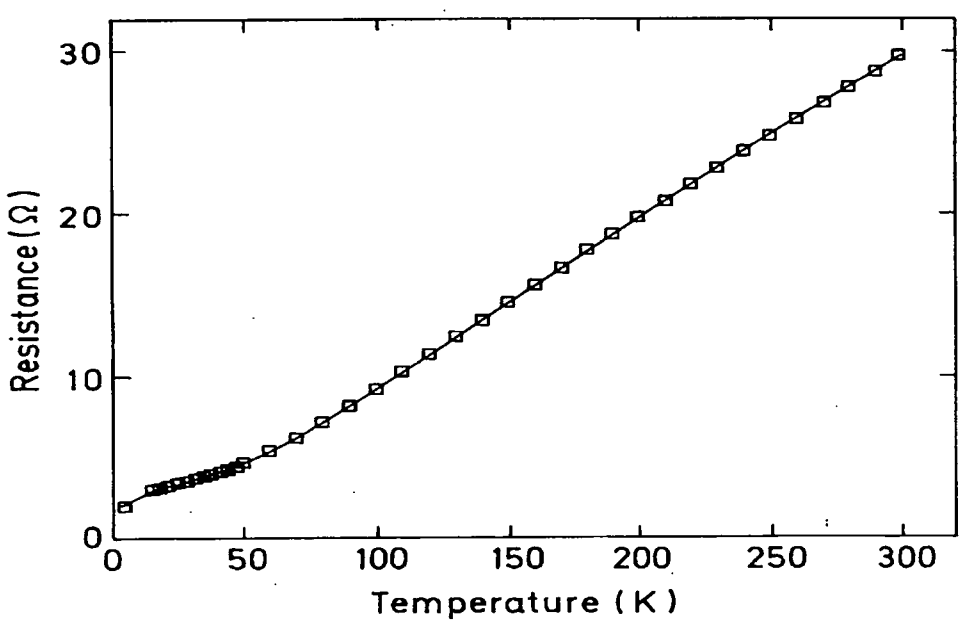

Fig.4.7. Calibration of RhFe-4029 Thermometer in 0-Field.

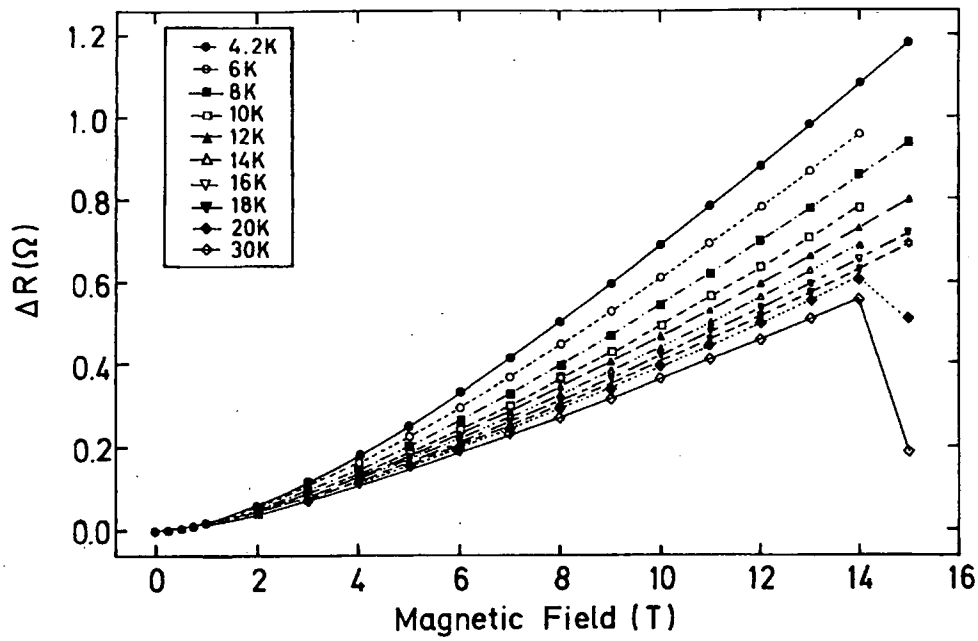

Fig.4.8. Graph showing the difference in resistance ΔR between the resistance of the RhFe-Thermometer in 0-field and that in High magnetic fields.

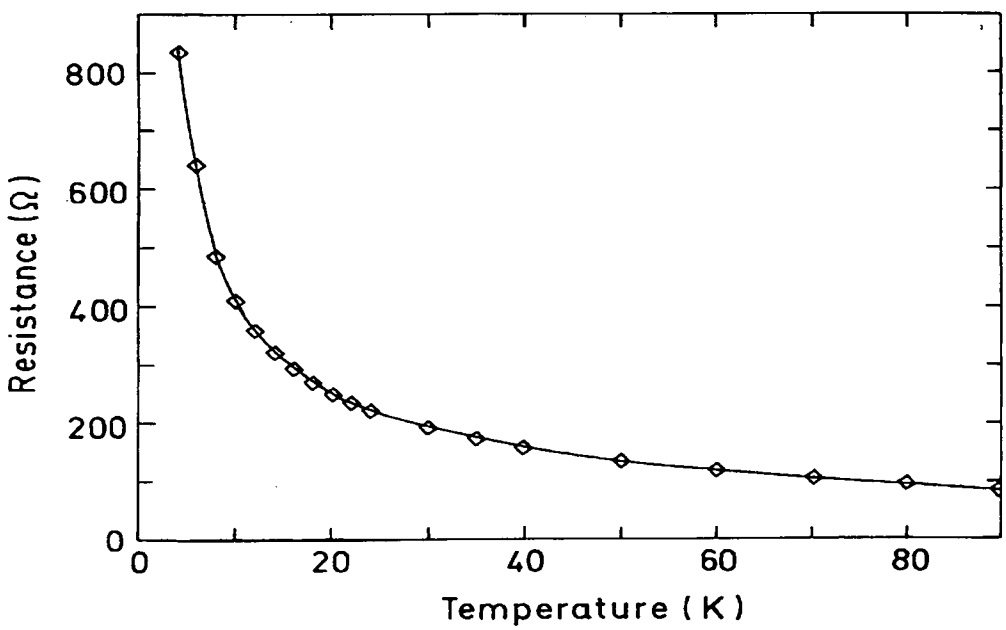

Fig.4.9. Calibration of Cernox (CX-1030) Thermometer in 0-Field as function of Temperature.

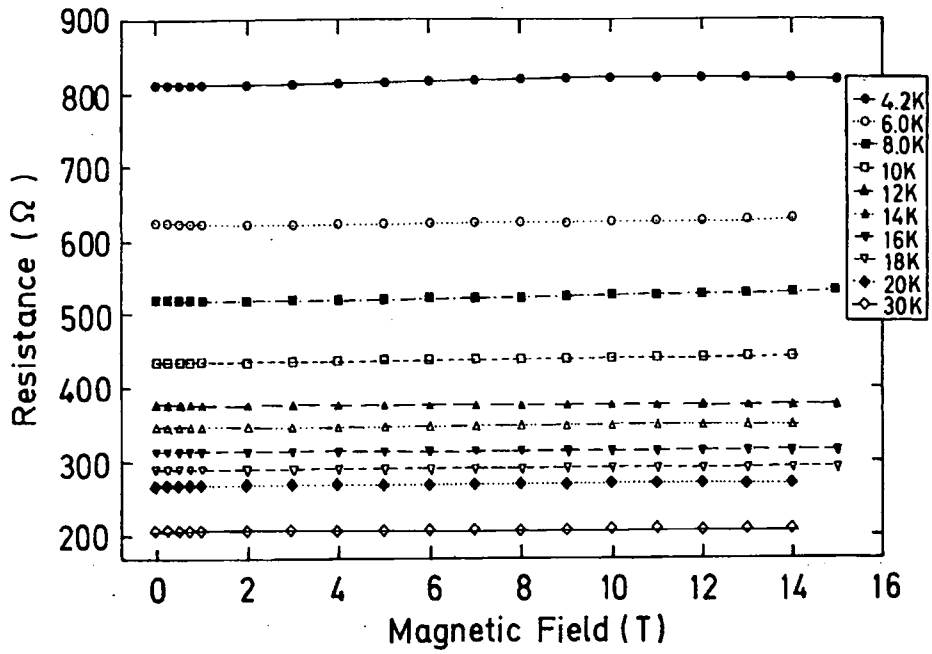

Fig.4.10 .Calibration of CX-1030 Thermometer in fields up to 15 T.

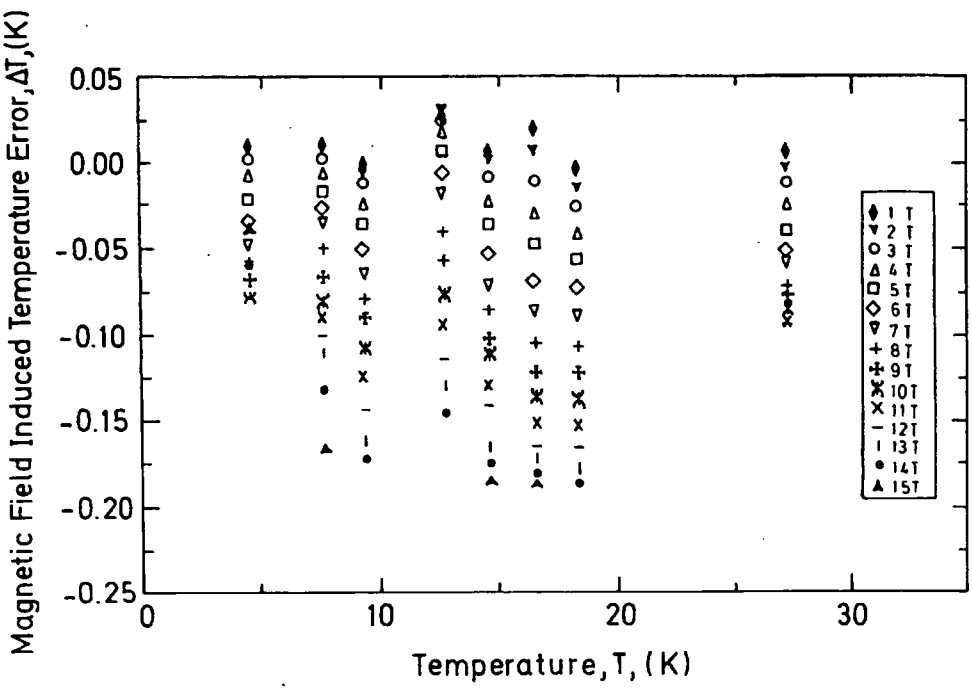

Fig.4.11. Magnetic Field-induced Temperature errors of a CX-1030 Thermometer from 4.2 K to 30 K in fields up to 15 T.

Another device used in the experiment is sample heater. A strain gauge is used as a sample heater. Its calibration was made using RhFe-Thermometer. It has an almost constant resistance of 350 Ω from room temperature to liquid helium temperature.

The 4029-RhFe Thermometer has an accuracy of ±16 mK at 4.2 K, ±18 mK at 77 K and ±18 mK at 273 K with a 30 point calibration. Similarly the accuracy of CX-1030 thermometer was, ±5 mK at T < 10 K, ±20 mK at 20 K and ±140 mK at 300 K in 0-field and ≤ 200 mK magnetic field-induced temperature error in 15 T.

4.7: Calibration of Instruments

In Durham to measure specific heat of the materials, a DRC-91CA temperature controller is used to control the background temperature. It was calibrated by a series of resistors read by DVM-196 using 4-probe method against the temperature controller. The temperature difference in resistances were plotted on a graph Figs. 4.12. and correction were made to temperature controller. A high precision multi meter-196, with an accuracy of 1.5 x 10^{-6} and resolution of 100 nA [1] was used as an ammeter. The multi meter-2000, with an accuracy of $3x10^{-6}$ and resolution of 0.1 uV [1] as a voltmeter and DRC-91CA temperature controller with a typical accuracy of 25 mK (depending on the thermometer used).

4.8: Experimental Results on Copper in 0-Field:

Copper has a very high thermal conductivity and well established values of specific heat which make it a good standard. It can be used to check the accuracy and the reliability of the technique. A typical chart recorder trace of the switch is shown in Fig. 4.13 and a typical resultant decay curve in Fig. 4.14.

Determining ΔT

The recorded decay curve can be used to determine ΔT. To overcome the problem of heat leak the decay curve back to zero is quite suitable. By taking the natural log of the decay curve a straight line fit provides the Y-intercept when time was zero. The number obtained from the Y-intercept is converted to ΔT by using the **Eq. 3.18.** The extrapolation back to zero is shown in Fig.4.15.

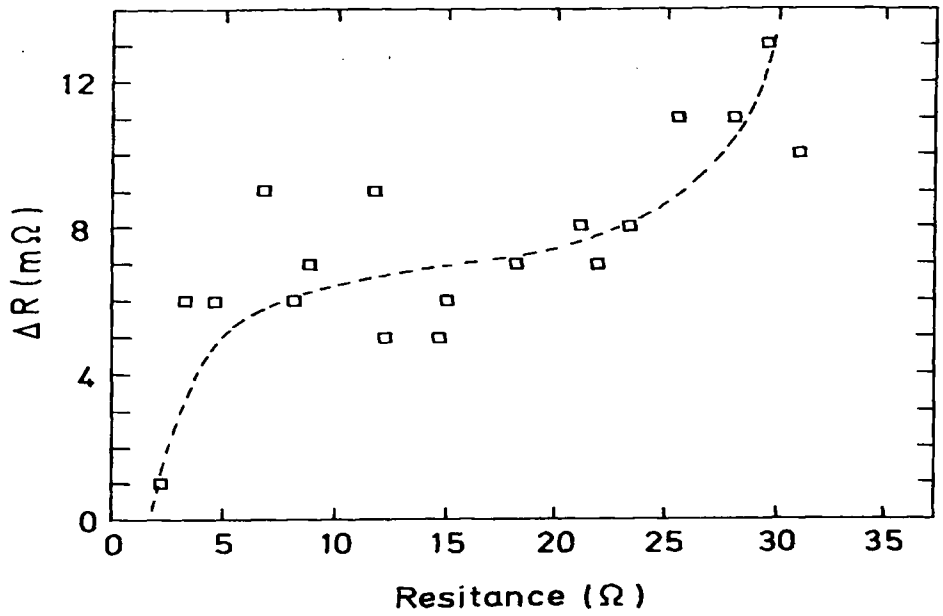

Fig.4.12. Graph showing the difference in resistance ΔR between that read by the Lakeshore Temperature Controller and the true resistance (R_{true}) read by DVM-196, using 4-terminal method.

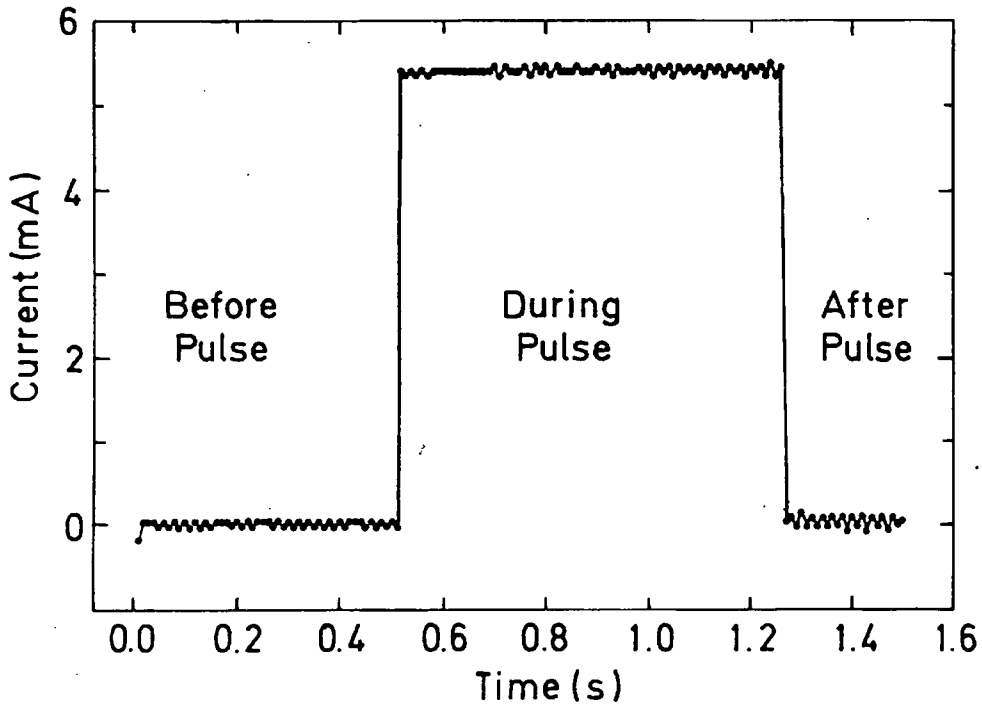

Fig.4.13. A Typical Pulse behaviour showing Current through the heater as a function of Time.

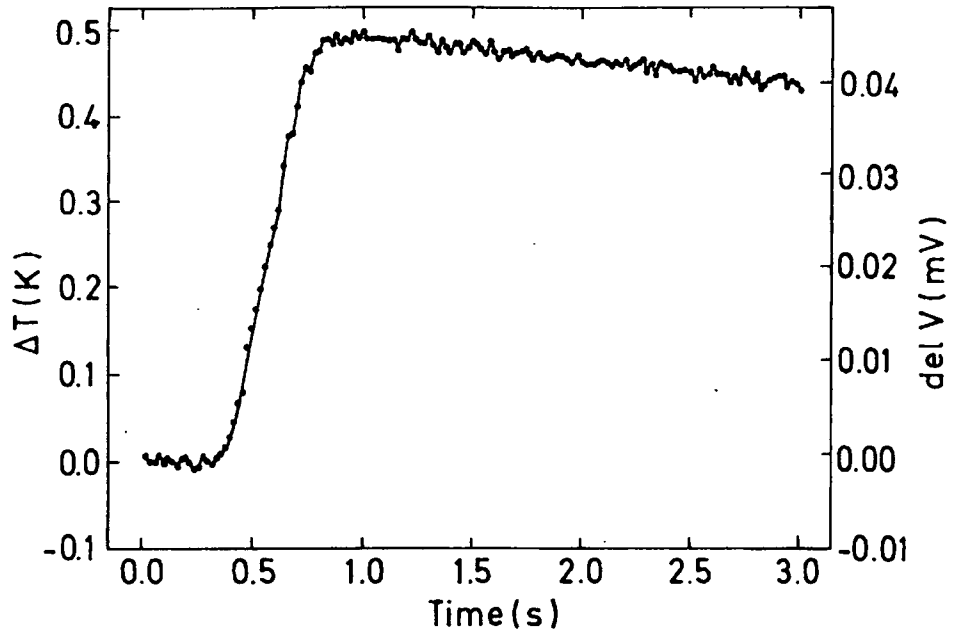

Fig.4.14. A typical trace showing the rate of warming before, during and after the heat pulse. ΔT represents the temperature change used to calculate the Heat Capacity.

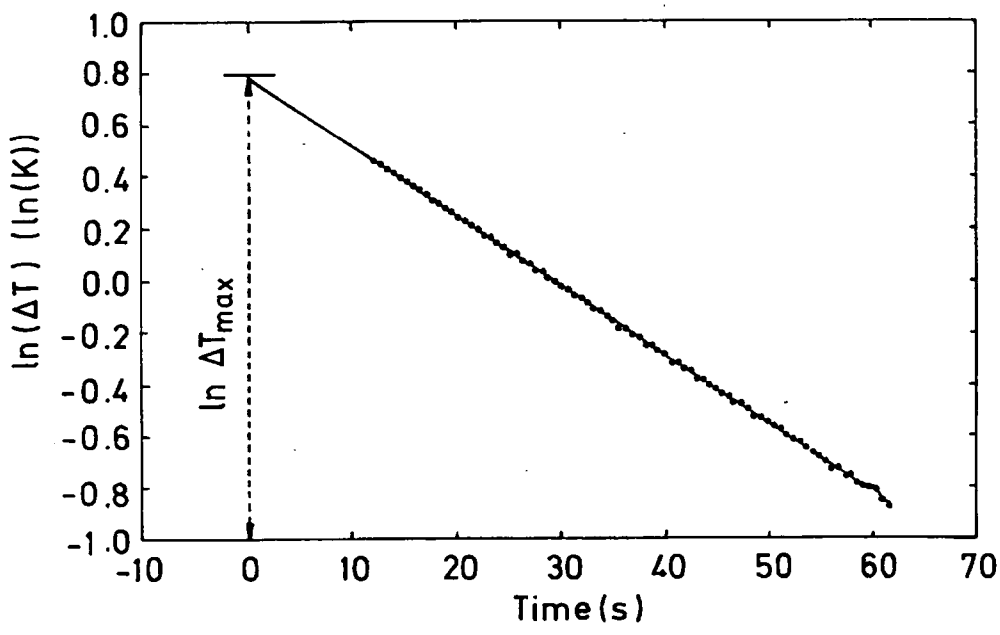

Fig.4.15. To measure ΔT_{max}, the decay curve is extrapolated back to zero time (when the pulse was triggered). $\ln\Delta T$ as a function of time is plotted and Y-intercept is determined which is converted ΔT after the exponential of $\ln(\Delta T_{max})$.

Analysis of Data.

Four Copper samples were studied thoroughly. For every sample, a graph between ΔT vs. heat dissipated has been plotted and shown in Fig.4.16. The slope of each sample was determined using a straight line fit, which gives the heat capacity of that sample at the corresponding temperature. This heat capacity of different samples is plotted against the mass of the sample. The slope of the straight line has been calculated which provides the specific heat of Cu at that temperature and the Y-intercept, the heat capacity of the addenda. Heat Capacity vs. Mass to calculate specific heat and the addenda is shown in Fig.4.17 at 80 K and 300 K.

From Fig. 4.17 it is noted that Heat Capacity is independent of ΔQ (Heat in) and is proportional to the mass of the sample as required. A plot of specific heat versus temperature of Cu is shown in Fig.4.18. The %age deviation of specific heat measured in Durham from literature [5] is shown in Fig.4.19 for data taken both with the DT-450 thermometer and the CX-1030 thermometer. The series of measurements at 21 K agreed with the literature value to ~ 2 %. Typical data from the literature are shown in Fig. 4.20. Similarly the heat capacity of Addenda from 80 K to 300 K using Cu samples is shown in Fig.4.21.

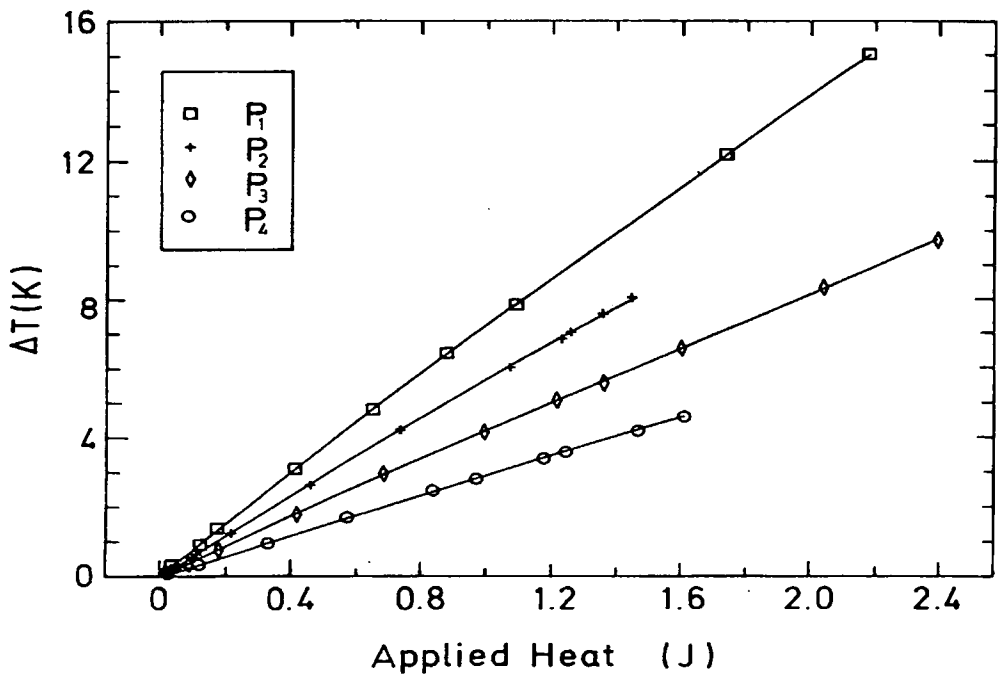

Fig.4.16. The temperature rise ΔT after the heat pulse as a function of heat ΔQ for four Cu-samples P1,P2,P3 and P4 of different mass at 80 K.

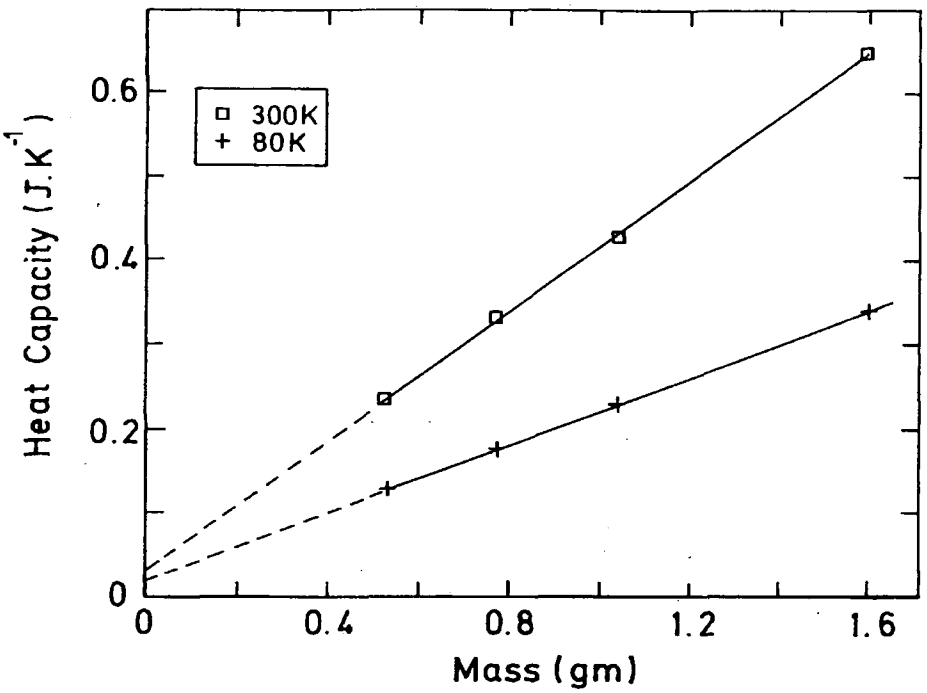

Fig.4.17. Heat Capacity as a function of Mass of Cu-Samples at 300 K and 80 K to calculate the Specific Heat and addenda.

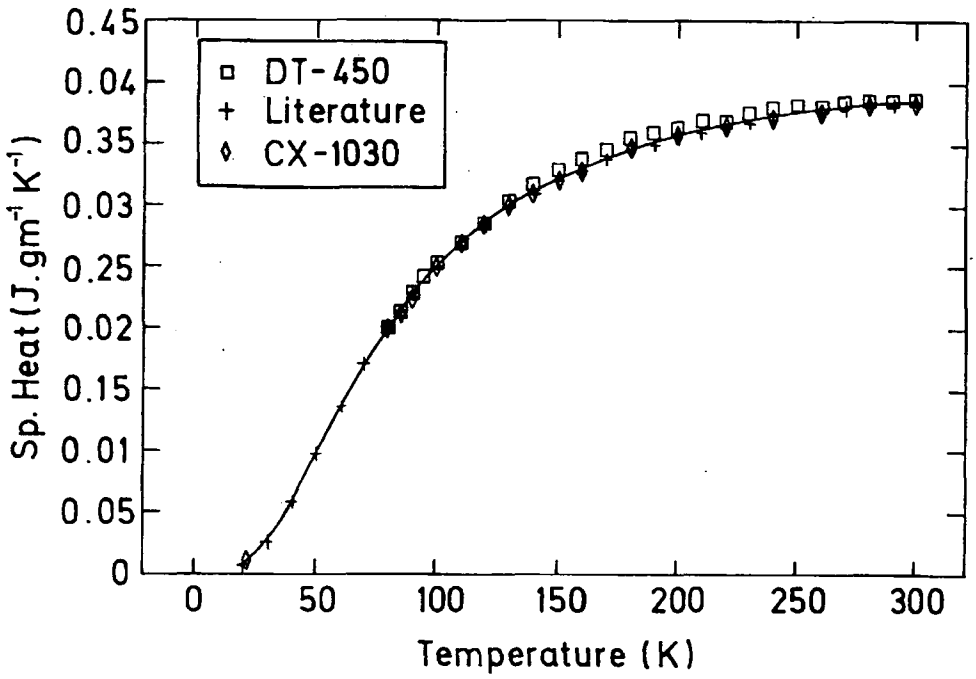

Fig.4.18. Comparison between the specific heat of Cu from 20 K to room temperature measured in Durham using DT-450 Thermometer and CX-1030 Thermometer with results from the literature [5].

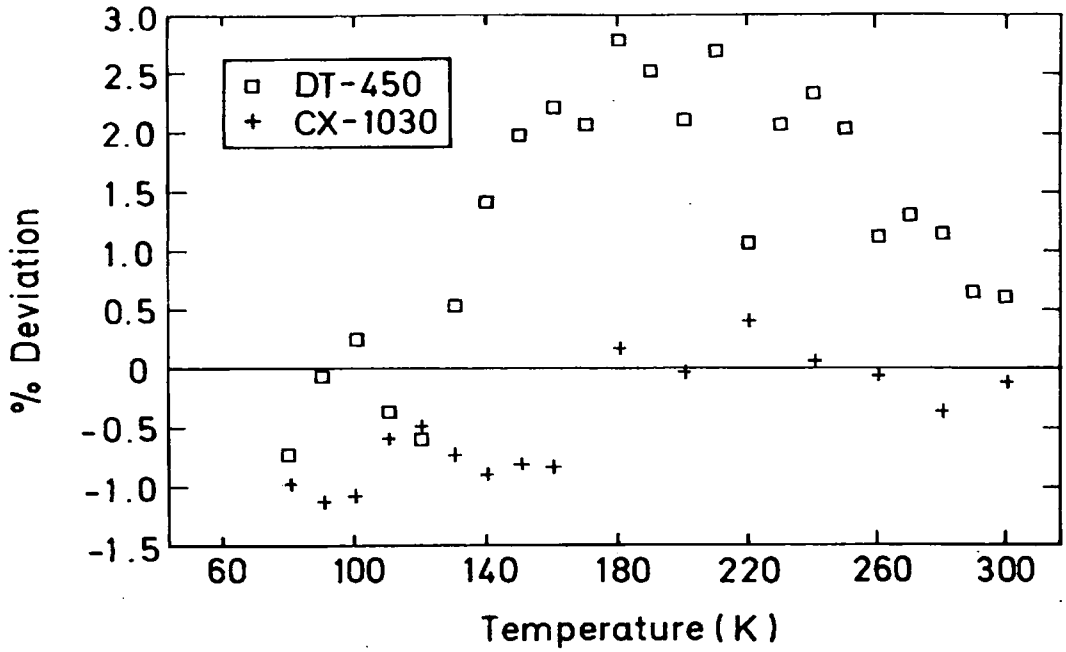

Fig.4.19. %age Deviation in specific heat as a function of temperature of Cu-results from literature for DT-450 and CX-1030 Thermometers.

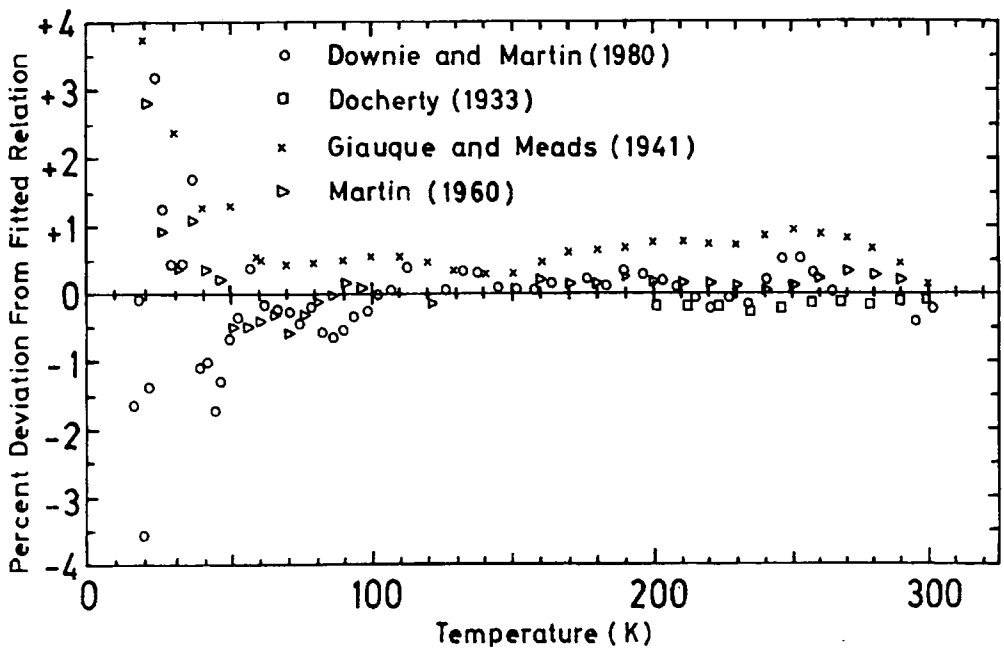

Fig.4.20. %age Deviation of literature results from the Cu Reference Equation (CRE) [5].

4.9: Experimental results in High Field on NbTi:

To test the reliability of Durham Specific heat probe in the magnetic fields, a well known superconductor material NbTi (Commercial) has been measured. In these measurements a long duration of heat pulse of 5-seconds was used in 0- and in high fields. The results are shown in Fig.4.22 and analysed using Eq. 3.21. In addition, the heat capacity was measured at 11 K using short duration of heat pulse and the data normalised to 11 K. The behaviour so obtained is shown in Fig. 4.23 and 4.24.

4.10: Discussion:

The gradual development of the system has been discussed in the previous sections. First of all a Type-T Thermocouple was tested. The results obtained were compared with literature, Fig. 4.5. It was found that the results were different by 10 to 20% with the literature. The RhFe-Thin film thermometer was tried after this and rejected due to its fragility. Due to its high sensitivity, DT-450 diode thermometer, we obtained very good results in 0-field in the range of ±3% of the literature value. The results are shown in Fig.4.18 and 4.19. But when it was tried in magnetic field, due to its strong dependence on magnetic field we found very poor results. After DT-450 thermometer, there were two choices, using a Carbon Glass thermometer or a Cernox (CX-1030) thermometer. It was verified that the CX-1030 was better thermometer as compared to carbon glass in high magnetic fields [6]. The Cu-results using CX-1030 thermometer are compared with literature in Fig. 4.18. As can be seen from Fig.4.19 the results obtained are ±1.5% in agreement with that of literature.

The thermometry of the probe was checked using the long duration heat pulse method in high magnetic fields. In the beginning, NbTi was investigated. It was found that the results are in good agreement with those of the literature [12]. The results so obtained are shown in Fig. 4.24.

Advantages and Disadvantages:

The probe developed is a multi purpose probe and can be used for different Cp techniques, other than heat pulse method with slight modifications. This probe can be used in a large temperature range of 2.2 K to 300 K. As CX-1030 thermometer has very high resolution close to liquid helium region, the probe gives very high resolution in that region. Using four samples of Cu, the addenda and pure specific heat has been determined which is very close to the literature value [5], ~ ± 2% in the whole temperature range.

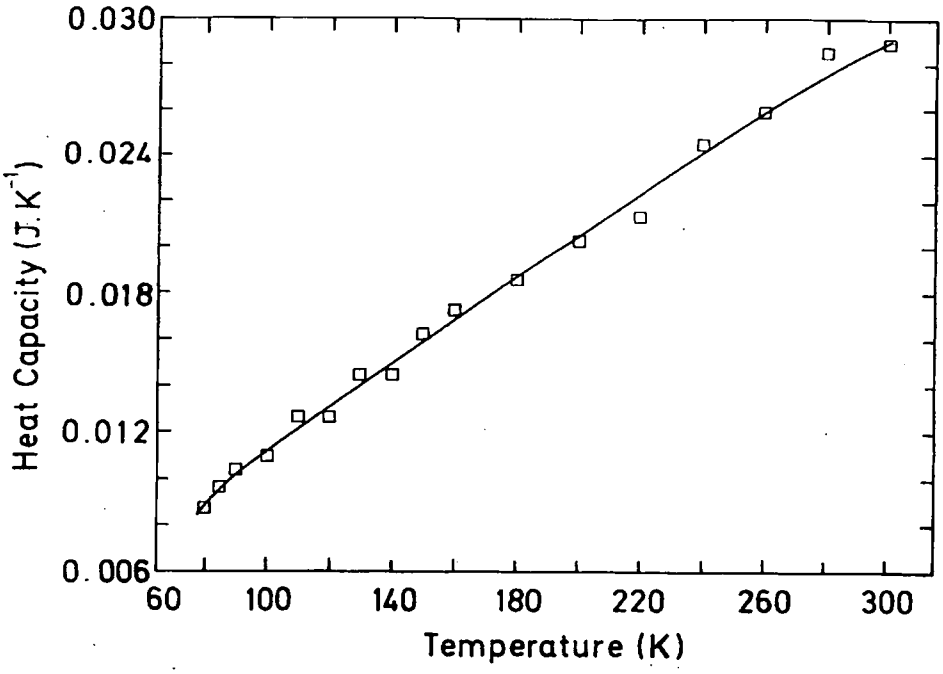

Fig.4.21. Heat Capacity of Addenda as a function of temperature calculated from Cu-Run on 4 samples.

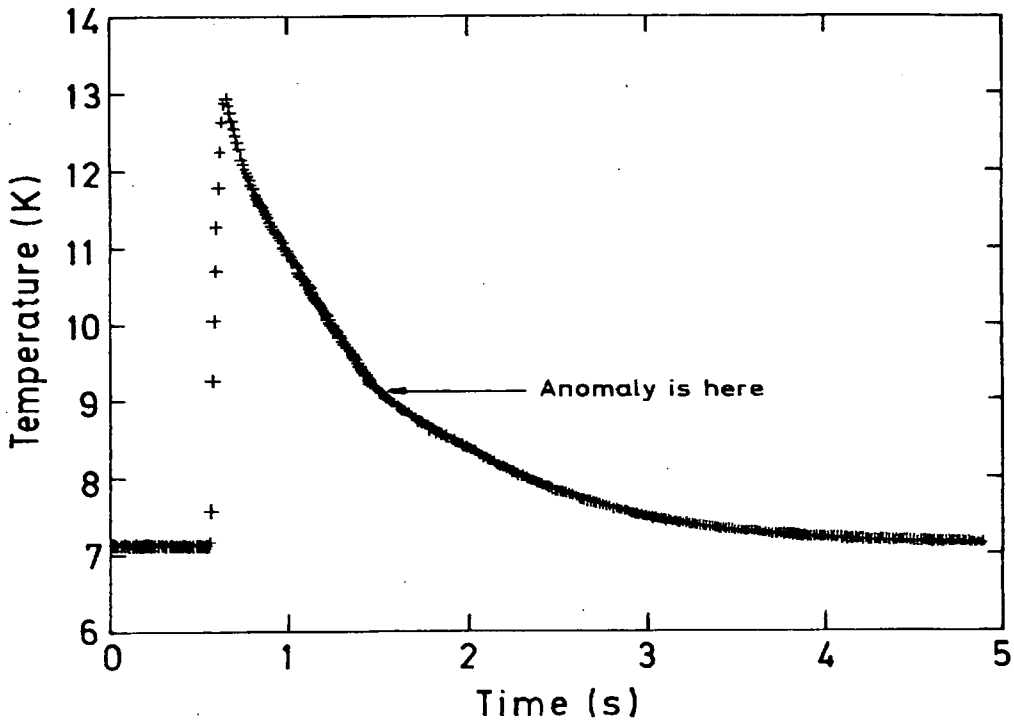

Fig.4.22. The decay curve, after a long duration of heat pulse for NbTi-Superconductor in 0 T.

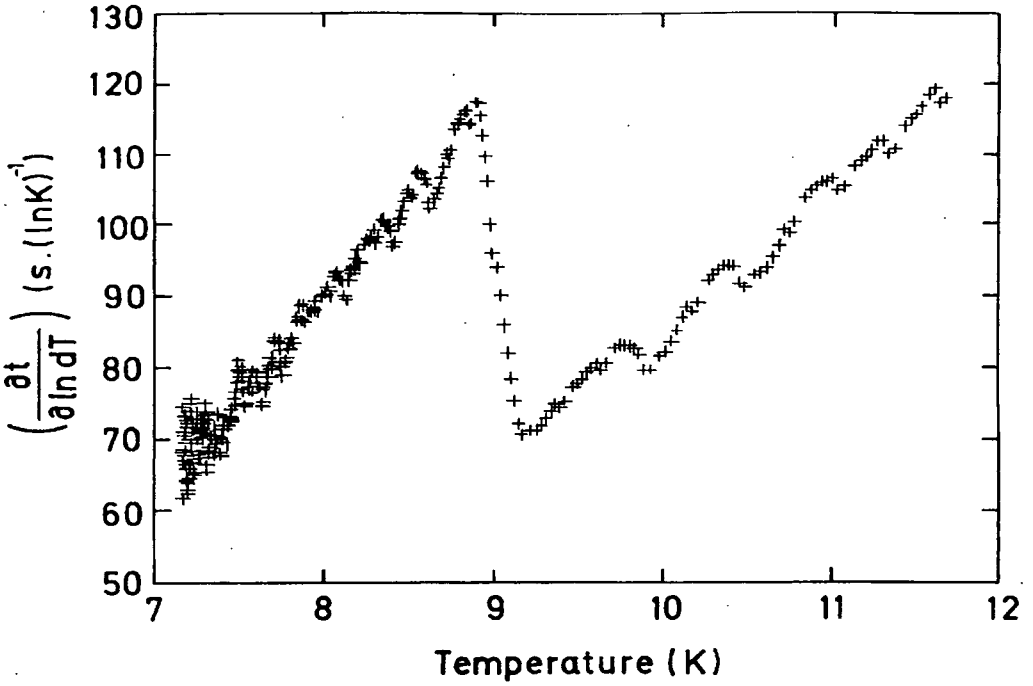

Fig.4.23. Analysing the decay curve, $\partial t/\partial \ln(dT)$ as a function of time, after the long duration of heat pulse to find the anomaly in 0 T.

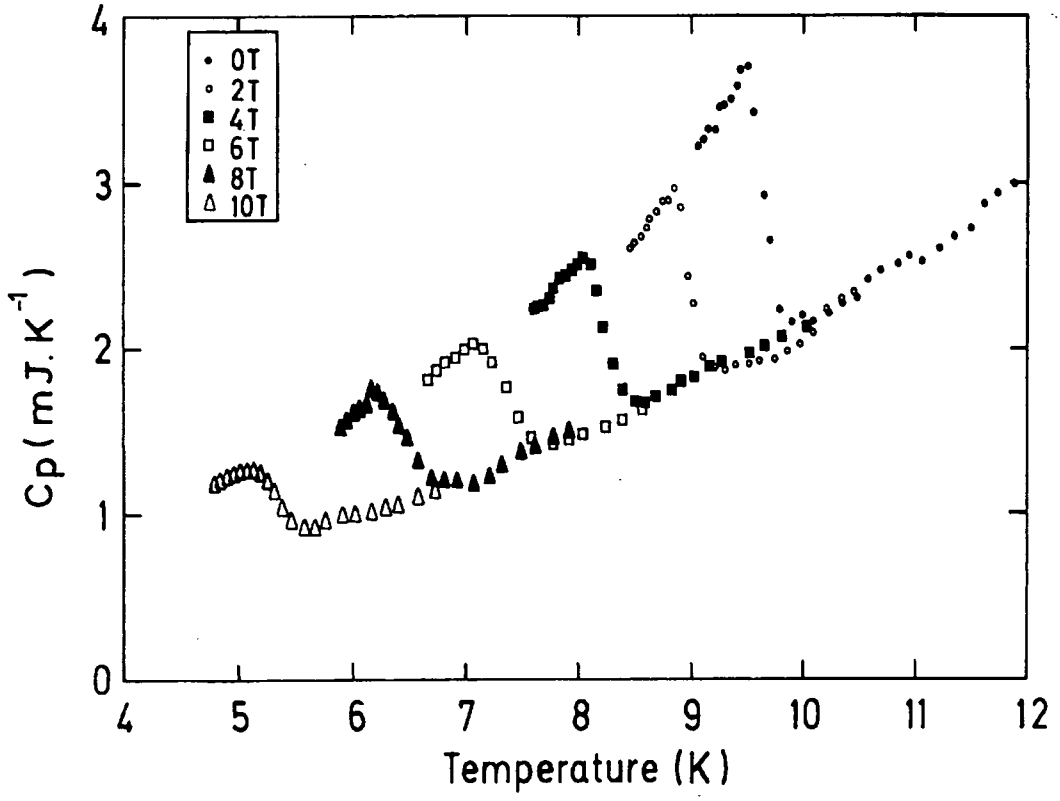

Fig. 4.24. The Heat Capacity of commercial NbTi as a function of temperature and magnetic field using long duration heat pulse and normalising it to 11 K.

region. Using four samples of Cu, the addenda and pure specific heat has been determined which is very close to the literature value [5], ~ ± 2% in the whole temperature range. The accuracy of thermometry is, ±30 mK at 4.2 K, ±35 mK at 50 K and ±140 mK at 300 K in fields. The probe is equally capable of being used in 0- or in very high magnetic fields.

4.11: Conclusion:

The results obtained using heat pulse method has been compared with literature and found to be within ±1.5% to the published values in the temperature range from 20 K to 300 K for the CX-1030 thermometer which is used in the high field measurements.

References:

1). Test Instrumentation Group, Keithley Instruments, Inc., 28775 Aurora Road, Cleveland, Ohio, 44139, USA.

2). Oxford Instruments, Scientific Research Division, Old Station Way, Eynsham Witney, Oxon, OX8 1TL, England.

3). Temperature Measurement and Control, 1995, pp.1-22. A Catalog by Lake Shore Measurement and Control Technologies, Lake Shore Cryotronics, Inc. 64 East Walnut St., Westerville, Ohio, 43081-2399, USA.

4). Micro-Measurements, Measurements Group, Inc. Raleigh, North Carolina, USA.

5). D.L. Martin, Rev. Sci. Instrum., 58 (1987), 639-646.

6). H.D. Ramsbottom, S. Ali, and D.P. Hampshire, Cryogenics, 36 (1996), 61-63.

7). D. R. Harper, Bull. Bur. Stand. 11 (1914), 259.

8). S. M. Dockerty, Canad. J. Research, 9 (1933), 84.

9). W. F. Giauque and P. F. Meads, J. Am. Chem. Soc. 63 (1941), 1897.

10). D. L. Martin, Canad. J. Phys. 38 (1960), 17.

11). D. B. Downie and J. F. Martin, J. Chem. Therm. 12 (1980), 779.

CHAPTER 5

Alternating Current Technique

5.1: Introduction

To investigate heat capacity at low and at very low temperatures, Sullivan and Seidal [1] introduced a very superb and efficient a.c. technique. Using this technique many traditional calorimetric problems can be overcome. In this chapter, the use of a.c. technique and its application to low thermal conductivity material will be used for Copper, a standard normal material, NbTi, a superconducting material, and $PbMo_6S_8$ a poor thermal conductivity superconductivity material. A very detailed and systematic study of the experiment conditions is provided, since there is no such study in the literature although such work is critical for achieving high quality data.

The chapter consists of nine sections. In section 5.2, the description of the system, including the principle of operation, external circuitry and sample geometry is described. Section 5.3, includes the experimental procedure, and section 5.4 consists of experimental results for Cu in 0-field, above liquid nitrogen temperature and in the liquid helium region. Section 5.5, includes the calculation of Cp for high and low thermal conductivity materials. Section 5.6, described the experimental results obtained using NbTi-superconductor in 0- and high fields and its analysis. Section 5.7 includes the experimental results acquired using 5 samples of Hot Isostatic Pressed (HIP) $PbMo_6S_8$ and its analysis. Section 5.8 provides the discussion of the measurements and the analysis of the data using a.c. technique. Section 5.9 provides the conclusion.

5.2: System Description

5.2.1: Principle of Operation:

To measure the specific heat of a material using the a.c. technique, the following principle is used. An alternating rms voltage (V_{IN}) of frequency (f) is applied to a heater attached to the sample. The corresponding power due to this voltage will oscillate with a frequency double that of the applied frequency, which can

be sensed with a temperature sensor. Hence the thermometer produces a d.c. voltage ($V_{d.c}$) characteristic of the mean temperature of the sample and an rms a.c. voltage V_{rms}(LIA), used to calculate the heat capacity which should lag the input current by 90^0 as explained in chapter 3. In this measurement the sample is heated continuously by the oscillatory power, and the corresponding variation in the signal is recorded by a Lock-In Amplifier (LIA).

5.2.2. External Circuitry:

The schematic diagram of the experimental arrangement is shown in Fig.5.1. A similar diagram has been discussed in chapter 4, (Fig.4.1) except that the d.c. power supply, the computerised switch, and d.c. Ammeter is replaced by a Lock-In Amplifier (LIA), used both as an input heat source and the output device to extract the a.c. signal from the thermometer. The d.c. signal from the thermometer is measured by a Keithley DVM-2000 multimeter. The Temperature Controller is used to control and ramp the background temperature. The whole system is controlled by the computer using the ASYST- language.

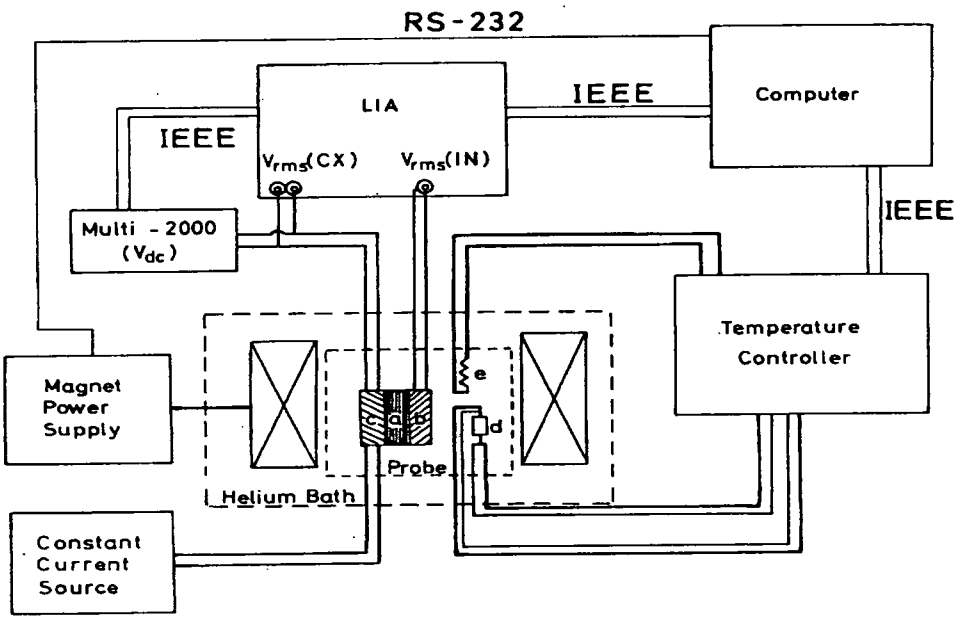

Fig.5.1: A Schematic of the Experimental Set-Up for A.C. Technique. In the Fig. 'a' denotes the sample, 'b' is the sample heater, 'c' stands for CX-1030 Thermometer. 'd' represents the RhFe-Thermometer to ramp and measure the background Temperature and 'e' shows the background heater,.

5.2.3: Sample Geometry:

It is clear from that the ideal sample for a.c. calorimetry measurements has very high thermal conductivity and diffusivity. But many interesting phenomena happen in materials which do not meet these requirements. By choosing a sample geometry with a sufficiently small thickness, one can approach the ideal. However the sample should be large enough to mount the heater (strain gauge) on one side of the sample and thermometer on the other side of the sample. If the sample is too thin and small, then there will be a relatively large addenda contribution. However if the sample is thick and large, there will be a non -90^0 phase shift (with the associated analytical problem) and reduced a.c. signal. We have found that ~4 mm x ~4 mm x ~1 mm is the best compromise for the Chevrel phase superconductors in this thesis.

5.2.4: Lock-in Amplifier, Initial Conditions:

In all measurements, we used an SR-830 Stanford Display Lock-In Amplifier [2]. The synchronous filter was on to reject the unwanted 2f and higher frequency noise. Also both notch filters were on to reject line noise. Except for the early NbTi data, a reference frequency of 0.5 Hz and output voltage, V_{IN}, 0.35 V was used in all measurements. The recommended time constant, of the LIA, is almost 3 times of the inverse reference frequency and was set to 3 seconds. The differential input terminals (A-B) of LIA were used. The reference phase was set equal to zero and data acquired at 2f. The LIA facilitates monitoring the incoming preamplified signal from CX-1030 through a rear panel BNC which was connected to a oscilloscope. Hence the difference between the input voltage and the a.c. voltage across the thermometer can be seen on the oscilloscope. The a.c. signal is double the frequency of the output of the LIA as shown in Fig. 5.2.

5.3: Experimental Procedure:

Initially the probe is precooled in liquid nitrogen temperature before cooling to liquid helium temperature. If the data is required in the magnetic field system, the distance between the bottom end of the top brass plate of probe and top end of Superconductor magnet is 272.5±0.5 mm. The pressure of He gas is set to be ≈ 5 Torr at the warm end of the probe. The background temperature is sensed by a RhFe-

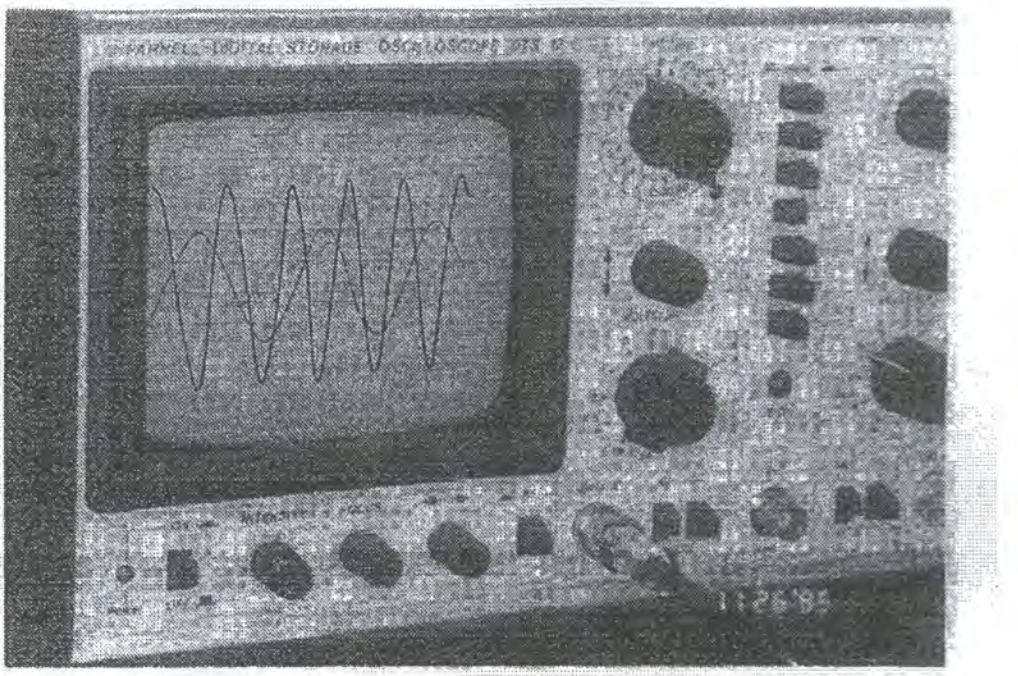

Fig.5.2: A photograph, showing the input signal of frequency f, forced to oscillate the output signal with a frequency of 2f.

Calibrated Thermometer and recorded by the Lakeshore Temperature Controller. It is ramped with a ramp rate of 0.125 $K.min^{-1}$. The sample temperature is sensed by a CX-1030 thermometer. The $V_{rms}(CX)$, across the Cernox and the phase shift of this signal with respect to the input voltage for the heater are recorded by the LIA at 2f and $V_{d.c}$ gives the temperature of the sample measured by the Multi-2000. $V_{rms}(CX)$ is converted to Tac and $V_{d.c}$ into the background temperature.

5.4: Experimental Results on Cu:

We have used copper of 99.999% purity bought from Johnson and Matthey [3], in a sheet form. From this sheet, 6 copper samples were cut of different thicknesses of 0.2 mm, 0.5 mm, 1.0 mm, 1.5 mm and 2 mm, with each of height 6 mm and width 5 mm and masses of 0.03178 gm, 0.13703 gm, 0.25221 gm, 0.38402 gm and 0.52643 gm respectively with the 6th Cu-sample with slightly different dimension of 1 mm thickness, 4.75 mm width and 5.90 mm of height with 0.23059 gm of mass. The first 5 Cu samples were used to investigate the heat capacity of Cu

in the range from 4.2 K to 20 K and the Cu sample with 0.2 mm thickness labelled Cu-1, and the 6th Cu sample, labelled Cu-3 in the following figures, were used to investigate heat capacity at and above 77 K.

5.4.1: Copper Samples (T > 77 K).

Before testing the technique at low temperature, it was tested at liquid nitrogen temperature on copper with known high thermal conductivity. A thorough investigation was made at atmospheric pressure at the warm end for fixed frequencies. First the applied voltage V_{IN} was changed and the corresponding ΔTac was noted, shown in Fig.5.3. The procedure was repeated for a pressure of 1 Torr at the warm end of the probe as shown in Figs. 5.4. Since all the data has been acquired using A.C. coupling, correction factors have been used to take account of the voltage drop across the internal impedance of the LIA and the non-ideal filters at low frequencies e.g. for frequency 0.2 Hz with a nominal applied voltage of 0.35 V, one will measure 0.273 V with A.C. coupling in LIA (78% of the reading). Equally the LIA has an internal impedance of only 50 Ω, so the voltage drop across the heater which has a resistance of 350 Ω is reduced to 87.5%.

Equation 3.48 derived in Chapter 3 [1,4-5],

$$C = \frac{\sqrt{2}\left(\frac{V^2_{IN}}{R_H}\right)}{8\pi f} \cdot \frac{I_{Thermometer}}{V_{rms}(CX)} \cdot \frac{\partial R_{Th}}{\partial T} Z \qquad (5.1)$$

can be written as

$$Tac \; . \; f = \frac{\sqrt{2}}{8\pi} \cdot \frac{Power}{C} \qquad (5.2)$$

where Tac = $(V_{rms}(CX)/I_{THERMOMETER} \cdot \partial T/\partial R_{Th})$ and Power = (V^2_{IN}/R_H). Hence Tac × f vs. power should be a straight line through the origin. The data in Figs. 5.3 and 5.4 have been replotted in Figs. 5.5 and 5.6. At atmospheric pressure, below ~ 10 mW and 0.5 Hz, we get linearity in agreement with Eq. 5.2. No agreement is found when the probe is pumped out. Hence we conclude that low pressure is not suitable for the

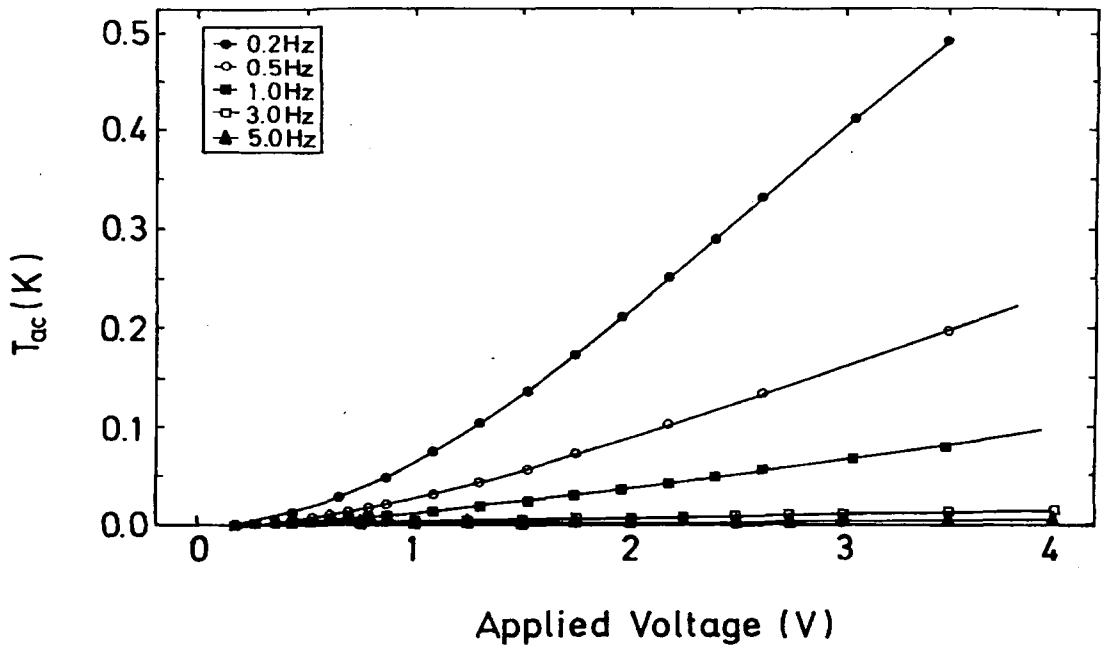

Fig.5.3a: Tac as a function of voltage for different frequencies at 77.8 K for Cu-1 sample with one atmospheric pressure at the warm end of the probe. Time Constant of the LIA = 30 sec.

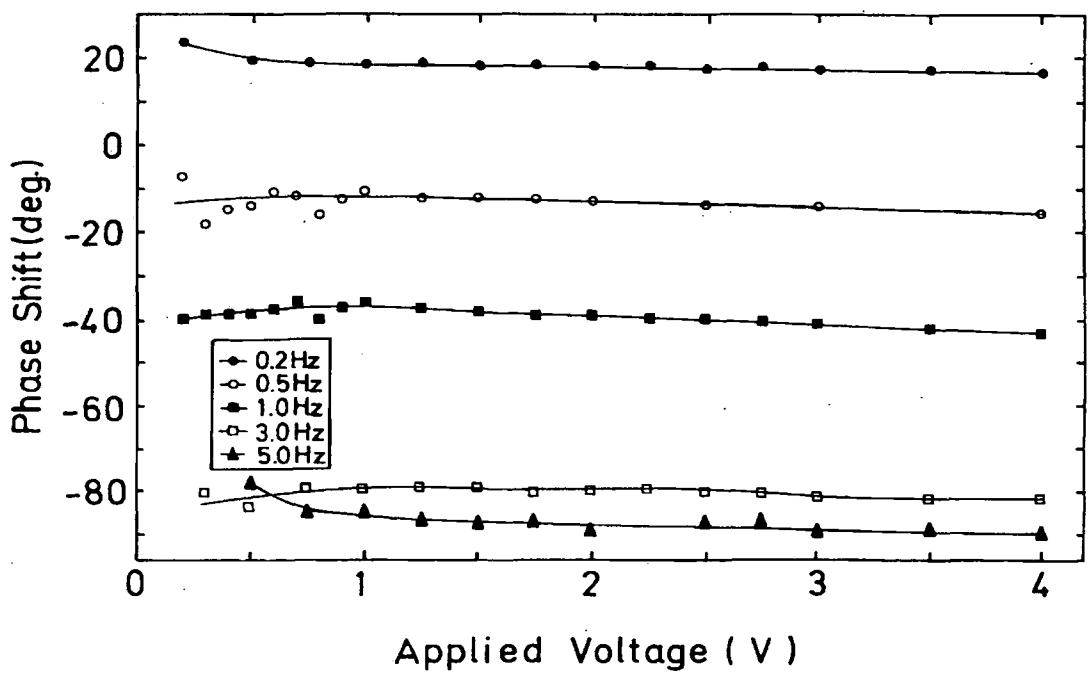

Fig.5.3b: Phase Shift as a function of voltage for different frequencies at 77.8 K for Cu-1 sample with one atmospheric pressure at the warm end of the probe. Time Constant of the LIA = 30 sec.

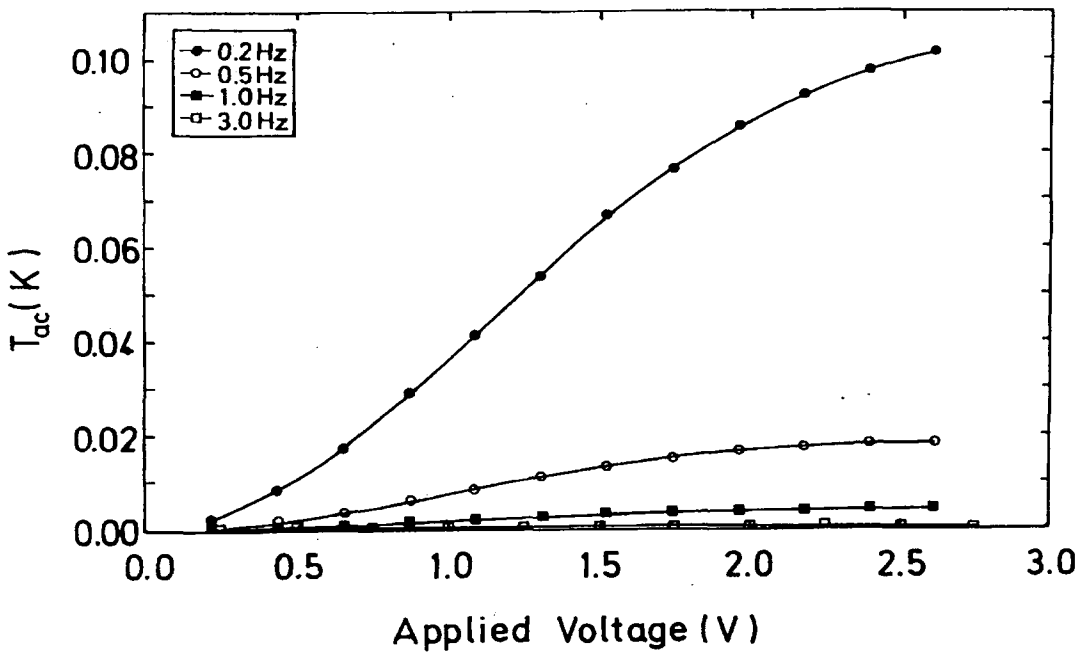

Fig.5.4a: Tac as a function of voltage for different frequencies at 77.8 K for Cu-1 sample with 1 Torr pressure at the warm end of the probe. Time Constant of LIA = 30 sec.

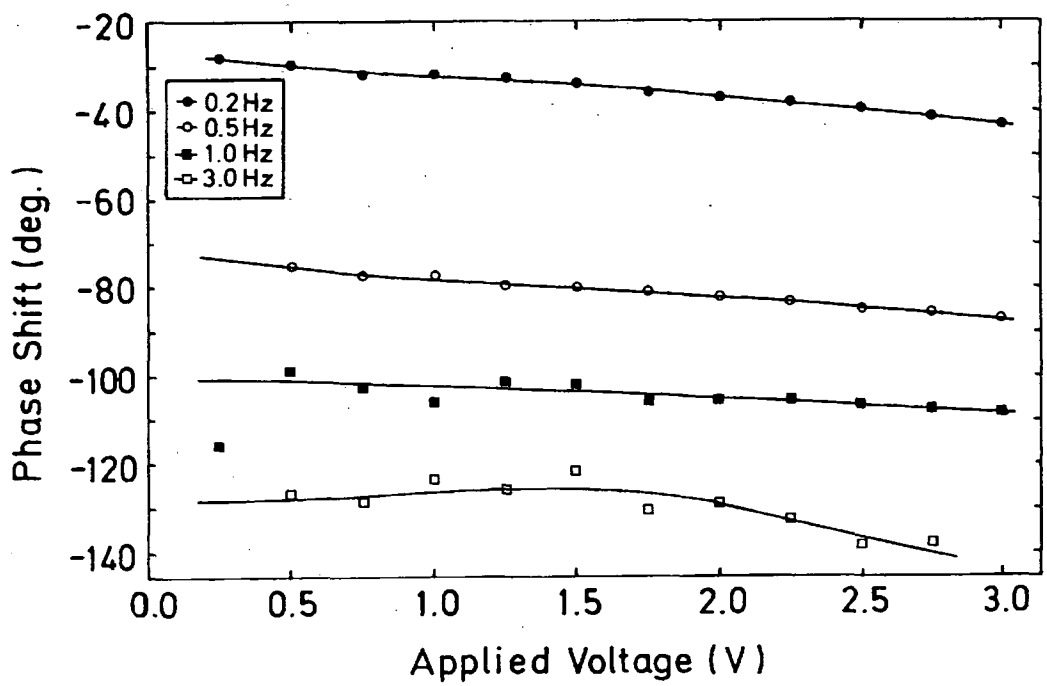

Fig.5.4b: Phase Shift as a function of voltage for different frequencies at 77.8 K for Cu-1 sample with 1 Torr pressure at the warm end of the probe. Time Constant of LIA = 30 sec.

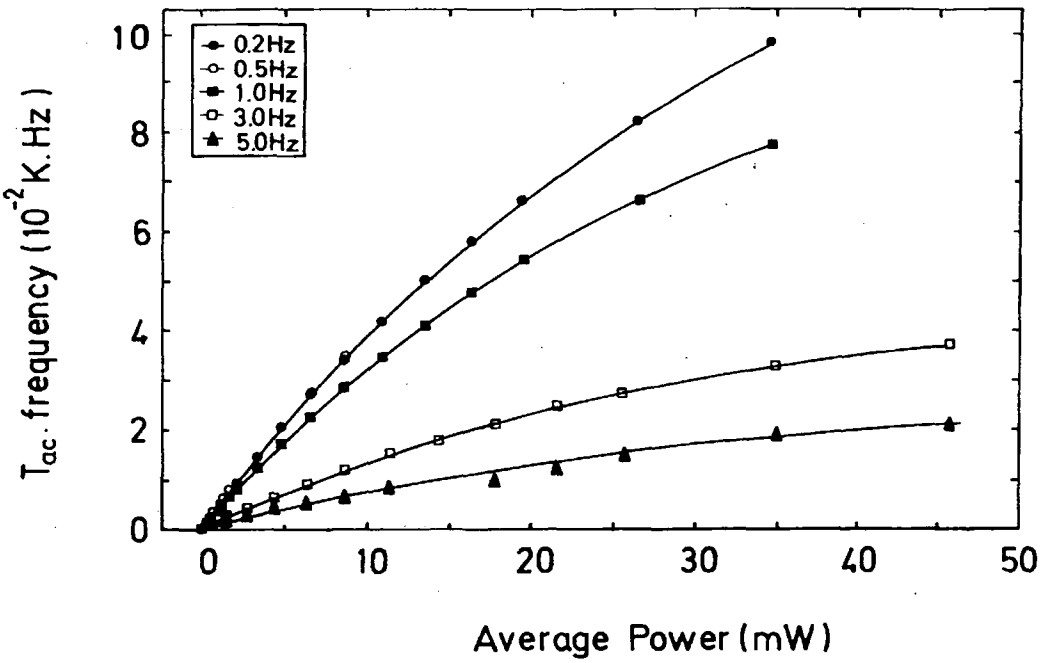

Fig.5.5: Tac x f as a function of Average Power at 77.8 K for Cu-1 sample at atmospheric pressure for 0.2 Hz, 0.5 Hz, 1.0 Hz, 3 Hz, and 5 Hz. Time Constant of LIA = 30 sec.

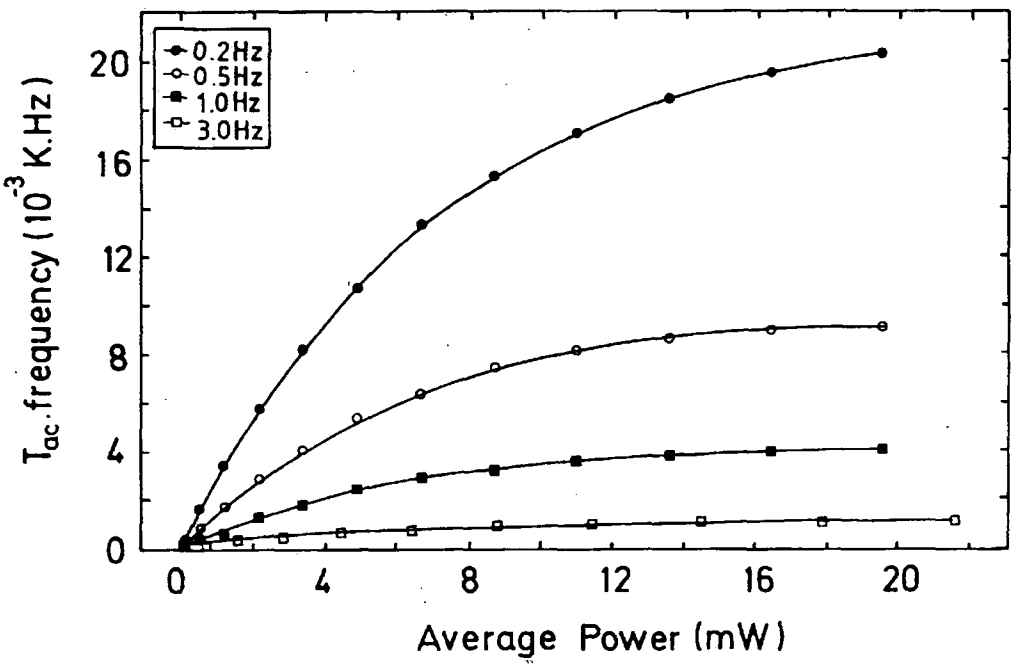

Fig.5.6: Tac x f as a function of Average Power at 77.8 K for Cu-1 sample at less than 1 Torr pressure for 0.2 Hz, 0.5 Hz, 1.0 Hz, 3 Hz, and 5 Hz. Time Constant of LIA = 30 sec.

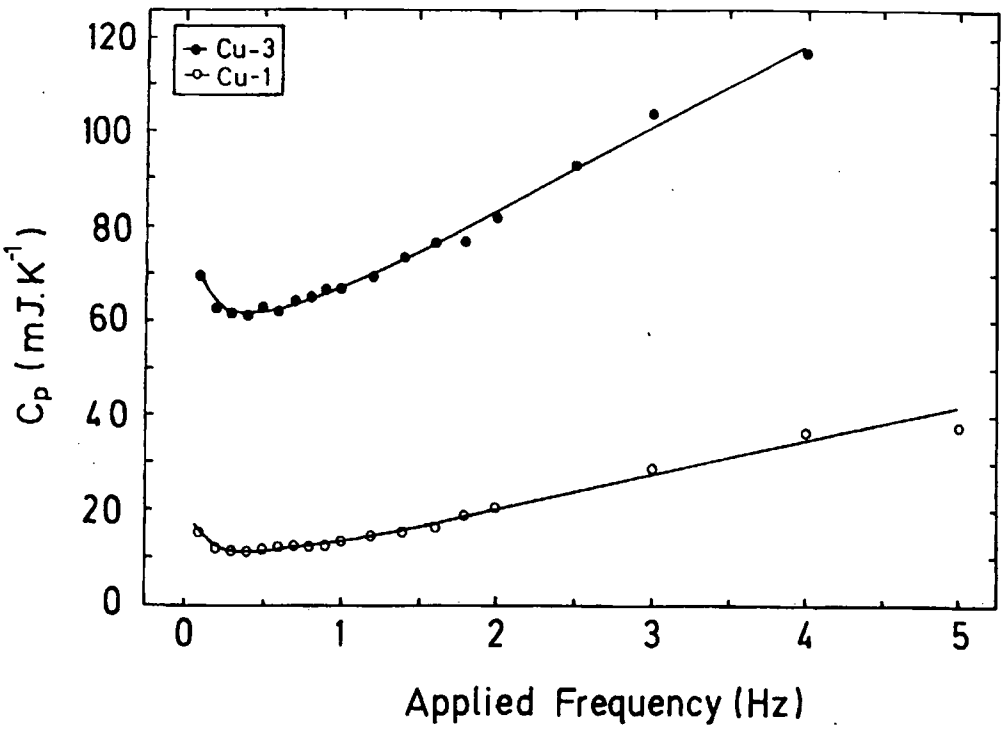

Fig.5.7: Heat Capacity of Copper samples of masses 0.03178 gm (Cu-1), and 0.23061 gm (Cu-3) as a function of Frequency at 77.8 K.

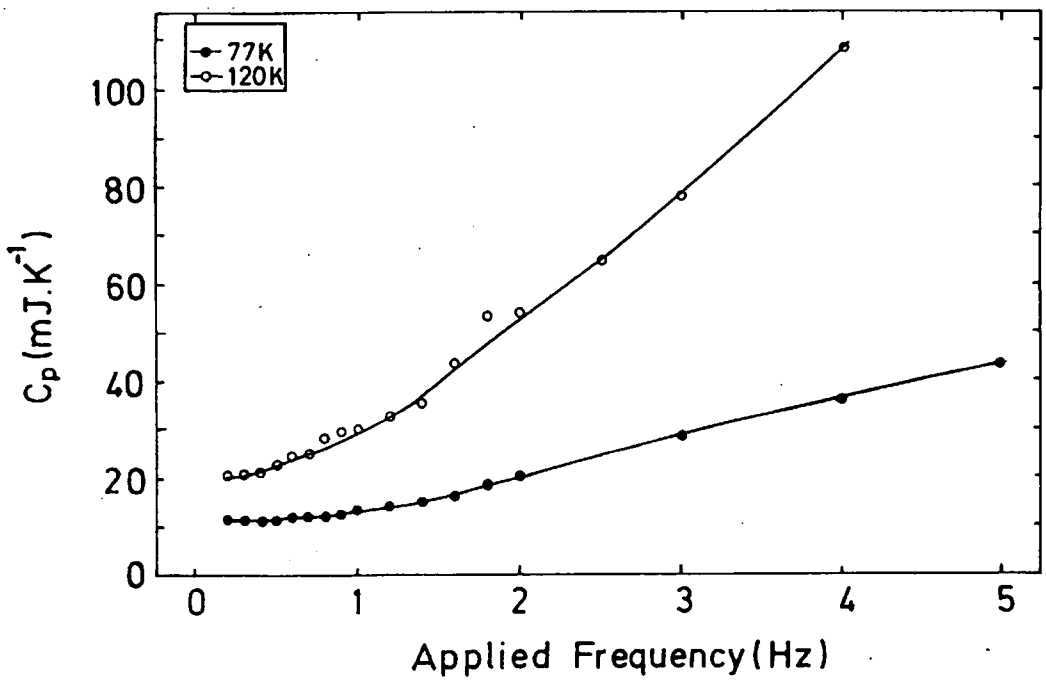

Fig.5.8: Heat Capacity of Cu-1 sample as a function of Frequency at 77.8 K and at 120 K with 0.5 V and 0.8 V respectively to find a suitable frequency at different temperatures. Cp after H. P. Method =12.1 and 19.3 mJ.K^{-1} at 77 K and 120 K respectively.

measurements at liquid nitrogen temperature.

To check the suitability of 0.5 Hz, measurements of Cp- derived using Eq. 5.1- were made on 2 different masses at 77.8 K. The data shown in Fig. 5.7 show that Cp is independent of frequency ~ 15 % as required at 0.5 Hz. The heat capacity of Cu-1 sample has been checked at 77 K and 120 K and displayed in Fig.5.8. It is found that at 0.5 Hz there is ~7% agreement of heat capacity values between the a.c. technique and the heat pulse method.

5.4.2: Copper Samples (4.2 K < T < 20 K).

To calculate the specific heat in the range of 4.2 K to 20 K of Cu, one needs to find a suitable ramp rate, pressure inside the probe and frequency. To find these parameters in this range a thorough investigation of Cu was made. Two Cu- samples with the thicknesses of 0.5 mm and 2 mm were measured. Typical results are shown in the interesting temperature range from 10 K to 14 K where we expect the superconducting phase transition to occur in our Chevrel phase materials.

In Figs.5.9-5.12, the raw data taken from 10 K to 14 K are plotted for the two Cu- samples. In light of Eq.5.1, we have plotted the raw data as $V^{-1}_{rms}(CX)$ and θ. It is clear from the data that higher ramp rate (2 $K.min^{-1}$) gives lower value of V^{-1}_{rms} (CX) and higher values of θ and a very low ramp rate (0.0625 $K.min^{-1}$) renders the experiment too long. We have chosen as a compromise (which is confirmed during the in-field NbTi data considered later) a ramp rate of 0.125 $K.min^{-1}$.

In Figs. 5.13 - 5.16, raw data taken at a ramp rate of 0.125 K. min^{-1} are shown. It can be seen in these figs. that $V^{-1}_{rms}(CX)$ is quite independent of pressure below 10 Torr. However the phase angle is strong function of pressure throughout the pressure range. We attribute these results to the change in the thermal link between the sample and the bath - in particular $V^{-1}_{rms}(CX)$ is a measure of the heat capacity of the sample whereas θ depends on the relative thermal conductivity of the sample and the heat link which is therefore pressure dependent. We have decided to take data in high fields at $\approx$ 5 Torr which is sufficiently low to be in the low pressure limit where $V^{-1}_{rms}(CX)$ is independent of pressure but sufficiently high that the pressure can be obtained easily and reproducibly.

Similarly, we have addressed finding a suitable frequency. In Figs. 5.17 - 5.20,

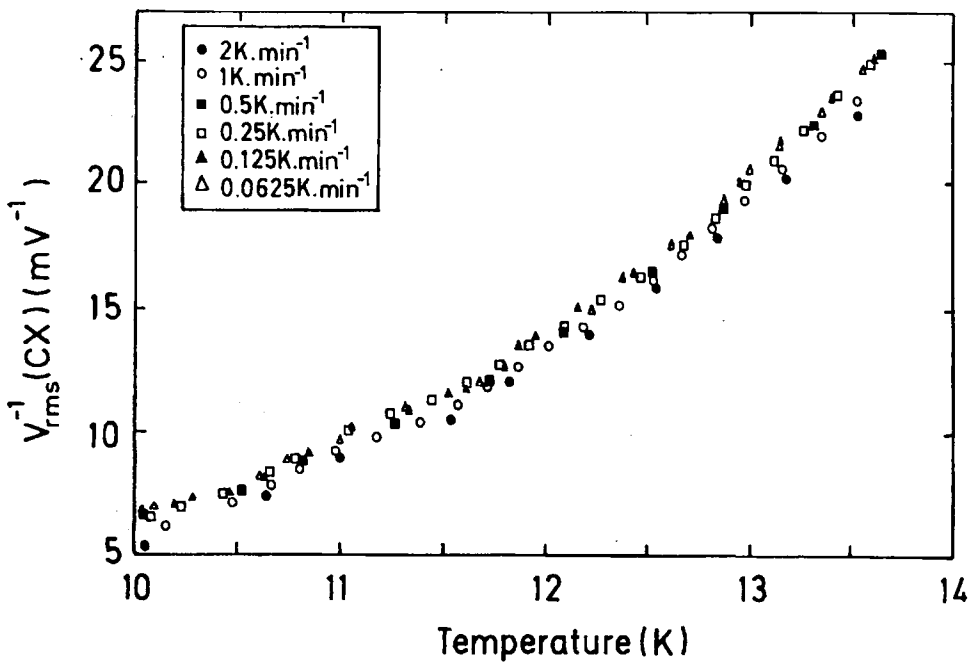

Fig.5.9: To find the suitable ramp rate, $V^{-1}_{rms}(CX)$ as a function of temperature has been plotted for the Cu-2 mm Sample.

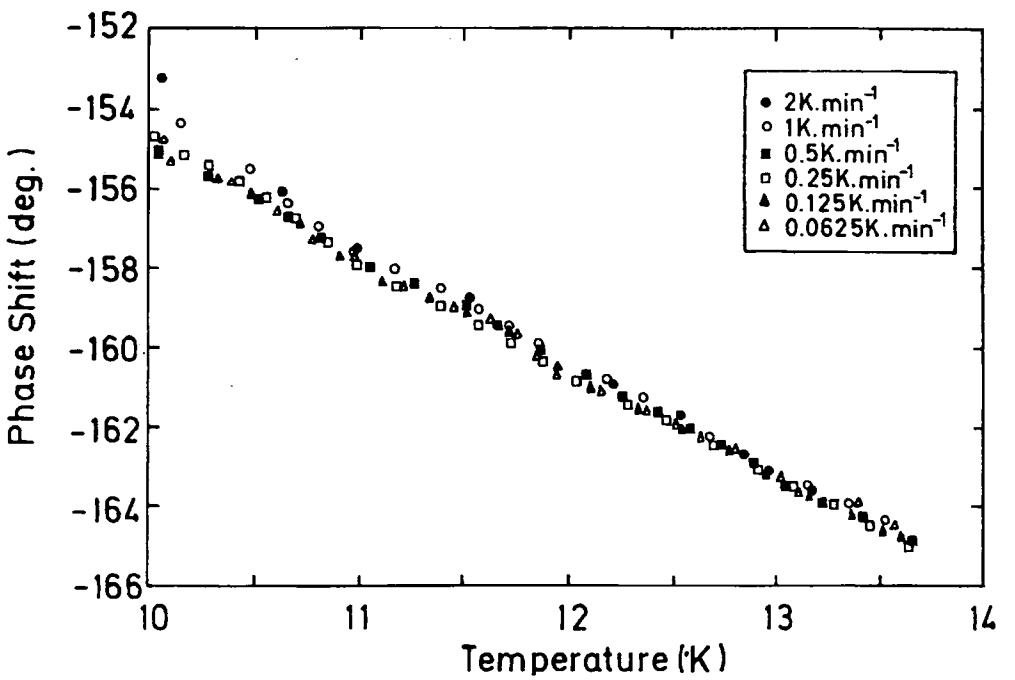

Fig.5.10: To find the suitable ramp rate, Phase Shift as a function of temperature has been plotted for the Cu-2 mm Sample.

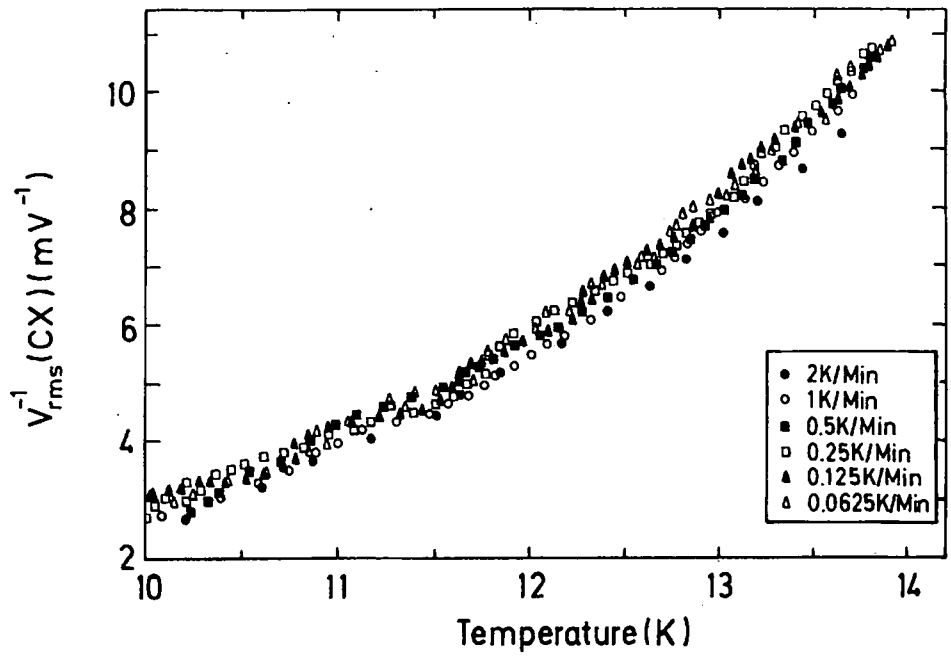

Fig.5.11: To find the suitable ramp rate, $V^{-1}_{rms}(CX)$ as a function of temperature has been plotted for the Cu-0.5 mm Sample.

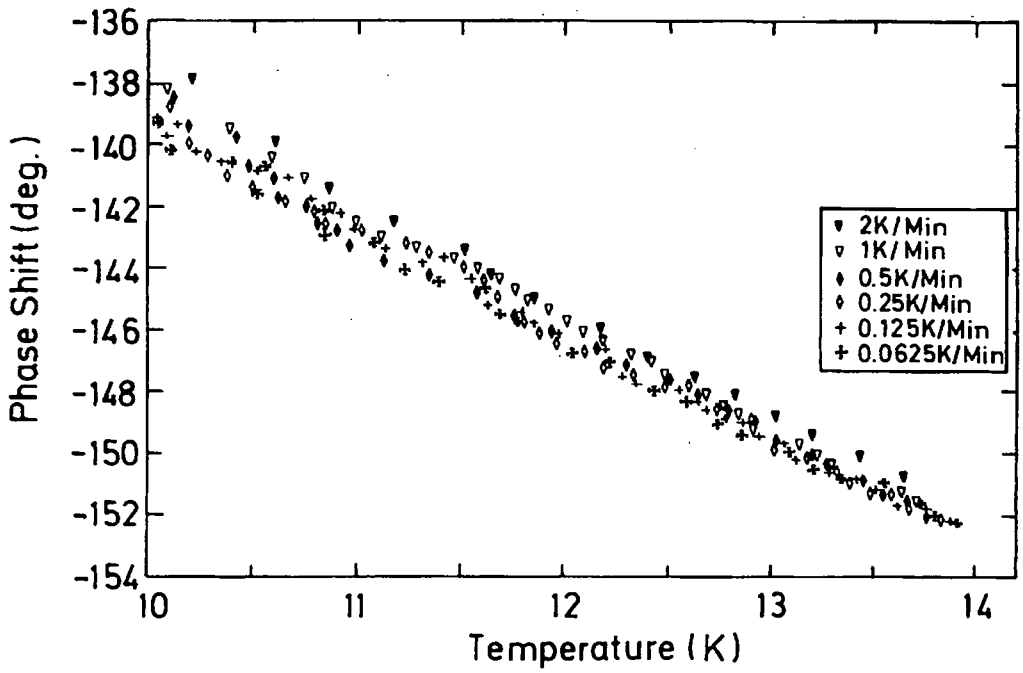

Fig.5.12: To find the suitable ramp rate, Phase Shift as a function of temperature has been plotted for the Cu-0.5 mm Sample.

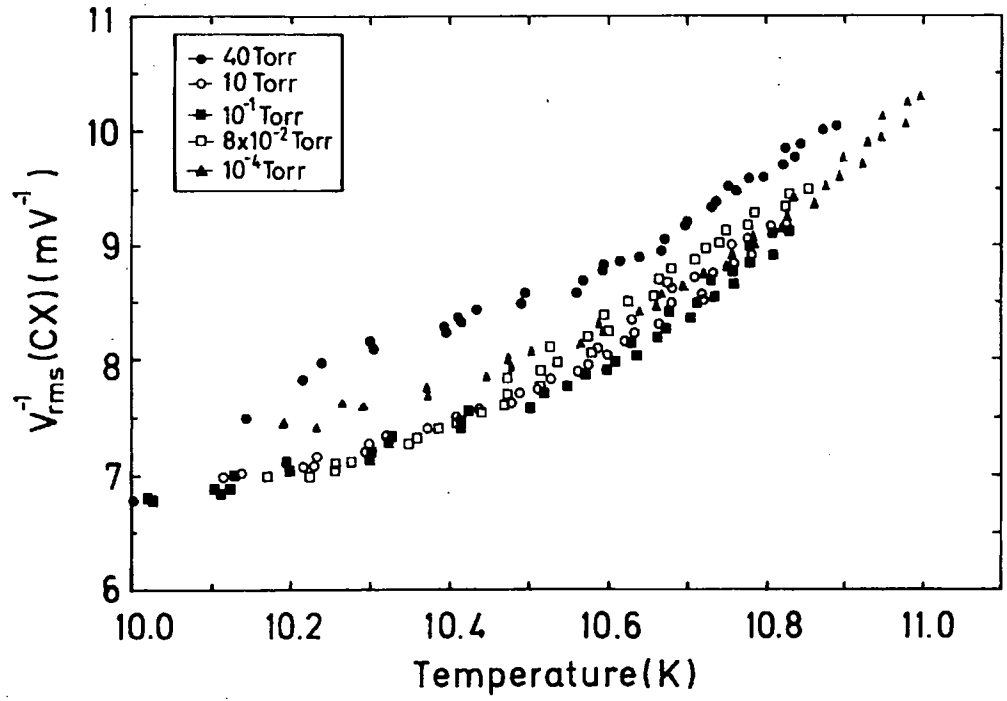

Fig.5.13: To find the suitable Pressure at the warm end, $V^{-1}_{rms}(CX)$ as a function of temperature has been plotted for the Cu-2 mm Sample.

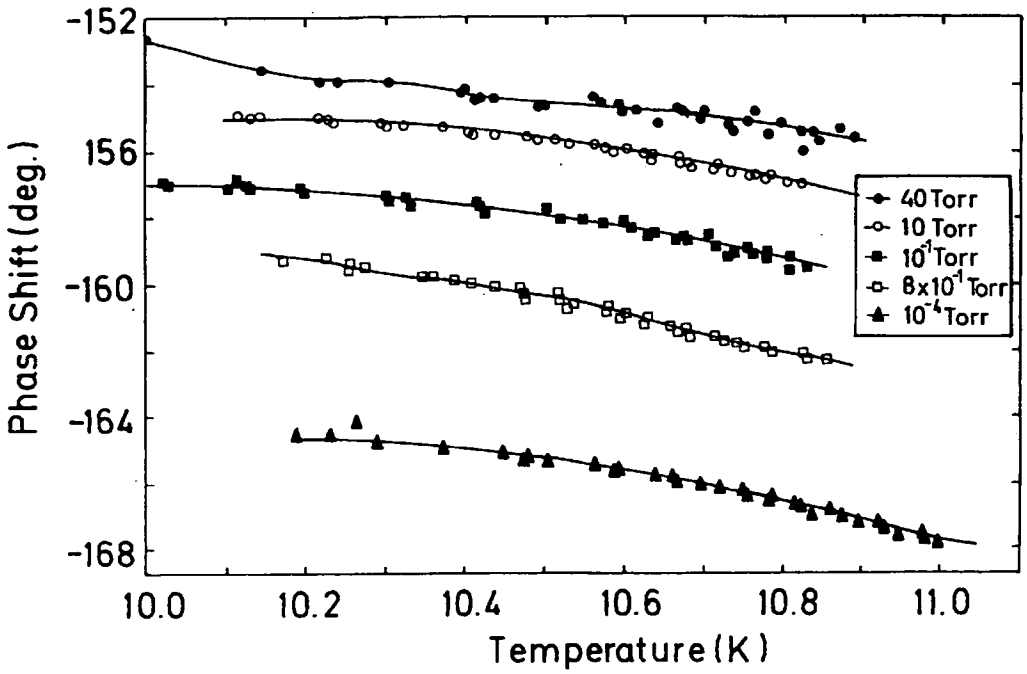

Fig.5.14: To find the suitable Pressure, at the warm end, Phase Shift as a function of temperature has been plotted for the Cu-2 mm Sample.

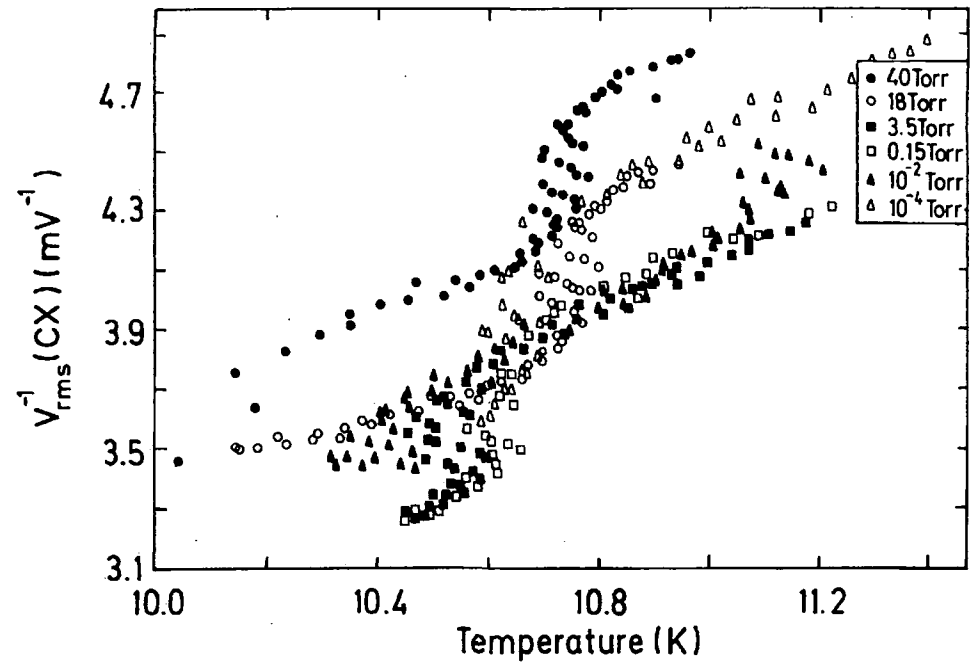

Fig.5.15: To find the suitable Pressure at the warm end, $V^{-1}_{rms}(CX)$ as a function of temperature has been plotted for the Cu-0.5 mm sample.

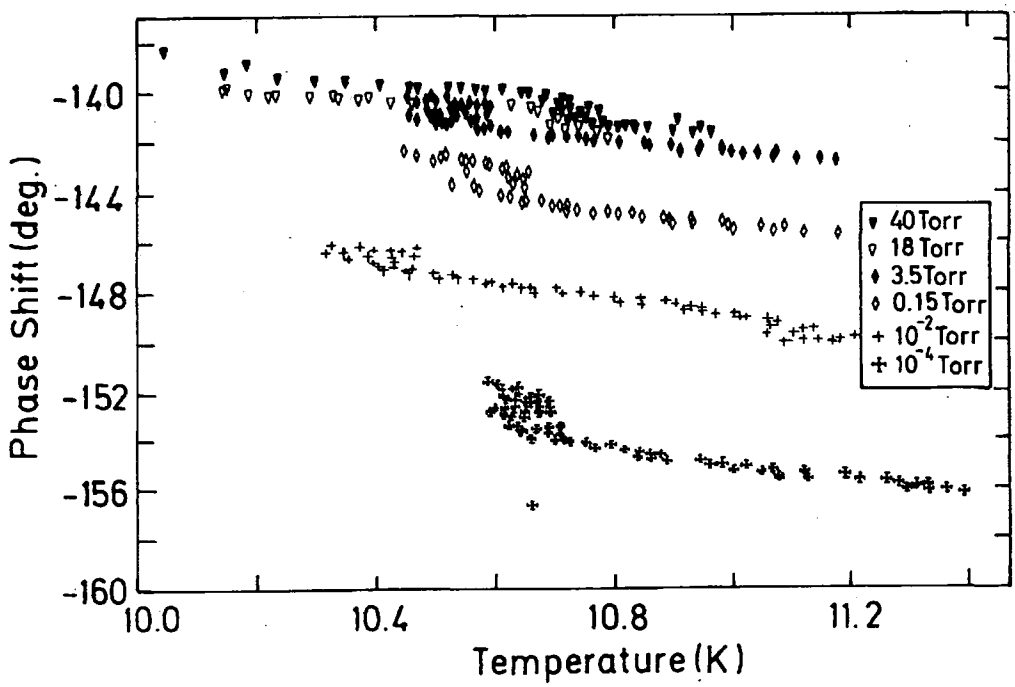

Fig.5.16: To find the suitable Pressure, at the warm end, Phase Shift as a function of temperature has been plotted for the Cu-0.5 mm sample.

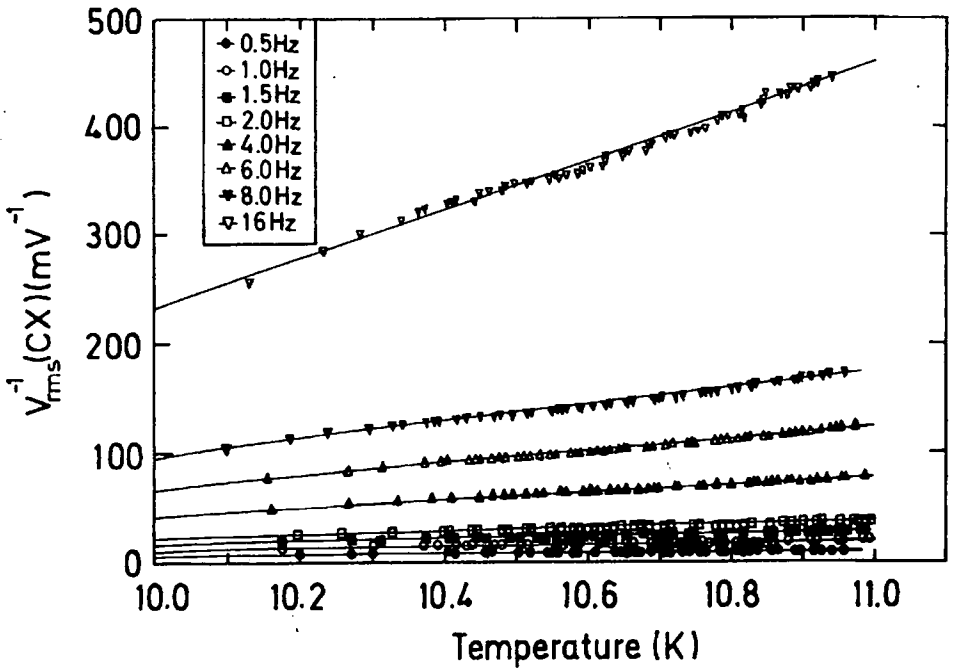

Fig.5.17: To find the suitable frequency, $V^{-1}_{rms}(CX)$ as a function of temperature has been plotted for the Cu-2 mm sample.

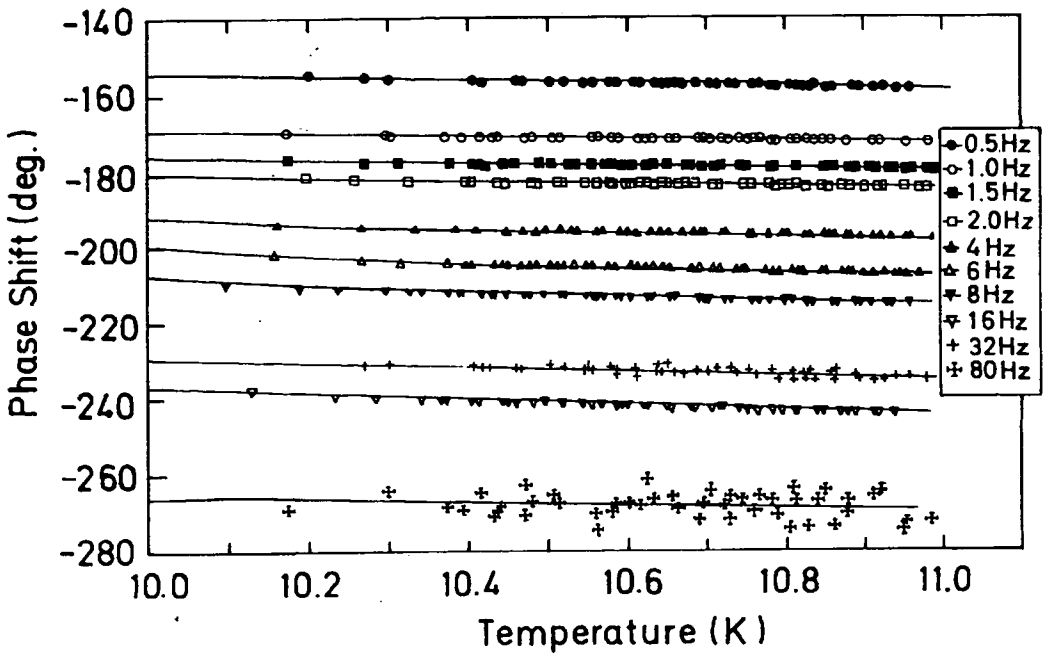

Fig.5.18: To find the suitable frequency, Phase Shift as a function of temperature has been plotted for the Cu-2 mm sample.

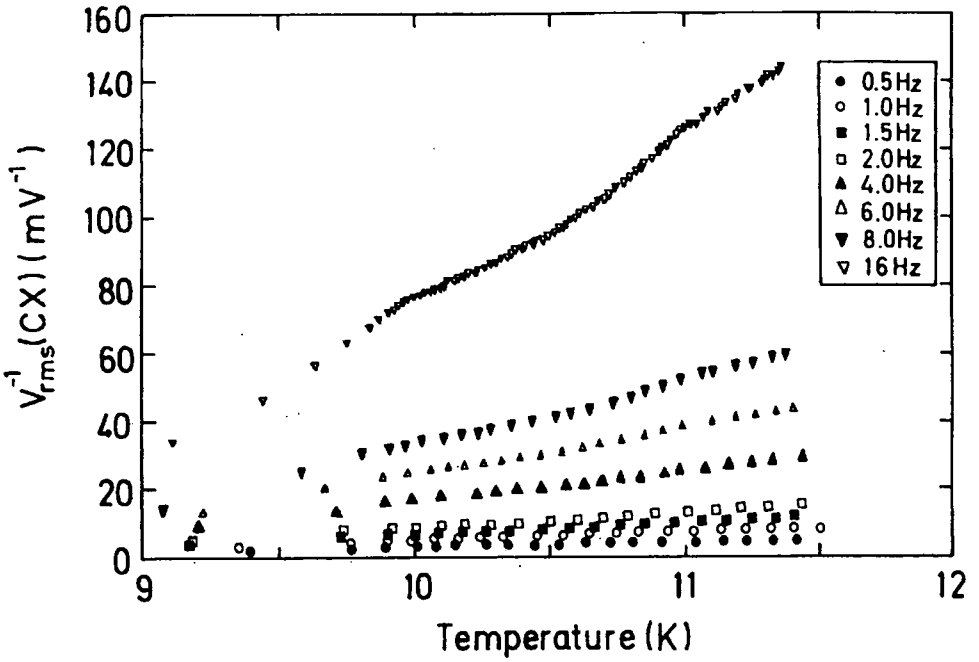

Fig.5.19: To find the suitable frequency, $V^{-1}_{rms}(CX)$ as a function of temperature has been plotted for the Cu-0.5 mm sample.

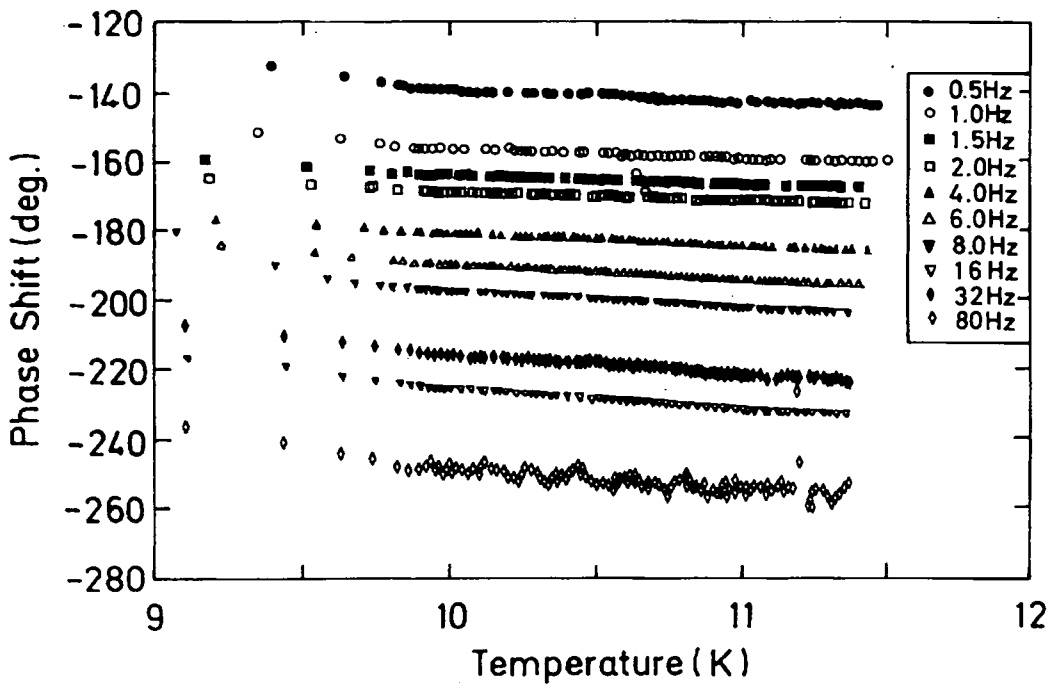

Fig.5.20: To find the suitable frequency, Phase Shift as a function of temperature has been plotted for the Cu-0.5 mm sample.

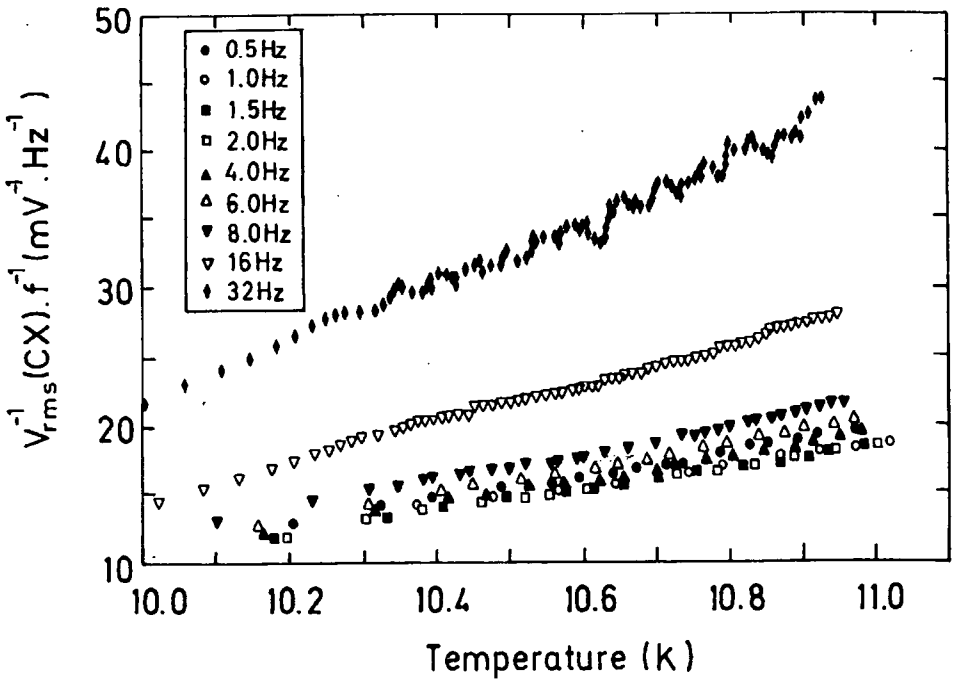

Fig.5.21: To find the suitable frequency, $V^{-1}_{rms}(CX)$ × freq. as a function of temperature has been plotted for the Cu-2 mm sample.

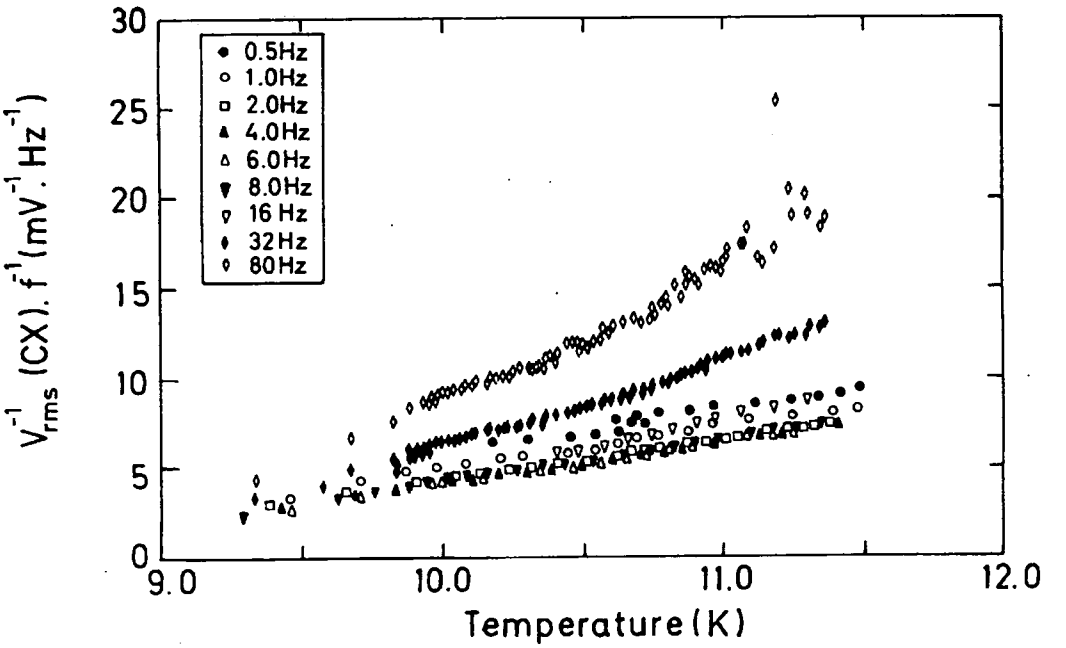

Fig.5.22: To find the suitable frequency, $V^{-1}_{rms}(CX)$×freq. as a function of temperature has been plotted for the Cu-0.5 mm sample.

raw data showing $V^{-1}_{rms}(CX)$ and θ for two Cu-samples acquired with different frequencies have been plotted. From Eq. 5.2, $V^{-1}_{rms}(CX) \times f^{-1}$ vs. temperature should be a single frequency independent line. This can be checked by replotting Figs. 5.17 and 5.19 in Fig. 5.21 and 5.22 respectively. It is clear that the data acquired from 0.5 Hz to 4 Hz for 2 mm thickness sample and 0.5 to 16 Hz for the 0.5 mm thick sample, frequencies are collapsing to a single line to within 5 % at low frequencies. From this analysis, we have chosen a frequency of 0.5 Hz to acquire the other data (Chap. 7 & 8) for Chevrel phase materials.

Using above optimum conditions for frequency (0.5 Hz), ramp rate = 0.125 $K.min^{-1}$, pressure ~ 5 Torr, and excitation current (100 uA) for CX-1030 thermometer, we acquired data for 5 Cu samples. The raw data showing $V^{-1}_{rms}(CX)$ and θ for these samples are displayed in Figs. 5.23-5.24.

5.5: Cp (Heat Capacity) Computer Analysis for Cu

In most simple case where:

a). the sample has infinite thermal conductivity,

b). the heater and the thermometer have infinitesimal response time, and

c). the sample is almost perfectly isolated from the thermal bath, following [1], and using Eq. 5.1, for our experimental set up:

$$C = 2.7623 \times 10^{-5} \frac{I_{Thermometer}}{V_{rms}(CX)} \cdot \frac{\partial R_{Th}}{\partial T} \qquad (5.3)$$

where $\partial R/\partial T$ is the slope of the thermometer, $V_{RMS}(CX)$ is the root mean square value measured by the Lock-In Amplifier and $I_{Thermometer}$ is the current to the thermometer.

In Fig. 5.25, the raw data of Fig. 5.23 have been replotted giving $V^{-1}_{rms}(CX)$ vs. Mass and we find good linearity at all temperatures. Eq. 5.3 holds good in this case. In Fig. 5.26, the data of Fig. 5.24 has been replotted giving theta vs. mass at different temperatures. In contrast with the Eq. 5.3, it was found that theta is a strong function of temperature and mass as shown. We attribute the value of theta not being -90^0 to the sample not being sufficiently isolated from the bath nor being of infinite thermal conductivity.

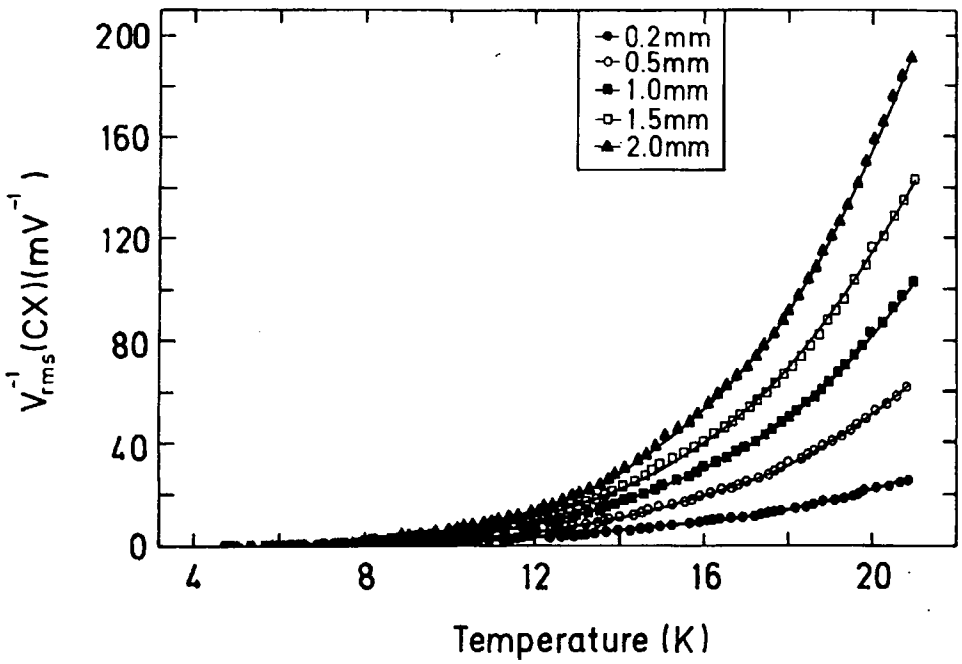

Fig.5.23: Raw data for 5 Cu samples of different masses, giving, $V^{-1}_{rms}(CX)$ versus temperature. Freq.=0.5 Hz, Excitation Current to CX-1030 thermometer=100 uA, Ramp Rate=0.125 K.min^{-1}, Pressure at the warm end of the probe≈5 Torr.

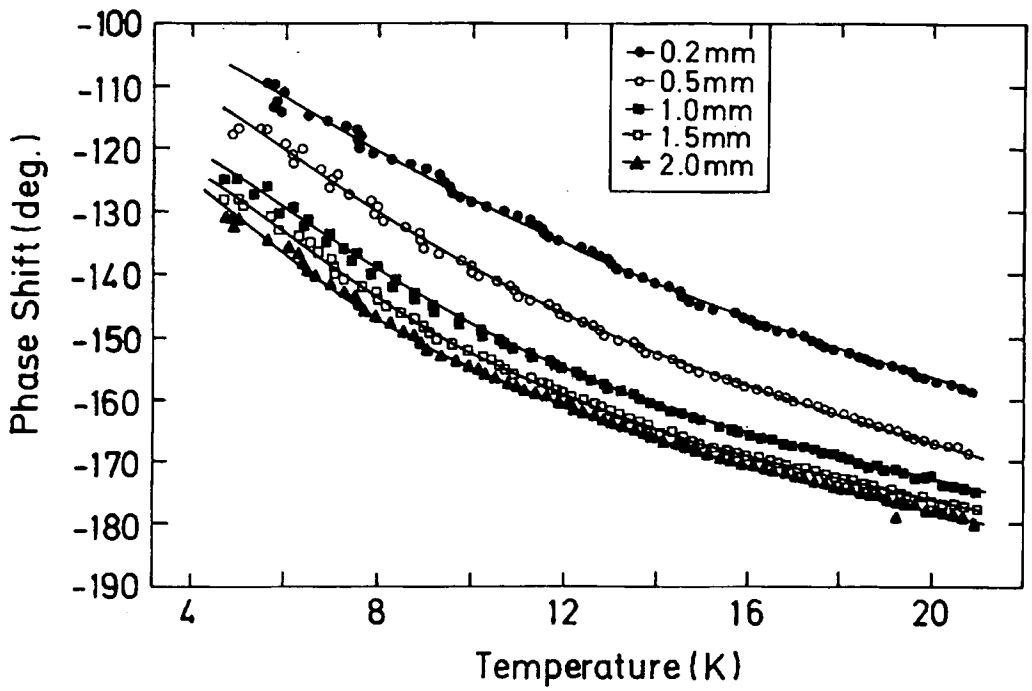

Fig.5.24: Raw data for 5 Cu samples of different masses, giving phase shift versus temperature. Freq.=0.5 Hz, Excitation Current to CX-1030 thermometer=100 uA, Ramp Rate=0.125 K.min^{-1}, Pressure ≈ 5 Torr.

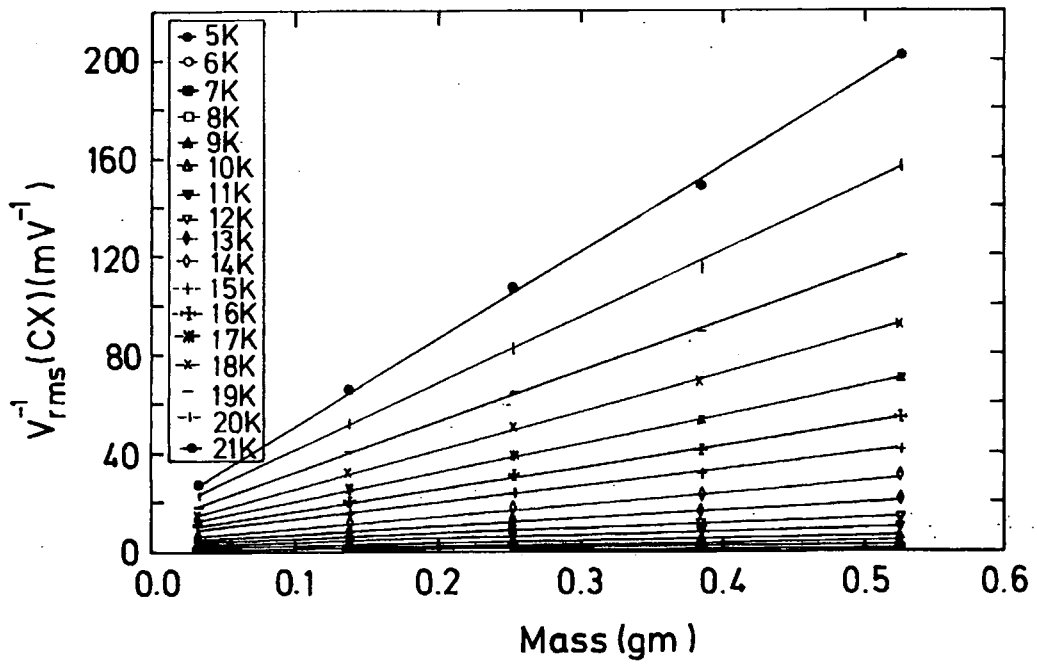

Fig.5.25: Raw data of Fig. 5.23 has been replotted, giving $V^{-1}_{rms}(CX)$ vs. Mass for Cu.

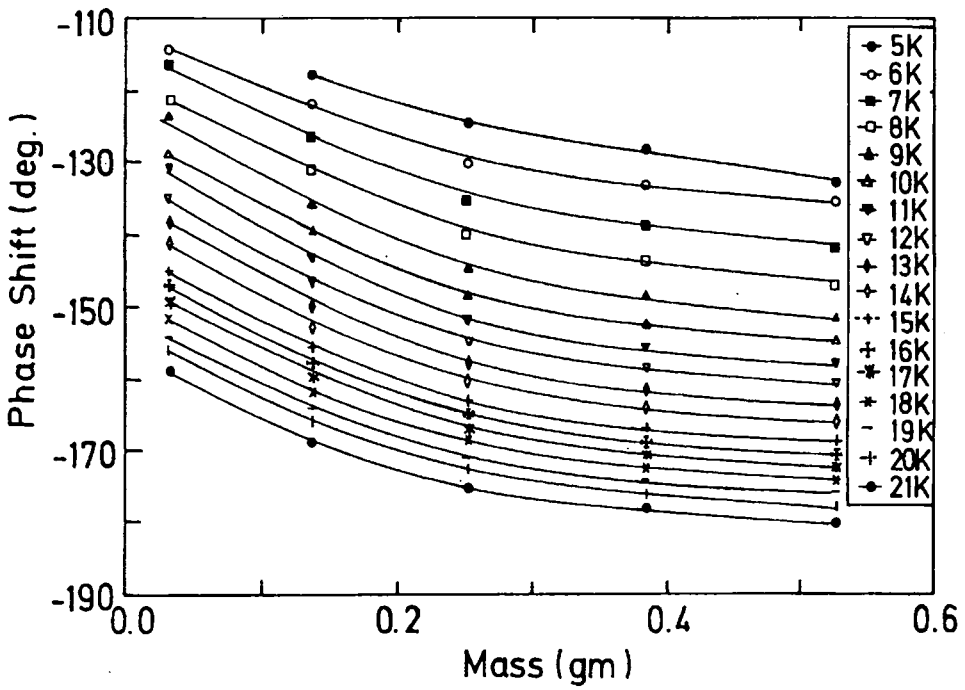

Fig.5.26: Raw data of Fig. 5.24 has been replotted, giving Theta vs. Mass for Cu.

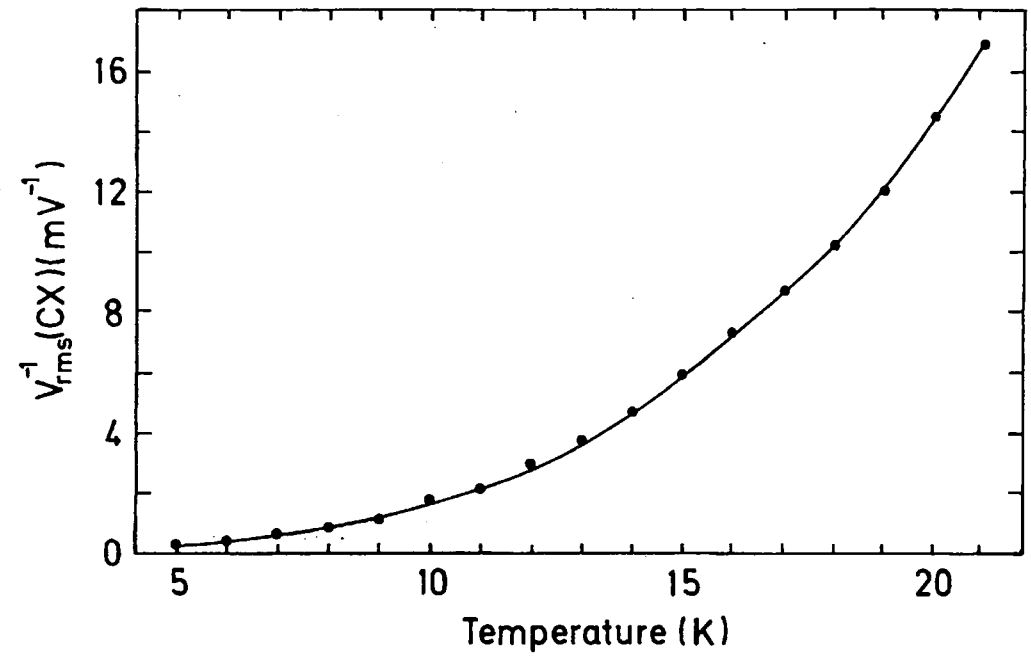

Fig.5.27: The value of $V^{-1}_{rms}(CX)$ obtained for the addenda (negative mass) as a function of temperature, after the straight line fit.

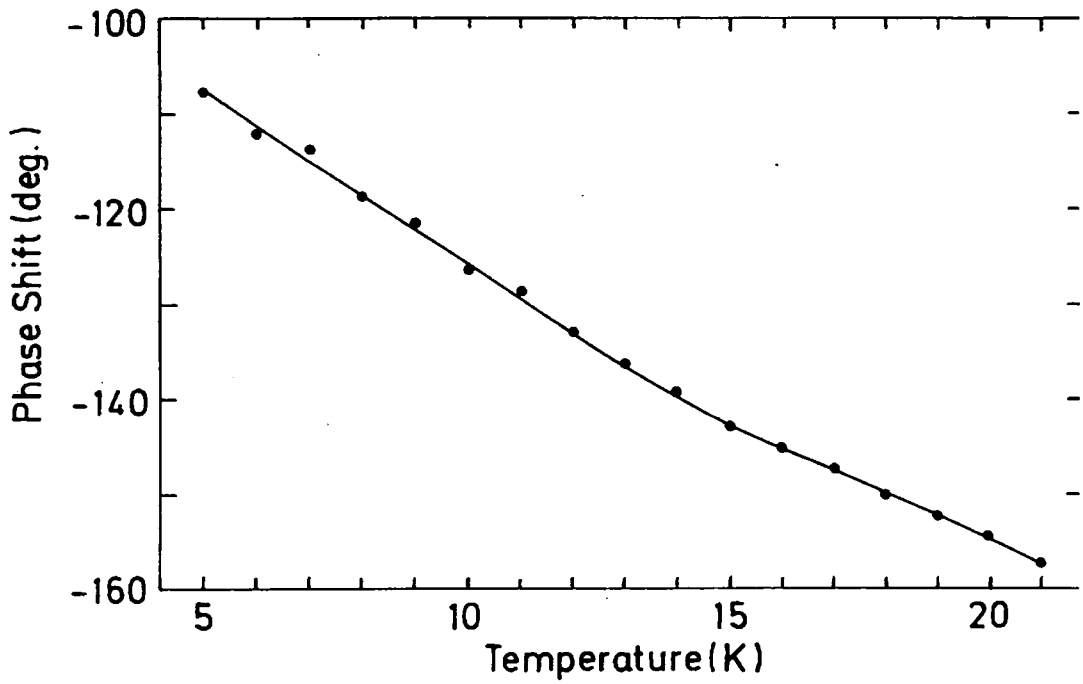

Fig.5.28: The value of theta obtained for the addenda (negative mass) as a function of temperature, after the straight line fit.

We have determined a first order correction term to take account of the variation of theta as follows:

By completing straight line fits to the data in Fig.5.25 and extrapolating to zero values of $V^{-1}_{rms}(CX)$, we have determined the (negative) effective mass of copper equivalent to the addenda. Similarly, by extrapolating the values of theta shown in Fig. 5.26 to these computed zero addenda values of (negative) mass, we have determined values of theta. In Fig. 5.27, the extrapolated values of (negative) mass in Fig. 5.28, theta values are shown.

Again following Sullivan and Seidal [1,4] and modifying Eq.(3.48), we have found an expression which includes the effect of a phase shift described in Chapter 3. One can write [5],

$$C = \frac{\sqrt{2}\left(\frac{V_{IN}^2}{R_H}\right)}{8\pi f} \cdot \frac{I_{Thermometer}}{V_{rms}(CX)} \cdot \frac{\partial R_{Th}}{\partial T} \cdot Z \qquad (5.4)$$

where

$$Z = kl\left[\frac{2}{\cos^2 kl \sinh^2 kl + \sin^2 kl \cosh^2 kl}\right]^{\frac{1}{2}} \qquad (5.5)$$

To determine kl, the phase shift analysis can be used as,

$$\tan \delta\theta = \frac{-1\left[1 + \frac{\tan kl}{\tanh kl}\right]}{\left[1 - \frac{\tan kl}{\tanh kl}\right]} \qquad (5.6)$$

where k is a constant defined by, $k = (\omega/2n)^{1/2}$, ω, the angular frequency and n is the thermal diffusitivity (defined in section 3.6.2) of the sample and l is the thickness of the sample and $\delta\theta$ is the phase shift observed due to the sample and the addenda. Hence using Eq. (5.4), the heat capacity of any material can be determined at any temperature as follows:.

a). From the measured value of theta, from Fig.5.28, we can determine $\delta\theta$ across the addenda and sample and from Eq. 5.6 determine kl.

b). Given kl and Vac, using Eqs.5.4 and 5.5, we can determine the heat capacity. Using the data in Figs. 5.23- 5.28, the heat capacity of Cu- samples has been

calculated and shown in Fig. 5.29. To find the specific heat and the addenda, the data of Fig.5.29 has been replotted in Fig. 5.30, giving heat capacity versus mass for different Cu-samples, from which the specific heat of Cu can be calculated at any temperature using a straight line fit. The slope of this fit gives the specific heat of Cu. In Fig. 5.31, a comparison between literature values [7] and the Durham values have been given and Fig. 5.32 reveals the %age deviation of Durham results from those of the literature. The values we found are ~10% different to the literature value which we attribute to the finite thermal conductivity of the thermal link.

The addenda of the system has been calculated from the above straight line fit and is shown in Fig. 5.33. To subtract easily the addenda from measured Cp values a 3rd order polynomial fit which fits to better than 0.35% was used. To check the validity of the above analysis for a single sample, Cu-2 mm sample was chosen. The raw data showing $V^{-1}_{rms}(CX)$ & θ is shown in Fig.5.34. The addenda was subtracted from the Cp computed and the result compared with literature is displayed in Fig.5.35. It is similar to the values we got using the above analysis for 5 Cu samples. In the subsequent chapters of this thesis, this analysis is used to determine the specific heat of our Chevrel phase materials.

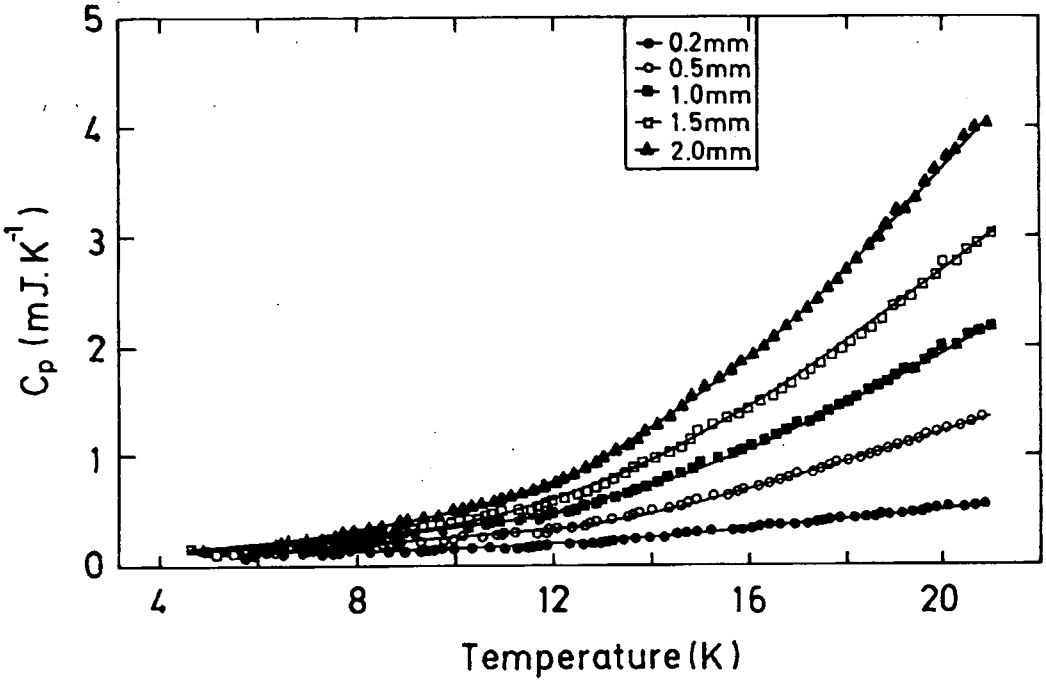

Fig.5.29: Cp (Heat Capacity) of 5 Cu-samples as function of temperature, after the Cp computer analysis.

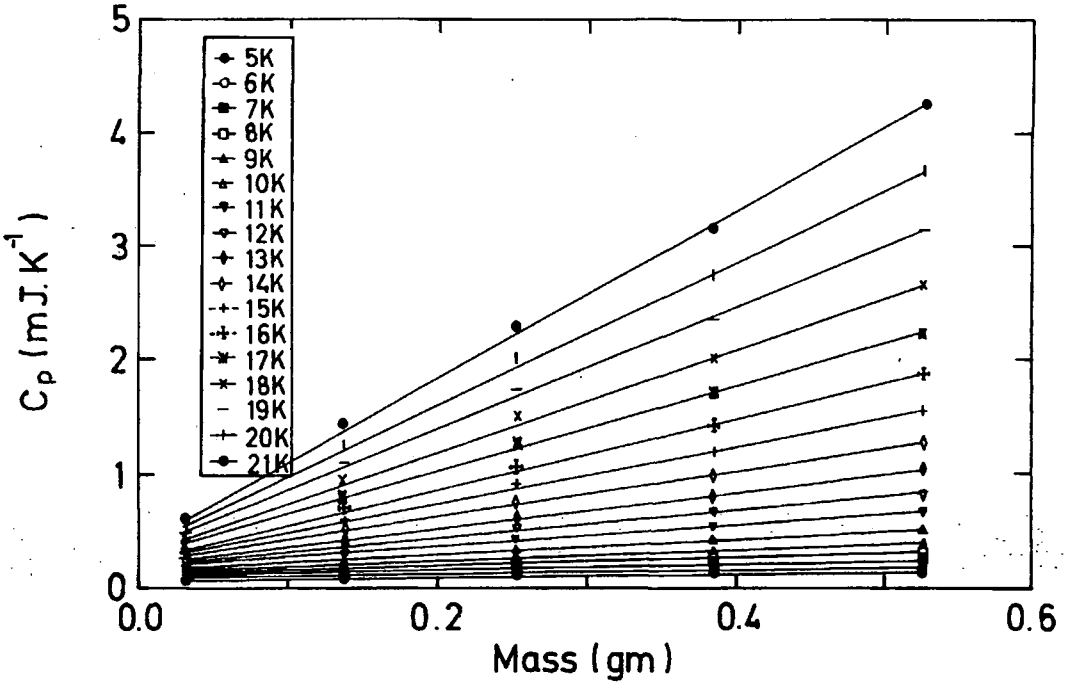

Fig.5.30: To find the specific heat and the addenda, the data of Fig.5.29 has been replotted as a function of mass at different temperatures.

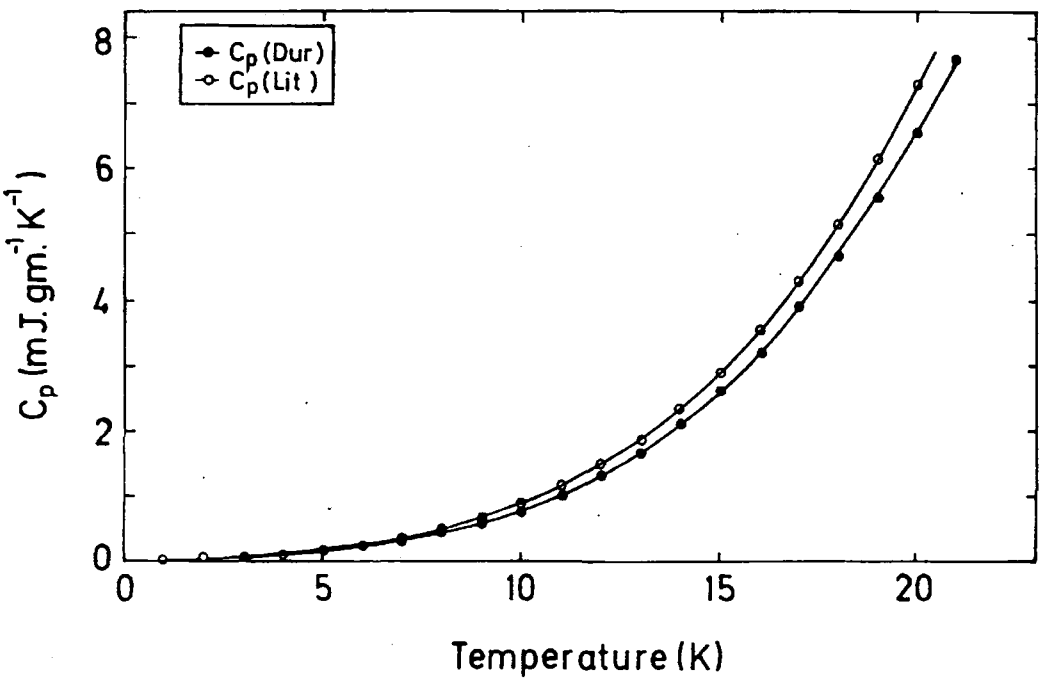

Fig.5.31: Comparison of specific heat obtained in Durham with that of Literature values [7].

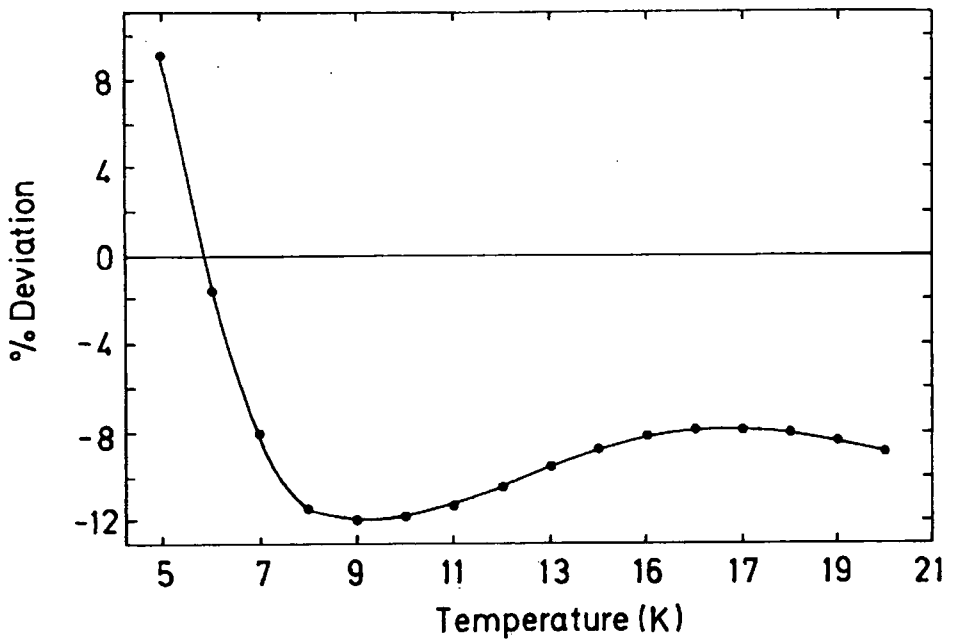

Fig.5.32: %age deviation of Durham specific heat results from that of literature [7].

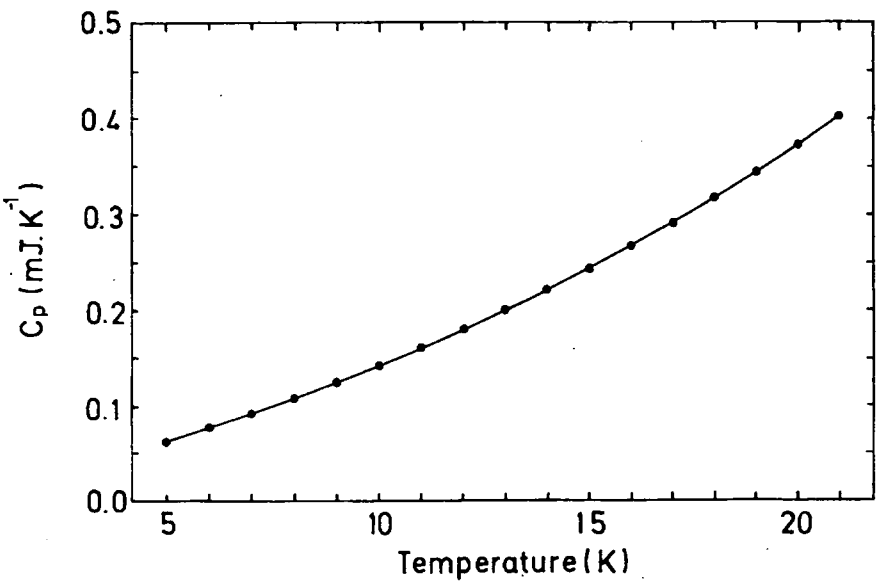

Fig.5.33: The heat capacity of addenda obtained from the straight line fit to Fig. 5.30. A comparison between addenda calculated from the straight line fit to the addenda generated using 3rd order Polynomial fit. The Polynomial used to generate the addenda are; a_0 = -0.0001170245, a_1 = 0.01132511, a_2 = 0.0002187534, a_3 = 7.3527×10^{-6}.

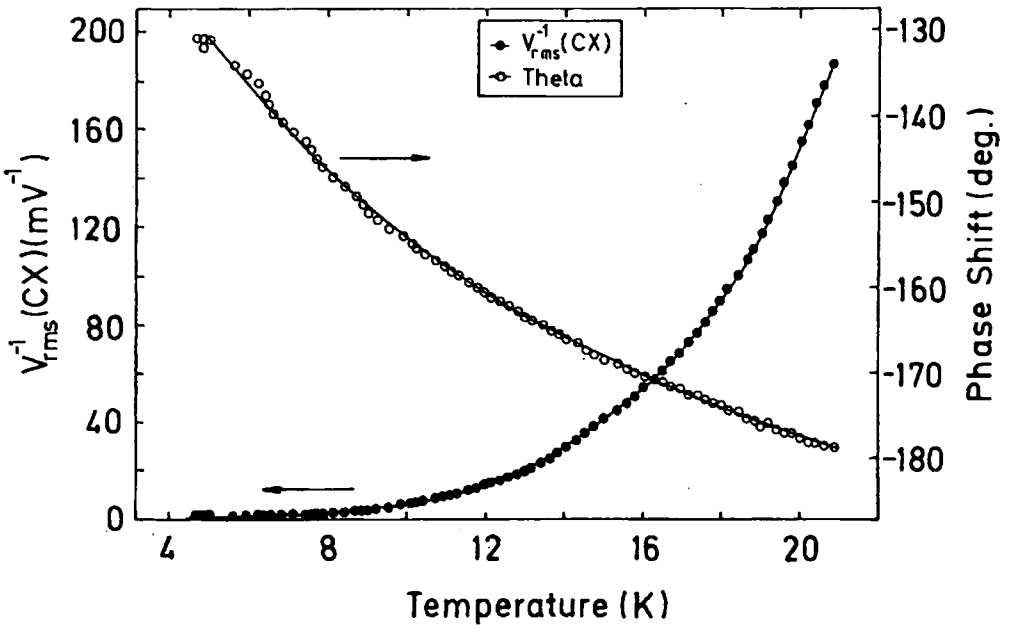

Fig.5.34: To check the validity of the Cp computer analysis on a single sample, $V^{-1}_{rms}(CX)$ and the phase shift as a function of temperature has been plotted for the Cu-2 mm sample.

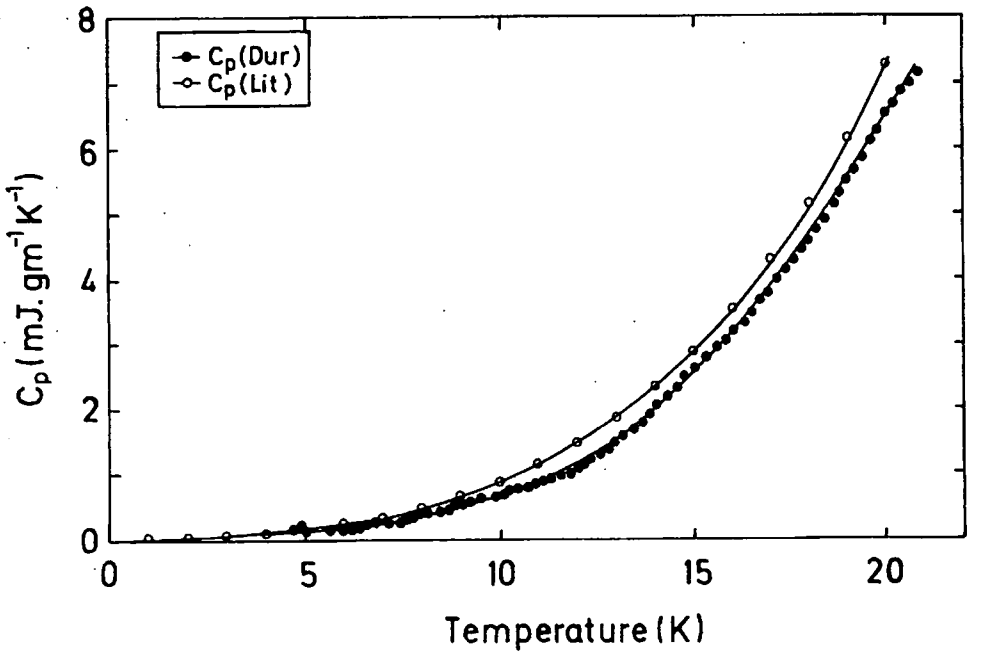

Fig.5.35: After computing Cp for Cu-2 mm sample, the addenda has been subtracted , and the results are compared with that of literature [7].

5.6: Experimental Results and Analysis for NbTi:

5.6.1: Early Experiments on NbTi:

As NbTi superconductor has a well established critical temperature Tc, jump ΔC, and B_{C2}, it was chosen to test the a.c. technique in high fields. In this preliminary series of experiments we found that a suitable frequency for NbTi material lies in the range of 0.5 Hz $\preceq$ f $\preceq$ 2 Hz, and a voltage range of 0.1 V $\preceq$ V$\preceq$ 0.5 V. Evidence for this is provided in Figs.5.36-5.37 where the data in these range collapse to a single line at low frequencies following Eq. 5.2. Different ramp rates were tried to see the effect of the ramp rate on transition temperature and specific heat jump. We found that if one uses a fast ramp rate, the jump and $V^{-1}_{rms}(CX)$ values are low whereas slower ramp rates gave better value of T_C and higher jumps as can be seen in Figs.5.38-5.39, where $V^{-1}_{rms}(CX)$ and θ are plotted against temperature. We chose a ramp rate of 0.25 K min^{-1} for our measurements. To find the suitable excitation current for the CX-1030 thermometer, different currents were tried. It was found that low excitation current gives no self-heating but the low signals (Tac) are poorly measured leading to steps in the data due to the limit in resolution (primarily due to the running exponential filter) [2, p.3.12] of the LIA and large noise in the data. On the other hand, using higher excitation current say 1 mA one can get better data, but it gives higher Tc values due to self-heating in the CX-1030 and additionally this may damage the thermometer. It is shown in Fig. 5.40-5.41, that the data due to 10, 100, and 300 uA excitation current are similar, so 100 uA excitation current was chosen to perform the experiments.

Additional data were obtained in a later series of experiments using the optimised conditions outlined in section 5.4.2. The raw data for NbTi in 0-field are displayed in Fig. 5.42, giving $V^{-1}_{rms}(CX)$ and phase shift vs. temperature. Using the analysis discussed in Section 5.5, Cp vs. temperature has been plotted in Fig. 5.43. The value of T_C, Cp and ΔC for the a.c. technique all agree to within experimental error with the results from the heat pulse method. The heat pulse data is shown in Fig. 5.44. Comparing our data with the literature [9] the transition temperature Tc, and Cp, quoted in literature is very similar, for materials of comparable composition.

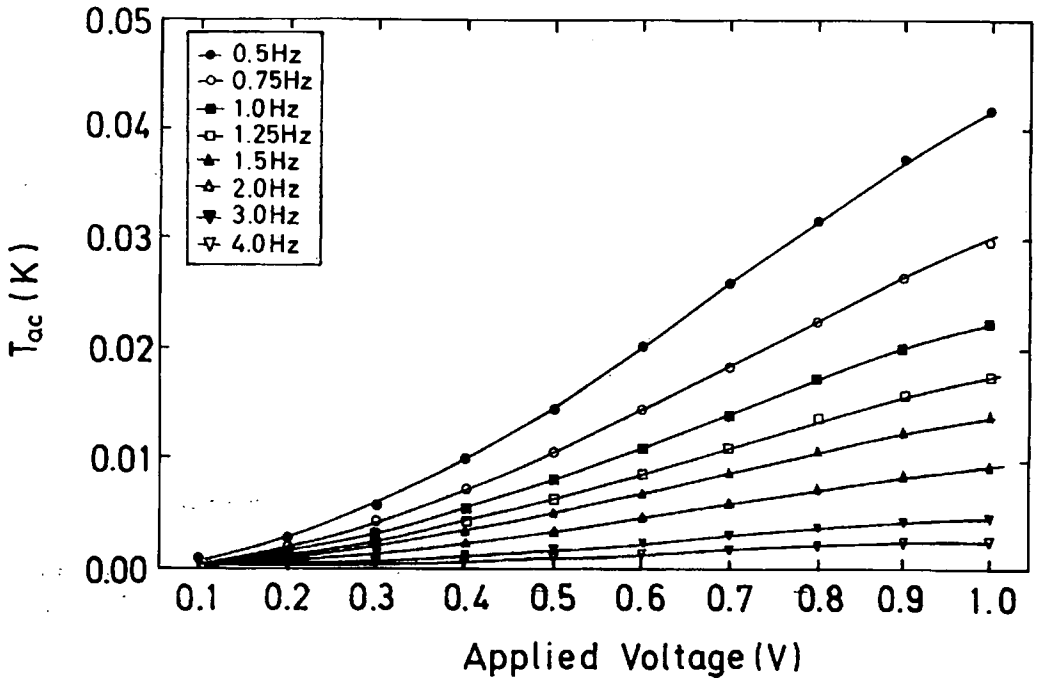

Fig.5.36: To find the suitable voltage V_{IN} for the NbTi superconductor, Tac has been plotted as a function of applied voltage at 12 K, with different frequencies for 18 Torr pressure at the warm end of the probe.

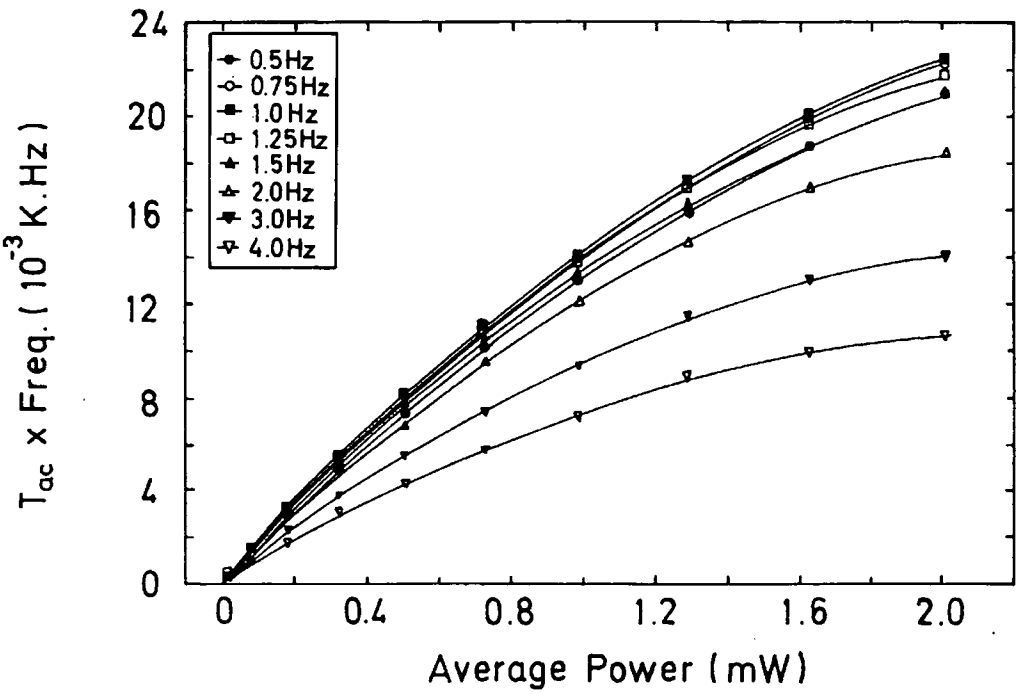

Fig.5.37: The data of Fig. 5.36 has been replotted giving Tac×frequency vs. Average Power for NbTi.

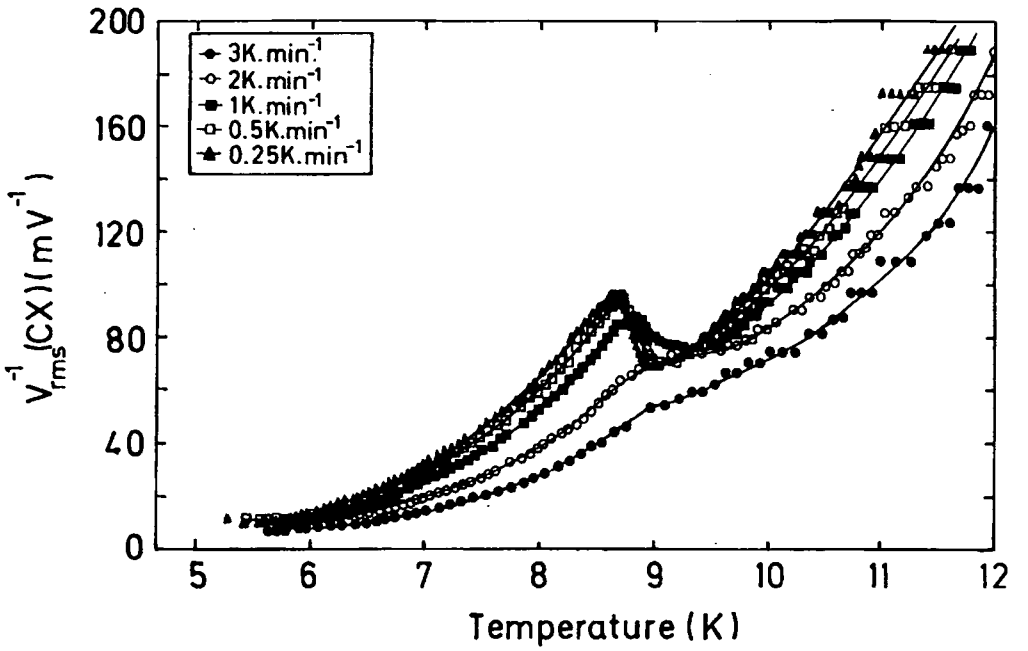

Fig.5.38: The effect of different ramp rates on $V^{-1}_{rms}(CX)$, position of T_C, and the jump height, for NbTi sample in 2 T. Voltage=0.35 V, Freq.=5 Hz, Time Constant of LIA=10 sec.

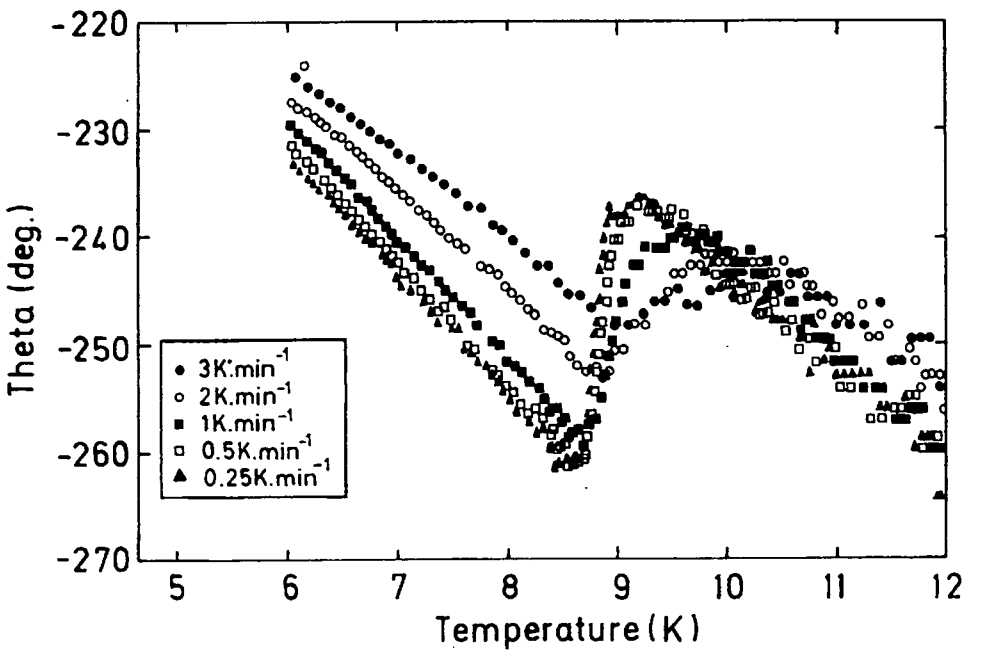

Fig.5.39: The effect of different ramp rates on phase shift for NbTi sample, in 2 T. Voltage=0.35 V, Freq.=5 Hz, Time Constant of LIA = 10 sec.

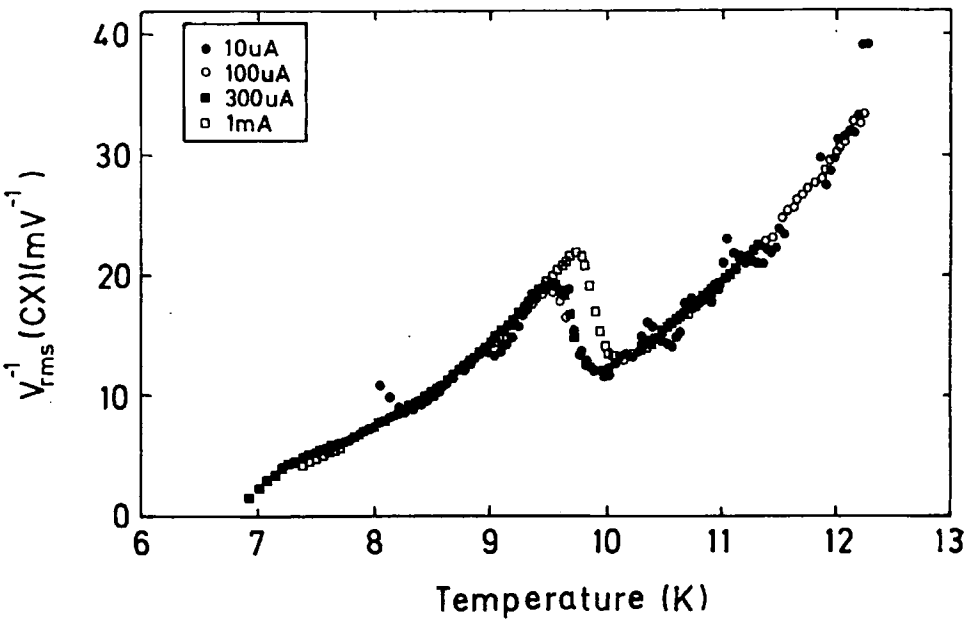

Fig.5.40: The effect of different excitation currents, to CX-1030 thermometer, on the V^{-1}_{rms}(CX) and the position of T_c for NbTi, as a function of temperature using a.c. Tech. in 0 T.

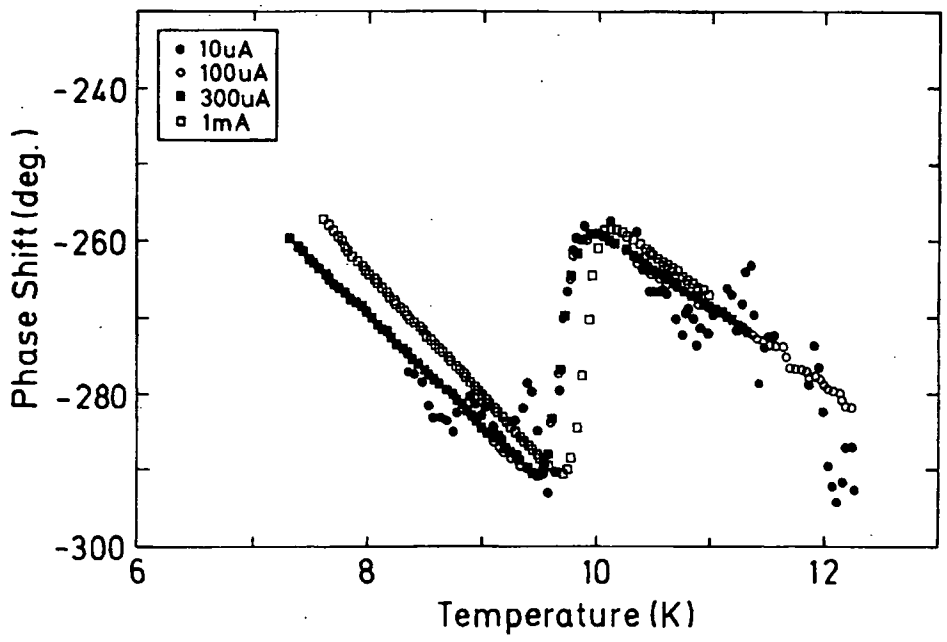

Fig.5.41: The effect of different excitation currents to CX-1030 thermometer, on the phase shift for NbTi sample, in 0 T.

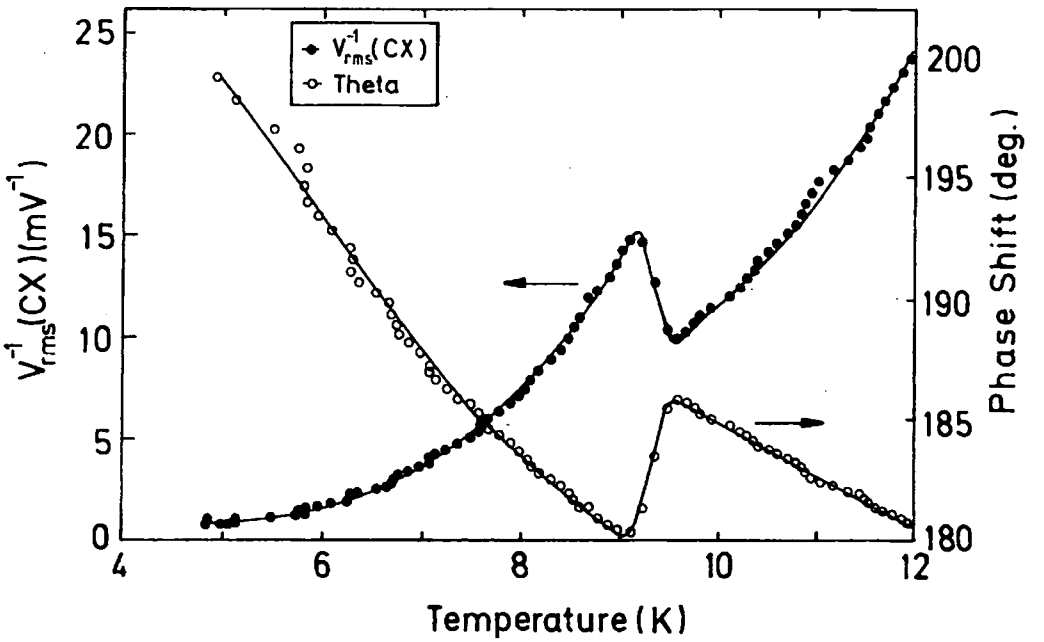

Fig.5.42: Raw data for NbTi sample, giving $V^{-1}_{rms}(CX)$ and the phase shift versus Temperature.

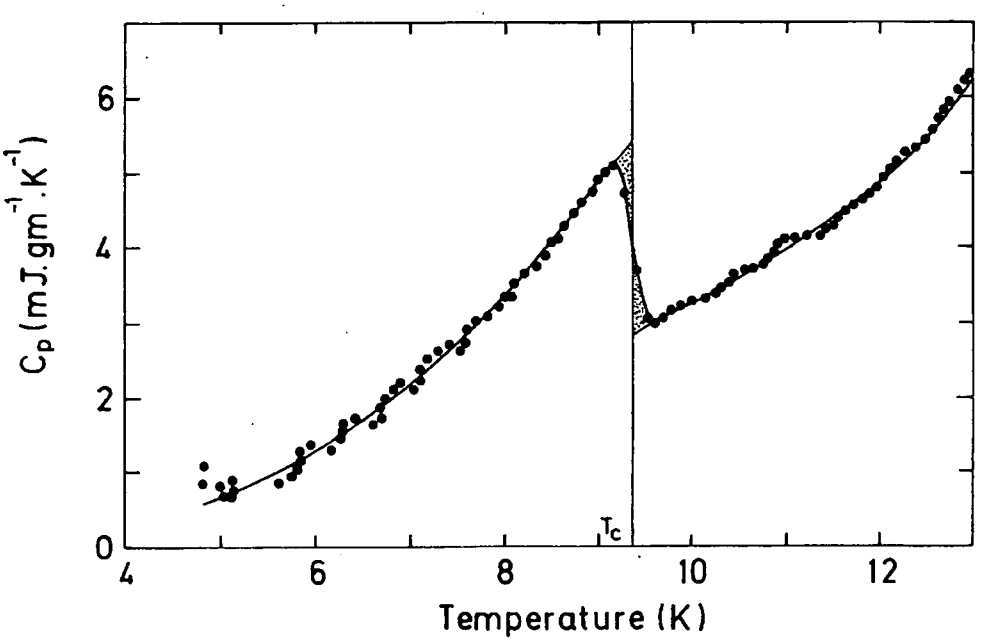

Fig.5.43: Cp as a function of temperature of NbTi, after the ASYST analysis.

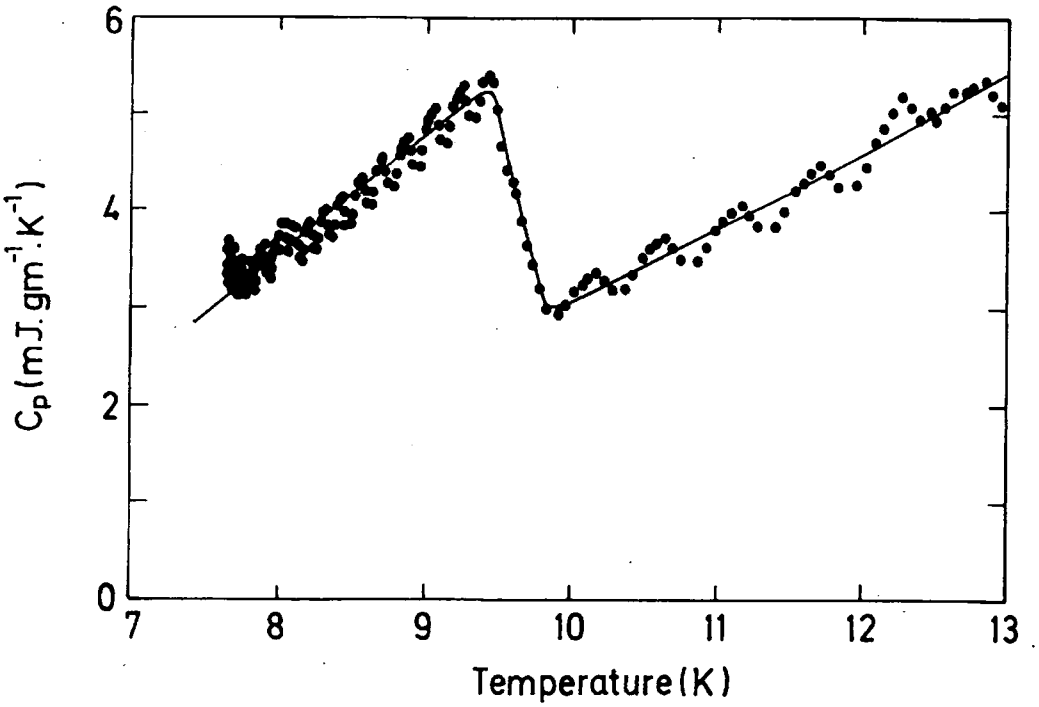

Fig.5.44: Cp as a function of temperature of NbTi, after the Heat Pulse Method.

5.6.2: NbTi Sample in High Fields:

A magnetic field of 0, 2, 4, 6, 8, and 10 Tesla was applied and the corresponding changes in the Tc, and ΔC for the NbTi, were noted. The raw data in magnetic fields of 0, 2, 4, 6, 8, and 10 Tesla, giving $V^{-1}_{rms}(CX)$ vs. temperature in Fig.5.45, and Phase Shift vs. temperature in Fig.5.46 are shown. The steps in the raw data are due to the limited resolution of the LIA, which can be eliminated by increasing the excitation current to CX-1030 thermometer (later data taken at 100 uA show no such steps, Fig.5.42). In Fig.5.47, Cp vs. temperature given using eq. 5.3, without taking into account the first order theta correction is shown. It was found that with the application of field, the temperature at which the phase transition occurs decreases and, the jump height ΔC, is reduced and smears out. From these data, we demonstrate that the a.c. technique developed in Durham is useful in the high fields.

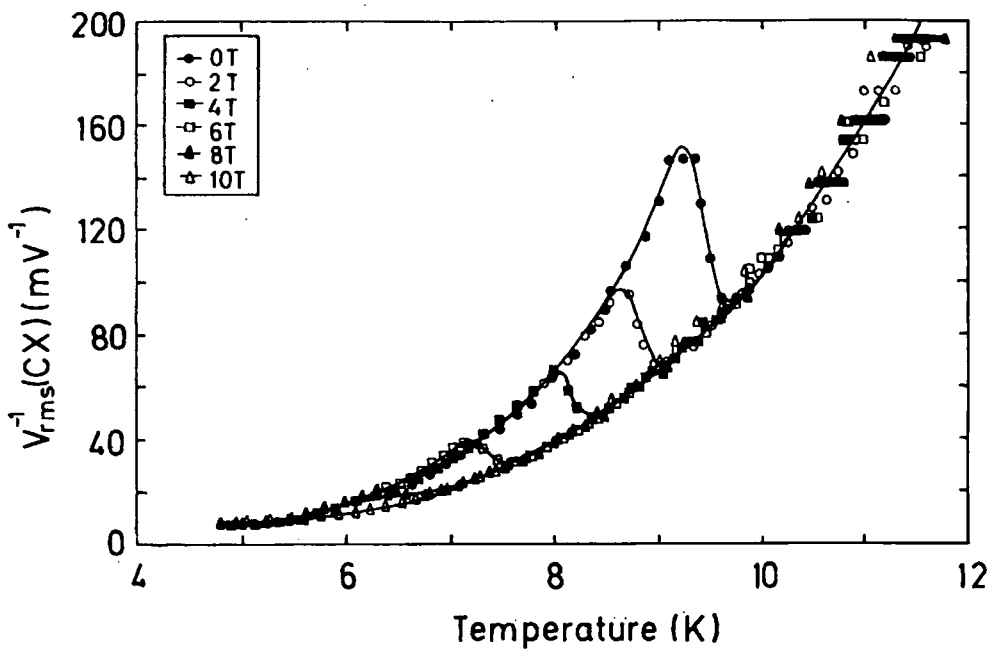

Fig.5.45: $V^{-1}_{rms}(CX)$ of NbTi as a function of temperature using a.c. technique in 0, 2, 4, 6, 8, and 10 Tesla. Ramp Rate=0.25 K.min^{-1}, Voltage=0.35 V, Freq. 5 Hz, TC of LIA=10 sec.

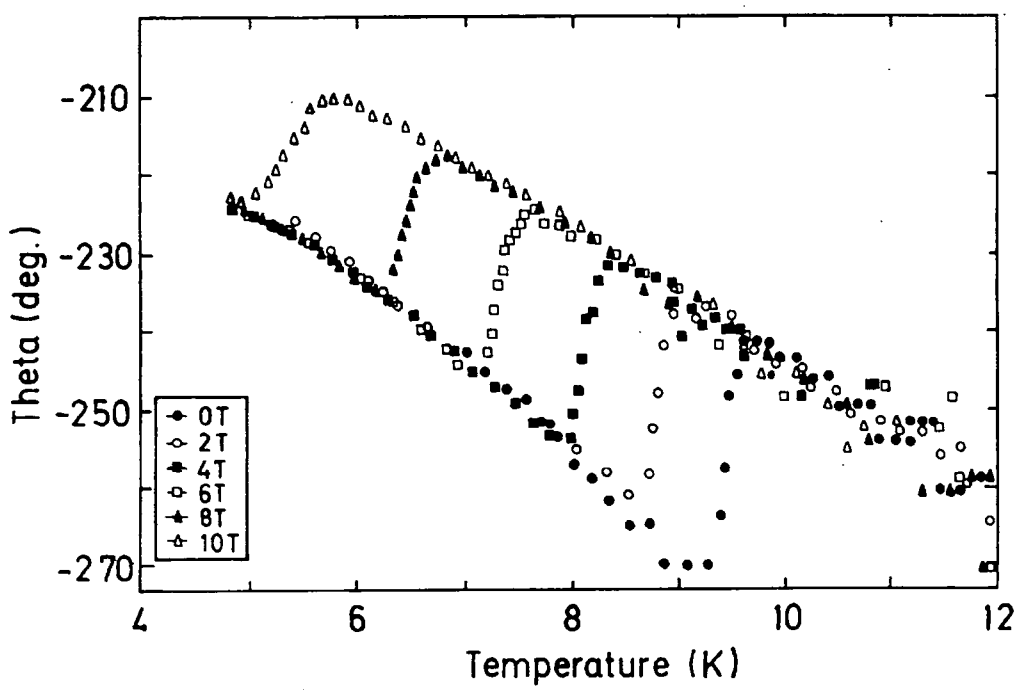

Fig.5.46: Phase shift of NbTi as a function of temperature using a.c. technique in 0, 2, 4, 6, 8, and 10 Tesla. Ramp Rate=0.25 K.min^{-1}, Voltage=0.35 V, Freq. 5 Hz, TC of LIA=10 sec.

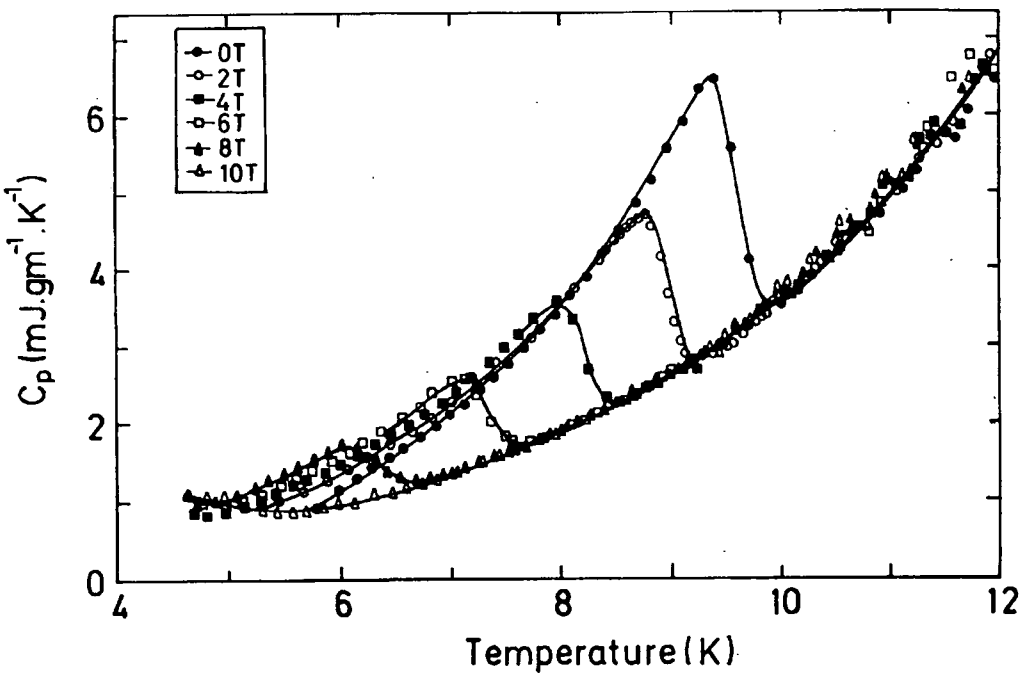

Fig.5.47: Specific heat of NbTi as a function of temperature using a.c. technique in 0, 2, 4, 6, 8, and 10 Tesla. Ramp Rate=0.25 K.min^{-1}, Voltage=0.35 V, Freq. 5 Hz, TC of LIA=10 sec.

5.7: Experimental Results and Analysis for ($PbMo_6S_8$).

The developed a.c. technique was tested on PMS which is considered to be a low thermal conductivity material. To do that, a sample of $PbMo_6S_8$ was fabricated using the Hot Isostatic Press (HIP) method. The fabrication method is described in Chapter 7. The dimensions of $PbMo_6S_8$, big sample named T4 was, thickness = 3.92 mm, width = 6.04 mm, and height = 6.80 mm, with a mass of 0.63870 gm. The second sample studied was the same material but made smaller by grinding it down, named T3, with thickness = 2.75 mm, width = 6.01 mm, and height = 6.80 mm, with a mass of 0.59308 gm. The same sample ground a second time was named T2, with thickness = 1.66 mm, width = 5.94 mm, and height = 6.80 mm, with a mass of 0.36455 gm. After a third grinding, the sample named T1, had a thickness = 0.95 mm, width = 4.78 mm, and height = 5.91 mm, with a mass of 0.14034 gm. The same sample was ground a fourth time, named T0.5, with thickness = 0.70 mm, width = 3.98 mm, and height = 4.46 mm, with a mass of 0.0611 gm was studied. The raw data are displayed in the Figs. 5.48-5.49 showing the behaviour of different samples with V^{-1}_{rms}(CX) and the phase shift vs. temperature.

5.7.1: Cp computer Analysis for the ($PbMo_6S_8$).

The heat capacity of the materials like $PbMo_6S_8$ which have a low thermal conductivity and large thickness can lead to a large phase shift as discussed in Chapter 3. Unlike Cu we do not find $V^{-1}_{rms}(CX)$ is proportional to mass. To calculate specific heat of PMS and the addenda of the system, the heat capacity versus mass of PMS has been shown, in Fig. 5.50 where the straight line fit will give the specific heat and the addenda for the system. In Fig. 5.51, Cp so obtained vs. temperature has been shown for first three masses and for the five masses. Similarly the addenda has been also calculated which is shown in Fig.5.52 taking into account first 3 masses and then all 5 masses. The Cp values are in good agreement with the literature [11]. This is considered in detail in chapters 7 & 8. The addenda has been compared with the addenda obtained from the Cu run and is shown in Fig. 5.52. We conclude that the analysis is self-consistent since the addenda obtained from Cu run is similar to that obtained by using the low thermal conductivity PMS samples.

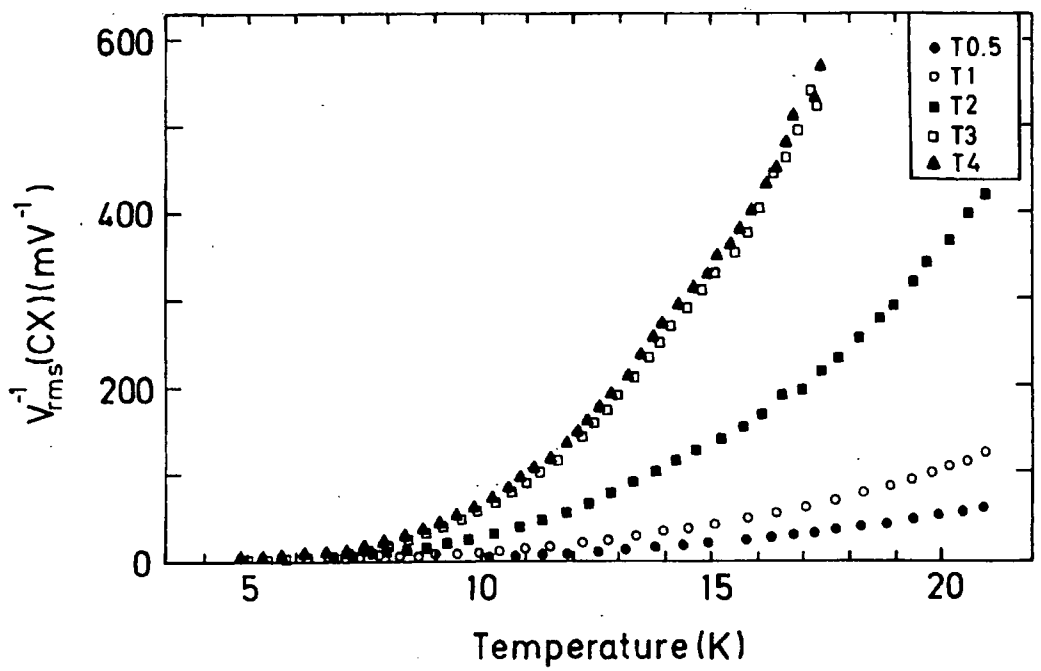

Fig.5.48: Raw data for 5 HIP-PMS samples with different masses and thicknesses, giving, $V^{-1}_{rms}(CX)$ versus temperature. Freq.=0.5 Hz, Excitation Current to CX-1030 thermometer=100 uA, Ramp Rate=0.125 $K.min^{-1}$, Pressure at the warm end of the probe≈5 Torr.

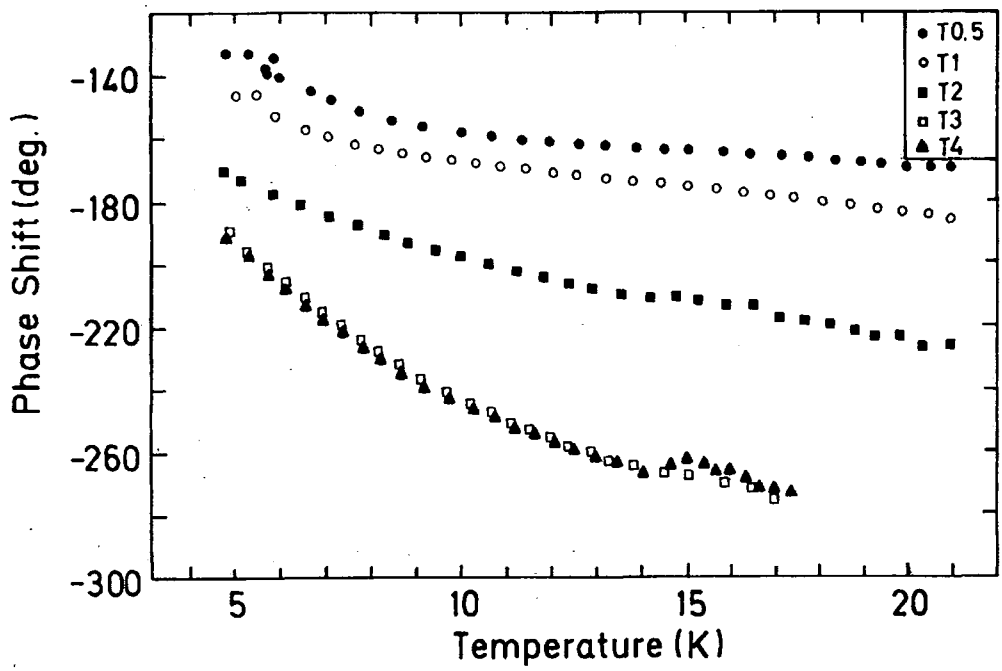

Fig.5.49: Raw data for 5 HIP-PMS samples of different masses and thicknesses, giving phase shift versus temperature.

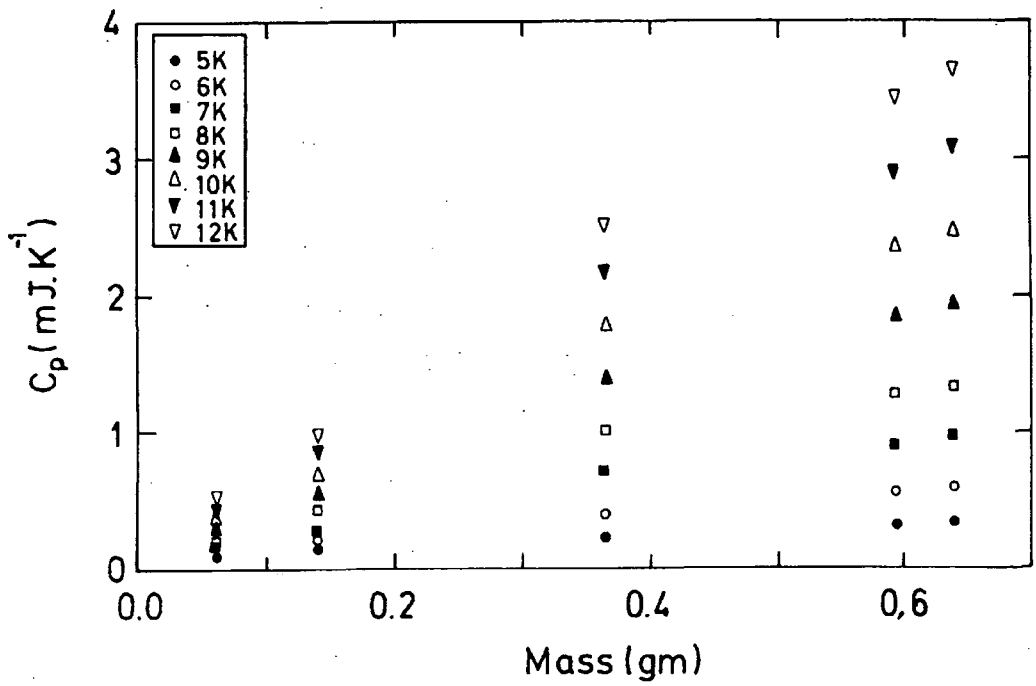

Fig.5.50: Cp(Heat Capacity) versus mass, to calculate the specific heat and the addenda for PMS material.

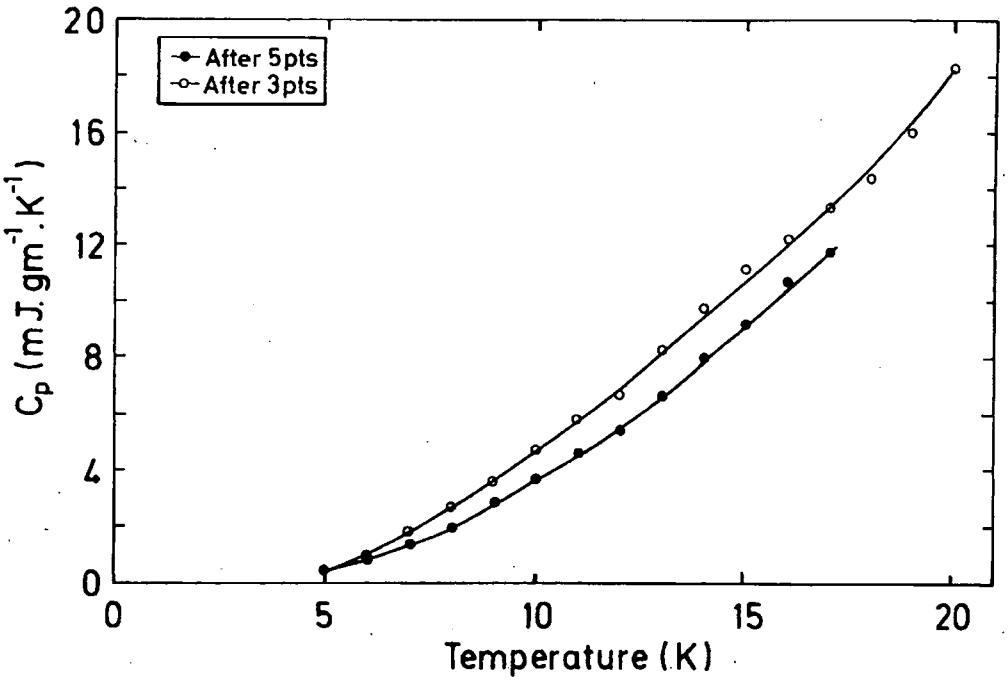

Fig.5.51: Comparison of specific heat versus temperature obtained after considering 3 and 5 masses.

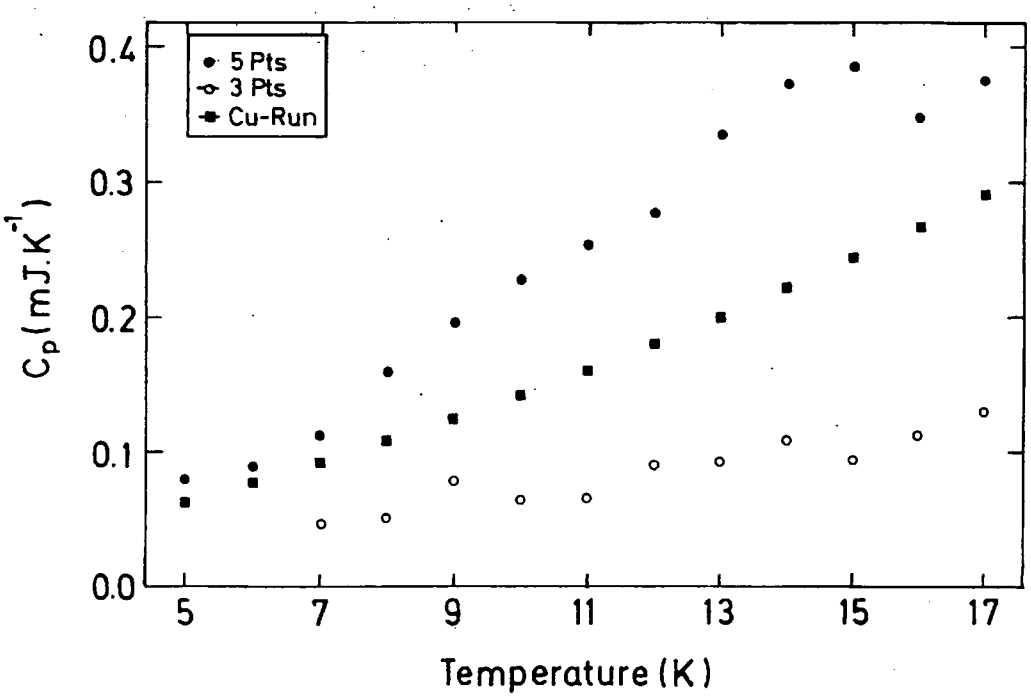

Fig.5.52: The comparison of addenda obtained from the straight line fit to Fig. 5.51, to the addenda obtained from the Cu-Run.

5.8: Discussion:

We carried out a series of experiments to find the most suitable environment to measure heat capacity of a material. The range of elements we looked at included frequency, pressure, voltage, excitation current with regard to CX-1030 thermometer, and the ramp rate for liquid nitrogen temperature and in liquid helium region.

From the experiments, we discovered, that a very low frequency (~0.5 Hz) is the most suitable frequency for the a.c. measurements. Below 0.5 Hz the LIA will not lock-in adequately. At very high frequencies, there are problems due to the thermal response time of the thermometer, and the finite thermal conductivity of the sample. The frequency dependency results are displayed in Figs.5.3-5.4 and 5.17-5.22. Consequently, we have chosen a 0.5 Hz, to acquire most of our data.

To choose the most suitable voltage, a thorough investigation was carried out. This resulted in a graph being plotted between, frequency×Tac vs. applied voltage, and can be seen in Fig.5.5-5.6. It is clear from Figs.5.5-5.6 and Fig.5.36-5.37, that at higher voltages, the graph deviates from a straight line, which indicates that a higher voltage is not suitable. We therefore chose to use 1 V at liquid nitrogen temperature and 0.35 V in liquid helium region.

Next a series of experiments were performed to select the suitable ramp rate for Cu samples. We have studied two Cu samples with thicknesses 0.5 mm and the 2 mm. The results are displayed in Figs. 5.9-5.12. It was found that a higher ramp rate does not meet the conditions necessary to produce a steady state, and accuracy is therefore poor. Yet, on the other hand, a very low ramp rate leads to excessive time for each measurement. The same ramp rate experiments were performed on a NbTi to identify a suitable ramp rate. It was found that for higher ramp rates, the jump is diminished and begins at higher temperatures, see Fig. 5.38-5.39. For very low ramp rates when steady states are to be met, one will see a sharp transition, and a reasonable Tc. It is hence very important to find a suitable ramp rate. It was found that the ramp rate of 0.125 $K.min^{-1}$ is quite reasonable.

To find a suitable pressure, a thorough investigation was made at liquid nitrogen and in the liquid helium region. At the liquid nitrogen temperature the small thickness sample of 0.2 mm show, Figs.5.5-5.6, that low pressure is not suitable at liquid nitrogen temperature. We therefore chose 1 atmospheric pressure at that temperature.

To find a suitable pressure in the liquid helium region, again two Cu-samples with thicknesses of 0.5 mm and 2 mm, were tested. Figs. 5.13- 5.16 reveal a small change in V^{-1}_{rms}(CX) and a large change in phase shift. If the pressure inside the probe is very high, it will consume too much helium, which is not economical, and if the pressure is too low, the temperature inside the sample chamber starts rising, due to conduction down through the leads, which increases the temperature inside the probe. Consequently, a steady state condition is not met and there is no control over the background temperature. In the liquid helium region, choosing 5 Torr of helium pressure at the warm end of the probe seems quite reasonable.

A series of experiments were then performed to find the suitable excitation current to the CX-1030 thermometer. To limit the self heating errors, the voltage read by the CX-1030 thermometer should be 10 mV or less [6]. To meet this requirement a current of 100 uA was used at the liquid nitrogen region. However, due to the high sensitivity of the CX-1030 in the liquid helium region, 10 uA should be used as the excitation current to CX-1030 thermometer. Yet, it is clear from the Figs 5.42-5.43, that if the excitation current is very low, one will get steps and noise in the measurements. Of course, higher currents gave very large signals, but these exceed the limits of the CX-1030 thermometer, and introduce the self heating errors. So for optimum conditions, 100 uA current was chosen.

After choosing all suitable parameters, the experiments were performed in 0- and in high fields in the liquid helium region. All of the Cu data were acquired in 0-field and the results for 5 samples obtained. A computer analysis was undertaken to get the heat capacity (Cp) of Cu. It is clear from the data that the results are almost ~10% different to the literature values. We attribute this to the finite thermal conductivity of the thermal link, which in the ideal case should be zero. The addenda obtained from the Cu run is used to calculate the heat capacity of all other samples in the following chapters.

The specific heat of NbTi and PMS have been measured. To test the reliability of this technique in magnetic fields, the results which were obtained using the a.c. technique, were compared with those of heat pulse method in Fig. 5.44. It is noted that a.c. technique gives the same results to within experimental errors, as those which were acquired using the heat pulse method . The critical temperature T_C, the specific heat

Cp and specific heat jump ΔC are similar with both techniques. The results were compared with those of literature [9,10], and it was found that the Durham results were very close to those of the literature values.

5.9: Conclusion:

It is concluded from the above, that the a.c. technique is better in many ways than that of traditional techniques. It gave continuous data read-out, and numerous conventional calorimetry problems have been overcome. From what was a noisy environment, the true signal has been extracted. We have detected temperature oscillations of 10^{-6} K. Due to its high sensitivity it can detect very minute changes that occur in the heat capacity of the material. This makes it most appropriate to investigate the materials, where relative measurements are more important than the absolute measurements. Yet the problem with this technique is that it is not suitable for low thermal conductivity materials. Nevertheless, we have successfully developed a method to analyse low thermal conductivity materials.

We have completed an extensive series of measurements on Cu, NbTi and PMS in zero field and in-field. We have found the results are accurate to ~10% and are consistent with the heat pulse data in Chapter 4. The optimised conditions for our experimental set-up are, frequency = 0.5 Hz, ramp rate = 0.125 $K.min^{-1}$ and the excitation current to be 100 uA. These conditions are used for the Chevrel phase materials considered later in this thesis.

References to chapter 5:

1) P. F. Sullivan and G. Seidel, Phy. Rev. Vol 173. 1968, pp. 679

2). Stanford Research Systems, Inc., 1290-D Reamwood Avenue, Sunnyvale, California 94089, Revision 1.3 (6/93).

3). Alpha, Johnson Matthey, Catalogue Sales, Materials Technology Division, Orchard Road, Royston, Hertfordshire, SG8 5HE. (U.K. Branch)

4) Specific heat of Solids, Edited by C. Y. Ho, Hemisphere Publishing Corporation, New York. 1988. ISBN 0-89116-834-6.

5) For more details, see Appendix B.

6). Cernox Resistance Temperature Sensors, A catalogue by LakeShore Measurement and Control Technologies, LakeShore Cryotronics, Inc. 64 East Walnut St., Westerville, Ohio, 43081-2399, USA.

7). D.L. Martin, L. L T. Bradley, W. J. Cazemier, and R. L. Snowdon, Rev. Sci. Instrum., 44 (1973), 675-684.

8). E. W. Collings, in Applied Superconductivity, Metallurgy, and Physics of Titanium Alloys, Vol.1. Plenum Press, New York. Chaps. 8, 10, 12.

9). Shchetkin, I. S., and Kharchenko, T. N., Sov. Phys. JETP 37 (1973) 491-493. [Translation of Zh. Eksp. Teor. Fiz. 64 (1973), 964-969].

10).Elrod, S.A., J.R. Miller, and L. Dresner, in Advances in Cryogenic Engineering Materials, (Edited by R.P. Reed and A.F. Clark), Vol 28, Plenum Press, New York, 1982.

11). Alekseevskii, N.E., G. Wolf, C. Hohlfeld, and N.M. Dobrovolski, J. Low Temp. Phys., 40 (1980) 479-493.

CHAPTER 6

Analysis of NbTi Superconductor

6.1: Introduction:

After the discovery of high field superconductors in late 1950s, soon afterwards superconducting wires and magnets were available for sale. NbTi wires were first mass produced in 1965, this was mainly because of their ductility, relative ease of manufacture when co-processed with Cu, excellent mechanical properties, and relatively low strain sensitivity. Consequently, this binary material became the preferred choice for use in large scale applications [1-3]. This material is currently used to wind into the magnets for use in energy storage, energy conversion, (i.e. generators and motors), high-energy particle detectors, beam-handling magnets and also to generate high magnetic fields. Since NbTi material is well characterised in terms of specific heat, transition temperature Tc, upper critical field $B_{C2}(T)$, and the specific heat jump height etc., we have decided to investigate this material to check the accuracy of our in-field measurements. After measuring the specific heat, we have compared our experimental results with that of literature. The details are given below.

The chapter consists of seven sections. Section 6.2, is devoted to resistivity data and the specific heat measurements on NbTi in the 0- and high fields. Section 6.3 provides the detailed analysis of the data in terms of Debye plot, the two fluid model, BCS and WHH theory. In section 6.4, the measured values have been compared with the theory and literature. Section 6.5 provides a comprehensive discussion, and finally section 6.6 concludes this chapter.

6.2: Experimental Results

The specific heat data of commercial NbTi have been acquired using the set up previously discussed in chapter 5. The Cp vs. T data of Fig. 5.43 (where the 100 uA excitation current to CX-1030 thermometer was used), have been replotted in **Fig.6.1.** This shows Cp/T versus T^2 in 0-field. The Cp vs. T data in magnetic field of Fig. 5.47 (where the 10 uA excitation current to CX-1030 thermometer was used), using the θ correction and normalised at 10 K of the 0-field value, has been replotted in **Fig.6.2** giving Cp/T versus T^2.

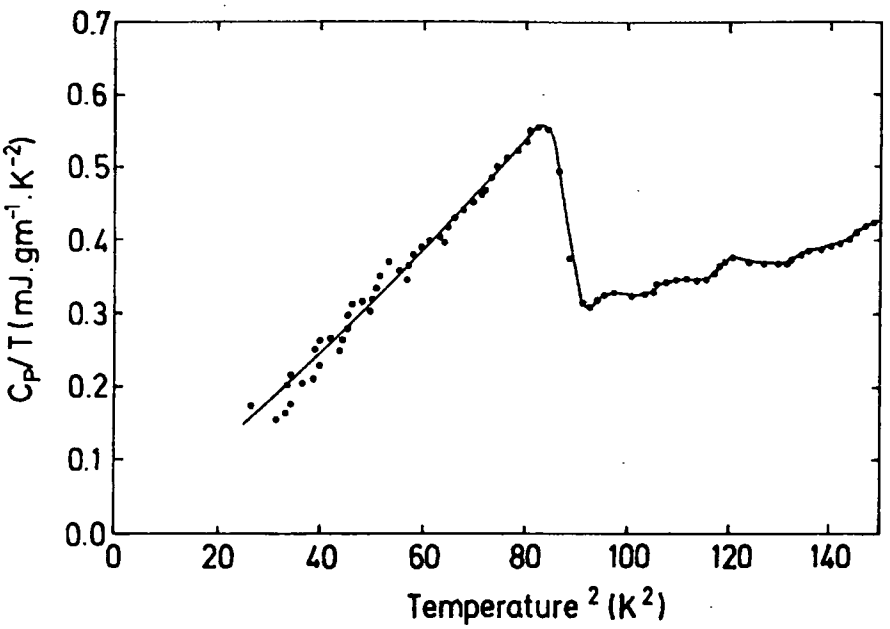

Fig. 6.1: The Cp vs. T data of Fig.5.43 has been replotted giving Cp/T versus T^2 for the NbTi. T_C has been calculated using the entropy conservation under the curve and found to be 9.37 K.

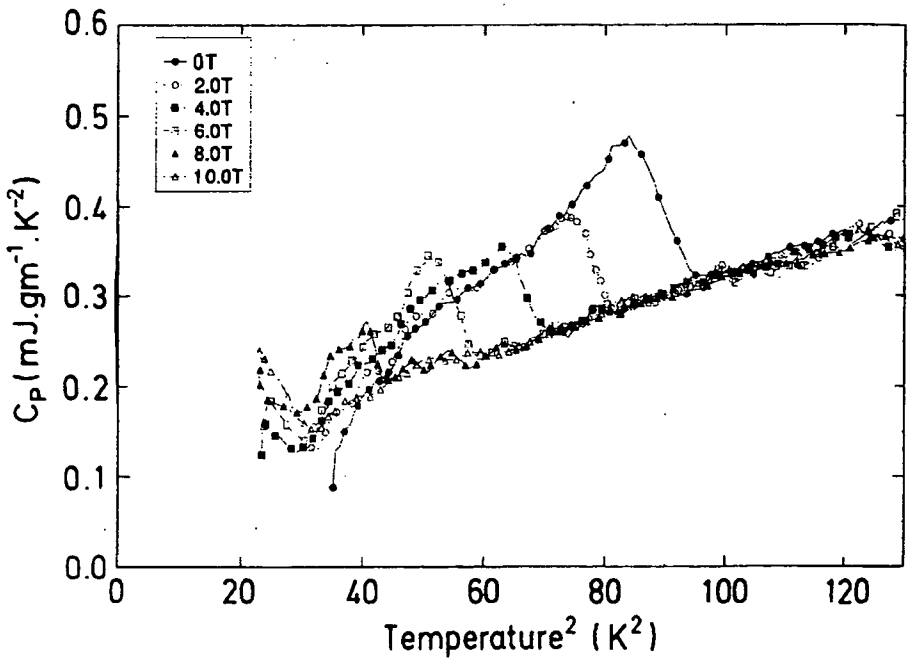

Fig. 6.2: The Cp vs. T data in magnetic field of Fig. 5.47 has been replotted giving Cp/T versus T^2 using 1st order theta correction and normalising at 10 K.

To compare theory and experiment for B_{C2}, the normal state resistivity data were obtained using the standard four-probe method. To minimise the errors in obtaining the length between voltage terminals, a large NbTi rod with a radius of 7.7 mm and a length of 21.5 mm was used. Using the formula; $R = \rho L/A$, we found a resistivity of 0.734 $\mu\Omega$-m of the rod.

6.3: Analysis of Data

Using the resistivity and Cp data, we can calculate the characteristic parameters for NbTi:

6.3.1. Specific Heat in 0-fields

Assuming that lattice specific heat obeys the T^3 behaviour in the superconducting state, the electronic specific heat can be evaluated using the Cp/T versus T^2 data (Debye Plot). In the normal state at low temperatures T ~ 10 K , Cp/T vs. T^2 should be a straight line, giving y-intercept as γ (the electronic specific heat co-efficient or the Sommerfeld constant), and the slope of the straight line as β. This has been explained more thoroughly in section 2.2. The Eq. of straight line can be written from the Eq. 2.29 as;

$$\frac{C_p}{T} = \gamma + \beta T^2 \qquad (6.1)$$

from where γ and β have been calculated using the straight line fit on the data acquired in 0 T of **Fig. 6.1,** and was found to be, γ=0.174(mJ.gm^{-1}.K^{-2}) and β=1.55(mJ.gm^{-1}.K^{-4}).

6.3.2): Specific Heat in High Fields

Different digitised values we obtained from the analysis of the data of specific heat measurements in high magnetic fields, (Fig. 6.2), are tabulated in **Table 6.1.** It is clear from the data, that the transition temperature T_S, and the jump height are reduced with the application of the magnetic field, while the width of the transition increases with increasing fields.

Using the two-fluid model, C_S (specific heat in superconducting state), has been calculated with the aid of Eq. 2.41, which can be modified as [4-6];

Appl. Field (T)	Trans.Temp. (T_S)± 0.1K	ΔC/T (%)	$\gamma H_a/H_{C2}(0)$ Theoretical	$\gamma H_a/H_{C2}(0)$ Experimental
0	9.48	75	0	0
2	8.86	67.3	0.0147	.01
4	8.21	56	0.0294	0.03
6	7.45	53.1	0.0442	.051
8	6.48	43.2	0.0589	.07
10	5.19	-	0.0736	-

Table 6.1. The effect of the magnetic field on the specific heat of NbTi. T_S is the critical temperature after the application of the field; Δ C/T(%), the percentage jump height; $\gamma H_a/H_{C2}(0)$, represents the increase in specific heat in the presence of a strong applied magnetic field.

$$C_S = \left[\beta + \frac{3\gamma}{T_C^2}\right]T^3 + \left[\frac{\gamma H_a}{H_{C2}(0)}\right]T \qquad (6.2)$$

It is noted that, the presence of the magnetic field has caused the specific heat to increase by an amount of almost $[\gamma H_a/H_{C2}(0)]T$ from its zero field value.

6.3.3): Determination of the $B_{C2}(0)$

$B_{C2}(0)$ can be determined by many methods. Some of them are described below;

1) To calculate $B_{C2}(T)$, we have plotted the applied magnetic field vs. the transition temperature T_S in **Fig. 6.3**. From this we have calculated the slope $dB/dT]_{T=Tc}$ to be -3.22 T/K, this can be used to determine $B_{C2}(0)$. The curve of this graph has been extrapolated back to 0 K in comparison with the curve obtained using WHH theory [7]. The y-intercept shows $B_{C2}(0)$ which can be seen from Fig. 6.3. The upper critical field was found to be 15.2 T.

2).Theoretical $B_{C2}(0)$ has been calculated using WHH theory [7], assuming there is no Pauli Paramagnetic Limiting (PPL) present; then from Eq. 2.63, $[B_{C2}=0.693\times T_C \times (dB/dT)_{T=Tc}]$, for a dirty type II superconductor, we found a $B_{C2}(0)$ of 20.94±1 T.

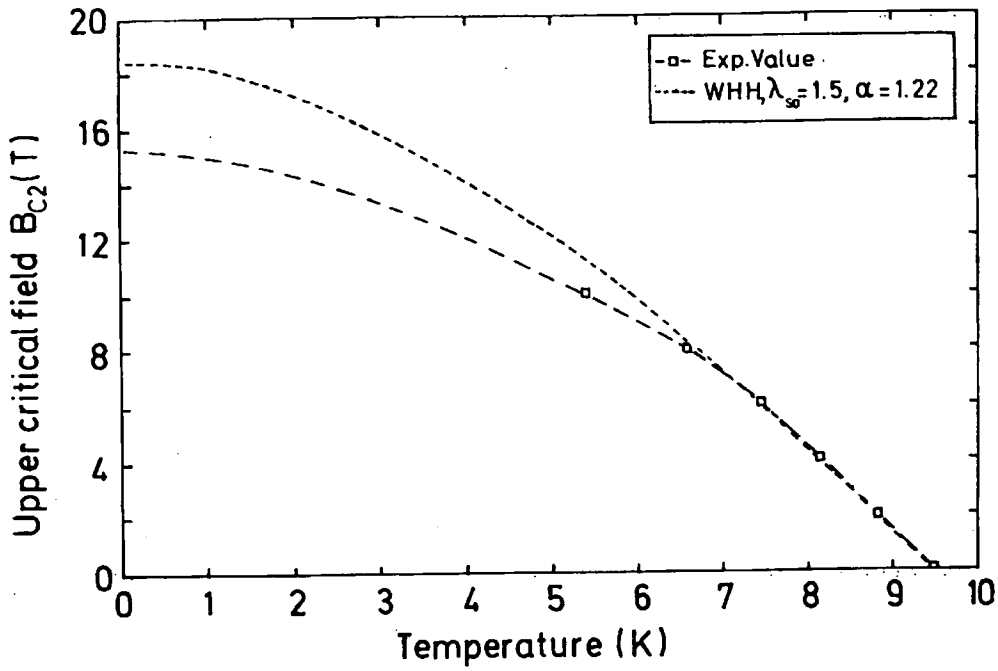

Fig. 6.3: Upper critical field versus the transition temperature for NbTi, giving an average slope of -3.14 T/K.

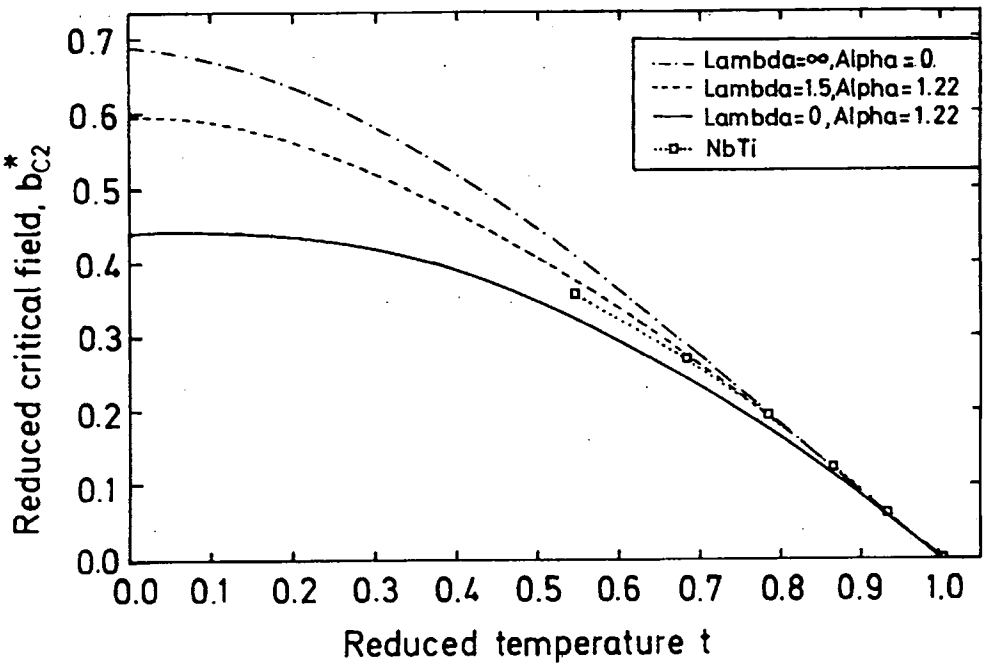

Fig. 6.4: Reduced upper critical field h^*_{c2} vs. reduced temperature t for different values of α and λ_{so}.

3). After the Clogston-Chanderashekher [8-9] paramagnetic limit, Eq. 2.56; (B_{P0} = 1.84 T_C Tesla), B_{P0} is found to be 17.24±0.2 Tesla. This high value demonstrates that paramagnetic corrections are needed in high field.

4). On the basis of jump height; since the jump height is reduced after the magnetic field. This suppression of the jump height can be used to determine the $B_{C2}(0)$. This has been done by plotting a graph between the % jump height vs. the applied field in Fig. 6.5. The curve has been extrapolated back to the 0 % jump height. Using WHH theory, $B_{C2}(0)$ has been estimated to be 18.2 T.

6.3.4): Resistivity Data

Using the normal state resistivity ρ_n data (as described in section 6.2), we can calculate $B_{C2}(0)$, $B_{C1}(0)$, $B_C(0)$, and the GLAG parameter κ:

We find:

$B_{C2}(0)$ = 17.27 Tesla using the Eq. 2.62 as [2, 3]:

$$B_{C2}(0) = 3.1 \times 10^3 \times \gamma_v \rho_n T_C \qquad (6.3)$$

$B_{C1}(0)$ = 0.049 Tesla using the Eq. 2.37 as [2, 3];

$$B_{C1}(0) = \frac{\ln[0.902 B_{C2}(0)/B_C(0)]}{[1.276 \times B_{C2}(0)/B_C(0)]} \qquad (6.4)$$

$B_C(0)$ has been found to be 0.204 Tesla making use of the Eq. 2.36 as [2, 3];

$$B_C(0) = 7.65 \times 10^{-4} \times (\gamma_v)^{1/2} T_C. \qquad (6.5)$$

The GLAG parameter κ was found to be 50.13 using the Eq. 2.51 as [2, 3];

$$\kappa = 2.4 \times 10^6 \times (\gamma_v)^{1/2} \rho_n \qquad (6.6)$$

When $B_{C2}(0)$ has been calculated using the relation [3, pp.283],

$$B_{C2}(0) = \sqrt{2}\, \kappa \times B_C(0) \qquad (6.7)$$

we found approximately 16% lower value of $B_{C2}(0)$.

6.3.5) Maki parameter α;

Maki [10] parameter α, gives some idea about the paramagnetic limiting present in the material. It can be calculated;

1). Using the Eq. 2.52 [2, 4];

$$\alpha \equiv \frac{\sqrt{2} B^*_{C2}(0)}{B_{p0}} \qquad (6.8)$$

where $B^*_{C2}(0)$ is the field assuming there is no PPL, and B_{P0} is the field at 0 K taking into account of the full paramagnetic limiting.

2). Using the slope at $T = T_C$ as [2,5];

$$\alpha \equiv -0.528 \left[\frac{dB_{C2}}{dT} \right]_{T=T_c} \qquad (6.9)$$

3). From the normal state resistivity ρ_n (Ω-m) and volumetric specific heat coefficient γ_v ($J.m^{-3}.K^{-2}$), using Eq. 2.53, as ;

$$\alpha = 2.35 \times 10^3 \gamma_v \rho_n \qquad (6.10)$$

It can be noted that all these methods give almost the same value of α as 1.5±0.2.

6.3.6: Measuring Spin-orbit scattering parameter λ_{so} and τ_{so}

The spin-orbit coupling parameter λ_{so} can be calculated using Eq. 2.55 or using the graphical solution for the different values of λ_{so}, and comparing with the experimental results. We used the graphical approach. The reduced upper critical field $b^*_{c2} = 0.693 \times B_{c2}(T)/(T_C \times dB^*_{c2}/dT)_{T=Tc}$ for different values λ_{so} has been plotted against the reduced temperature $t = T/T_C$ in **Fig. 6.4.** We noted that the experimental values of reduced critical field b^*_{c2} are very close to the theoretical curve for $\alpha = 1.22$, $\lambda_{so} = 1.5$, from where we have estimated that λ_{so} is very close to 1.51.

6.3.6): Height of the Specific Heat Jump;

It is noted that the specific heat jump in the 0-field, using 10 uA excitation current to Cernox-1030 thermometer, is ≈ 15 % less than the jump height we got using the 100 uA excitation current (see Chap. 5). We attribute this to the first order theta correction not being suitable for data acquired using 10 uA excitation current to CX-1030 thermometer. The height of the specific heat jump is reduced with the application of the field. The % jump height vs. applied field has been displayed in **Fig. 6.5.** Using Eq. 2.49, the normalised relative jump height $(\Delta C/Ts)/(\Delta C/Tc)$, has been measured. The data giving normalised jump height, vs. the reduced temperature $t_s^2 = (Ts/Tc)^2$ is shown in **Fig. 6.6.**

6.4): Comparison with the Literature;

As the application of the magnetic field reduces the jump height, this implies

that one can obtain the normal state specific heat with the application of a higher magnetic field than the $B_{C2}(T)$ below the transition temperature, after that the straight line fit holds well at lower temperatures. We have calculated the Sommerfeld constant γ ($mJ.gm^{-1}.K^{-2}$), and the slope β from the Cp/T vs T^2 in 10 T data after using the straight line fit, and compared it with the literature [11-13] values in Table 6.2. The γ value is ~ 5% and β value is ~ 20% lower than the literature [11] value. Using these values, the electronic and lattice contribution to specific heat has been separated from the total specific heat, and both specific heats are displayed in **Fig. 6.7.** Debye Temperature, θ_D differs for different compositions. It was calculated and was found to be 255.32 K for Nb-35%at-Ti, which is ≈ 7% higher than the literature value [11].

A comparison between Cp (total experimental specific heat), and C_S (calculated specific heat in the superconducting state), versus temperature is shown in **Fig. 6.8.** This comparison reveals that the calculated values are within ±10% of the experimental results in the temperature range of 5 - 6.5 K, and within ±2% in the temperature range of 6.5 K to 9 K. The oscillations in the lower temperature range is due to the large input power applied to the sample.

The theoretical values of the superconducting state specific heat C_S in the magnetic field, calculated using Eq. 6.2, and the experimental values are compared in **Table 6.1.** We found that the experimental values are in good agreement with the theoretical values at low field, but have large deviations in high fields.

The effect of the magnetic field on the specific heat has been calculated using the two fluid model, and it was found that the two fluid model is quite acceptable when the applied magnetic field is low. However, in high fields, the experimental and calculated values differ remarkably, this demonstrates that the two fluid model is not valid in high magnetic fields.

The other parameters have been calculated using Eqs. 6.3 - 6.6, and were compared with the literature in Table 6.3. But if one uses Eq. 6.7 to calculate $B_{C2}(0)$, one finds a very close value to that of the experimental value of 15 T [3].

The slope we found was -3.22. Using Eqs. 6.8 and 6.9, we found a value of α = 1.55 ± 0.2, both these methods show a strong effect of paramagnetic limit on NbTi in fields. However, if α is calculated using the relation; $\alpha = 2.32 \cdot 10^3 . \rho_0 \gamma_v$, (Eq. 6.10) one finds a value ~16.5% lower, which is ~12% higher than the literature [2, Colling]

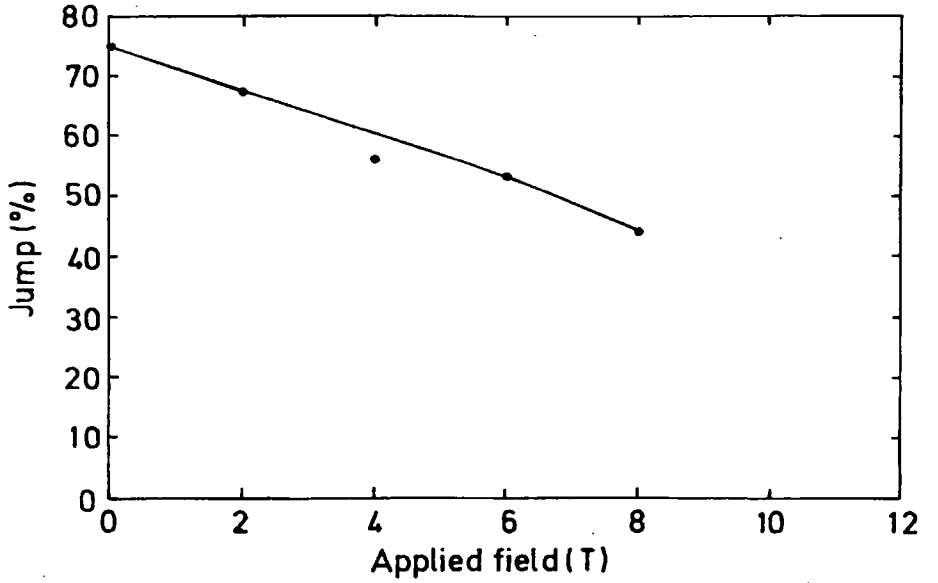

Fig. 6.5: The %age jump height has been plotted as a function of Applied Magnetic Field. With the application of the field, the jump height is reducing, leaning toward its normal state value. The graph is just guide to the eye.

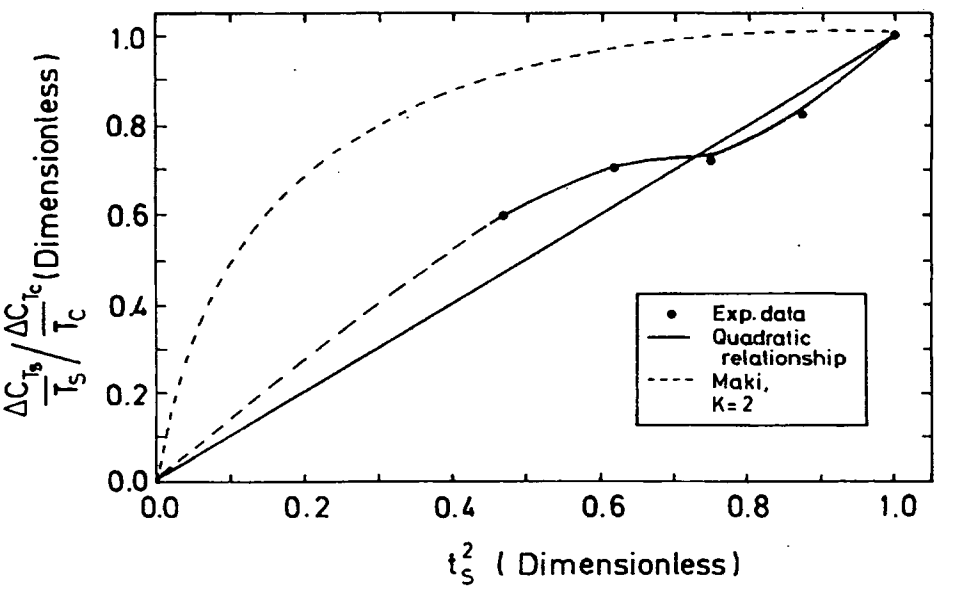

Fig. 6.6: Reduced relative jump height of the specific heat jump at the transition temperatures T_S has been plotted against the square of the reduced transition temperature, $ts^2 = (T_S / T_C)^2$. The straight line represent the quadratic relationship.

Ref.	T_C (K)	γ (mJ.gm^{-1}.K^{-2})	β (mJ.gm^{-1}.K^{-4})	$\beta + (3\gamma/T^2_C)$ (mJ.gm^{-1}.K^{-4})
Elrod, Miller, & Dresner[11]	9.1	0.145	2.3×10^{-3}	7.5×10^{-3}
Corsan[12] & Zbasnik[13]	9.2	0.175	2.6×10^{-3}	9.0×10^{-3}
This work	9.37*±0.1	0.138 ± 0.04	$(1.835\pm0.07)\times10^{-3}$	$(6.55\pm0.23)\times10^{-3}$

Table 6.2. *T_C is the midpoint of the superconducting transition (constructing the entropy conservation under the area and taking the midpoint), and has been calculated from the experimental data. [$\beta + (3\gamma/T^2_C)$] (mJ.gm^{-1}.K^{-4}); is the coefficient of T^3 term in the presence of the magnetic field.

values. The value of λ_{so} calculated after the graphical solution is very close to the value of 1.5, as quoted in literature [2, Colling, pp.549]. Using, α =1.22 and λ_{so} = 1.5, we have calculated $B_{C2}(T)$ curve using WHH theory in Fig. 6.3. It is clear that the curve obtained after the experiment is lower than the WHH curve in high fields.

6.5): Discussion:

The specific heat of NbTi superconductor in the zero field has been analysed in the vicinity of the transition temperature and below. After plotting Cp/T versus T^2, the γ (y-intercept) and β (the slope of the straight line fit), have been calculated in the normal state region. To get the values of γ and β, we have used the data of 10 T of Fig. 6.2. The value of γ we achieved is within ≈ 5% in agreement with that of the literature, and β is almost 20% lower that of the literature value [11]. All other calculations has been undertaken using these values. Using the formula, $\theta_D = (1944/\beta)^{1/3}$, where β is in J.mole^{-1}.K^{-4}, Debye temperature has been calculated and was found to be 7% higher than the literature value [11].

Using the two fluid model, the experimental specific heat in the superconducting state has been compared with the theoretical evaluated specific heat values in Fig. 6.8, and was found to be in very good agreement with the Eq.6.2. This reveals the validity of the two fluid model in relation to the strong coupled type II superconductor. Other

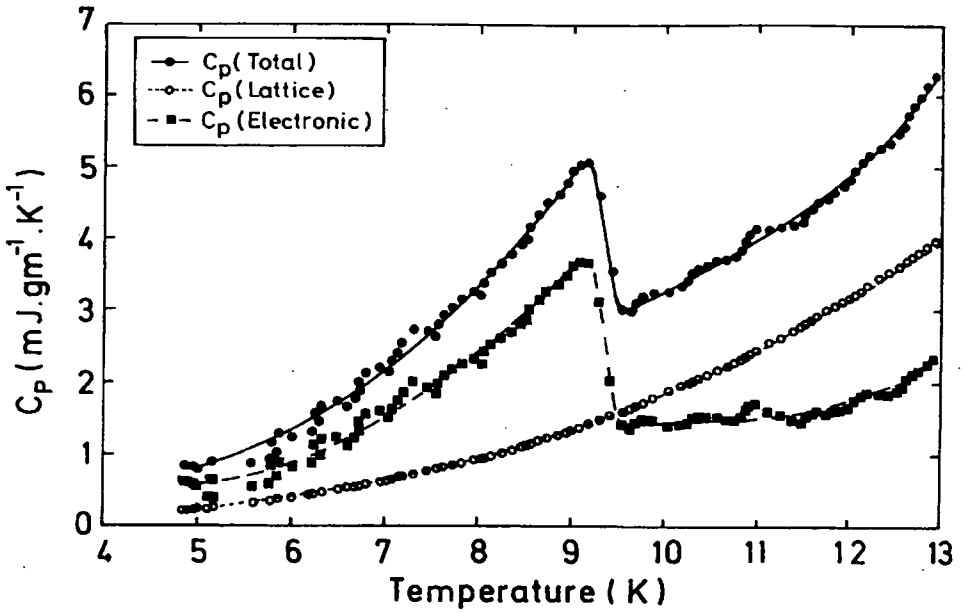

Fig. 6.7: Separation of Electronic and Lattice Specific Heat from the total specific heat. $\gamma = 0.13836$ mJ.gm^{-1}.K^{-2}, and $\beta = 1.835 \times 10^{-3}$ mJ.gm^{-1}.K^{-4} has been found from the 10 T data.(See Text).

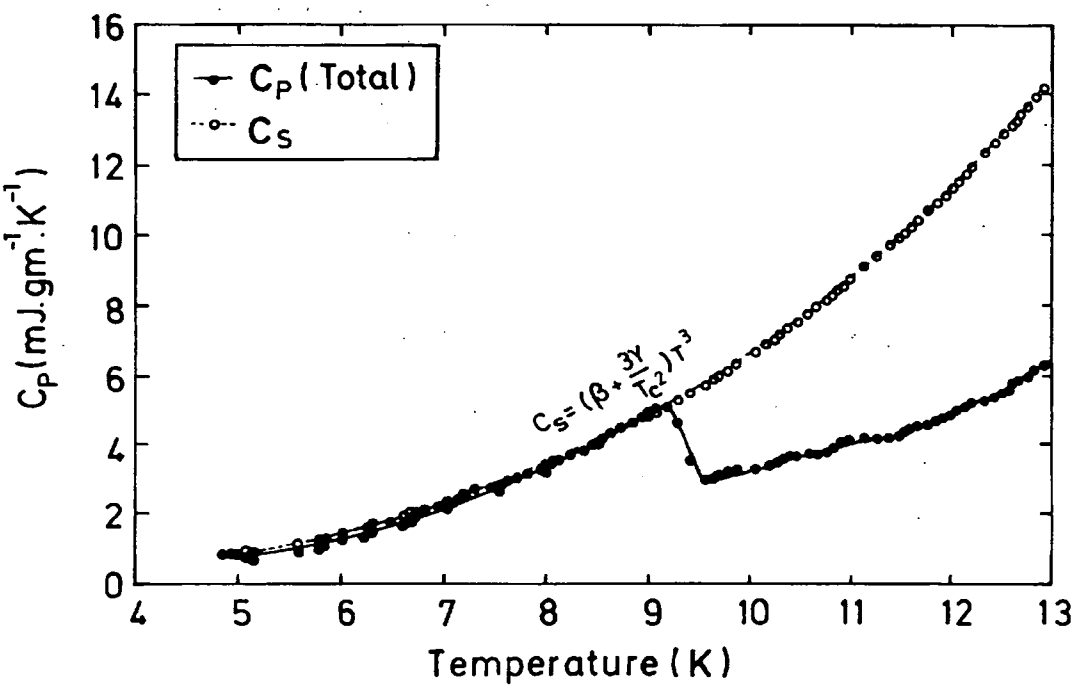

Fig. 6.8: A comparison between C_p and C_S versus Temperature. The validity of the two-fluid model is clear.

Parameter	Calculated Value	Literature Value
$B_{C2}(0)$, (Tesla)	17.27 ± 0.3	18.5*
$B_{C1}(0)$, (Tesla)	0.0459 ± 0.01	0.035**
$B_C(0)$, (Tesla)	0.204 ± 0.02	0.222*
GLAG, κ	50.13 ± 1	49*

Table 6.3. *The data has been taken from the Superconducting Magnets by M.N. Wilson [3]. ** The data has been taken from Applied Superconductivity by E.W. Collings [2].

indication, that NbTi is a strong coupled superconductor came after comparing the jump height ($\Delta C(T_C)/\gamma T_C$) = 2.07, which according to the BCS theory should be 1.43, it instead obeys the Gorter-Casimir relative jump height formula, where $\Delta C(T_C)/\gamma T_C$=2. The BCS gives a relation where the electronic specific heat in the superconducting state C_{es} should be equal to electronic specific heat in the normal state C_{en} at T/Tc = 0.51, while for NbTi, Ces = Cen at T/Tc = 0.63.

The height of the specific heat jump ($\Delta C(T_S)$ is reduced with the application of the magnetic field, and varies as T^3_S (Eq. 2.48, section 2.6.3) within experimental errors. The normalised relative jump height should obey the quadratic relationship giving a straight line, but the results we obtained deviated from this behaviour, which was rather similar to the Maki' [10] for κ=2. Also, the application of the magnetic field tends to increase the specific heat in the superconducting state with an amount of $\gamma H/H_{C2}(0)$. It is clear from **Fig. 6.7** that only electronic specific heat has contributed in the superconducting state and the lattice specific heat remains almost constant obeying T^3 law.

The $B_{C2}(T)$ curve has been calculated using WHH theory for α =1.22 and λ_{so} = 1.5. The WHH curve is shown in **Fig. 6.3.** It can be seen that the WHH curve is higher than the experimental curve. It may be due to the fact that we have calculated $B_{C2}(T)$ for α =1.22 and not for α =1.5 or the PPL is very strong in high fields.

The experimental value of $B_{C2}(0)$ for NbTi is 15 Tesla [3]. It is noted that our calculated values of $B_{C2}(0)$ for NbTi after the different methods are scattered, and higher than this value. This discrepancy may be explained on the basis of paramagnetic limiting. From Eq. 6.8 - 6.10, it is shown that NbTi has a strong paramagnetic limiting

factor in the high fields. It is also concluded on the basis of graphical solution from **Fig. 6.4**, that α = 1.22 and λ_{so} = 1.5. It emerges that, Eq. 2.63 is quite a reasonable approximation which reveals that with the application of higher fields, orbital and paramagnetic effects have to be taken into account while calculating $B_{C2}(T)$.

6.6): Conclusion

The theory developed in chapter 2 has been tested, and was found to be in good agreement with the experimental results. The analysis developed in this chapter is quite suitable for calculating γ, β, and the jump height. The Cp, γ, θ_D, $\Delta C(T)/\gamma T_C$, T_S, B_{C2}, α = 1.5 and λ_{so} = 1.5 are very close to the theoretical, as well as literature values within the experimental errors.

References to Chap. 6

1): Thomas P. Sheahen, in Introduction to High Temperature Superconductivity, Plenum Press, New York, 1994, ISBN 0-306-44793-2. pp.31-35

2): E. W. Collings, in Applied Superconductivity, Metallurgy, and Physics of Titanium Alloys, Vol.1, Plenum Press, New York, 1986, ISBN 0-306-41690-5. pp.ix.

3): Martin N. Wilson, in Superconducting Magnets, Oxford University Press, New York, 1983, reprinted, 1990. ISBN 0-19-854810-9 (pbk). Chap.12.

4). Parks, R. D., in: Superconductivity, Marcel Dekker, Inc. New York, (1969), pp.19-20, 891.

5). Cody, G. D., Phenomena and Theory of Superconductivity, in: Superconducting Magnet Systems, (Edited by H. Brechna), Springer-Verlag, Berlin (1973).

6): Same as ref. 2, pp. 403-404.

7). N.R. Werthamer. E. Helfand and P.C. Hohenberg, Physical Review, 147 (1966) 288.

8). A.M. Clogston, Phys. Rev. Lett. 9 (1962) 266-67.

9). B.S. Ckandrasekhar, App. Phys. Lett. 1 (1962) 7-8.10).

10). Maki, K., Phys. Rev., 139 (1965) A702-A705.

11). Elrod, S.A., J.R. Miller, and L. Dresner, in Advances in Cryogenic Engineering Materials, (Edited by R.P. Reed and A.F. Clark), Vol 28, Plenum Press, New York, 1982.

12). Corsan, J. M, cited as private communication in: Elrod, S.A., J.R. Miller, and L. Dresner, in Advances in Cryogenic Engineering Materials, (Edited by R.P. Reed and A.F. Clark), Vol 28, Plenum Press, New York, 1982.

13). Zbasnik, J. cited as private communication in: Iwasa, Y., C. Weggel, D. B. Montgomery, R. Weggle, and J. R. Hale, J. Appl. Phys. 40 (1969) 2006-09.

CHAPTER 7

Specific Heat Measurements on HIPed and unHIPed $PbMo_6S_8$

7.1: Introduction:

As described earlier in Chapter 1 and 2, Lead Chevrel phase (PMS) has very high $B_{C2}(0)$ and $(dB_{C2}/dT)_{T=Tc}$ values and relatively high T_C compared to other Chevrel phase compounds [1-7]. In order to understand these properties, the knowledge of electronic specific heat C_{el} and phonon contribution C_{ph} is essential. To explain this, we have completed Cp measurements on these materials which are presented here.

We have fabricated PMS with two methods, simple sintering at ambient pressure and a Hot Isostatic Press (HIP) method. Both methods will be described in section 7.2. In section 7.3, the specific heat measurements in high magnetic field using both the heat pulse method and the a.c. technique are been presented. Section 7.4 provides the analysis, and section 7.5 the discussion on these measurements. In section 7.6 the conclusions of this chapter are provided.

7.2: Fabrication of PMS

Two methods were used to fabricate the PMS samples. First, ceramic $PbMo_6S_8$ samples are prepared by a two step reaction procedure. Pure elements, Pb, Mo, and S are used as starting materials. In the beginning, 10 g of starting materials with nominal composition $PbMo_6S_8$ are sealed under vacuum in a pre-cleaned silica tube. The tube is then placed in a tube furnace and annealed at 450^0 C for 4 hours in an Ar atmosphere. The furnace temperature is slowly increased to 650^0 C at a rate of 33^0 $C.h^{-1}$ and held for 8 h. After this heat treatment, the sample is air quenched to room temperature. The reacted intermediate powder is ground thoroughly using a mortar and pestle and is pressed into discs of 10 mm diameter. The discs are again sealed under vacuum in a pre-cleaned silica tube and reacted at 1000^0 C for 44 h in flowing Ar gas to form the $PbMo_6S_8$ phase.

Before performing the hot isostatic pressing treatment on the samples, the sintered ceramic samples are ground into powder and re-pelletised. The pellets are

wrapped with Mo foil (99.95%, 0.25 mm thick), so that $PbMo_6S_8$ powder does not react with the container and are sealed in a stainless tube under vacuum using hot-spot-welding. The hot isostatic pressing treatment is carried out at 2000 bar at 800^0 C for 8 h. The sample is then extracted from the Mo foil and cut. The HIP'ed sample used in the heat pulse measurements was obtained by this method named as 1HIP. In addition, a second HIP'ed sample was obtained named as T3PMS. Better control of oxygen contamination, was achieved by keeping the Mo powder in the Glove box and reducing the Mo in hydrogen-nitrogen to extract oxygen. All other steps were the same as described above. The specific heat of this sample was measured using the a.c. technique.

7.3: Cp Measurements

Cp measurements have been made using two methods. The long duration heat pulse method and the a.c. technique. The experimental results obtained are described below:

7.3.1: Cp Measurements using long duration H. P. Method:

The heat pulse measurements in magnetic field on unHIP'ed $PbMo_6S_8$ and HIP'ed $PbMo_6S_8$ material have been made using the set-up described in chapter 4. The measurements were made in constant magnetic field of 0, 2.5, 5, 7.5, and 10 Tesla. The results are shown in Figs.7.1 and 7.2 for unHIP'ed and 1HIP PMS respectively. The magnitude of Cp/T for the unHIP'ed and 1HIP samples are similar above 15 K. The transition temperature T_C and the specific heat jump for each field is obtained after extrapolating the measured transition in Cp/T to an idealised sharp transition, assuming entropy conservation under the transition curve as has been explained in chapter 5. The same results are tabulated in Tables 7.1 and 7.2 in digitised form.

App.Field (Tesla)	T_{CO}(K) ± 0.2 K	T_{peak}(K) ± 0.2 K	ΔT_C ± 0.2(K)	T_C** ± 0.2 (K)	Jump % ($\Delta C/C_{Tc}$)
0	14.20	12.60	1.60	13.30	15.34
2.5	13.50	12.20	1.30	12.90	12.24
5.0	12.95	12.0	0.95	12.45	11.21
7.5	12.6	11.50	1.10	12.0	10.69
10	11.8	11.25	0.55	11.50	6.44

Table 7.1: The effect of magnetic field on unHIP-ped $PbMo_6S_8$. T_{CO} is the onset temperature where the anomaly starts, T_{peak} is the maximum value in the transition curve, ΔT_C is the difference between the T_{CO} and the T_{peak}. T_C** has been calculated, considering entropy conservation under the curve. The Jump % ($\Delta C/C_{Tc}$) has been calculated on the basis of entropy conservation under the curve and taking the minimum and maximum value of Cp obtained.

App.Field (Tesla)	T_{CO}(K) ± 0.2 K	T_{peak}(K) ± 0.2 K	ΔT_C ± 0.2(K)	T_C** ±0.2 (K)	Jump % ($\Delta C/C_{Tc}$)
0	14.40	13.45	0.95	13.85	11.55
2.5	14.0	13.1	0.90	13.50	8.8
5.0	13.6	12.7	0.90	13.10	8.64
7.5	13.2	12.47	0.73	12.82	8.56
10	12.6	11.85	0.75	12.15	6.41

Table 7.2: The effect of magnetic field on 1HIP $PbMo_6S_8$. T_{CO}, T_{peak}, ΔT_C, T_C** and Jump % ($\Delta C/C_{Tc}$) have been defined in the caption for Table 7.1.

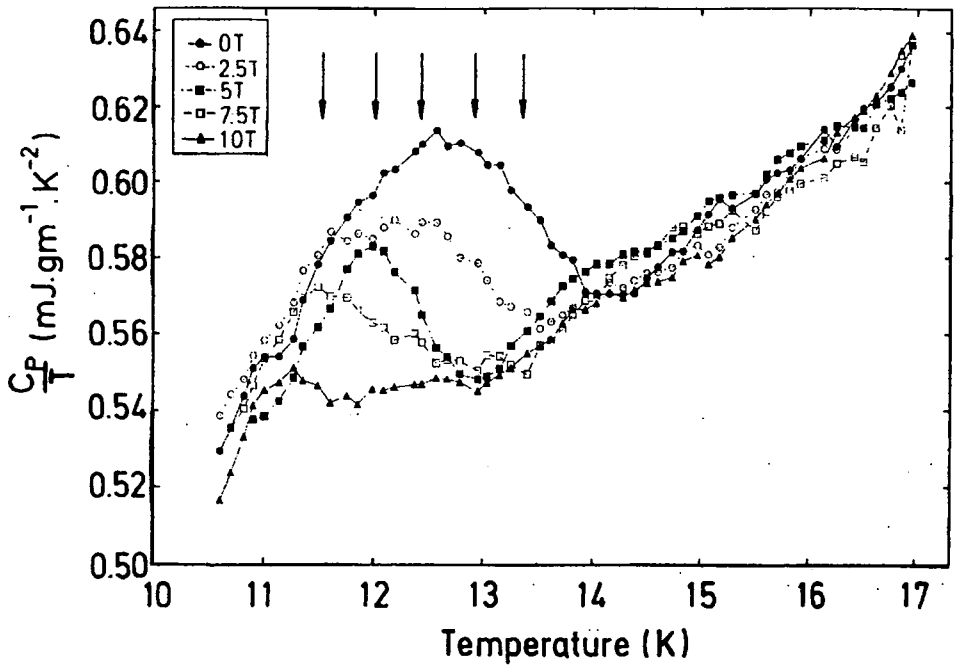

Fig.7.1). Cp /T. as a function of Temperature for unHIP'ed PMS in 0-10 Tesla. (After Heat Pulse Method. The arrows pointed toward the transition temperature Tc for each field.

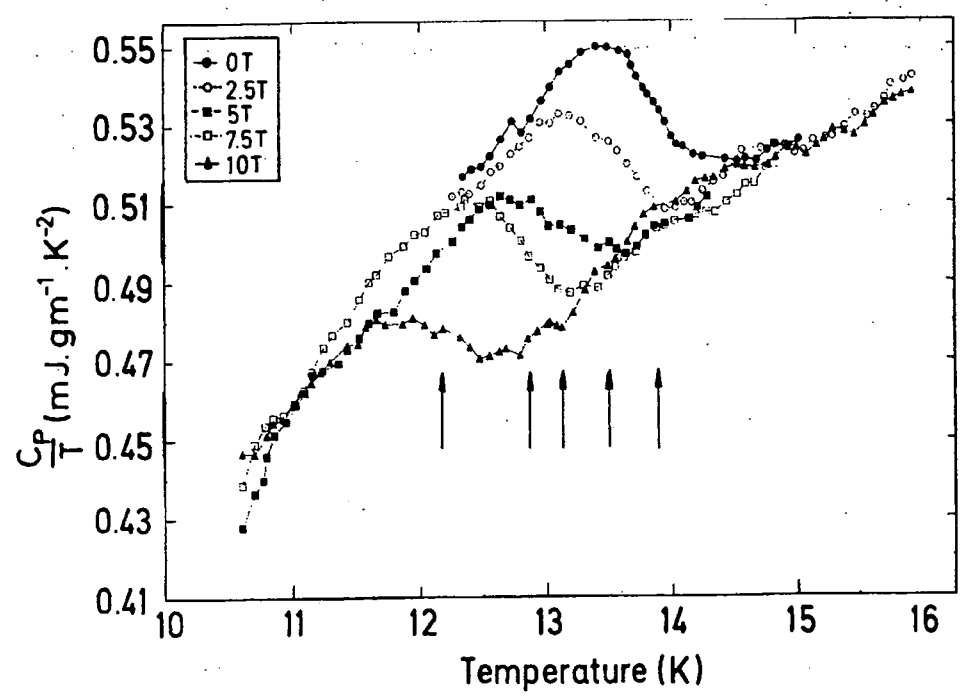

Fig.7.2). Cp /T. as a function of Temperature for 1HIP PMS in 0-10 Tesla. (After Heat Pulse Method). The arrows pointed toward the transition temperature Tc for each field.

7.3.2: Cp Measurements using A.C. Technique:

The a.c. measurements have been made on T3PMS. V^{-1}_{rms} vs. temperature and phase shift vs. temperature in field in the interval of 0, 2.5, 5.0, 7.5, 10.0 and 12.5 T are displayed in Fig. 7.3a and Fig.7.3b respectively. In addition we have plotted V^{-1}_{rms} * T^{-3} vs. T in Fig. 7.3c in order to amplify and clarify the position of the small change in V^{-1}_{rms} from the superconducting phase transition. Because of the large variations in V^{-1}_{rms} and Cp throughout the measured range of temperature, it is not possible to distinguish where the transition (which causes a jump in ΔV^{-1}_{rms} ~4%) occurs. However, the product of V^{-1}_{rms} and T^{-3} is a very weak function of temperature and so because the noise levels are sufficiently low, we can distiguish a discontinuity of ~4%. Hence we can determine the temperature at which the superconducting anomaly occurs in each field. This procedure is repeated in the following chapters to calculate Tc** and $B_{C2}(T)$. Cp and phase shift vs. T at 2.5 T only is plotted in Fig. 7.4. The clear indication of the phase transition comes from the V^{-1}_{rms}* T^{-3} vs. T in Fig. 7.3c as explained above and from the phase shift data explained in Fig.7.4. This is consistent with the Eq. 3.50 and Fig. 5.42 along with Fig. 5.43, where a phase transition is observed in both V^{-1}_{rms} and phase shift together at the same temperature in NbTi. Therefore, with reference to Figs. 5.42 and 5.43, it is appropriate to measure Tc** from the phase shift transition or from the V^{-1}_{rms} * T^{-3} vs. T data. The values of Tc** so obtained are tabulated in Table. 7.3 for each field. However, Cp vs. T, and Cp/T vs. T^2 are also plotted in Figs. 7.5 and 7.6 respectively.

App.Field (Tesla)	T_C**±0.2 (K)
0	14.50
2.5	14.20
5.0	13.90
7.5	13.45
10.0	13.10
12.5	12.65

Table 7.3: The effect of magnetic field on T3PMS HIP'ed material. The T_C** has been measured from the Fig. 7.3c which is consistant with the phase shift data described in Fig. 7.4.

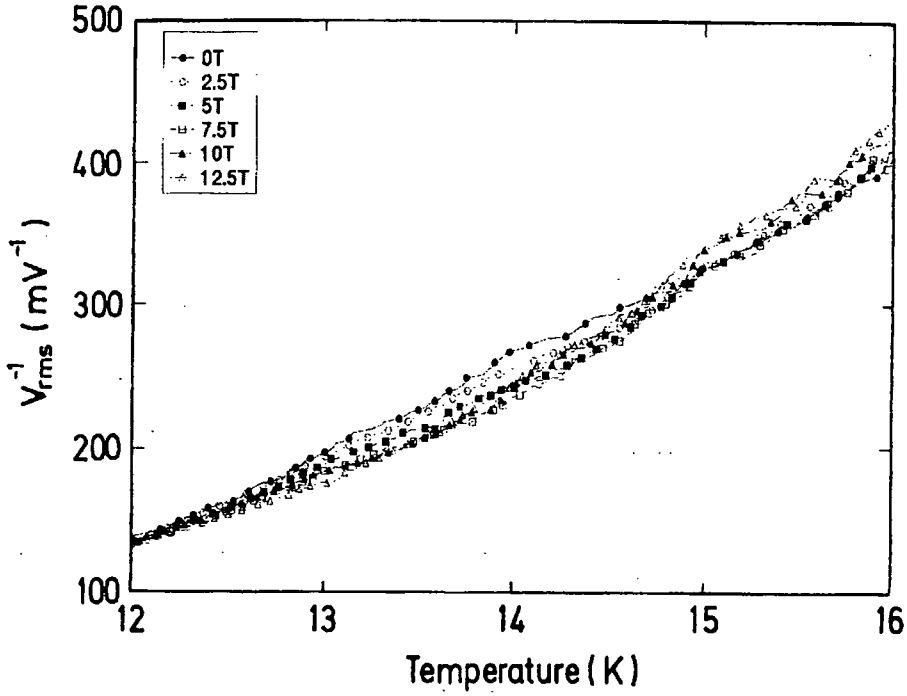

Fig.7.3a). V^{-1}_{rms} (CX) as a function of Temperature for HIPped T3PMS in 0-12.5 Tesla. (After A.C.Technique).

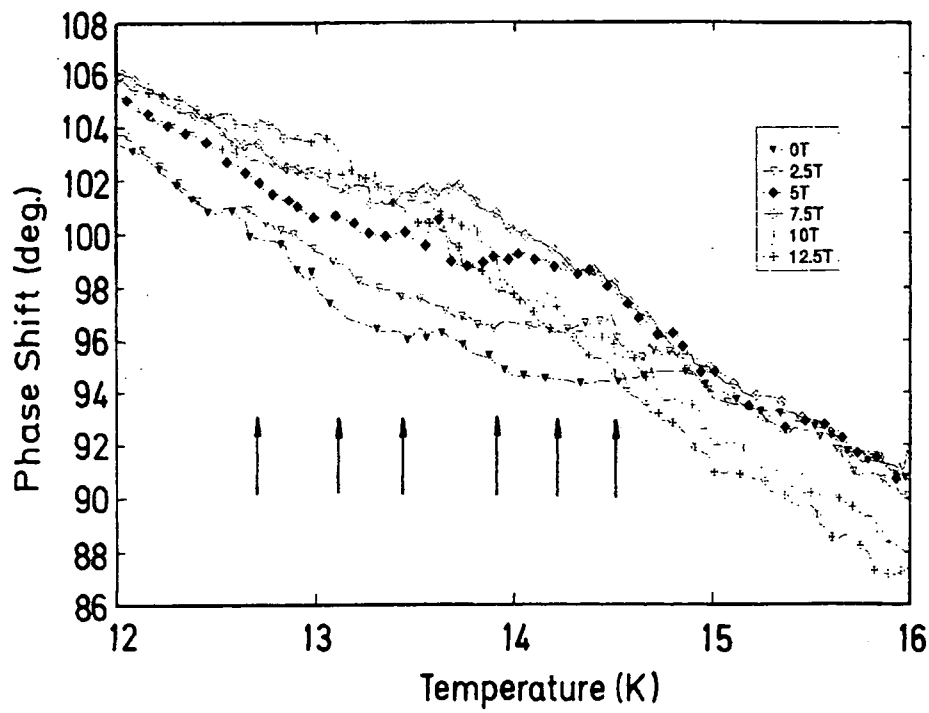

Fig.7.3b). Phase Shift as a function of Temperature for HIPped T3PMS in 0-12.5 Tesla. (After A.C.Technique). The arrows points to the transition temperture Tc after the application of the magnetic field.

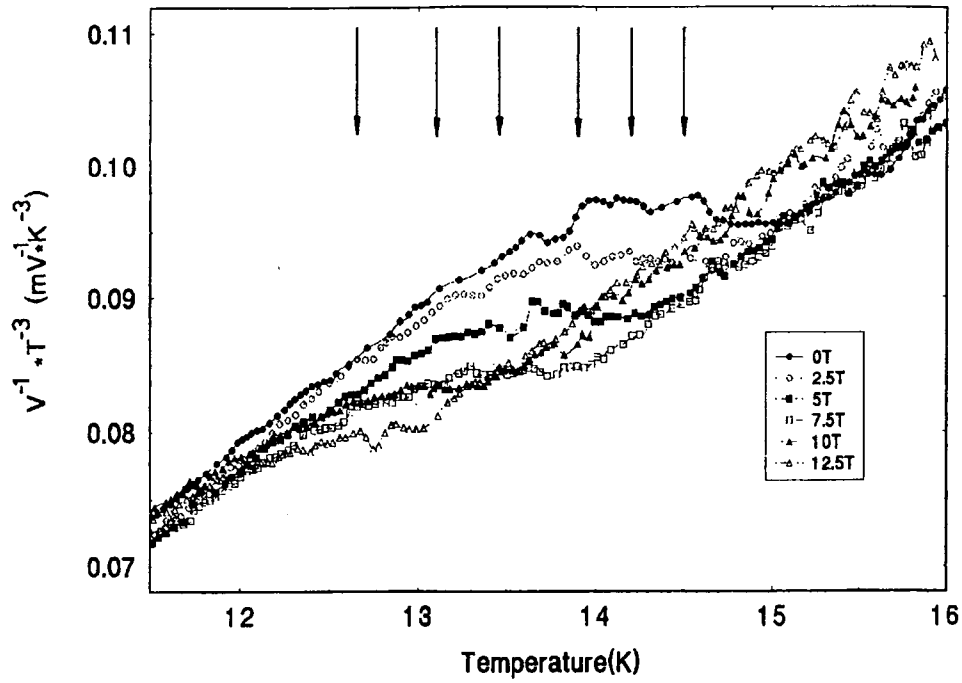

Fig.7.3c). The data of Fig. 7.3a has been replotted, giving V^{-1}rms * T^{-1} vs. T to show the clear evidence in phase transition for HIPped T3PMS in 0-12.5 Tesla. The arrows points to the transition temperture Tc after the application of the magnetic field.

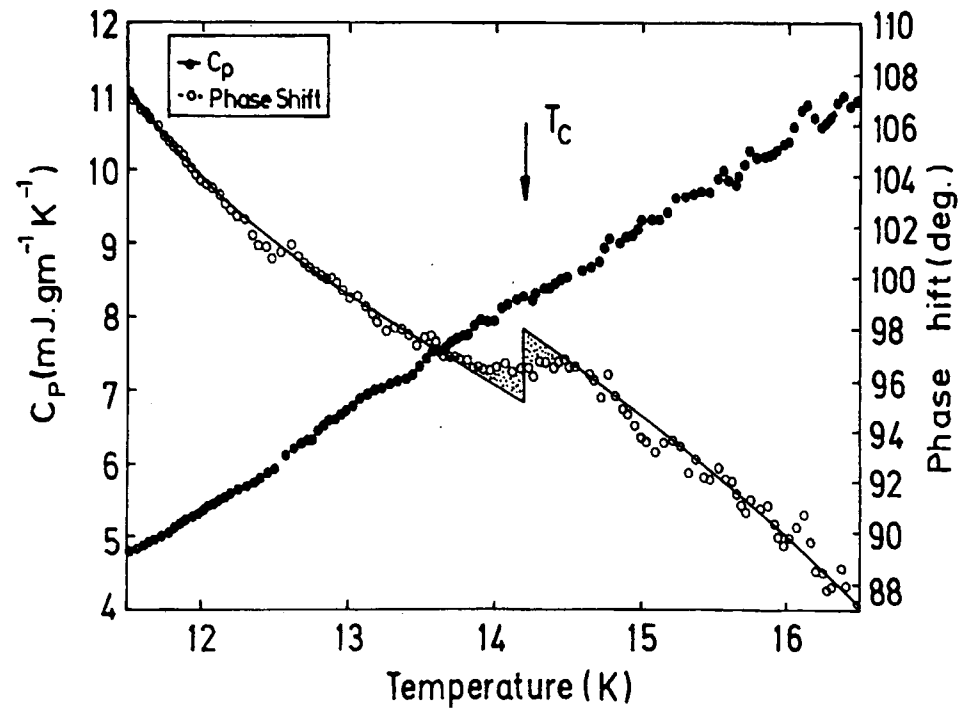

Fig.7.4). Cp and Phase Shift vs. Temperature for HIPped T3PMS in 2.5Tesla. The T_C* is calculated from the phase shift change, instead from the Cp. (It is not accurate when measurnig from Cp vs. T). The arrow points to Tc*.

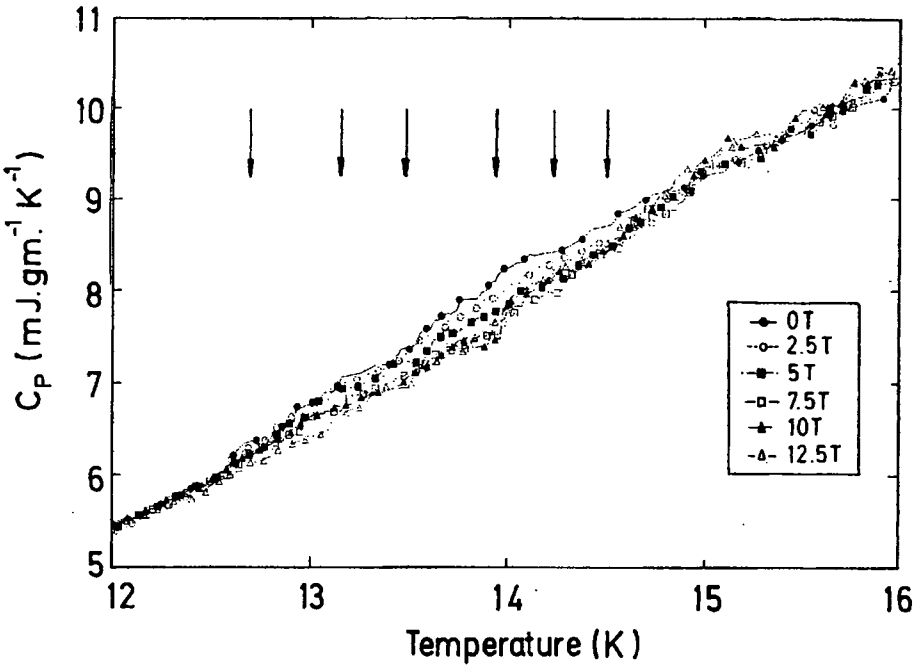

Fig.7.5). Cp as a function of Temperature for HIP'ed T3PMS in 0-12.5 Tesla. (After A.C.Technique). The arrows have been replotted from Figs. 7.3c and 7.4.

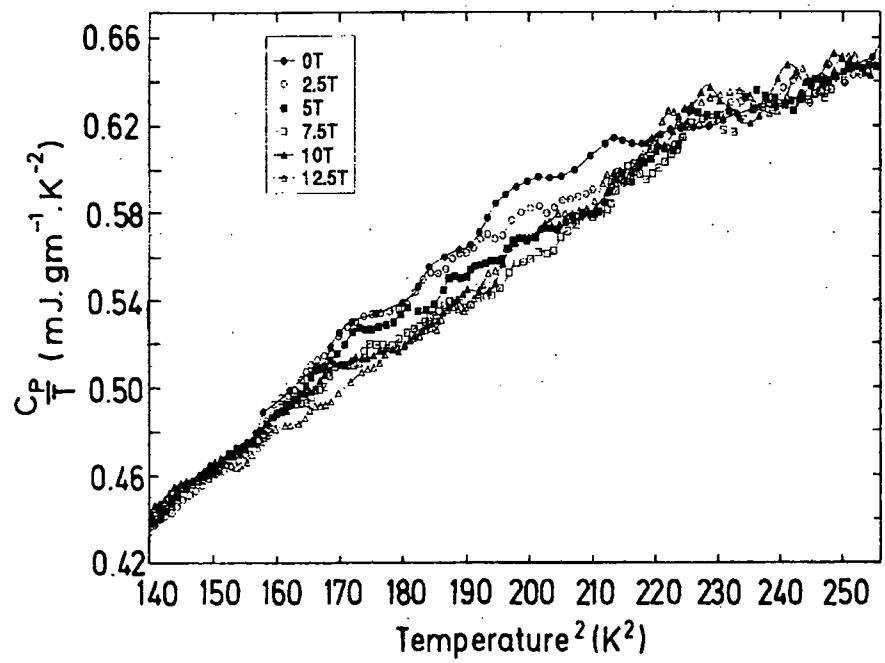

Fig. 7.6). Cp/T vs. T^2 for HIP'ed T3PMS in 0-12.5 Tesla to calculate γ, β. (After A.C. Technique).

7.4: Analysis of the Data

7.4.1: Comparison of Cp/T with the Literature

We have compared the values got in Durham with different experimental set-up with that of the Literature values. The values are calculated at 15 K, assuming 1 mole = 1039 gm of PMS. They are summarised in Table 7.4.

	Cp ($mJ.gm^{-1}.K^{-2}$)
Ref. 9,	≈ 0.5967
Ref. 17,	≈ 0.655
Ref. 14,18	≈ 0.789
Ref. 7	≈ 0.794
unHIP'ed	≈ 0.587±.02
1HIP	≈ 0.523±.02
T3PMS	≈ 0.62±.02

Table: 7.4: Different values of Cp ($mJ.gm^{-1}.K^{-2}$). Literature values are compared with the three samples named as unHIP'ed, 1HIP, and T3PMS measured in Durham.

7.4.2: Estimating γ and θ_D

We have found the values of γ and θ_D using a Debye plot. Since PMS has a high T_C ~ 14 K in the 0-field, this procedure has been applied to the data at 10 T to reduce the T_C**. The values for the γ and θ_D are displayed in Table 7.5. However, the values are far different than the literature values obtained over different temperature ranges. This is due to the fact that PMS has very complex phonon spectrum.

7.4.3: Measuring $B^*_{C2}(0)$:

As has been explained in previous chapters, the application of magnetic field suppresses the specific heat jump. This suppression of the specific heat jump can be used to determine the initial slope $(dB_{C2}/dT)_{T=Tc}$. To measure the slope $(dB_{C2}/dT)_{T=Tc}$ and the upper critical field $B_{C2}(T)$, we have plotted the upper critical $B_{C2}(T)$ as a function of transition temperature Tc in Fig. 7.7.

Material	γ (mJ.mol^{-1}.K^{-2})	$\theta_{D1}=(1944*15/\beta)^{1/3}$	$\theta_{D2}=(1944/\beta)^{1/3}$
un-HIP PMS	443.3	341.6	138.5
HIP-PMS	377.1	339.0	137.5
T3 HIP-PMS	82.4	226.1	91.0
Literature [Kinoshita, 14]	79-125	411	166.7

Table 7.5: Sommerfeld constant γ and Debye temperature θ_D have been calculated using the simple analysis using the straight line fit to Cp/T vs. T^2 in the normal state. θ_{D1} and θ_{D2} has been calculated using the formula $\theta_{D1}=(1944\times R/\beta)^{1/3}$[15], R represents the no. of atoms in the unit cell of PMS, and $\theta_{D2}=(1944/\beta)^{1/3}$, β is the slope in a Debye plot.

Material	T_C**±0.2 (K)	dB_{C2}/dT± 0.2 (T/K)	$B^*_{C2}(0)$± 5 (T)
PMS unHIP'ed	13.3	-5.88	54.19
PMS HIP'ed	13.85	-6.67	64
T3PMS HIP'ed	14.5	-6.67	67

Table 7.6: T_C, $(dB_{C2}/dT)_{T=Tc}$, and $B^*_{C2}(0)$ for the Chevrel phase PMS samples, fabricated without using Hot Isostatic Press and after using Hot Isostatic Press. $B_{C2}(0)$ has been calculated using WHH theory [8].

It is shown in chapter 2, that paramagnetic limit term is important in high fields and well below T_C, while it disappears in the limit $T \to T_C$. In such case we have [see section 2.6],

$$\left(\frac{dB_{C2}(T)}{dT}\right)_{T=T_c} = \left(\frac{dB^*_{C2}}{dT}\right)_{T=T_c} \qquad (7.1)$$

We find a slope of -5.88 T/K for the unHIP'ed PMS, -6.667 T/K for the 1HIP PMS and same -6.667 for the T3PMS HIP'ed sample. These are tabulated in Table 7.6.

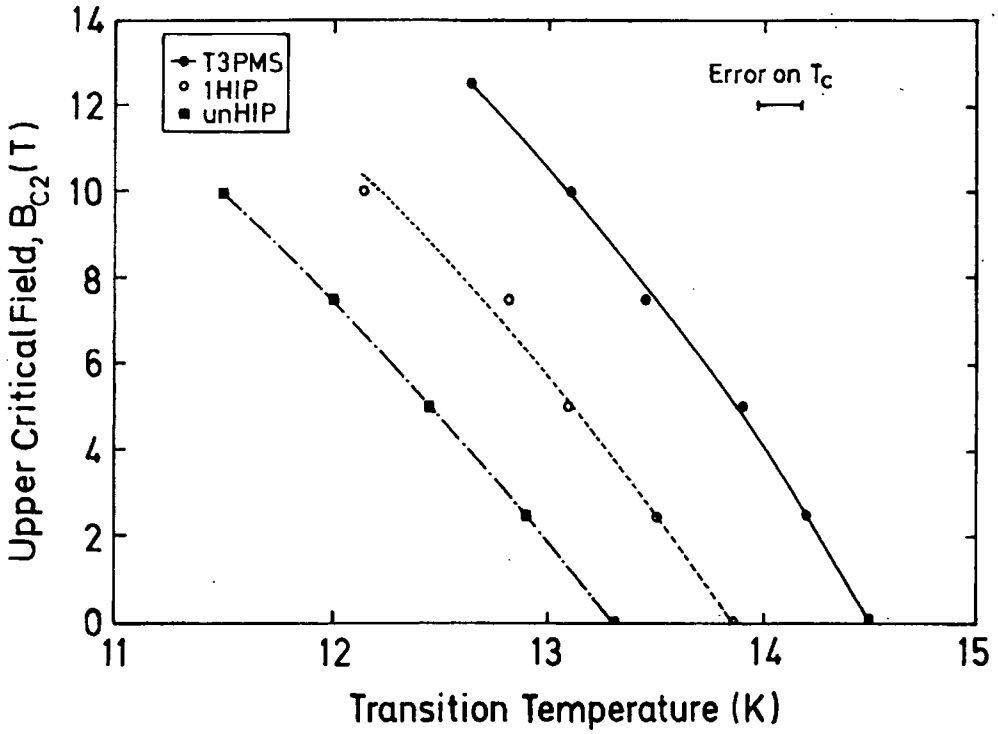

Fig.7.7). Upper Critical field $B_{c2}(T)$ as a function of Transition Temperature Tc for three samples of PMS, fabricated without using HIP and with HIP process.

The WHH theory [8] has been used to calculate $B^*_{C2}(0)$ with the aid of Eq. 2.63, considering no paramagnetic limit as;

$$B^*_{C2}(0) = -A T_C \left(\frac{dB_{C2}}{dT}\right)_{T=T_c} \qquad (7.2)$$

where A has values of 0.693 for the dirty limit superconductors and 0.726 for the clean limit superconductors [2,9-10]. As PMS is a type II superconductor with a very high GL-parameter $\kappa \sim 130$ [11], $\xi_{GL} \approx 30$ Å, $\xi_0 = \xi_{BCS} \approx 48$ Å, and mean free path $\ell \approx 23$ Å, [6,12] it can be considered as a dirty limit type II superconductor. Using the dirty limit in Eq.7.2, we find a $B^*_{C2}(0)$ of 54.19±5 Tesla for the unHIP'ed PMS and a $B^*_{C2}(0)$ of 64 ± 5 Tesla for the 1HIP PMS.

The same analysis described above has been repeated for T3PMS sample. The slope $(dB_{C2}/dT)_{T=Tc}$ for this sample was found to be -6.667 T/K. The $B^*_{C2}(0)$ has been calculated using Eq. 7.1 and found to be 67± 5 T. The T_C and $B^*_{C2}(0)$ of T3PMS sample are probably higher than the first 1HIP PMS sample. It is probably due to less oxygen contamination during the fabrication in the HIP process. The values we got

for T_C, $(dB_{C2}/dT)_{T=Tc}$, and $B^*_{C2}(0)$ are close to the literature values [1-7]. These all values are tabulated in Table 7.6.

7.4.4: Measuring Maki parameter α:

The Maki parameter α [13] is the measure of the paramagnetic limit in any material. A greater value of α, leads to strong paramagnetic limiting. It can be calculated by following ways, (described in chapter 2 and 6).

1). From the initial slope [4,6,12] as,

$$\alpha = -0.528 \times \left(\frac{dB_{C2}}{dT} \right)_{T=T_c} \qquad (7.3)$$

2). From the ratio of orbital critical field $B^*_{C2}(0)$ and paramagnetically limited upper critical field B_{P0}, Eq. 2.52, (Clogstan and Chandrashekher limit) [15,16] as;

$$\alpha = \sqrt{2} \frac{B^*_{C2}}{B_{P0}} \qquad (7.4)$$

From Eqs. 7.3 and 7.4 we find the average value of α as; 3.1±0.03, 3.53±0.03, and 3.53±0.04 for unHIP'ed, 1HIP and T3HIP PMS samples respectively.

3). From the normal state resistivity ρ_n (Ω-m) and volumetric specific heat coefficient γ_v ($J.m^{-3}.K^{-2}$), using Eq. 2.53 as;

$$\alpha = 2.35 \times 10^3 \, \gamma_v \rho_n \qquad (7.5)$$

We have taken the values of γ_v = 640 $J.m^{-3}.K^{-2}$ and ρ_n = 2.2 μΩ-m from the literature, Fischer, 1978, [4] and found α to be 3.308 with the Eq. 7.5. All values of α calculated with different methods for different samples are summarised in Table 7.7-7.8.

Material ⇉	unHIP'ed±0.03	1HIP±0.03	T3PMS±0.04
α, after Eq. 7.3	3.11	3.52	3.52
α, after Eq. 7.4	3.13	3.55	3.55
α, after Eq. 7.5	3.31	-	-

Table 7.7; Illustrating the calculation of Maki's parameter α after 3 different ways for unHIP'ed, 1HIP and T3PMS samples.

Material	α (Maki parameter)	λ_{SO}	$\tau_{SO\times(10^{-14})}$
PMS unHIP'ed	3.10±0.03	2.77	4.4
1HIP PMS	3.52±0.03	3.56	3.29
T3PMS HIP'ed	3.52±0.03	3.56	3.14

Table 7.8. α, (Maki paramagnetic limitation parameter) defined by Eq.7.3 & 7.4; λ_{SO}, spin-orbit coupling parameter and τ_{SO}, the spin-orbit scattering relaxation time has been calculated using WHH theory [8].

7.4.5: Measuring Spin-orbit scattering parameter λ_{SO} and τ_{SO}

Spin orbit scattering parameter λ_{SO} can be measured using Eq. 2.55 and 2.57. We have measured λ_{SO} using Eq. 2.57 as;

$$B_{C2}^*(0) = 1.33 \sqrt{\lambda_{SO}}\, B_{P0} \qquad (7.6)$$

and found to be λ_{SO}=2.77, 3.56, and 3.56 for unHIP'ed, 1HIP and T3PMS respectivly. These values are summarised in Table 7.8.

Similarly the Spin-orbit scattering relaxation time τ_{SO}, has been calculated using Eq.2.55 as;

$$\lambda_{SO} = 2\hbar / 3\pi k_B T_C \tau_{SO} \qquad (7.7)$$

The values of τ_{SO} for three samples named unHIP'ed, 1HIP and T3PMS are shown in Table 7.8.

7.4.6: Jump Height

It can be seen from the Fig. 7.1 and 7.2 for unHIP'ed and 1HIP samples respectively that the % jump height ($\Delta C/C_{Tc}$) is reduced with the application of the field. It is very difficult to measure specific heat jump height in the third sample, T3PMS due to reasons explained later in section 7.5. We have compared the % jump height of unHIP'ed and 1HIP PMS with a PMS sample fabricated at 1460 ^{0}C -1600 ^{0}C and hot pressed at 1200 ^{0}C by Cors et. al. [1,2]. The results obtained are tabulated in Table 7.9.

Applied Field (T)	unHIP'ed	1HIP	Cors et.al. [1,2]
0	15.34	11.55	20.93
2.5	12.24	8.8	
5	11.21	8.64	
6			16.87
7.5	10.69	8.56	
8			14.97
10	6.44	6.41	13.42

Table 7.9: The % jump height of unHIP'ed and 1HIP PMS samples are compared with Literature [1,2].

7.5: Discussion:

The unHIP'ed sample obtained after the simple sintering method, is inhomogeneous, has low density, and poor connectivity between the grains which badly affects the transport properties of this material. To get rid of all these problem, the Hot Isostatic Press (HIP) method was used.

The Durham values of Cp/T at 15 K are compared with the literature values as can be seen in Table 7.4. It is noted that the literature values of Cp/T are scattered from 0.59 to 0.79 $mJ.gm^{-1}.K^{-2}$. The Durham results agree with the literature values within the accuracy of the experimental set-up.

As described in the literature Bader et. al. [17], and Alekseevskii, et. al [18]; it is almost impossible to use the simple Cp/T vs. T^2 analysis for PMS to get γ and θ_D, since above its high T_C value, the T^3 behaviour is not observed. PMS has a very complicated phonon spectrum. Equally, applying a strong magnetic field will decrease T_C** by only a few Kelvin because of the high $(dB_{C2}/dT)_{T=Tc}$ of this material. It is clear some new technique should be used to explain the data.

A more complex analysis has been developed which describes the lattice specific heat, C_L, in terms of a sum of three independent terms [18];

$$C_L = A_1C_{L1} + A_2C_{L2} + A_3C_{L3} \qquad (7.8)$$

where, A_1 ~1, A_2 =1, and A_3 =13, are the appropriate weight factors for the ternary

molybdenum sulfides and can be found during the analysis. C_{L1}, is from the very low frequency modes due to the weakly coupled, large atomic mass, Pb atoms in the crystal structure, C_{L2}, represents the low frequency modes in the cluster, while the term C_{L3}, represents the higher frequency intercluster and interacluster modes. We have not proceeded with this analysis because of the limited temperature range of our data.

As the slope is very high, consequently $B_{C2}^*(0)$ is very high. At present, it is difficult to produce a field beyond 33 T [Nijmen] using the high field magnet laboratories. To compare the experimental $B_{C2}(T)$ with that of the theoretical value, WHH [8] has given a very useful relation considering spin-orbit scattering parameter λ_{SO}, which gives some idea about the strength of the spin-orbit scattring, (see Chapter 2). λ_{SO} minimises the paramagnetic effect, and reduces the effect of pair breaking. It implies that spin-orbit scattering overcomes the effect of pair breaking by the paramagnetic effect and therefore enhances the $B_{C2}(0)$ limit and only the interaction of the external field with the orbits will destroy the superconductivity in these materials, [4, 5]. We have taken α =3 in general to compare the value with the literature [4,5] and find out the value of λ_{SO} graphically. After determining α, λ_{SO} can be determined using Eq. 2.55 and 2.57.

If one compares the spin-orbit relaxation time parameter τ_{SO} of three PMS samples, it revealed that the value of τ_{SO} is decreasing after HIP process, which is the case, as after HIP process, the material becomes more dense.

The values of $B_{C2}(T)$ calculated using methods other than Cp [19] have been compared in Fig.7.8. It can be seen that the values obtained from the reversible V.S.M. measurements [11] are very close to the Cp measurements on the same sample 1HIP. However, the irreversibility line is far below that of $B_{C2}(T)$ line [11]. The data for other samples show the similar trend.

The reduced upper critical field $b_{c2}=0.281B_{C2}(T)/B^*_{C2}(0)$ calculated [4,6] using Eq. 2.59 vs. reduced critical temperature $t=T/T_C$ for fixed value of α =3 and different values of λ_{SO} has been plotted in Fig. 7.9. In Fig. 7.10, the area close to the transition temperature is blown up for α =3, and different values of λ_{SO} and is compared with that of reduced upper critical field of three samples. It is clear from the Fig. 7.10 that the value of λ_{SO} is either greater than 50 or infinity. As has been explained in section

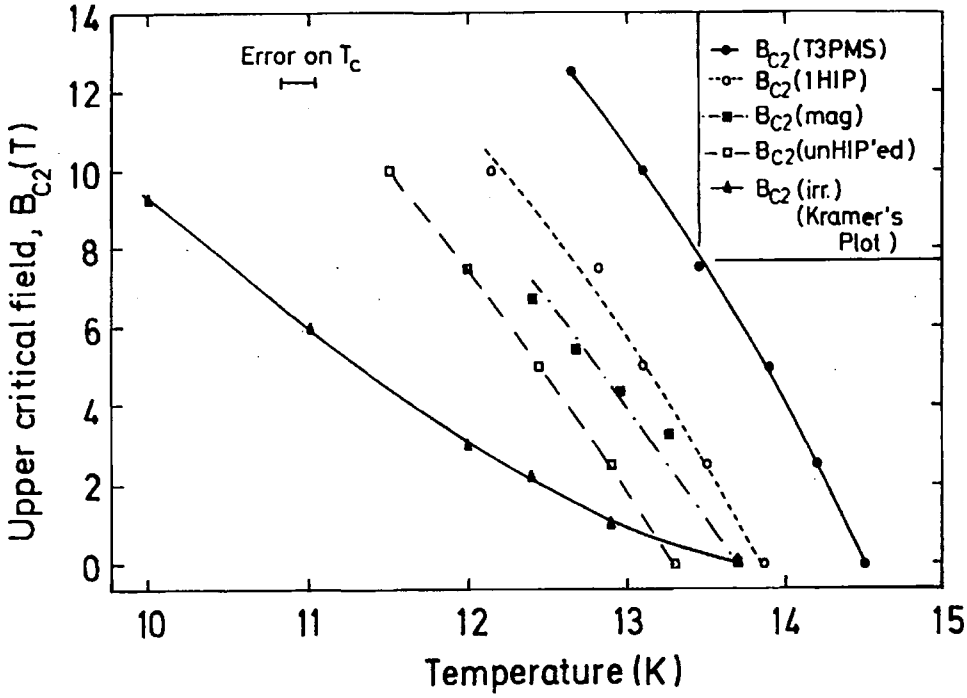

Fig.7.8). Upper Critical field $B_{C2}(T)$ as a function of Temperature calculated using different methods. $B_{C2}(T)$(mag), and B_{C2}(irr) obtained from magnetic measurements on 1HIP [11]. Other data from specific heat measurements of this work.

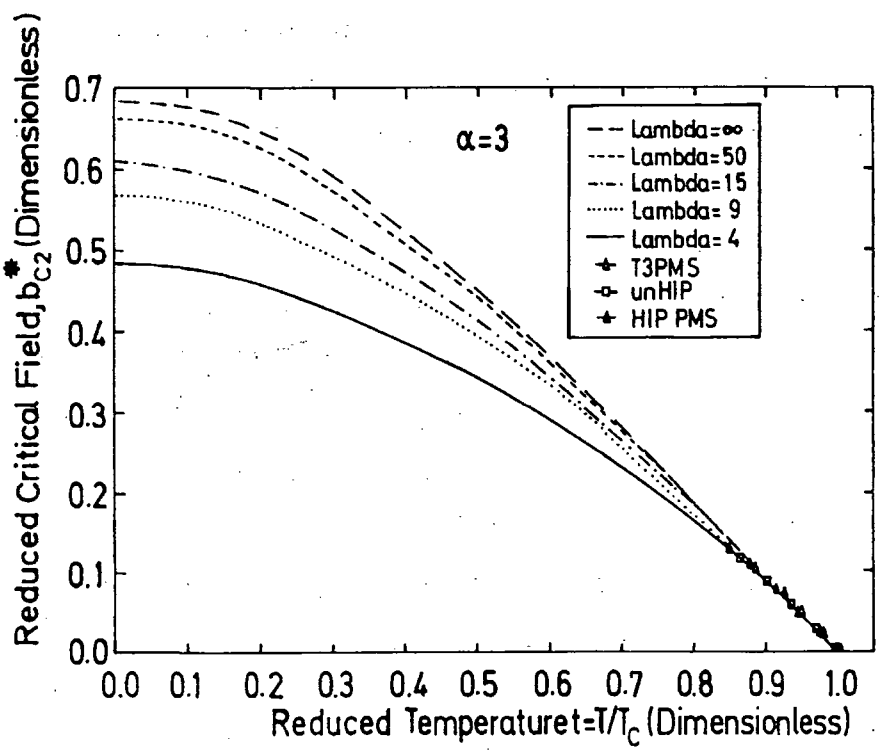

Fig.7.9). Reduced Upper Critical field $b^*_{C2}(t)$ versus reduced transition temperature t for different values of λ_{so} compared with the experimental values obtained after unHIP'ed, 1HIP and T3PMS samples.

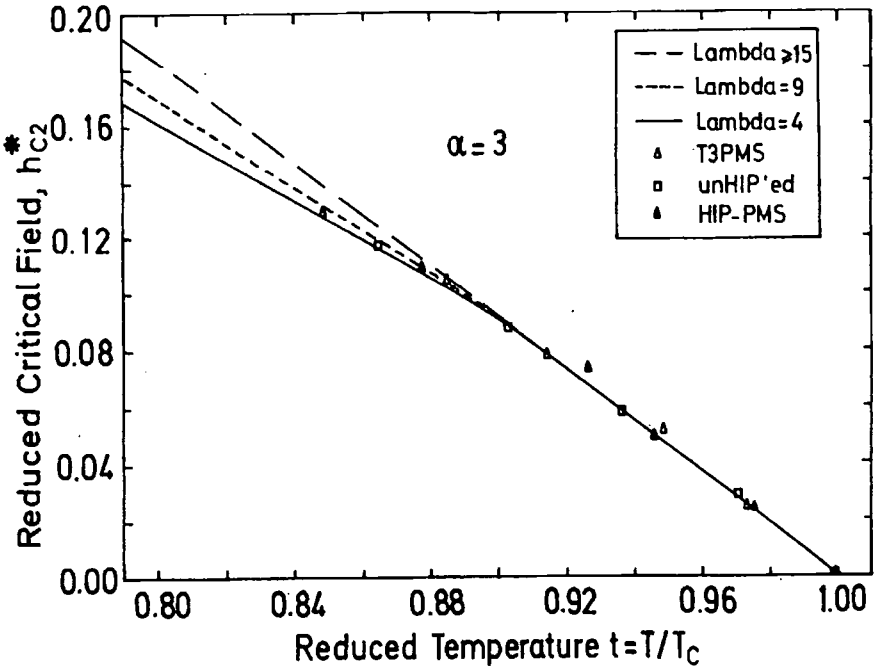

Fig.7.10). The data of Fig. 7.9 is blown up close the Tc values to compare with experimental values obtained for unHIP'ed, 1HIP and T3PMS samples.

2.8, the role of λ_{so} is to reduce the paramagnetic effect and enhanced the upper critical field, reaching toward the theoretical limit. The value of α can be determined from the slope as, $-0.528(dB_{c2}/dT)_{Tc}$ and thus one can determine the value of λ_{so} from the temperature dependence of $B_{c2}(T)$. However, the values of λ_{so} so obtained are far higher. It implies that the value of upper critical field obtained is close to the orbital critical field [4,6]. These higher values of λ_{so} may be due to the very simple assumptions have been made, ([6],pp.68) e.g. weak-coupling, spherical Fermi surface, no exchange effects in the electron and one conduction band.

The T_c and $B_{c2}(0)$ are slightly improved for the HIP'ed samples over the unHIP'ed sample. Indeed the critical current density has been improved almost 20 times of the unHIPped material [11,20], which is a major achievement of the fabrication technique using Hot Isostatic Press.

The height of the specific heat jump is not as high as that quoted in the literature [1-2]. Since specific heat measurements are bulk volumetric measurements, we suggest the large width (~ 1 K) of the transition or rounded calorimetric transition may be due to one of the possibilities;

1). There is a distribution in T_C throughout the sample (inhomogeneity).

2). There are internal cracks in the sample which have led to temperature gradiants across the sample.

3). The thermal conductivity of these samples is so low that there is a temperature gradient across the sample.

Using the two fluid model [21-22], the normalised relative jump height should obey the quadratic relationship giving a straight line, but the results we obtained are below the straight line. Even the literature [1,2] values are below that of the straight line which can be seen in Fig. 7.11, where we have plotted reduced relative jump height in specific heat at different fields as a function of the square of the reduced transition temperature t_s, showing the invalidity of the two fluid model for the PMS material.

Complementary magnetic and transport measurements have been completed on the PMS samples [11,20]. An irreversibility line B_{IRR} was found significantly

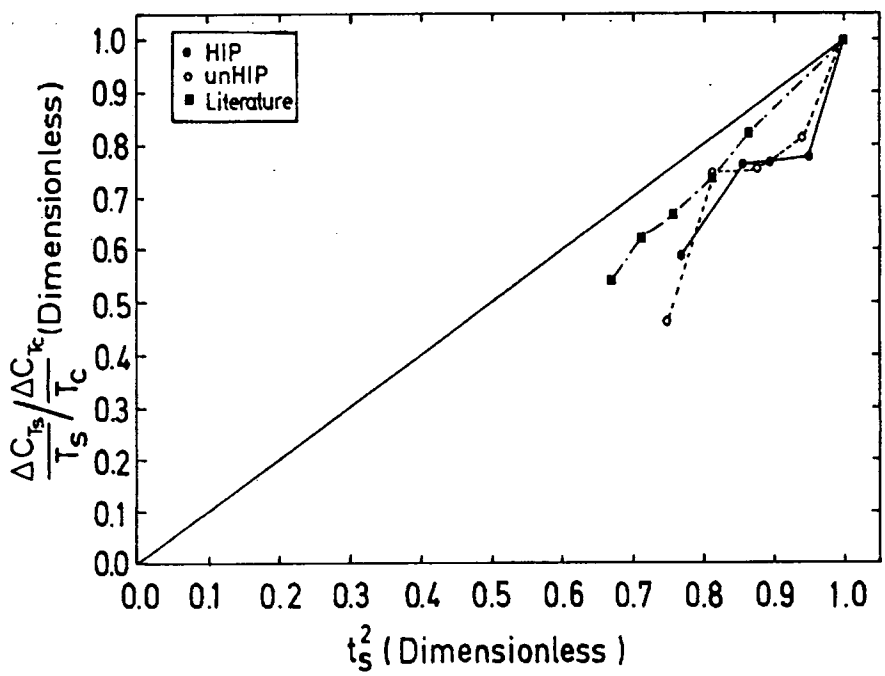

Fig.7.11). Reduced relative jump height of the specific heat jump at the transition temperatures T_S has been plotted against the square of the reduced transition temperature, $ts^2 = (T_S / T_C)^2$. The straight line represents the quadratic relationship.

below $B_{C2}(T)$. A marked difference between B_{IRR} and $B_{C2}(T)$ is a well established result in high T_C-oxide superconductors. The magnetic measurements have shown a typically twenty-fold increase in the critical current density of the HIP'ed PMS sample over the unHIP'ed PMS sample. The data described above demonstrate that this improvement cannot be attributed to changes in the bulk superconducting critical parameters. Better connectivity between the grains and improved grain boundary structure are more probable explanations.

7.6: Conclusion:

We found that after HIP, the Tc has been increased about 0.5 K while reducing oxygen contamination during the fabrication process has increased another of 0.5 K in Tc. The slope has been enhanced to about 13 % and consequently, $B_{C2}(0)$ has been increased to about 65 T, about 20 % higher after the HIP process. The HIP process increases the T_C probably because of the improved homogeniety. The higher values of $\lambda_{so}>3$ leads to screening the effect of paramagnetic limitation by spin-orbit scattering mechanism. The rounded form of the specific heat jump pointed the possibility of the T_C distribution in the sample.

References to Chapter 7:

1). Cors, J., D. Cattani, M. Decroux, A., Stettler and Φ. Fischer, Physica B., 165 &166 (1990) 1521-22.

2). Cors, J., Thesis. No. 2456, University of Geneva (1990).

3). Φ. Fischer, Ferromagnetic Materials, Vol. 5, Edited by K. H. J. Buschow and E. P. Wohlfarth, Elsevier Science Publishers B.V., 1990. pp.465-576.

4). Φ. Fischer, Appl. Phys. 16 (1978) 1 - 28.

5). Foner, S., in Superconductivity in d- and f- Band Metals. Edited by D.H. Douglass, Plenum Press. New York and London (1976), pp.161-174.

6). M. Decroux, and Φ. Fischer, in Superconductivity in Ternary Compounds II, 1982, Topics in Current Physics 34, eds. M.B. Maple and Φ. Fischer (Springer, Berlin) p.57.

7). Decroux, M., P. Selvam, J.Cors, B. Seeber, Φ. Fischer, R. Chevrel, P. Rabiller, and M. Sergent, IEEE Trans. on Appl. Supercond., 3 (1993) 1502-09.

8) N.R. Werthamer. E. Helfand and P.C. Hohenberg, Physical Review, 147 (1966) 288.

9). van der Meulen, H. P., J.A.A.J. Perenboom, T.T.J.M. Berendschot, J. Cors, M. Decroux, and Φ. Fischer, Physica B., 211 (1995) 269-271.

10). Selvam, P., D. Cattani, J.Cors, M. Decroux, A. Junod, Ph. Niedermann, S. Ritter, Φ. Fischer, P. Rabiller, and R. Chevrel, J. Appl. Phys. 72 (1992) 4232-39.

11). Zheng D.N., H. D. Ramsbottom, amd D.P. Hampshire, Phys. Rev. B, 1995.11).

12). Woollam, J.A., S.A. Alterovitz, and H.-L. Luo, in Superconductivity in Ternary Compounds I, 1982, Topics in Current Physics 32, eds. Φ. Fischer M.B. Maple (Springer, Berlin) p.161.

13). Maki, K., Phys. Rev., 139 (1965) A702-A705.

14). Kinoshita, K., Phase Transition, 23 (1990) 73-250. (Properties of Superconducting materials I).

15). A.M. Clogston, Phys. Rev. Lett. 9 (1962) 266-67.

16). B.S. Ckandrasekhar, App. Phys. Lett. 1 (1962) 7-8.

17). Bader, S.D., G. S. Knapp, S. K. Sinha, P. Schweiss, and B. Renker; Phys. Rew. Lett. 37, (1976) 344-48.

18). Alekseevskii, N. E., G. Wolf, C. Hohlfeld, and N. M. Dobrovolskii; J. Low Temp. Phys. 40 (1980) 479-93.

19). S.Ali, H. D. Ramsbottom, Zheng D.N., and D.P. Hampshire, in Applied Superconductivity 1995, Proceedings of EUCAS 1995, Edinburgh, Scotland, 3-6 July 1995, edited by D. Dew-Hughes, IOP conference Series No.148.

20). Hamid, H.A., D. N. Zheng, and D .P. Hampshire, in Applied Superconductivity 1995, Proceedings of EUCAS 1995, Edinburgh, Scotland, 3-6 July 1995, edited by D. Dew-Hughes, IOP conference Series No.148.

21). Elrod, S.A., J.R. Miller, and L. Dresner, in Advances in Cryogenic Engineering Materials, (Edited by R.P. Reed and A.F. Clark), Vol 28, Plenum Press, New York, 1982.

22): E. W. Collings, in Applied Superconductivity, Metallurgy, and Physics of Titanium Alloys, Vol.1, Plenum Press, New York, 1986, ISBN 0-306-41690-5.

CHAPTER 8

Specific Heat of High Gd-doped $Pb_{1-x}Gd_xMo_6S_8$

8.1. Introduction

It was discovered by Fischer et.al [1-2] that after doping Gadolinium, (Gd) in the $PbMo_6S_8$ (PMS) material this enhanced, the T_C (≈14.3 K), dB_{C2}/dT (≈6T/K) and $B_{C2}(0)$ (≈60 T). We have chosen to investigate the effect of the high doping of Gd (low doping will be discussed in chapter 9) systematically in the $Pb_{1-x}Gd_xMo_6S_8$ system. Where x = 0, 0.1, 0.2, and 0.3 represents the nominal concentration of the Gd. The stoichiometry subsequently is always nominal.

This Chapter consists of six sections. Section 8.2 describes the sample fabrication. Section 8.3 is devoted to the experimental results obtained using the experimental set-up described in chapter 5. The analysis of the above data has been provided in section 8.4. Section 8.5 discusses the results and section 8.5 concludes the chapter.

8.2: Sample Fabrication

We have completed the specific heat measurements on a series of bulk Gd-doped PMS samples, fabricated with the simple sintered method at ambient pressure, and fabricated at a pressure of $2x10^8$ $N.m^{-2}$ (2000 bar) using a Hot Isostatic Press (HIP), described in Chapter 7 with a more detailed method. These samples were pressed in the glove box under Argon. To extract Oxygen from the Mo, the powder was reduced in flowing hydrogen gas. Thereafter, the Mo was kept continuously in the glove box to reduce contamination. The volumetrically averaged upper critical field $B_{C2}(T)$ has been determined as a function of temperature for these materials.

8.3. The experimental Results

8.3.1. Gd=0 ($PbMo_6S_8$)

To investigate the effect of a magnetic field on different concentrations of Gd, in $PbMo_6S_8$, a sample of mass, 0.17196 gm, with no doping of Gd was fabricated using the Hot Isostatic Process (HIP) described above and in chapter 7. The magnetic

field was applied at intervals of 0, 2.5, 5, 7.5, 10, and 12.5 Tesla. The graphical form of V^{-1}_{rms} vs. T, phase shift vs. T and $V^{-1}_{rms} * T^{-3}$ vs. T are shown in Figs. 8.1a, 8.1b and 8.1c respectively.

To calculate transition temperature T_C, alongwith Fig. 8.1b and 8.1c, we have plotted Cp vs. T and Cp/T vs. T for Gd-0 sample as shown in Figs. 8.2 and 8.3 respectively. The transition temperature Tc, has been calculated from the $V^{-1}_{rms} * T^{-3}$ vs.T and the phase shift data in Figs. 8.1b and 8.1c respectively as has been explained in section 7.3.2. The arrows in the Figs. are situated at the phase transition. In Table 8.1 we have shown the effect of magnetic field on the transition temperature T_C for Gd-0.

Applied Field (T)	Transition Temp. T_C*±0.2 (K)
0	14.45
2.5	14.17
5.0	13.65
7.5	13.25
10	12.65
12.5	12.30

Table: 8.1. The effect of applied magnetic field B, on the transition temperature T_C of $PbMo_6S_8$. T_C*; The T_C* has been calculated after taking area under the curve to be equal on both sides when extrapolating to the sharp transition in Figs. 8.1b, 8.1c and 8.3.

8.3.2. Gd=0.1 ($Pb_{0.9}Gd_{0.1}Mo_6S_8$)

Two Gd-doped samples with a concentration of 0.1, as suggested in the formula ($Pb_{0.9}Gd_{0.1}Mo_6S_8$), have been investigated. One sample with a mass of 0.08066 gm was not fabricated using the HIP process (unHIP), whilst the other sample, with a mass of 0.21301 gm, was fabricated using the HIP process described above. These two samples were investigated in the 0-field only. The raw data giving V^{-1}_{rms} vs. T and phase shift vs. T for unHIP-0.1 and HIP-0.1 samples are shown in

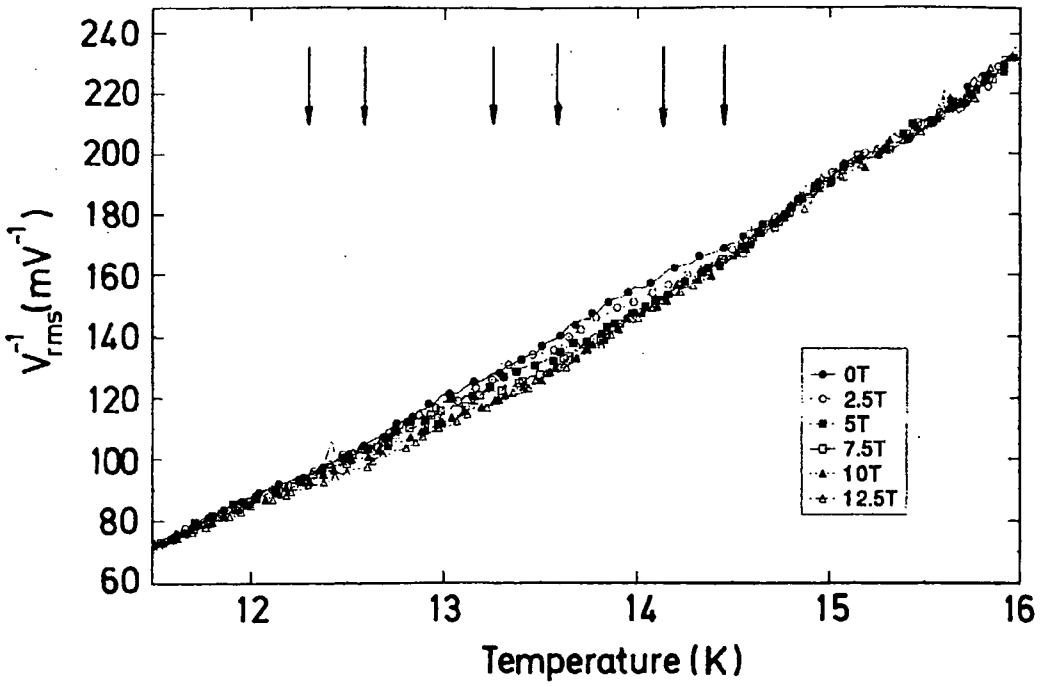

Fig.8.1a). V^{-1}_{rms} as a function of Temperature in an applied field of 0, 2.5, 5.0, 7.5, 10, 12.5 T for pure HIP'ed $PbMo_6S_8$, (Gd-0, without Gd-doping).

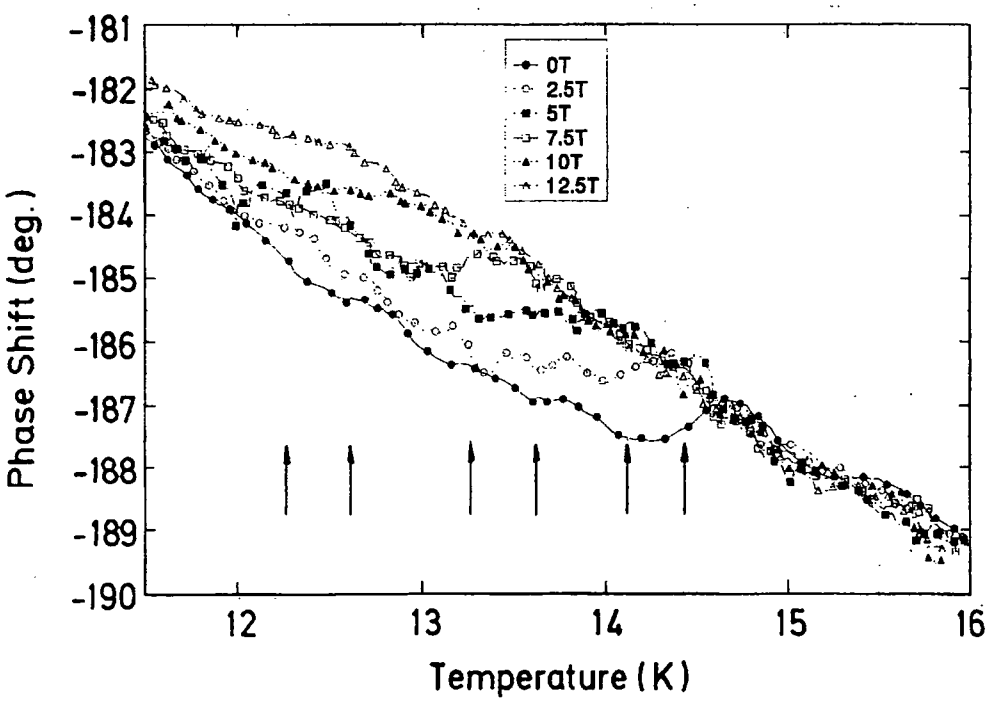

Fig.8.1b). Phase Shift as a function of Temperature in an applied field of 0, 2.5, 5.0, 7.5, 10, 12.5 T for pure HIP'ed $PbMo_6S_8$, (Gd-0, i.e. x=0).

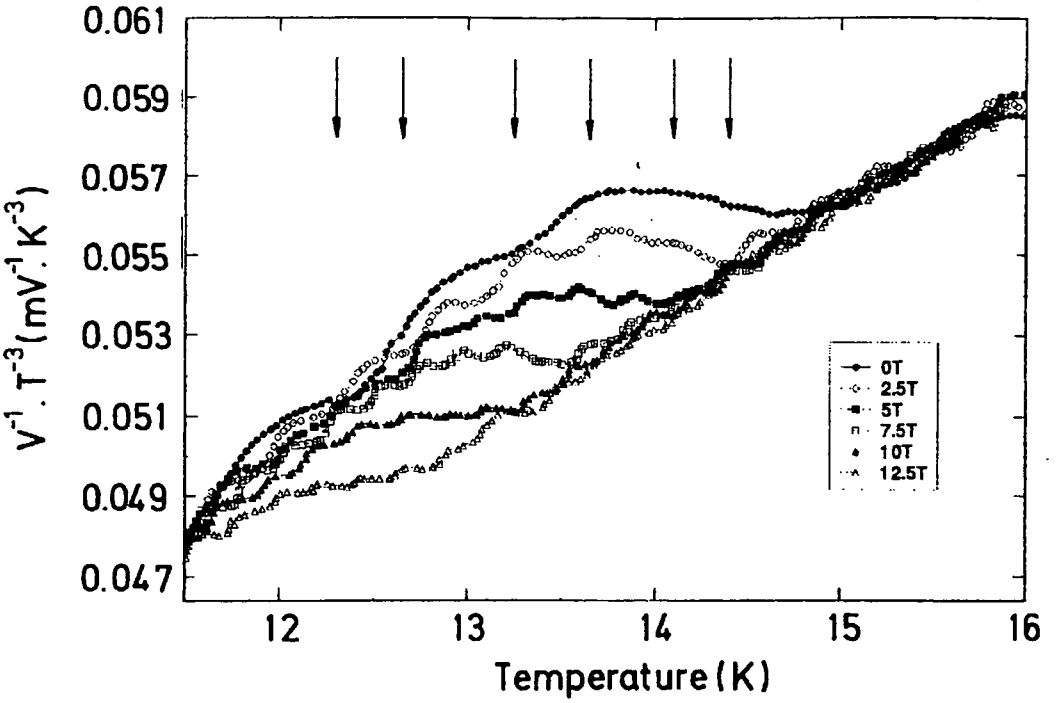

Fig. 8.1c). $V^{-1}_{rms} * T^{-3}$ as a function of temperature in the applied field of 0, 2.5, 5.0, 7.5, 10 and 12.5 Tesla for pure HIP'ed $PbMo_6S_8$, Gd-0, (without Gd-doping, x =0).

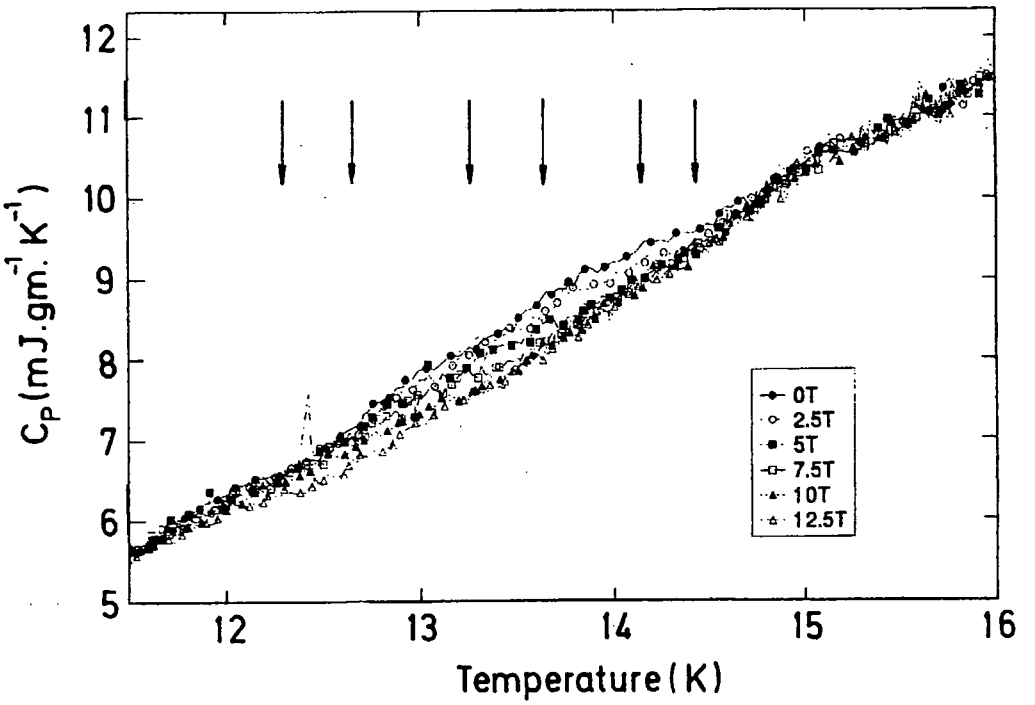

Fig. 8.2). Cp. as a function of temperature in the applied field of 0, 2.5, 5.0, 7.5, 10 and 12.5 Tesla for pure HIP'ed $PbMo_6S_8$, Gd-0 (without Gd-doping, x =0).

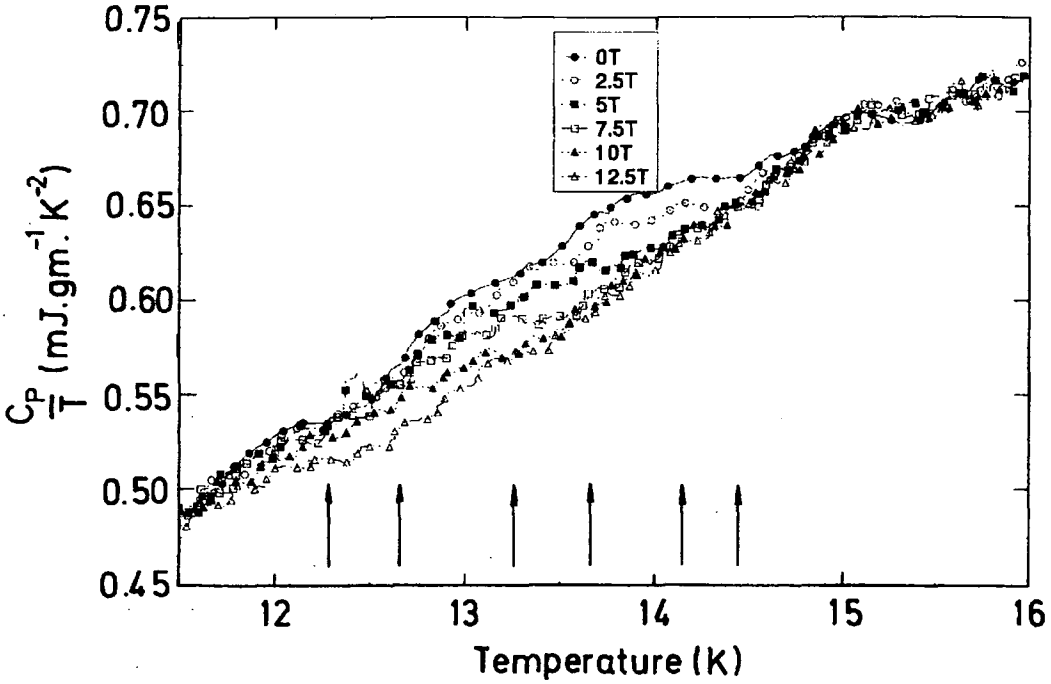

Fig. 8.3). Cp/T. as a function of temperature in the applied field of 0, 2.5, 5.0, 7.5, 10 and 12.5 Tesla for pure HIP'ed $PbMo_6S_8$ Gd-0 (without Gd-doping, x =0).

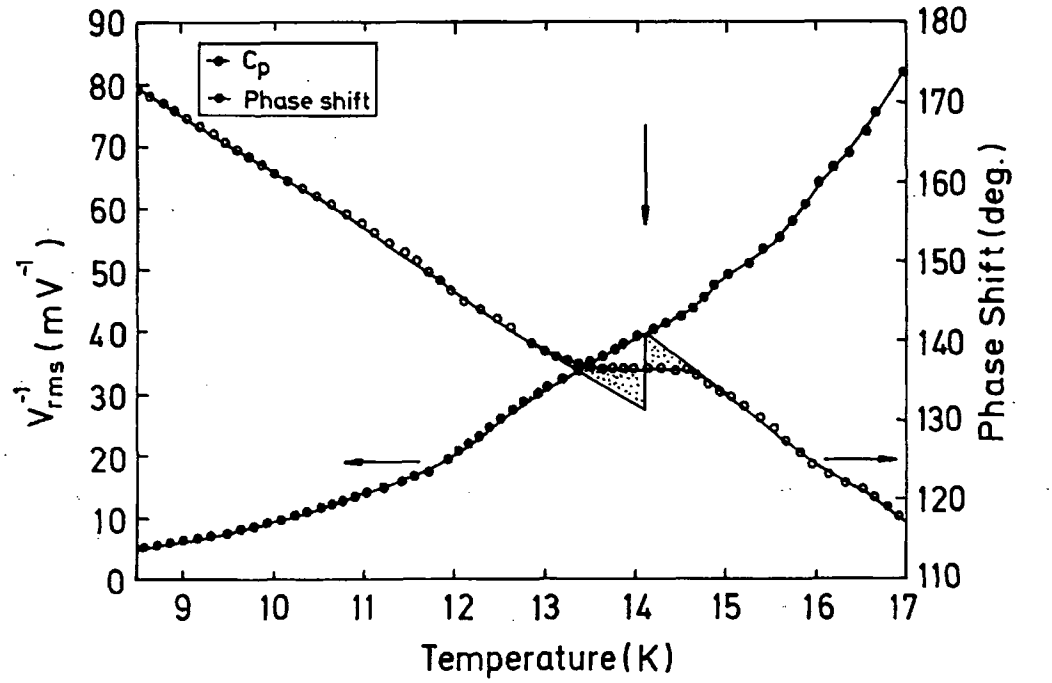

Fig.8.4) V^{-1}_{rms} and Phase Shift as a function of temperature for an unHIP'ed $Pb_{0.9}Gd_{0.1}Mo_6S_8$, unGd-0.1, in 0-field (x=0.1).

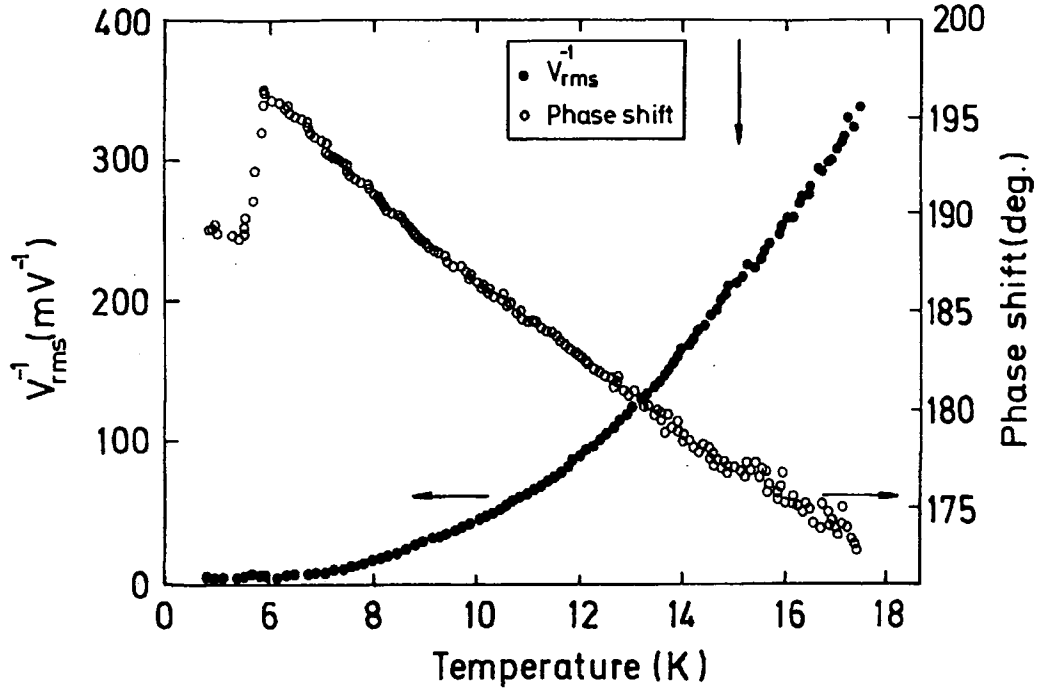

Fig.8.5) V^{-1}_{rms}(CX) and Phase Shift as a function of temperature for the HIP'ed $Pb_{0.9}Gd_{0.1}Mo_6S_8$, Gd-0.1, in 0-field (x=0.1).

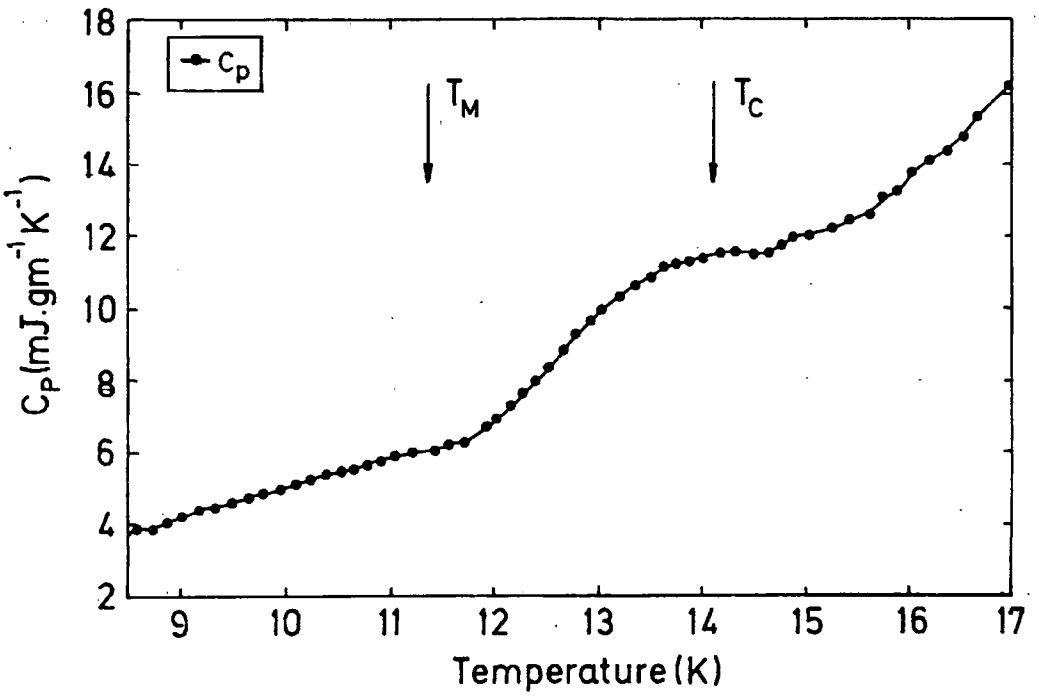

Fig.8.6).Cp vs. T for an unHIP'ed $Pb_{0.9}Gd_{0.1}Mo_6S_8$, unGd-0.1, in 0-field (x=0.1).

Figs. 8.4 and 8.5 respectively. The graphical form of unHIP-0.1 and HIP-0.1 PMS giving Cp vs. T are shown in Figs. 8.6 and 8.7, while Cp/T vs T are shown in Figs. 8.8 and 8.9. respectively. The transition temperature has been determined as explained in section 8.3.1. The results for both samples are tabulated in Table 8.2.

$Pb_{0.9}Gd_{0.1}Mo_6S_8$	Applied Field (T)	T_{C1}* ±0.2 (K)	T_{M1}* ±0.1 (K)	T_{M2}* ±0.1 (K)
unHIP	0	14.20	11.15	5.9
HIP	0	15.10	11.30	5.9

Table: 8.2. The effect of HIP process on $Pb_{0.9}Gd_{0.1}Mo_6S_8$ in 0-applied field. T_C*; The T_C* has been measured as explained in section 8.3.1.

8.3.3. Gd=0.2 ($Pb_{0.8}Gd_{0.2}Mo_6S_8$)

The Gd-doped sample with a concentration of 0.2, as suggested in the formula $Pb_{0.8}Gd_{0.2}Mo_6S_8$, has been investigated. It was fabricated using the HIP process described in above. The mass of the sample was=0.21412 gm. It was investigated on the applied magnetic field of 0, 2.5, 5.0, 7.5, 10 and 12.5 T. (The sample shows a multiphase behaviour). To have a clear look at $V^{-1}_{(rms)}CX$, we have added 5 units to 2.5 T, 10 to 5 T, 15 to 7.5 T, 20 to 10 T and 25 to 12.5 T data. Similarly, in the phase shift data, we have added 2° to 2.5 T, 4° to 5 T, 6° to 7.5 T, 8° to 10 T and 10° to 12.5 T. The same procedure is repeated for Cp vs. T and Cp/T vs. T data, where we have added, 0.5 units to 2.5 T, 1.0 to 5 T, 1.5 to 7.5 T, 2.0 to 10 T and 2.5 to 12.5 T data, and 0.05 units to 2.5 T, 0.1 to 5 T, 0.15 to 7.5 T, 0.2 to 10 T and 0.25 to 12.5 T data respectively. The results so obtained, for $V^{-1}_{(rms)}$ vs. T are shown in Fig. 8.10a for Phase Shift vs. T in Fig. 8.10b and in Fig. 8.10c (for 11 K to 17 K only), Cp vs. T in Fig. 8.11 and Cp/T vs. T in Fig. 8.12. The digitised data is tabulated in Table 8.3.

8.3.4. Gd=0.3 ($Pb_{0.7}Gd_{0.3}Mo_6S_8$)

Two Gd-doped samples with a concentration of 0.3 as suggested in the

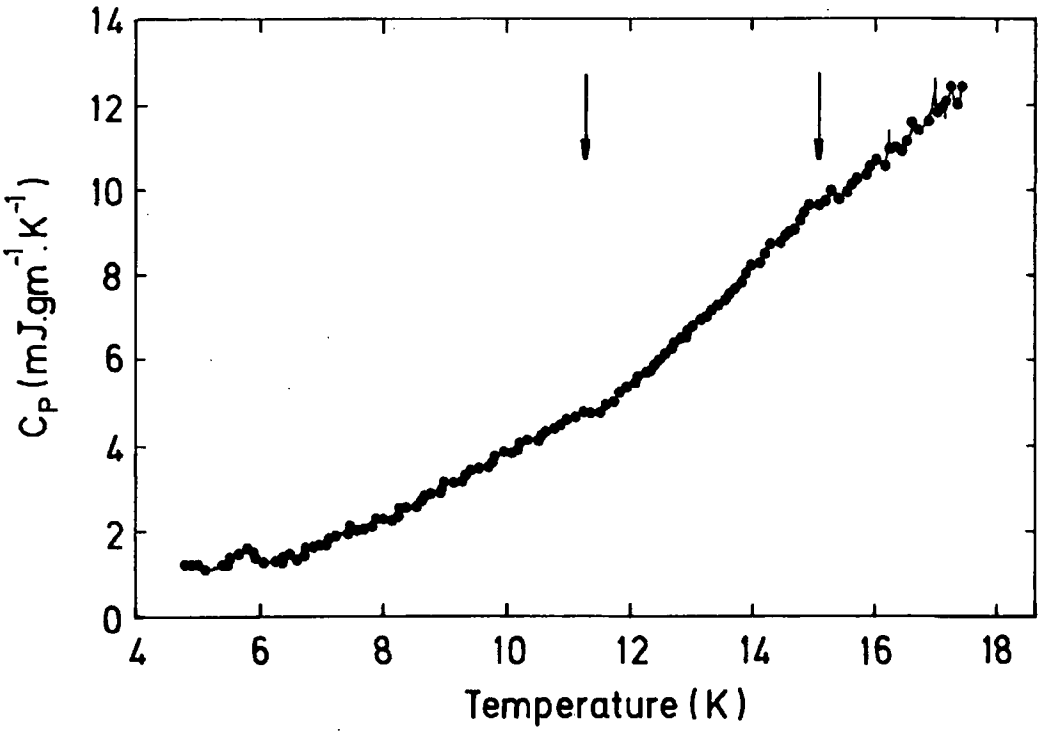

Fig.8.7). Cp versus T for a HIP'ed $Pb_{0.9}Gd_{0.1}Mo_6S_8$, Gd-0.1, in 0-field (x=0.1).

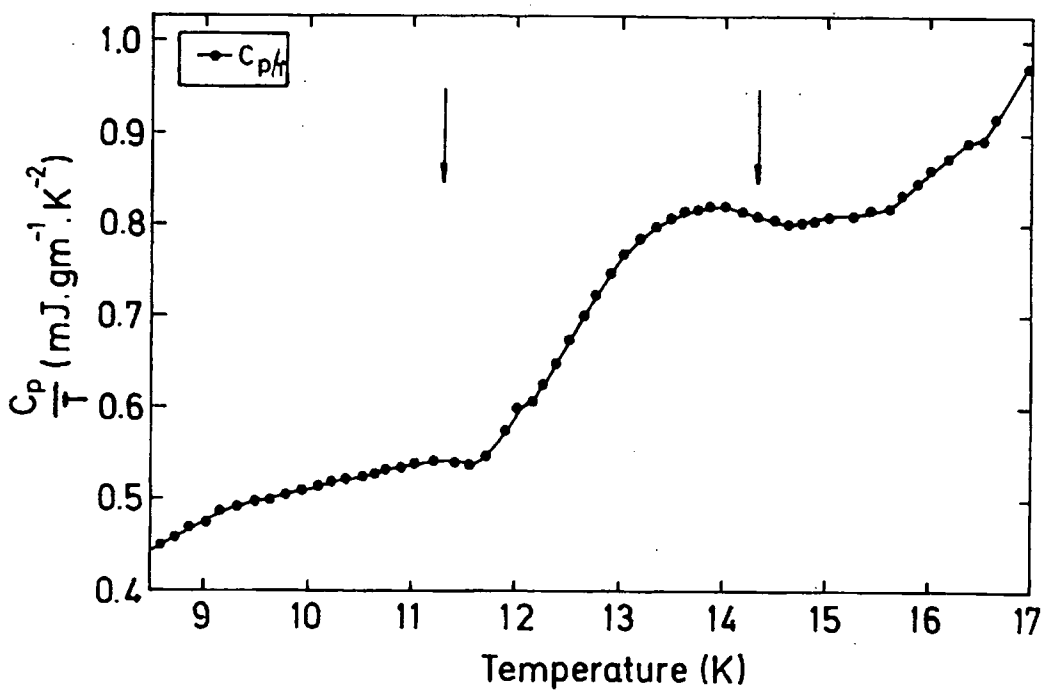

Fig.8.8). Cp/T vs. T for an unHIP'ed $Pb_{0.9}Gd_{0.1}Mo_6S_8$, unGd-0.1, in 0-field (x=0.1).

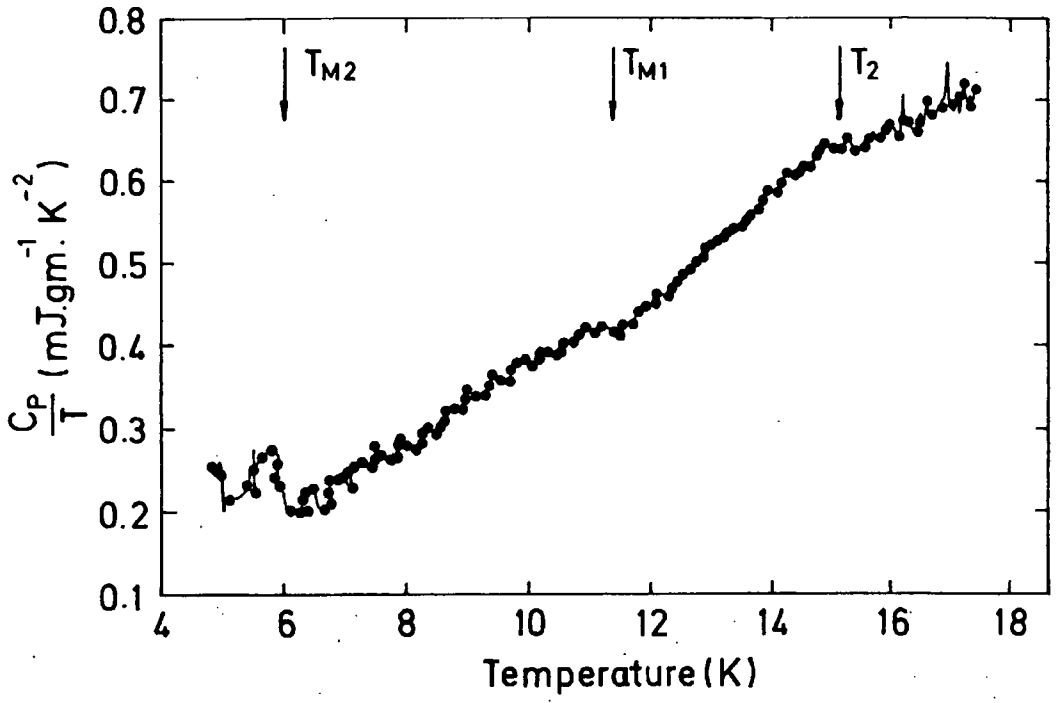

Fig.8.9). Cp/T versus T for a HIP'ed $Pb_{0.9}Gd_{0.1}Mo_6S_8$, Gd-0.1, in 0-field (x=0.1).

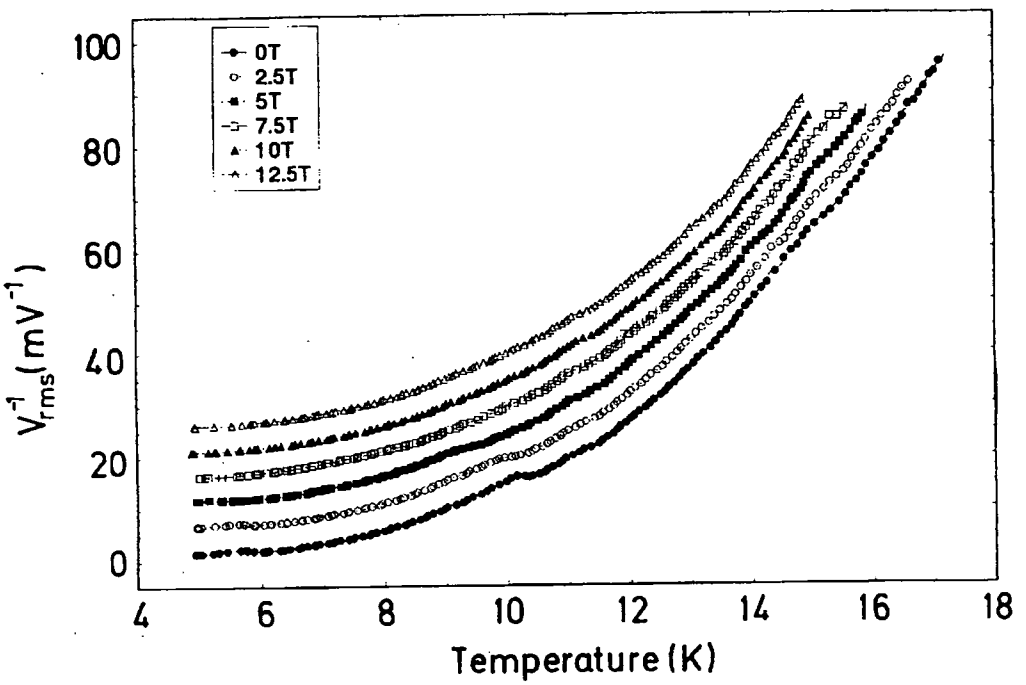

Fig. 8.10a). V^{-1}_{rms}(CX) as a function of temperature in the applied field of 0, 2.5, 5.0, 7.5, 10 and 12.5 Tesla for HIP'ed $Pb_{0.8}Gd_{0.2}Mo_6S_8$, Gd-0.2, (x =0.2). To make it more clear, 5 units have been added to 2.5 T data, 10 units to 5 T, 15 units to 7.5 T, 20 units to 10 T and 25 units to 12.5 T data.

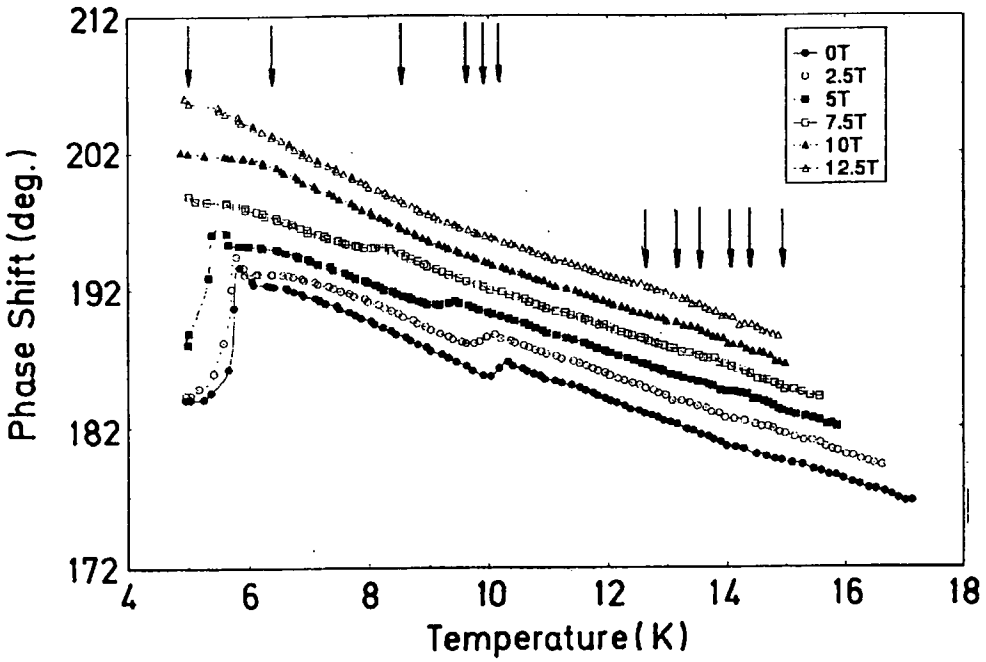

Fig. 8.10b). Phase Shift as a function of temperature in the applied field of 0, 2.5, 5.0, 7.5, 10 and 12.5 Tesla for HIP'ed $Pb_{0.8}Gd_{0.2}Mo_6S_8$, Gd-0.2, (x =0.2). To make it more clear, 2° has been added to 2.5 T data, 4° to 5 T, 6° to 7.5 T, 8° to 10 T and 10° to 12.5 T data.

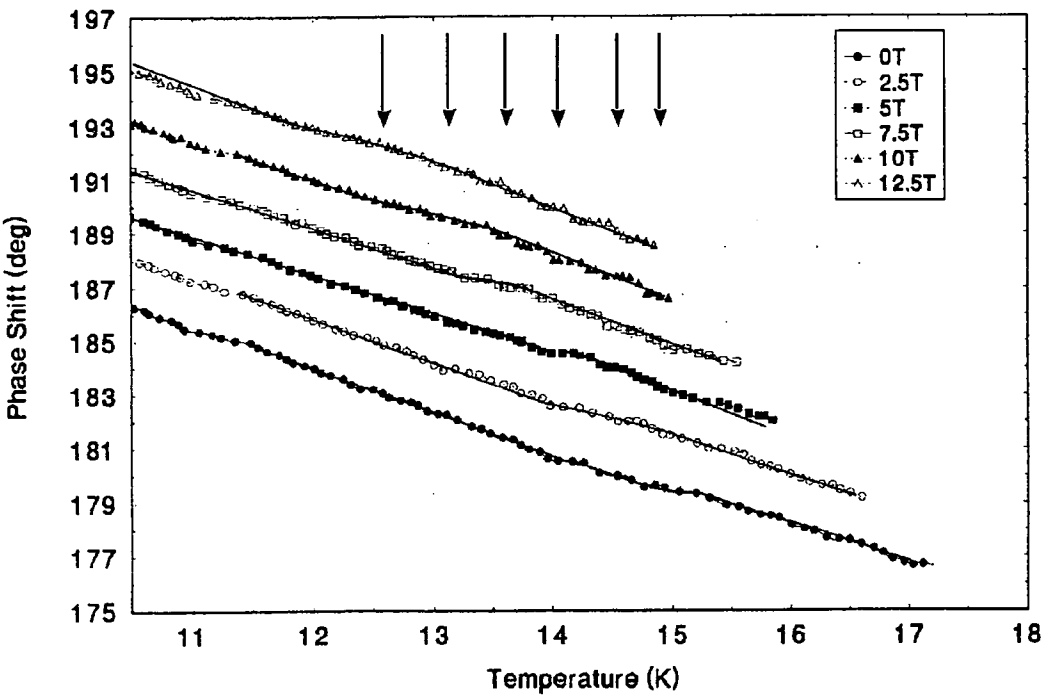

Fig. 8.10c). The data of Fig. 2.12b has been blown up for the temperature range of 10.5 K to 17 K to find the transition temperature. The arrows shows the transition temperature for each field.

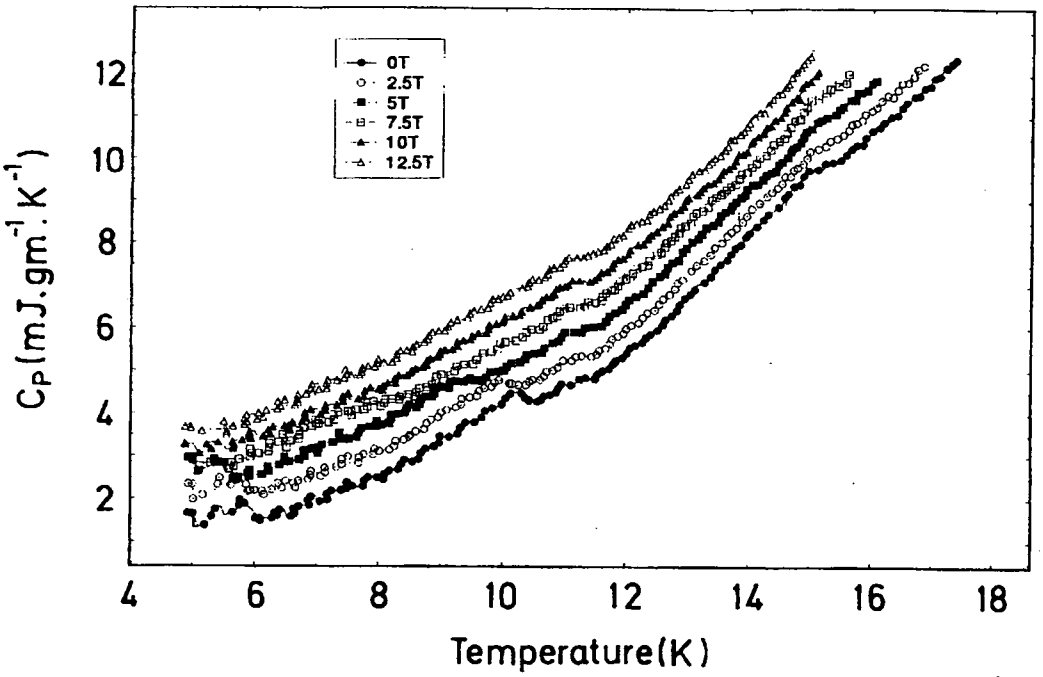

Fig. 8.11). Cp as a function of temperature in applied field of 0, 2.5, 5.0, 7.5, 10 and 12.5 Tesla for HIP'ed $Pb_{0.8}Gd_{0.2}Mo_6S_8$, Gd-0.2, (x =0.2). To have a better idea of transition, we have added 0.5 units to 2.5 T data, 1.0 to 5 T, 1.5 to 7.5 T, 2.0 to 10 T and 2.5 units to 12.5 T data.

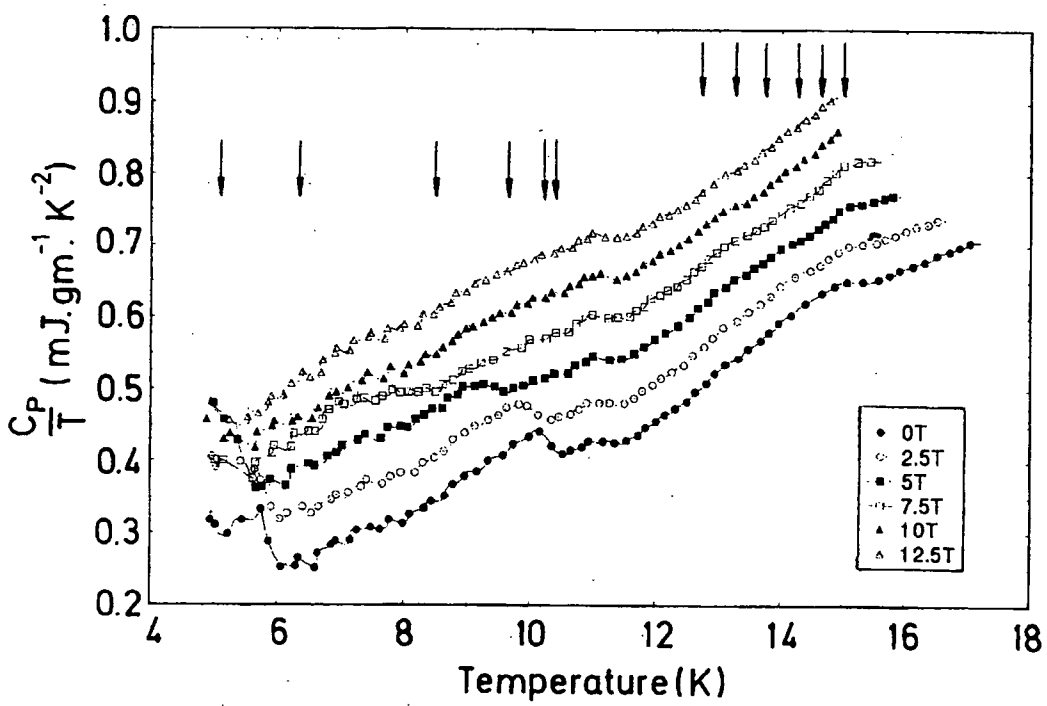

Fig. 8.12). Cp/T. as a function of temperature in applied field of 0, 2.5, 5.0, 7.5, 10 and 12.5 Tesla for HIP'ed $Pb_{0.8}Gd_{0.2}Mo_6S_8$, Gd-0.2, (x =0.2). To have a better idea of transition, we have added 0.5 units to 2.5 T data, 0.1 to 5 T, 0.15 to 7.5 T, 0.2 to 10 T and 0.25 units to 12.5 T data.

Applied Field (T)	T_{C1}* ±0.2 (K)	T_{M1}* ±0.1 (K)	T_{M2}* ±0.1 (K)
0	14.95	10.45	5.9
2.5	14.65	10.25	5.8
5.0	14.1	9.6	5.4
7.5	13.65	8.3	≈5
10.0	13.15	6.1	-
12.5	12.6	≈5	-

Table: 8.3. The effect of applied magnetic field on the different phases of $Pb_{0.8}Gd_{0.2}Mo_6S_8$. T_C*, denoting the superconducting phase transition, T_{M1}*,and T_{M2}* the magnetic phase transition due to magnetic impurities.

; The calculation of T_C has been explained in section 8.3.1.

Sample→	Gd-0.3 HIP	Gd-1 unHIP
Applied Field (T)	T_M* ±0.1 (K)	T_M* ±0.1 (K)
0	10.4	10.40
2.5	10.15	10.07
5.0	9.4	9.45
7.5	8.25	8.30
10.0	6.0	~ 6.0
12.5	≈5	-

Table: 8.4. The effect of applied magnetic field (H) on the magnetic transition temperature T_M* of $Pb_{0.7}Gd_{0.3}Mo_6S_8$ (Gd-0.3) and $GdMo_6S_8$ (Gd-1).

; The T_M has been measured as explained in section 8.3.1 above.

formula $Pb_{0.7}Gd_{0.3}Mo_6S_8$ have been investigated. One sample with a mass of 0.13439 gm was not fabricated using the HIP process (unGd-0.3), and the other sample, with a mass of 0.20527 gm, was fabricated using the HIP (Gd-0.3) process. The unGd-0.3 sample was investigated in 0-field giving a possible Tc of ~14.9 K. The raw data giving $V^{-1}_{(rms)}$ vs. T and phase shift vs. T are shown in Fig. 8.13 and Cp vs. T is shown in Fig. 8.14. The Gd-0.3 sample was investigated in an applied magnetic field of 0, 2.5, 5.0, 7.5, 10, and 12.5 T. The raw data giving $V^{-1}_{(rms)}$ vs. T and phase shift vs. T are shown in Figs. 8.15a and 8.15b respectively and Cp vs. T is shown in Fig. 8.16 for only Gd-0.3 sample. The arrows point to the phase transitions. The higher phase (T_C~14.9) is the superconducting phase, while we provide evidence later that the lower phase (T_C~10.4), is a magnetic phase. The effect of magnetic field on different phases is presented in Table 8.4.

8.3.5. Gd=1.0 ($GdMo_6S_8$)

To check the effect of Gd only on the Mo_6S_8, an unHIP sample of mass 0.23741 gm with the suggested formula $GdMo_6S_8$ (Gd-1) has been prepared (without Pb). The Gd-1 sample was investigated in 0, 2.5, 5.0, 7.5, 10.0 and 12.5 T field. The raw data giving $V^{-1}_{(rms)}$ vs. T and phase shift vs. T are shown in Figs. 8.17a and 8.17b respectively. The effect of magnetic field on the specific heat Cp, of this sample is shown in Fig. 8.18, while the tabulated form of the data is presented in Table 8.4.

8.4. Analysis.

The specific heat Cp of all Gd-doped HIP'ed PMS samples in 0-field are displayed in Fig.8.19. Gd-1 (unHIP and without Pb) is added for comparison. It is noted that Cp decreases above T_C with the addition of Gd. The effect of Gd-concentration (x=0, 0.1, 0.2, 0.3) on the T_C of PMS in the 0-field for the higher phase is plotted in Fig.8.20 and tabulated in Table 8.5, including literature values [3-4] for x=0.6 and 1. It is clear that the T_C values increased after Gd-doping and is maximised for x =0.1. However, Tc values are decreased dramatically for x=0.6 &1.

The Gd-1 sample did not show any superconducting transition in the investigated temperature region (5-15 K) using a.c. susceptibility technique [5].

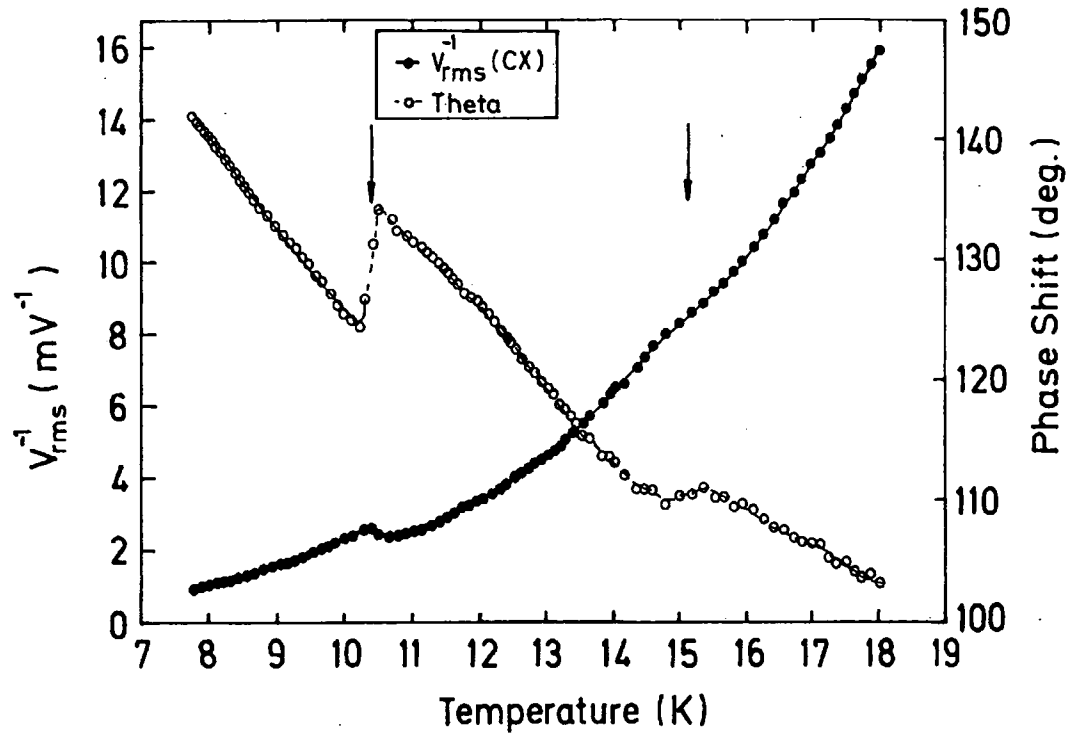

Fig.8.13). V^{-1}_{rms} and Phase Shift as a function of temperature for an unHIP'ed $Pb_{0.7}Gd_{0.3}Mo_6S_8$, unGd-0.3, in 0-field (x=0.3).

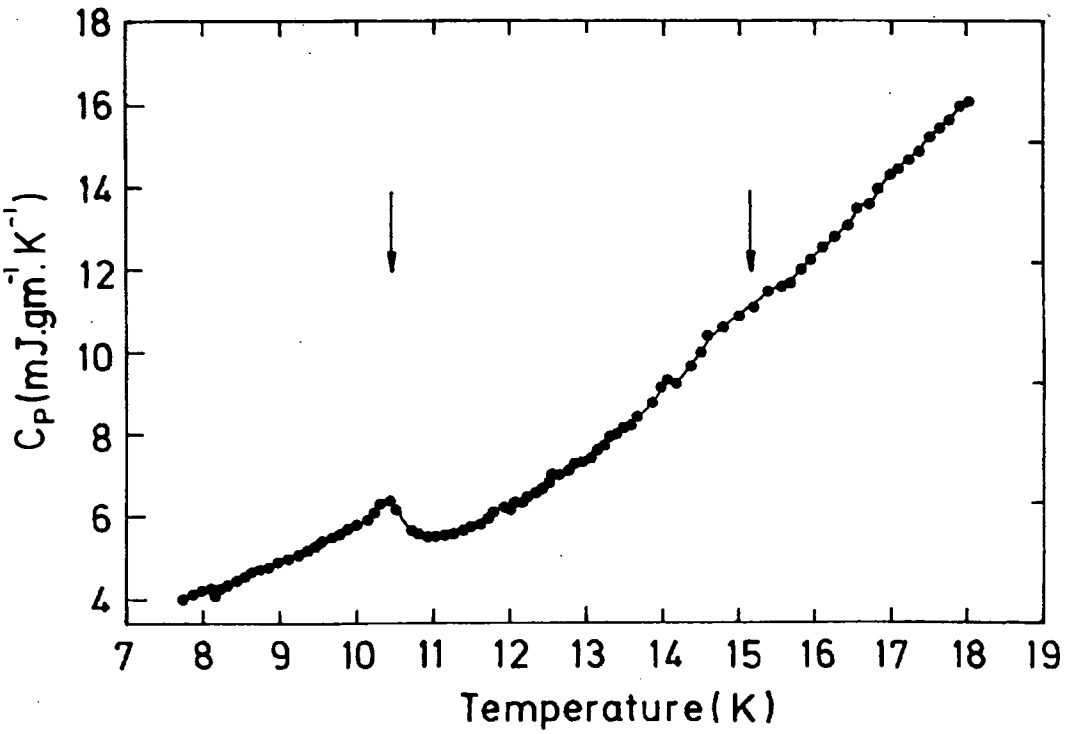

Fig.8.14). Cp vs. temperature for an unHIP'ed $Pb_{0.7}Gd_{0.3}Mo_6S_8$ unGd-0.3 in 0 Field (x=0.3).

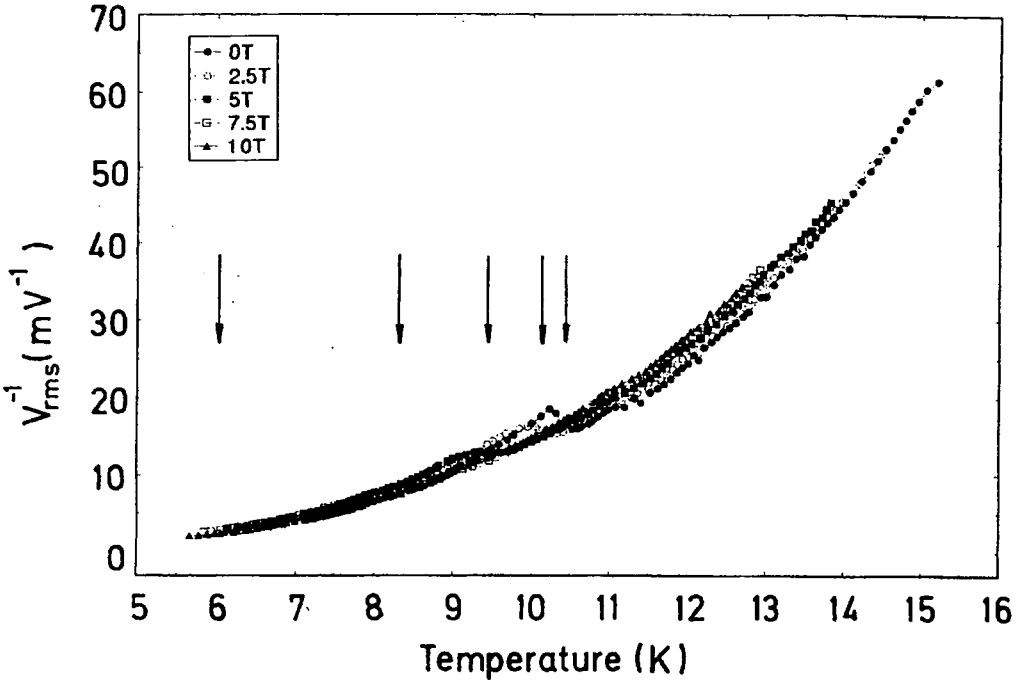

Fig. 8.15a). V^{-1}_{rms} as a function of temperature in the applied field of 0, 2.5, 5.0, 7.5, 10 and 12.5 Tesla for HIP'ed $Pb_{0.7}Gd_{0.3}Mo_6S_8$, Gd-0.3 (x =0.3).

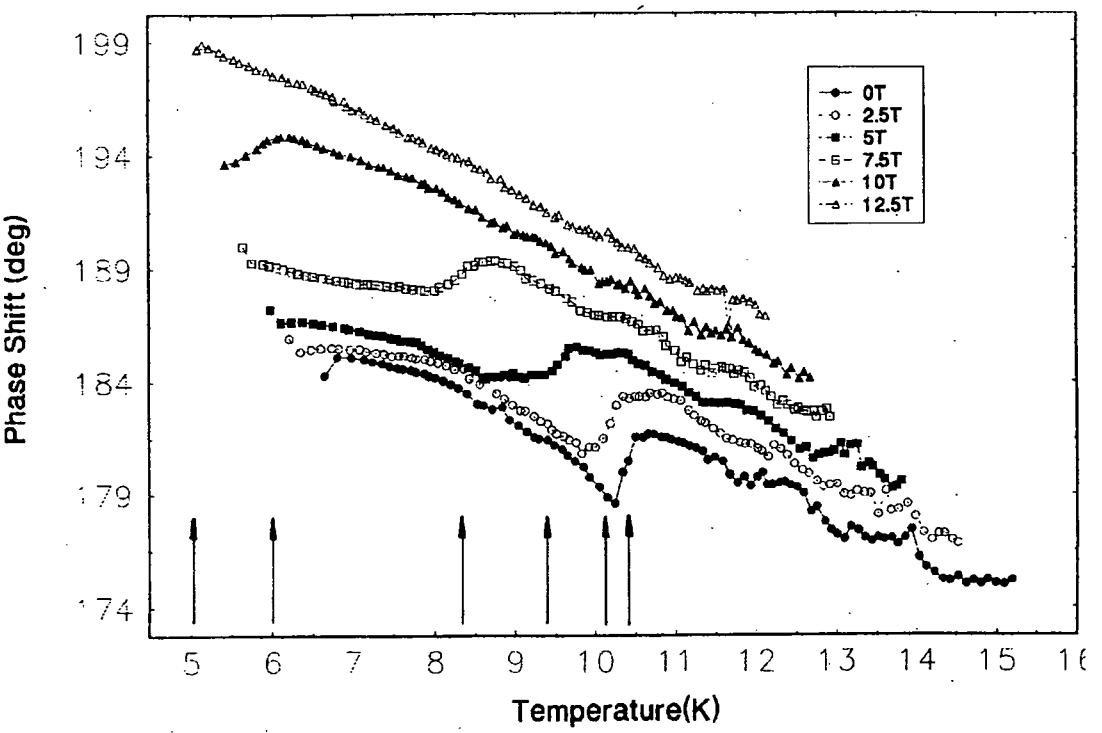

Fig. 8.15b). Phase Shift as a function of temperature in the applied field of 0, 2.5, 5.0, 7.5, 10 and 12.5 Tesla for HIP'ed $Pb_{0.7}Gd_{0.3}Mo_6S_8$, Gd-0.3 (x =0.3).

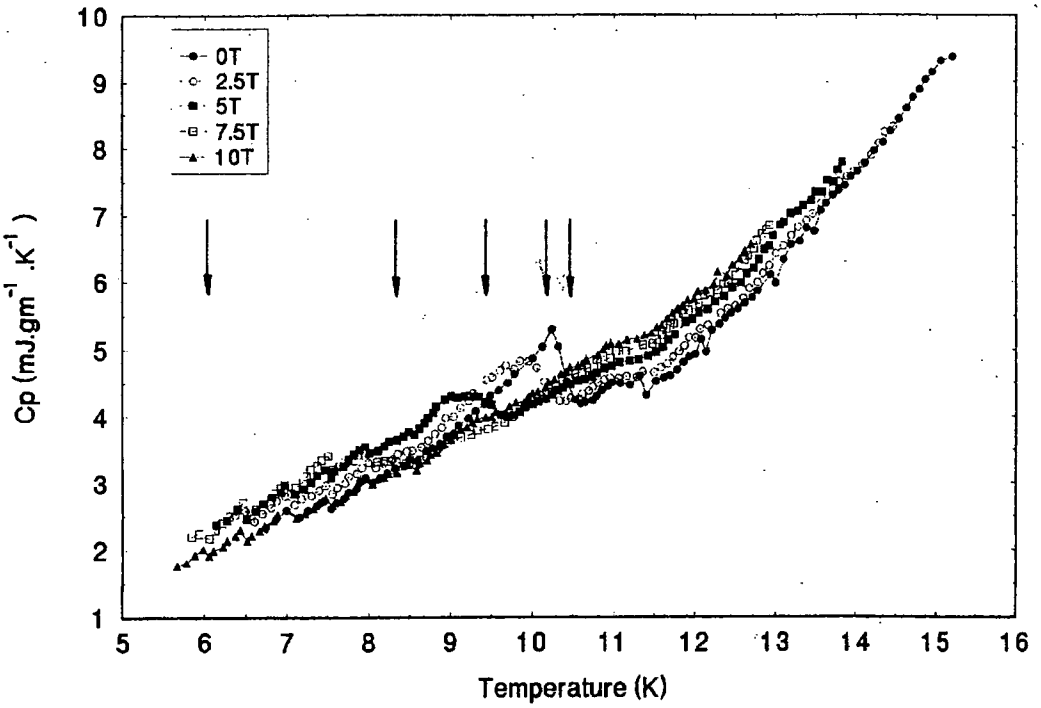

Fig. 8.16). Cp as a function of temperature in applied field of 0, 2.5, 5.0, 7.5, and 10 T for HIP'ed $Pb_{0.7}Gd_{0.3}Mo_6S_8$, Gd-0.3, (x =0.3).

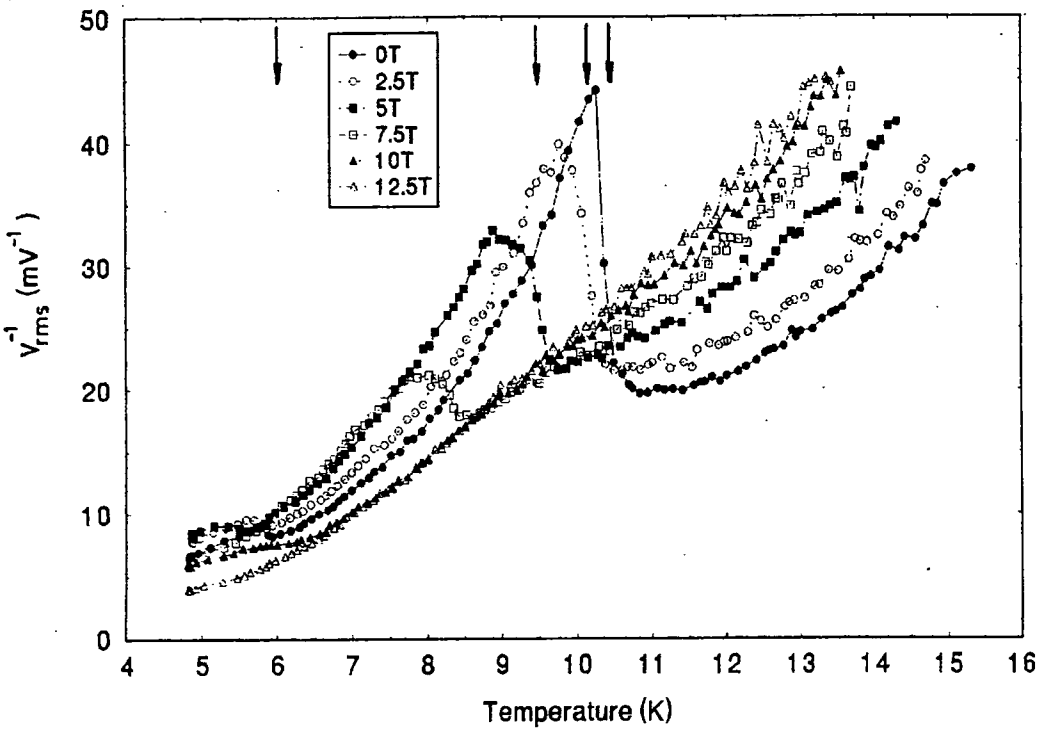

Fig. 8.17a). V^{-1}_{rms} as a function of temperature in the applied field of 0, 2.5, 5.0, 7.5, 10 and 12.5 Tesla for unHIP'ed $GdMo_6S_8$, Gd-1, (x =1.0).

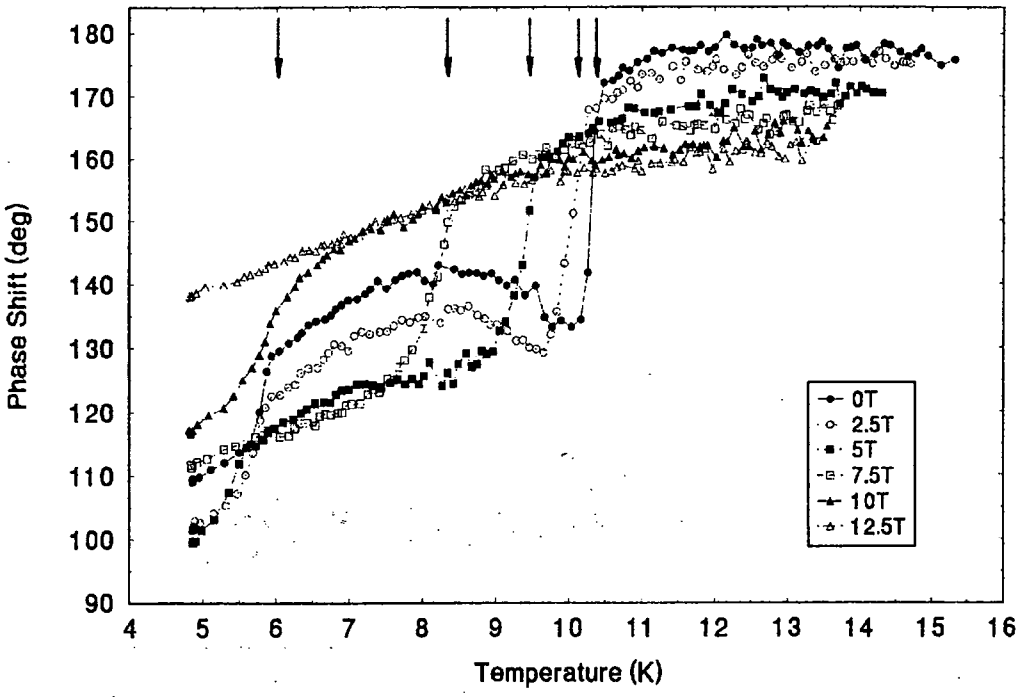

Fig. 8.17b). Phase Shift as a function of temperature in the applied field of 0, 2.5, 5.0, 7.5, 10 and 12.5 Tesla for unHIP'ed $GdMo_6S_8$, Gd-1 (x =1.0).

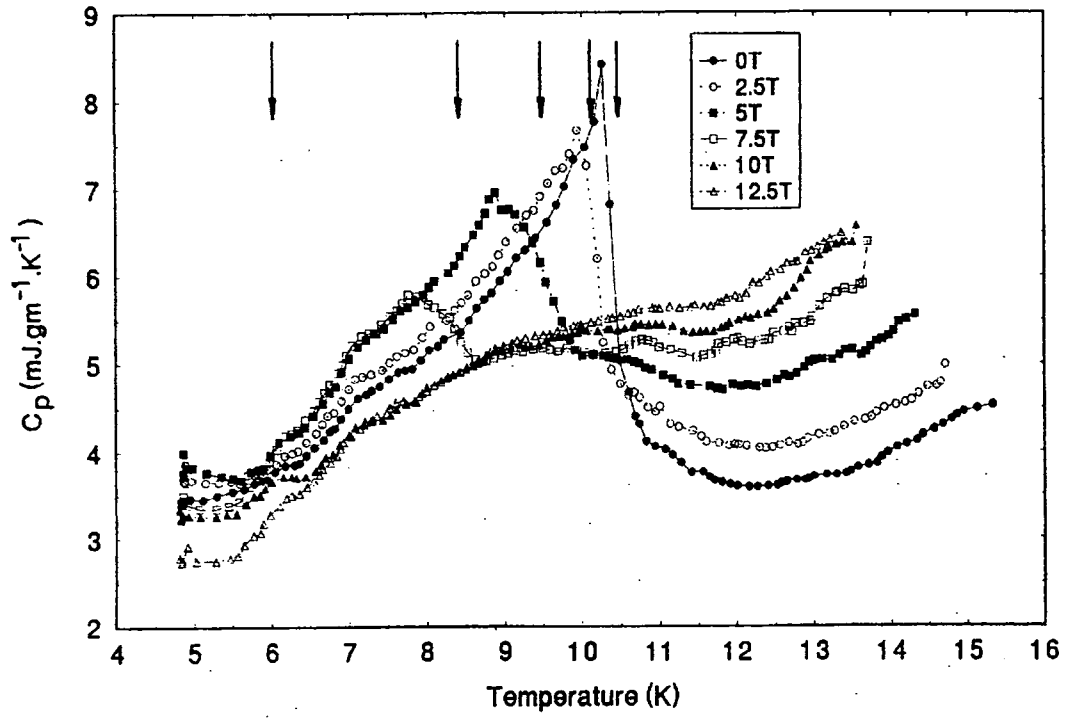

Fig. 8.18). Cp as a function of temperature in applied field of 0, 2.5, 5.0, 7.5, 10, and 12.5 T for unHIP'ed $GdMo_6S_8$, Gd-1, (x =1.0).

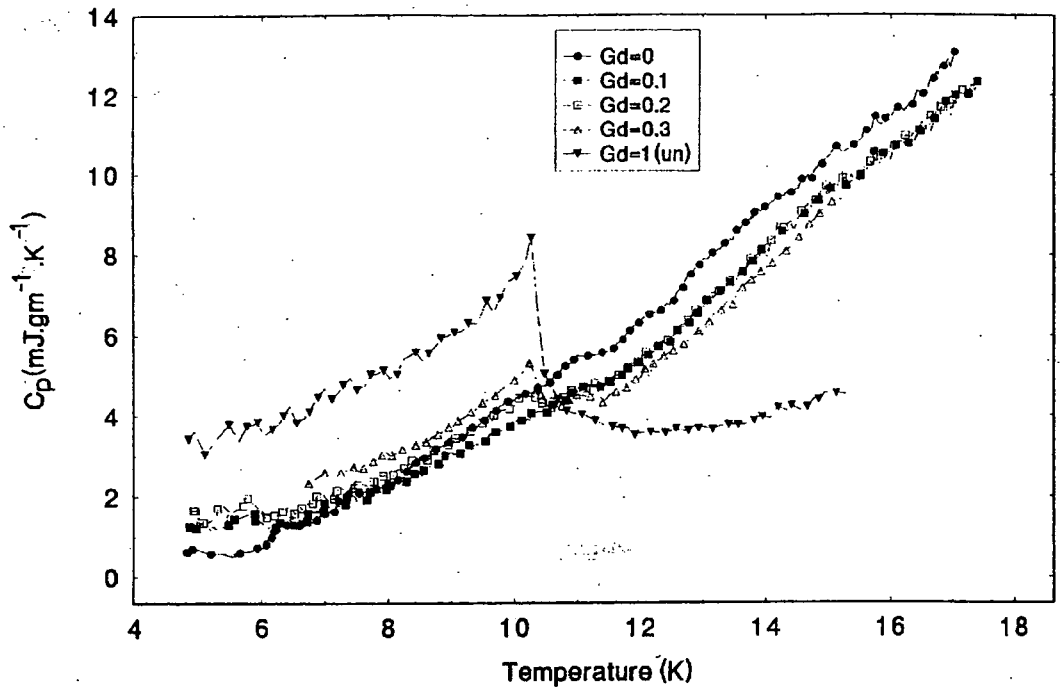

Fig.8.19). Cp as a function of temperature for all HIP'ed $Pb_{1-x}Gd_xMo_6S_8$ in 0-Field, i.e. x =0, 0.1, 0.2, 0.3 and 1.0. Gd=1 has been plotted for comparison.

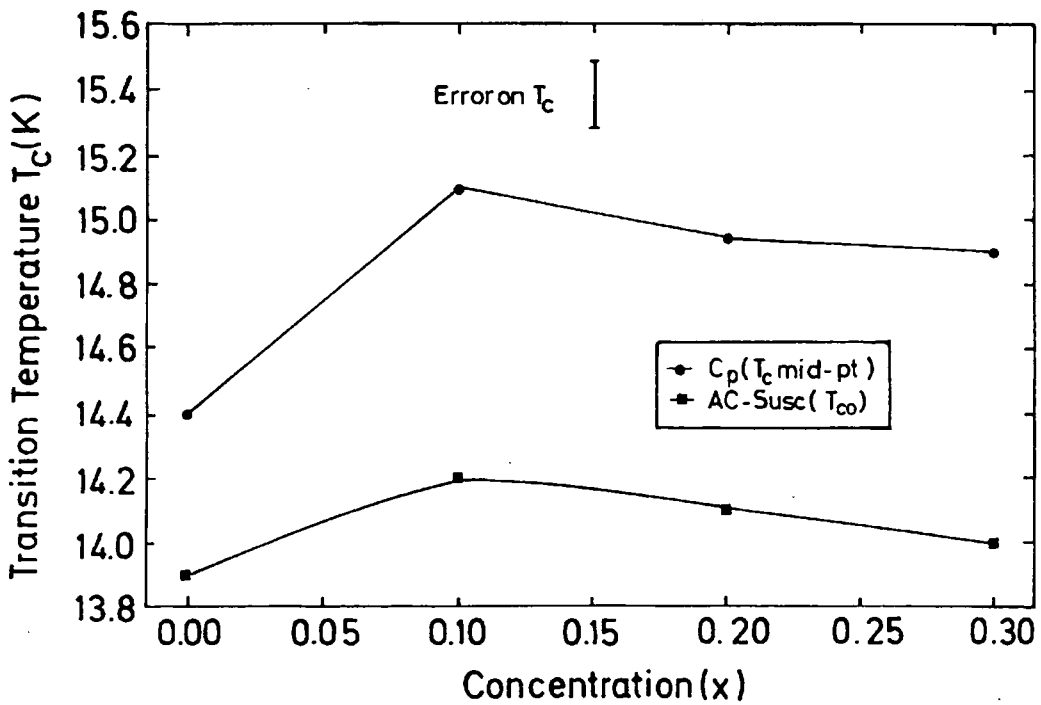

Fig.8.20). The effect of high Gd-doping on the Tc of $Pb_{1-x}Gd_xMo_6S_8$, where x=0, 0.1, 0.2 and 0.3 using Cp- and a.c. susceptibility measurements.

Gd-doping (x)	T_C* ±0.2 (K) After Cp	T_C*(onset) ±0.1 (K) After AC-Susc.	T_C*(mid pt.) ±0.1 (K) After AC-Susc.
0	14.45	14.20	14.0
0.1	15.10	14.20	14.0
0.2	14.95	14.10	13.80
0.3	14.90	14.0	13.80
0.6**	3.2	-	-
1.0***	1.4	-	-

Table:8.5.The effect of Gd-doping (x) on the transition temperature of $Pb_{1-x}Gd_xMo_6S_8$.

*; The T_C has been measured after the entropy conservation under the curve.

**; From Φ. Fischer et. al.(1976) pp.181.[3].

***; From Ternary Compounds I, pp.4 [4].

However, it shows a magnetic transition T_M in the Cp measurements at about ~10.4 K in zero field. It can be noted that the Cp/T values increased after the application of the field for $T > T_M$ from its zero field value, while the magnetic transition temperature T_M decreased for higher magnetic fields.

The thermodynamic upper critical field $B_{C2}(T)$ vs. transition temperature T_C of Gd-doped HIP'ed PMS samples for x=0, and 0.2 has been shown in Fig.8.21. We found a slope close to $T \approx T_C$ for Gd=0.2, of -5.21 T/K. Using WHH theory [6], [Eq.2.63], $B_{C2}(0)$ was calculated, assuming no paramagnetic limiting and found to be 54 T. Although Gd-doping increased the T_C of the material, the slope $dB_{C2}/dT]_{T=Tc}$ is lower than the slope of Gd-0 PMS. This can be seen in Table 8.6.

We also plotted the effect of applied field on the magnetic transition temperature T_M of all Gd-doped PMS samples. This is shown in Fig. 8.22 for the magnetic phase only.

The Maki [7] parameter has been calculated using Eqs. 7.3 and 7.4 and was found to be 2.3 ±0.03. The Spin-orbit scattering parameter λ_{SO} has been calculated using Eq. 2.57, viz. $B_{C2}(0)=1.33\sqrt{\lambda_{SO}}\,B_p$, where $B_{C2}(0)$ is the upper critical field assuming there is no PPL, and B_p is the Clogstan-Chandrashekher limiting field [8], which is found to be 1.55 ± 0.03.

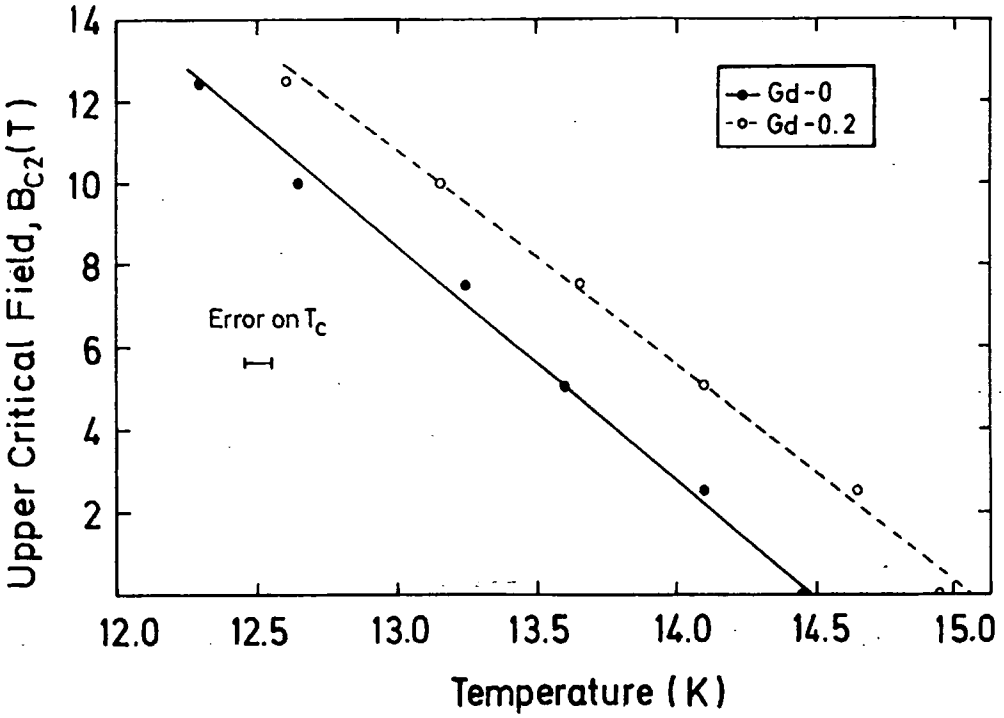

Fig.8.21). Upper Critical field $B_{C2}(T)$ as a function of superconducting transition temperature Tc for two HIP'ed $Pb_{1-x}Gd_xMo_6S_8$ samples, (x=0, 0.2).

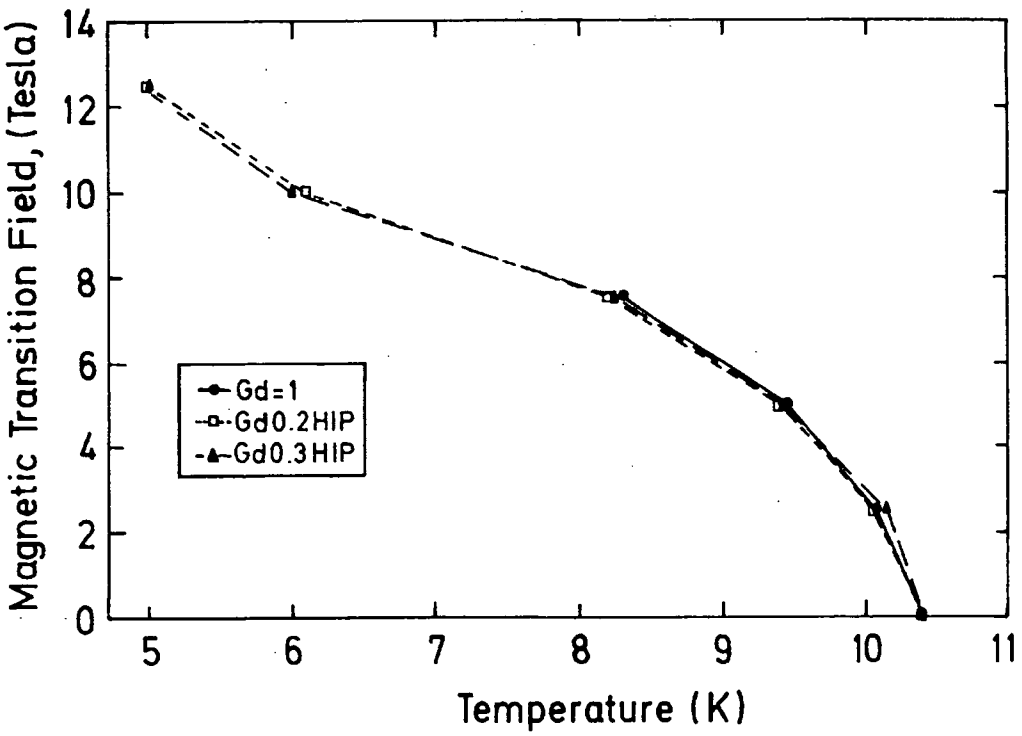

Fig.8.22). Upper Critical field $B_{C2}(T)$ as a function of higher magnetic transition temperature T_M for $Pb_{1-x}Gd_xMo_6S_8$ samples, (x=0, 0.1, 0.2, 1.0).

Material	T_C**±0.2 (K)	dB_{C2}/dT± 0.2 (T/K)	$B^*_{C2}(0)$±5 (T)
Gd=0 PMS HIP'ed	14.45	-5.74	57.28
Gd=0.2 PMS HIP'ed	14.95	-5.21	53.97

Table 8.7: T_C, $(dB_{C2}/dT)_{T=Tc}$, and $B^*_{C2}(0)$ for Gd=0 (Pure PMS) and Gd=0.2 ($Pb_{0.8}Gd_{0.2}M0_6S_8$) samples. $B_{C2}(0)$ has been calculated using WHH theory [6].

8.5. Discussion:

It is evident from the Cp measurements shown in Figs. 8.1- 8.20 that after Gd-doping, the materials show a three-phase behaviour, with a higher temperature superconducting phase, and lower temperature magnetic phases. We have plotted $B_{C2}(T)$ vs. temperature for the superconducting phase and middle temperature magnetic phase in Figs. 8.21-22 respectively. The presence of the superconducting phase, is confirmed by complementary a.c. susceptibility measurements [9] on these materials. The data of reference 9 has been replotted in Fig. 8.23. This reveals that the material is superconducting at the same temperature found in the Cp measurements. However, the other phases observed in Cp measurements at ~10 K and ~6 K may be due to some other unreacted materials present in the sample. This has been confirmed on the basis of the x-rays diffraction (XRD) and preliminary results of transmission electron microscopy (TEM) [10] on the Gd-0.3 and Gd-1 samples, where most of the peaks are identified as pure PMS. The rest of the peaks are MoS_2 and Mo_2S_3, with some traces of Gd_2S_3. By comparing the data of Gd-0.3 and Gd-1 samples, it is revealed that both materials have a second phase identified as Gd_2S_3, which is a possible origin of the magnetic ordering in all the Gd-doped PMS at ~10 K.

After applying magnetic field, Cp/T increases for $T > T_C$, the magnetic transition temperature T_M is reduced and there is no anomaly in the a.c. susceptibility measurements. This consequently reveals the possible origin of the magnetic transition at ~10 K in Gd_2S_3 as being antiferromagnetic [11, 12] as MoS_2 and Mo_2S_3 are paramagnetic materials.

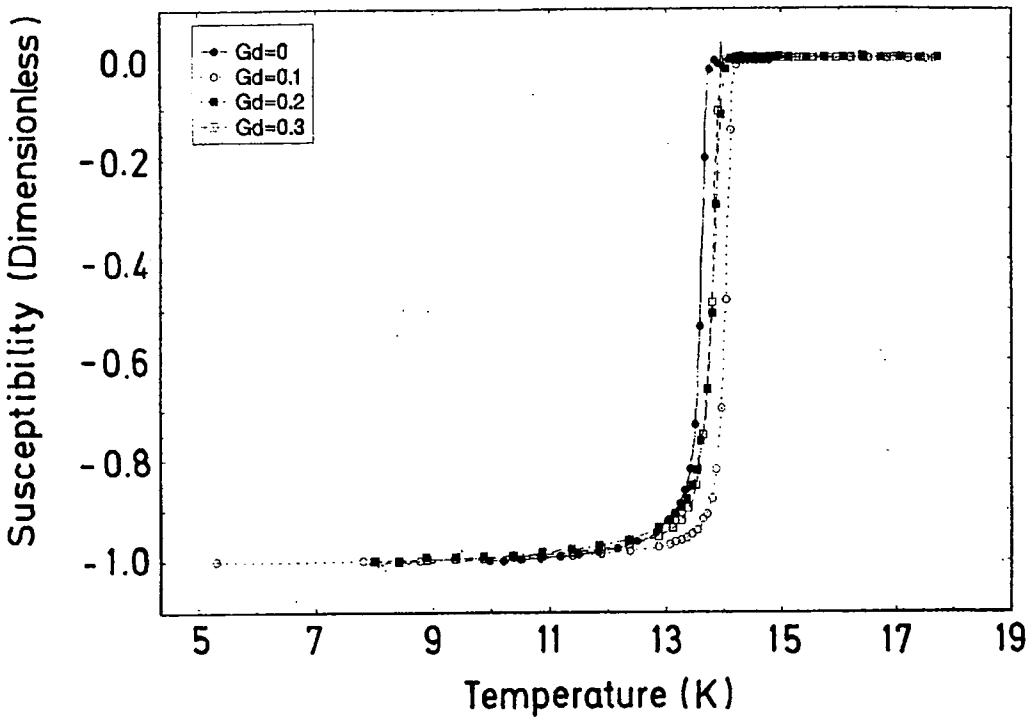

Fig.8.23). Normalised AC-Susceptibility data vs. temperature for $Pb_{1-x}Gd_xMo_6S_8$ samples, (x=0, 0.1, 0.2, 0.3), for comparison with Cp data (DNZ-data).

We have plotted $B_{C2}(T)$ vs. magnetic transition temperature for the middle temperature magnetic phase in Fig. 8.22. From the above discussion it can be concluded, that for the materials with x =0.1, 0.2 and 0.3, the magnetic phase transition at ~10 K is of the antiferromagnetic nature. One possibility is Gd has replaced the Pb sites in $Pb_{1-x}Gd_xMo_6S_8$ pointed to the co-existence of superconductivity with the magnetic ordering [13] but more probably the anti-ferromagnetic transition is due to Gd_2S_3 which has not reacted with the PMS during the fabrication process.

It is likely from the Table 8.5 and Fig. 8.20, that after doping Gd, T_C has been increased. If so the Gd-doping has an optimum value of x=0.1, for which the Tc is the highest one as 15.1±0.2 K, which is slightly higher than the values quoted in literature for the Chevrel phase materials [14-19]. This trend is also confirmed after a.c. susceptibility measurements [9] shown in Figs. 8.20 and 8.23. However, Tc values measured with Cp measurements are about 6% higher than those measured with a.c. susceptibility. This may be due to the thermometry used in these two separate methods, or due to the inhomogeneity in the samples or both. Cattani et. al.

[20] showed that different Tc obtained after different methods is not artifact of the measurements but due to the materials itself. So different Tc could be intrinsic. The reason why Gd-doping has slightly improved T_C is still not clear but Gd acting as an oxygen getter may be a contributing factor.

Using WHH theory [6] we have calculated $B_{C2}(0)$ assuming that there is no paramagnetic limiting present in the material and the material is a dirty limit type II superconductor, (this has been explained in chapter 2 & 7) for Gd-0.2. We found a $B_{C2}(0)$ of the order of ~54 T, which is ~6 % lower than the Gd-0. Although after doping with Gd, T_C has been increased by approximately 6 %, the slope $[dB/dT]_{T=Tc}$ has been dropped to almost 9 %, which has been also confirmed by Foner et.al. [19].

Spin-orbit scattering parameter λ_{SO} has been calculated using Eq.2.57, and was found to be 1.55 ± 0.03. This is considerably lower than the theoretical value (described in Chapter 7) obtained from the temperature dependence of $B_{C2}(T)$ shown in Fig. 8.24, where we have plotted reduced upper critical field $b_{C2}^*(t)$ versus reduced temperature t and provided data for pure $PbMo_6S_8$ and $Pb_{0.8}Gd_{0.2}Mo_6S_8$ materials.

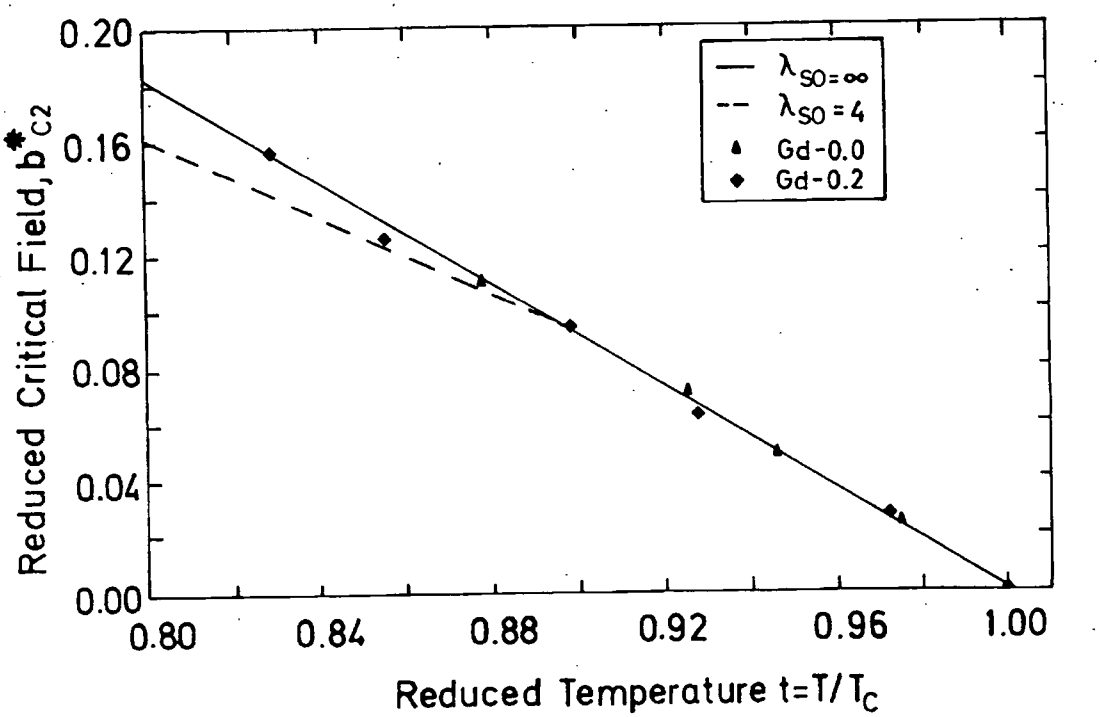

Fig.8.24). Reduced upper critical field $b^*_{c2}(t)$ versus reduced temperature t for $\lambda_{so} > 50$ or ∞, compared with experimental values obtained for pure $PbMo_6S_8$ ($\alpha=3$) and $Pb_{0.8}Gd_{0.2}Mo_6S_8$ samples.

From the Fig. 8.24, it is clear that λ_{so} could be greater than 4. We therefore suggest that the paramagnetic limiting is broadly compensated by the spin-orbit scattering.

8.6. Conclusion:

Doping of Gd in the PMS may have improved the T_C with Gd=0.1 giving a maximum value of 15.1±0.2 K. The reason why Tc has been improved after doping Gd is not clear. It may be due to the reason that Gd is a good getter for oxygen, which has extracted the oxygen from the material resulted in improvements in Tc or the improvements in fabrication in the controlled environment and reducing the Mo powder in hydrogen. The different values of Tc obtained in the same material in Cp and a.c. susceptibility measurements is probably intrinsic and not an artifact of the measurements. The magnetic transition discovered in Cp measurements at ~10 K, is absent in a.c. susceptibility measurements. Probably, Gd-doped PMS can be considered as a possible material where co-existence of superconductivity with anti-ferromagnetic ordering is present. On the basis of XRD and TEM, the magnetic transition is more probably due to Gd_2S_3 material present in the sample. The reduction in slope $[dB/dT]_{T=Tc}$ has compensated for by the improvement in Tc so $B_{C2}(0)$ is ~6% lower. The λ_{so} values are greater than 4 suggesting that paramagnetic limiting plays little or no role. Extensive complementary magnetic and transport measurements are underway which help clarify the role of electromagnetic granularity and also show the strong similarities for these materials with the high temperature superconductors.

References to Chap. 8:

1). Fischer, Φ., H. Jones, G. Bongi, M. Sergent, and R. Chevrel, J.Phys. C: Solid State Phys. 7 (1974) L450-53.

2). Fischer, Φ. Appl. Phys. 16 (1978) 1 - 28.

3). Fischer, Φ., M. Decroux, R. Chevrel, and M. Sergent; in Superconductivity in d- and f- Band Metals. Edited by D.H. Douglass, Plenum Press. New York and London (1976), pp.175-187.

4). Fischer, Φ., and M. B. Maple, in Superconductivity in Ternary Compounds I, 1982, Topics in Current Physics 32, eds. Φ. Fischer and M.B. Maple; Springer-Verlag, Berlin) p.4.

5). Zheng D.N, D.P Hampshire, (unpublished results)

6). Werthamer, N.R., E. Helfand and P.C. Hohenberg, Phys. Rev., 147 (1966)295.

7). Maki, K., Phys. Rev., 139 (1965) A702-A705.

8). Clogston, A.M. Phys. Rev. Lett. 9 (1962) 266-67; B.S. Ckandrasekhar, App. Phys. Lett. 1 (1962) 7-8

9). Zheng D.N., and D.P.Hampshire, in Applied Superconductivity 1995, Proceedings of EUCAS 1995, Edinburgh, Scotland, 3-6 July 1995, edited by D. Dew-Hughes, IOP Conference Series No.148. pp.255-58.

10). Ramsbottom H.D., Thesis, 1996, University of the Durham, England.

11). Bredl, C. D., and F. Steglich, J. Mag. and Mag. Mat.; 7 (1978) 286-89.

12). Remeika, J.P., G.P. Espinosa, A.S. Cooper, H. Barz, J.M. Rowell, D.B.McWhan, J.M. Vandenberg, D.E. Moncton, Z. Fisk, L.D. Woolf, H.C. Hamaker, M.B. Maple, G. Shirane, and W. Thomlinson; Solid State Comm. 34 (1980) 923-26.

13). Ishikawa, M., and J. Muller; Solid State Comm. 27 (1978) 761-66;. Ishikawa M., and Φ. Fischer: Solid State Comm. 24, (1977) 747-

14). Fischer, Φ., Ferromagnetic Materials, Vol. 5, Edited by K. H. J. Buschow and E. P. Wohlfarth, Elsevier Science Publishers B.V., 1990. pp.465-576.

15). Decroux, M., and B. Seeber, in Concise Encyclopedia of Magnetic & Superconducting Materials, edited by J. Evetts, Pergamon Press Ltd., Oxford, 1992, pp. 61-67.

16). Yamasaki, H., and Y. Kimura, Solid State Comm. 61 (1987) 807-812.

17). Selvam, P., J. Cors, M. Decroux, and Φ. Fischer, Appl. Phys. A., 60 (1995) 459

- 465.

18). Selvam, P., D. Cattani, J. Cors, M. Decroux, Ph. Niedermann, S. Ritter, Φ. Fischer, P. Rabiller, R. Chevrel, L. Burel and M. Sergent, Mat. Res. Bull. 26 (1991) 1151-1165.

19). Foner, S., E. J. McNiff, Jr.,and D. G. Hinks, Phys. Rev. B., 31 (1985) 6108-11.

20). Cattani, D., J. Cors, M. Decroux, B. Seeber, and Φ. Fischer, Physica C., 153-155 (1988) 461-462.

CHAPTER 9

Specific Heat of Low Gd-doped $Pb_{1-x}Gd_xMo_6S_8$

9.1. Introduction

As previously described in Chapter 8 the doping of Gd in $Pb_{1-x}Gd_xMo_6S_8$, where x represents the concentration of the doping, may increase the T_C of the material, with the highest value of 15.1±0.2 K has found with x =0.1, which is slightly higher than the transition temperature Tc quoted in literature [1-7] . In this chapter we aim to carry out a thorough study, to find the highest T_C, the optimum Gd-concentration x and the highest $B_{C2}(0)$. To do this, we have investigated four samples with Gd-concentration at x =0.01, 0.02, 0.03, and 0.04 named, Gd-0.01, Gd-0.02, Gd-0.03, and Gd-0.04 respectively.

This Chapter consists of six sections. Section 9.2 gives some of the details of sample fabrication described in chapter 7 and 8, section 9.3 is devoted to the experimental results obtained using the experimental set-up as described in chapter 5. The data obtained are analysed in section 9.4. The discussion on this data is provided in section 9.5. Section 9.6 concludes the chapter with important findings.

9.2. Fabrication of the Sample

It is clear from the conclusion of chapter 7 and 8, that the HIP process enhanced the properties toward the Tc, as well as $B_{C2}(T)$. Therefore, we have completed the specific heat measurements on the aforementioned four bulk Gd-doped PMS materials, which were fabricated at a pressure of $2x10^8$ $N.m^{-2}$ (2000 bar) using a Hot Isostatic Press (HIP) method, as described in Chapter 7 and 8. The Mo powder was reduced in a hydrogen-nitrogen mix rather than pure hydrogen. The T_C values and the volumetrically averaged upper critical field $B_{C2}(T)$ have been determined by Cp measurements as a function of temperature for these materials.

9.3. The Experimental Results

9.3.1. Gd-0.01 ($Pb_{0.99}Gd_{0.01}Mo_6S_8$)

The Cp measurements in 0-field have been carried out on the Gd-0.01 sample.

The chemical formula for this sample is suggested to be $Pb_{0.99}Gd_{0.01}Mo_6S_8$ giving the concentration x =0.01. The mass of this sample was 0.1874 gm which was fabricated using Hot Isostatic Process (HIP), as described in chapter 7. The graphical form of the raw data giving V^{-1}(rms) vs. T and Phase shift vs. T for this sample is shown in Fig. 9.1a.

It is noted from the Fig. 9.1a that the superconducting jump height is not prominent in V^{-1}(rms) vs. T, as well as in phase shift vs. T and consequently, it is difficult to find the accurate Tc. To enhance the jump height and find the Tc as before, we have plotted V^{-1}(rms) * T^{-3} vs. T in Fig. 9.1b. Before plotting V^{-1}(rms) * T^{-3} vs. T, we tried different powers of T, but we found T^{-3} is the best to find the phase transition. The transition temperature Tc* has been calculated after taking area under the curve of Fig. 9.1b to be equal on each side when extrapolating to a sharp transition. The Tc* was found to be 14.93±0.1 K for Gd-0.01.

Similarly, we have plotted Cp vs. T in Fig. 9.2 for Gd-0.01 sample and added the arrow as a guide to the eye, and to compare the values obtained in Durham to that of the literature values for this sample.

9.3.2. Gd-0.02 ($Pb_{0.98}Gd_{0.02}Mo_6S_8$)

To find the effect of magnetic field on the transition temperature T_C, and to find the $B_{C2}(0)$ of low doped Gd, a HIP sample with a mass of 0.15656 gm and concentration, x =0.02 as suggested in the formula $Pb_{0.98}Gd_{0.02}Mo_6S_8$ has been investigated. The sample was investigated in the field of; 0, 2.5, 5.0, 7.5, 10 and 12.5 Tesla. To have a clear look at $V^{-1}_{(rms)}$, we have added 5 units to 2.5 T, 10 to 5 T, 15 to 7.5 T, 20 to 10 T and 25 to 12.5 T data. Similarly, in the phase shift data, we have added 2° to 2.5 T, 4° to 5 T, 6° to 7.5 T, 8° to 10 T and 10° to 12.5 T. The results so obtained, for $V^{-1}_{(rms)}$ vs. T are shown in Fig. 9.3a, for Phase shift vs. T in Fig.9.3b. As explained earlier in section 9.3.1, that to enhance the jump height and find the Tc, we plotted V^{-1}(rms) * T^{-3} vs. T in Fig. 9.3c. The transition temperatures obtained in magnetic field for Gd-0.02 material are displayed in Table 9.1.

Similarly, we have plotted Cp vs. T in Fig. 9.4 for Gd-0.02 sample to guide to the eye, and to compare the values obtained in Durham to that of the literature values for this sample.

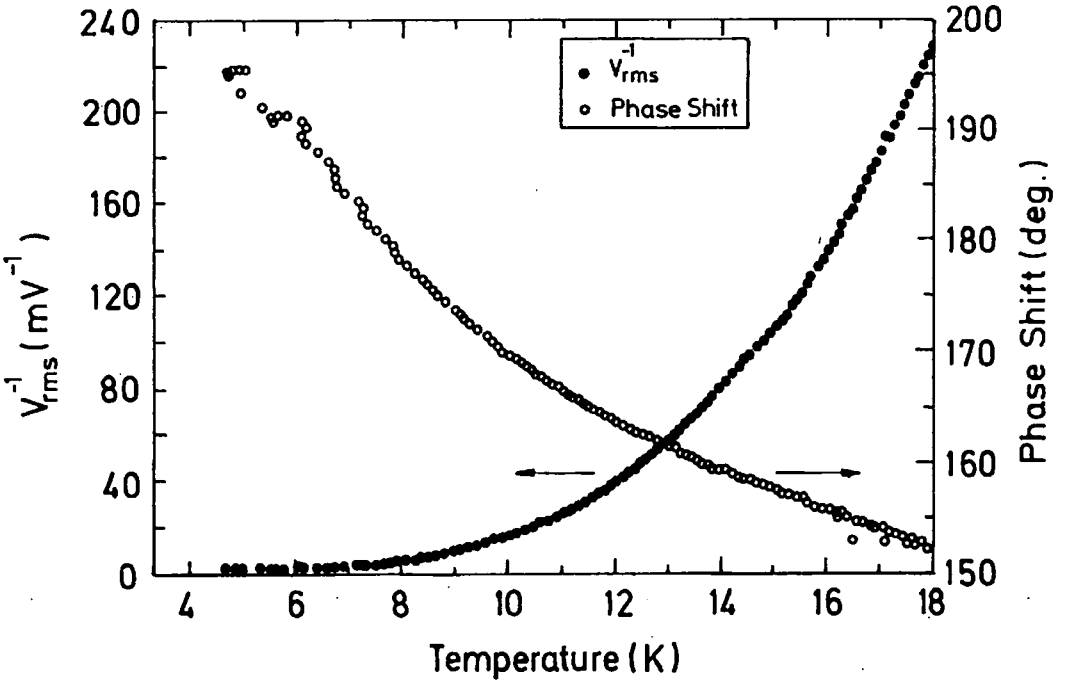

Fig. 9.1a). V^{-1}(rms) Vs. T and Phase Shift vs. T for Gd-0.01 HIP'ed $Pb_{0.99}Gd_{0.01}Mo_6S_8$ (Gd-doping, x =0.01).

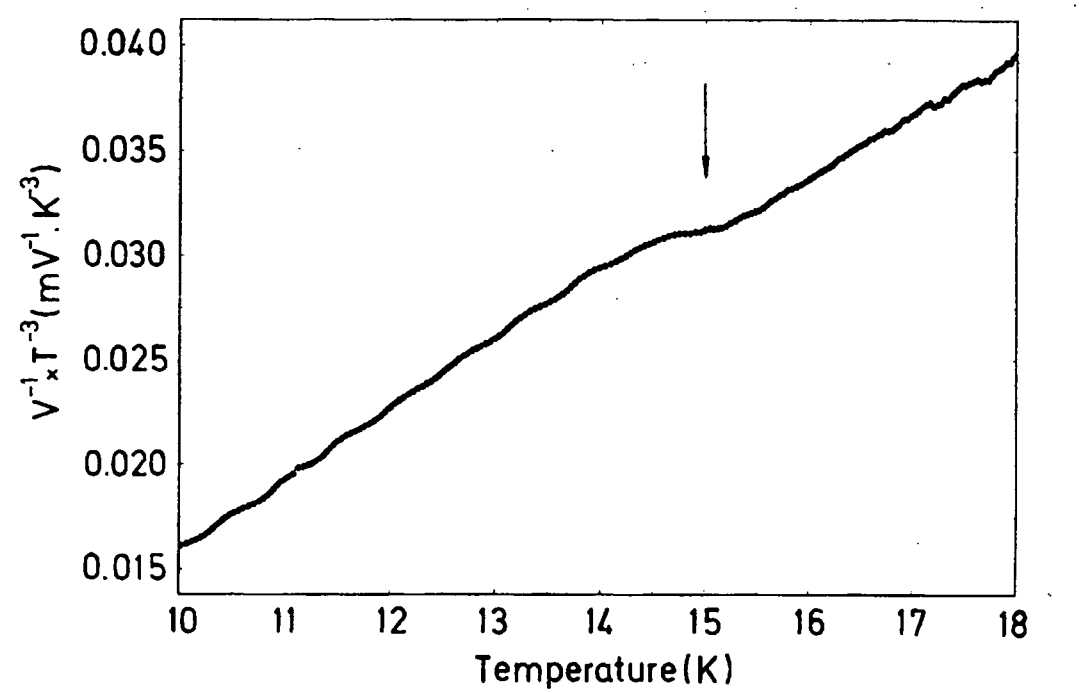

Fig. 9.1b). V^{-1}(rms)* T^{-3} as a function of temperature in 0-field to enhance the superconducting jump height, and to find the transition temperature T_c, for Gd-0.01 HIP'ed $Pb_{0.99}Gd_{0.01}Mo_6S_8$ (Gd-doping, x =0.01).

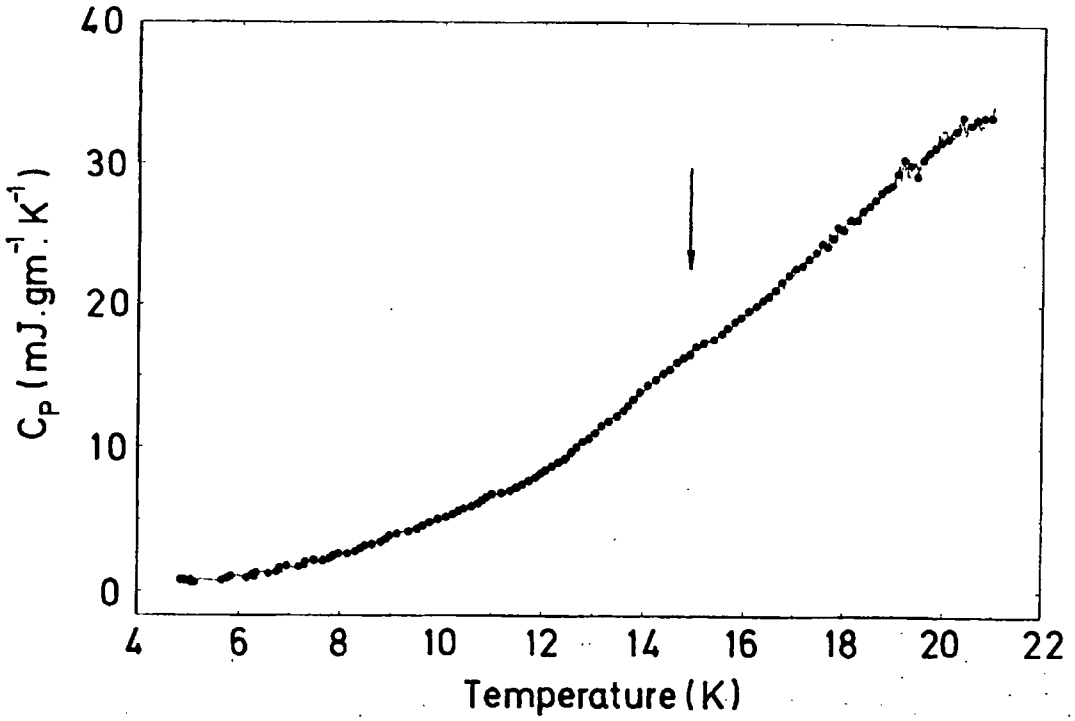

Fig. 9.2). Cp Vs. T for Gd-0.01 HIP'ed $Pb_{0.99}Gd_{0.01}Mo_6S_8$ (Gd-doping, x =0.01) in 0- field.

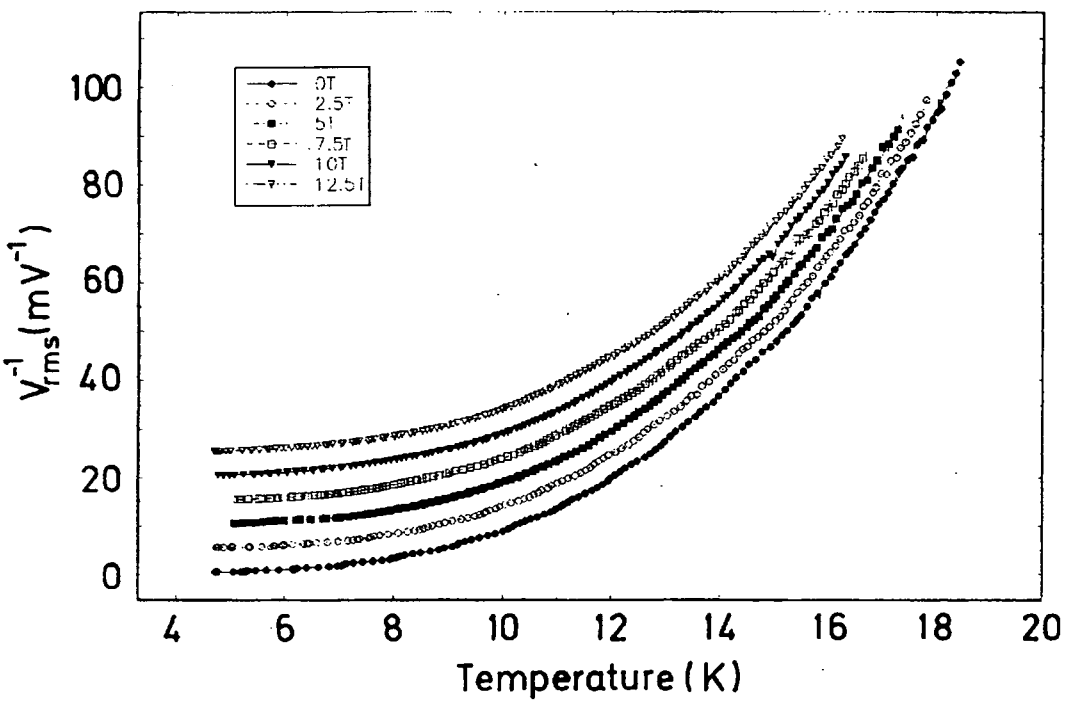

Fig. 9.3a). V^{-1}(rms) Vs. T in magnetic field in the interval of 0, 2.5, 5.0, 7.5 10.0 and 12.5 T Gd-0.02 HIP'ed $Pb_{0.98}Gd_{0.02}Mo_6S_8$ (Gd-doping, x =0.02). (Addition of 5, 10, 15, 20, 25 units to 0, 2.5, 5, 7.5, 10, and 12.5 T respectivly).

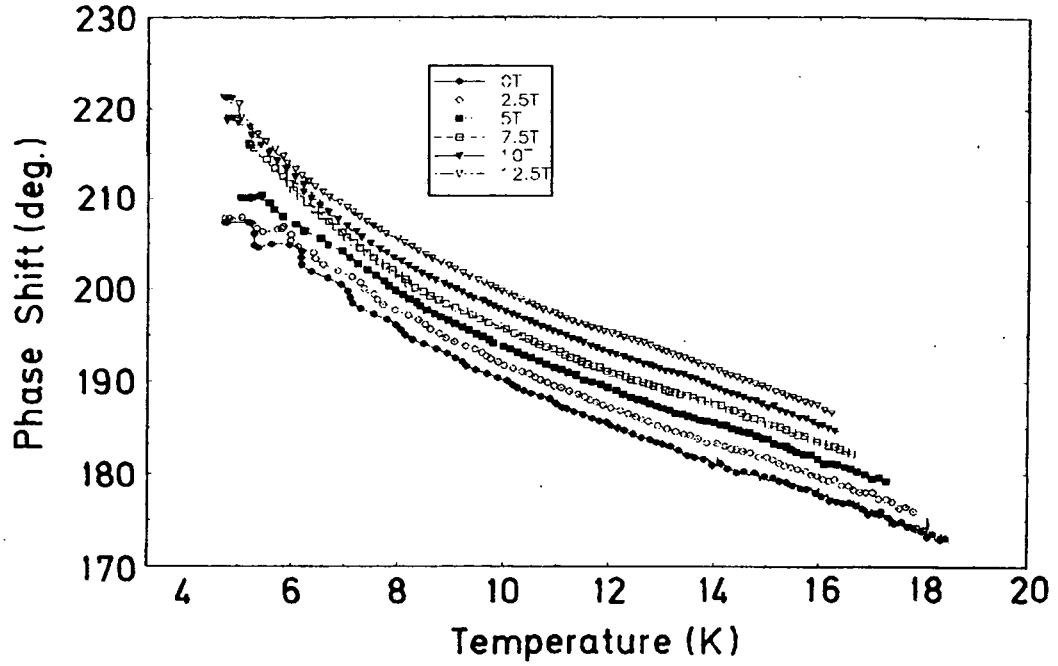

Fig. 9.3b). Phase Shift as a function of temperature in magnetic field in the interval of 0, 2.5, 5.0, 7.5 10.0 and 12.5 T for Gd-0.02 HIP'ed $Pb_{0.98}Gd_{0.02}Mo_6S_8$ (Gd-doping, x =0.02). (Addition of 2, 4, 6, 8, 10 degree to 0, 2.5, 5, 7.5, 10, and 12.5 T respectivly).

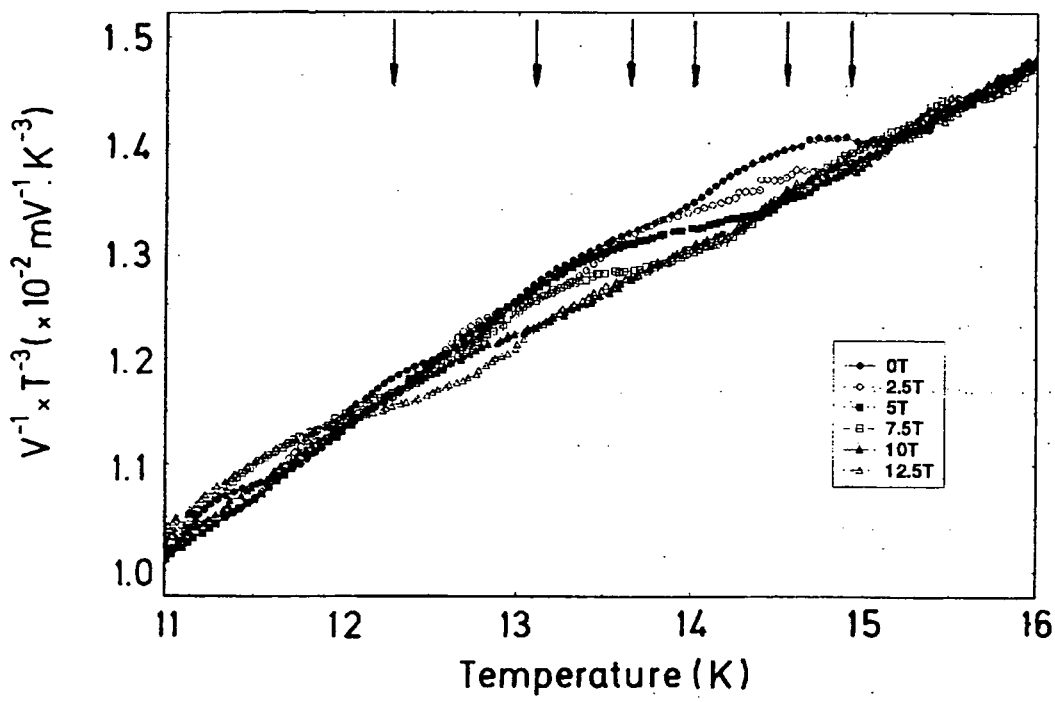

Fig. 9.3c). $V^{-1}(rms)^* T^{-3}$ as a function of temperature, in magnetic fields of the interval 0, 2.5, 5.0, 7.5, 10.0, and 12.5 T, to enhance the superconducting jump height, and to find the transition temperature T_C, for Gd-0.02 HIP'ed $Pb_{0.98}Gd_{0.02}Mo_6S_8$ (Gd-doping, x =0.02).

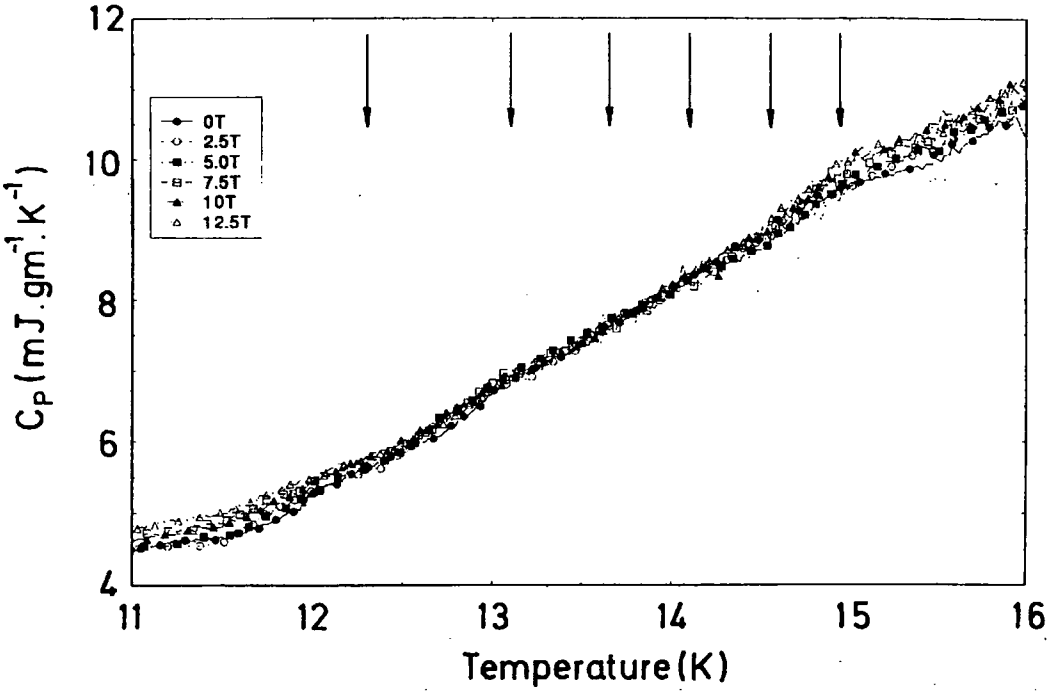

Fig. 9.4). Cp Vs. T in magnetic field in the interval of 0, 2.5, 5.0, 7.5 10.0 and 12.5 T for Gd-0.02 HIP'ed $Pb_{0.98}Gd_{0.02}Mo_6S_8$ (Gd-doping, x =0.02).

Materials⇒	Gd-0.02	Gd-0.04	Gd-0.2
Applied Field (T)	Transition Temp. T_C*±0.2 (K)	Transition Temp. T_C*±0.2 (K)	Transition Temp. T_C*±0.2 (K)
0	14.94	14.90	14.95
2.5	14.55	14.60	14.65
5.0	14.01	14.10	14.10
7.5	13.65	13.50	13.65
10	13.10	13.10	13.15
12.5	12.30	12.25	12.60

Table: 9.1. The effect of applied magnetic field (B) on the transition temperature T_C for Gd-0.02, Gd-0.04 and Gd-0.2 samples.

T_C*; The T_C* has been measured after taking area under the curve of the graph $V^{-1}(rms) * T^{-3}$ vs. T to be equal on each side when extrapolating to a sharp transition.

9.3.3. Gd-0.03 ($Pb_{0.97}Gd_{0.03}Mo_6S_8$)

The HIP sample, named Gd-0.03 with a doping concentration of 0.03 as suggested in the formula $Pb_{0.97}Gd_{0.02}Mo_6S_8$, has been investigated in the 0-field. The mass of the sample was 0.05953 gm. The graph giving V^{-1}(rms) vs. T and the Phase shift vs. T is shown in Fig. 9.5a. As explained earlier, we have measured the transition temperaturte Tc from the graph giving V^{-1}(rms) * T^{-3} vs. T in Fig. 9.5b. The Tc* was found to be ~15.04±0.2 K for this material. The Cp vs. T is plotted in Fig. 9.6 for this sample.

9.3.4. Gd-0.04 ($Pb_{0.96}Gd_{0.04}Mo_6S_8$)

A Gd-doped HIP sample of mass 0.25331 gm, with a concentration of 0.04 as suggested in the formula $Pb_{0.96}Gd_{0.04}Mo_6S_8$ has been investigated in magnetic field. The field was applied with the intervals of 0, 2.5, 5.0, 7.5, 10, and 12.5 T. As explained above in section 9.2.2, to have a clear view in fields of $V^{-1}_{(rms)}$, we have added 5 units to 2.5 T, 10 to 5 T, 15 to 7.5 T, 20 to 10 T and 25 to 12.5 T data. Similarly, in the phase shift data, we have added 2° to 2.5 T, 4° to 5 T, 6° to 7.5 T, 8° to 10 T and 10° to 12.5 T. The results so obtained, for $V^{-1}_{(rms)}$ vs. T are shown in Fig. 9.7a, for Phase shift vs. T in Fig.9.7b. To enhance the jump height and find the Tc, we plotted V^{-1}(rms) * T^{-3} vs. T in Fig. 9.7c. The transition temperatures obtained in magnetic field for Gd-0.04 material are displayed in Table 9.1.

Similarly, we have plotted Cp vs. T in Fig. 9.8 for Gd-0.04 sample and added arrows as a guide to the eye, and to compare the values obtained in Durham to that of the literature values for this sample.

9.4. Analysis.

9.4.1: Effect of Gd-Doping in 0-field

All the values of T_C in the 0-field for different Gd-concentrations x, in the formula $Pb_{1-x}Gd_xMo_6S_8$, have been compared. The graphical form illustrating transition temperature T_C, vs. the Gd-concentration x, is shown in Fig. 9.9. We found the optimum value for the low Gd-concentration in PMS to be x = 0.03. From this we achieved the highest T_C of ~15.04±0.2 K. The results are summarised in Table. 9.2.

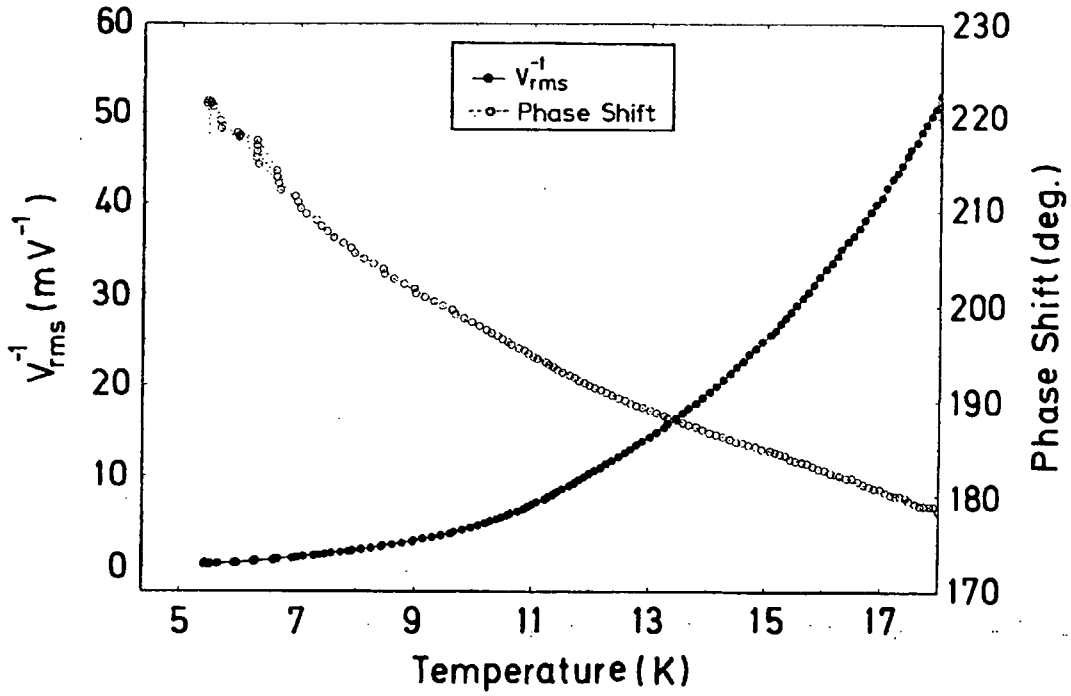

Fig. 9.5a). V^{-1}(rms) Vs. T and Phase Shift vs. T for Gd-0.03 HIP'ed $Pb_{0.97}Gd_{0.03}Mo_6S_8$ (Gd-doping, x =0.03) in 0-field.

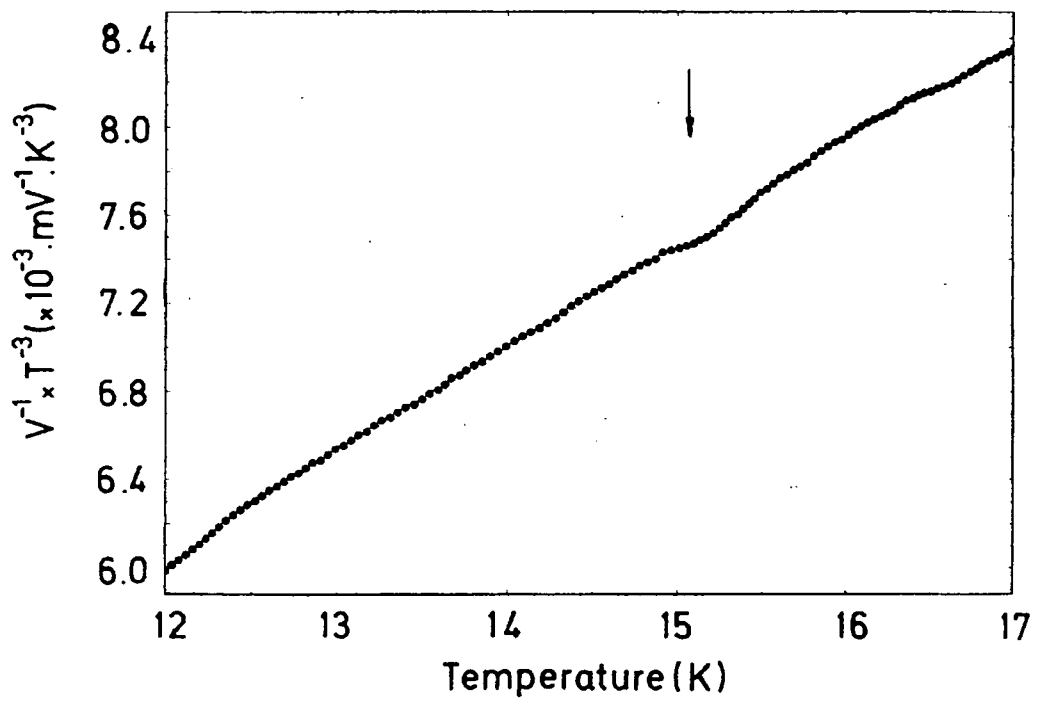

Fig. 9.5b). V^{-1}(rms)* T^{-3} as a function of temperature in 0-field to enhance the superconducting jump height, and to find the transition temperature T_C, for Gd-0.03 HIP'ed $Pb_{0.97}Gd_{0.03}Mo_6S_8$ (Gd-doping, x =0.03).

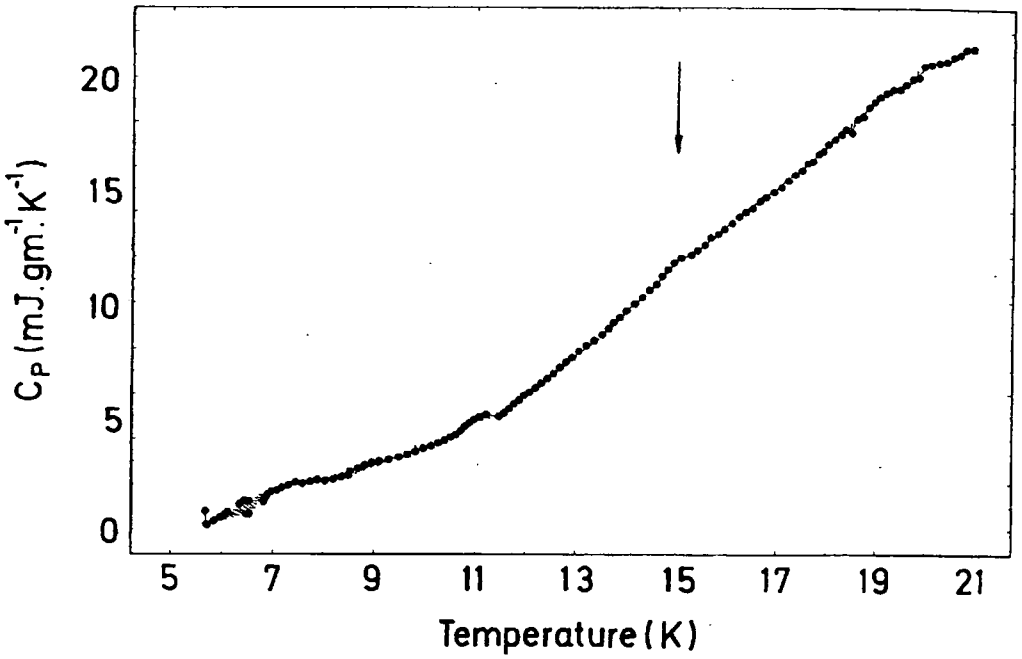

Fig. 9.6). Cp Vs. T for Gd-0.03 HIP'ed $Pb_{0.97}Gd_{0.03}Mo_6S_8$ (Gd-doping, x =0.03) in 0-field.

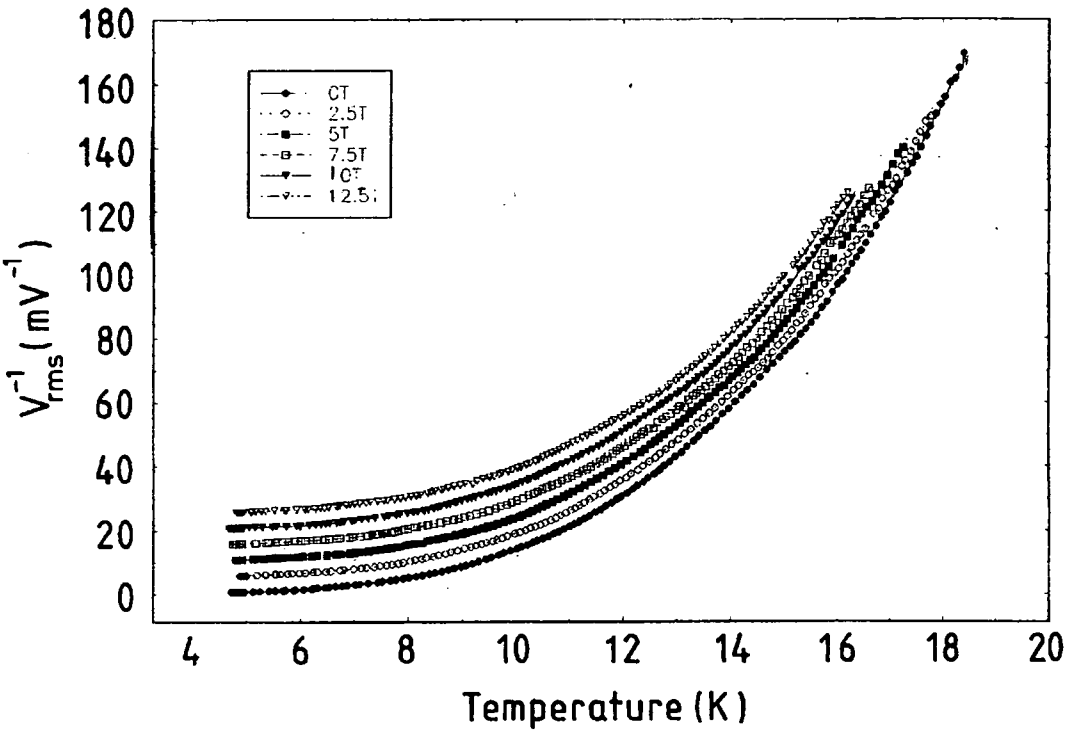

Fig. 9.7a). V^{-1}(rms) Vs. T in magnetic field in the interval of 0, 2.5, 5.0, 7.5 10.0 and 12.5 T for Gd-0.04 HIP'ed $Pb_{0.96}Gd_{0.04}Mo_6S_8$ (Gd-doping, x =0.04). (Addition of 5, 10, 15, 20, 25 units to 0, 2.5, 5, 7.5, 10, and 12.5 T respectivly).

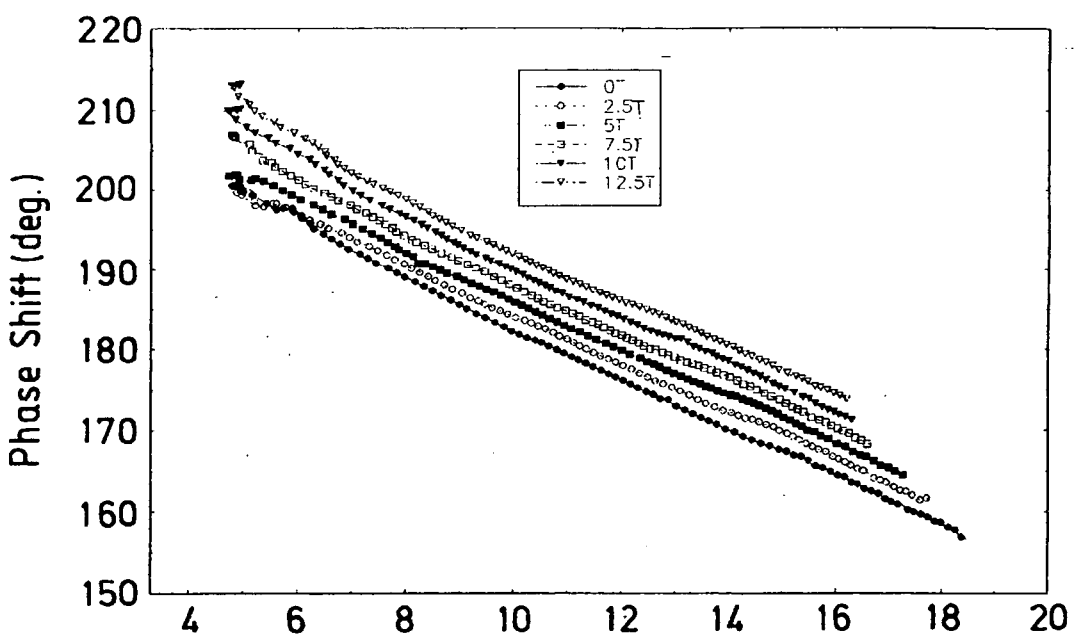

Fig. 9.7b). Phase Shift as a function of temperature in magnetic field in the interval of 0, 2.5, 5.0, 7.5 10.0 and 12.5 T for Gd-0.04 HIP'ed $Pb_{0.96}Gd_{0.04}Mo_6S_8$ (Gd-doping, x =0.04). (Addition of 2, 4, 6, 8, 10 degree to 0, 2.5, 5, 7.5, 10, and 12.5 T respectivly).

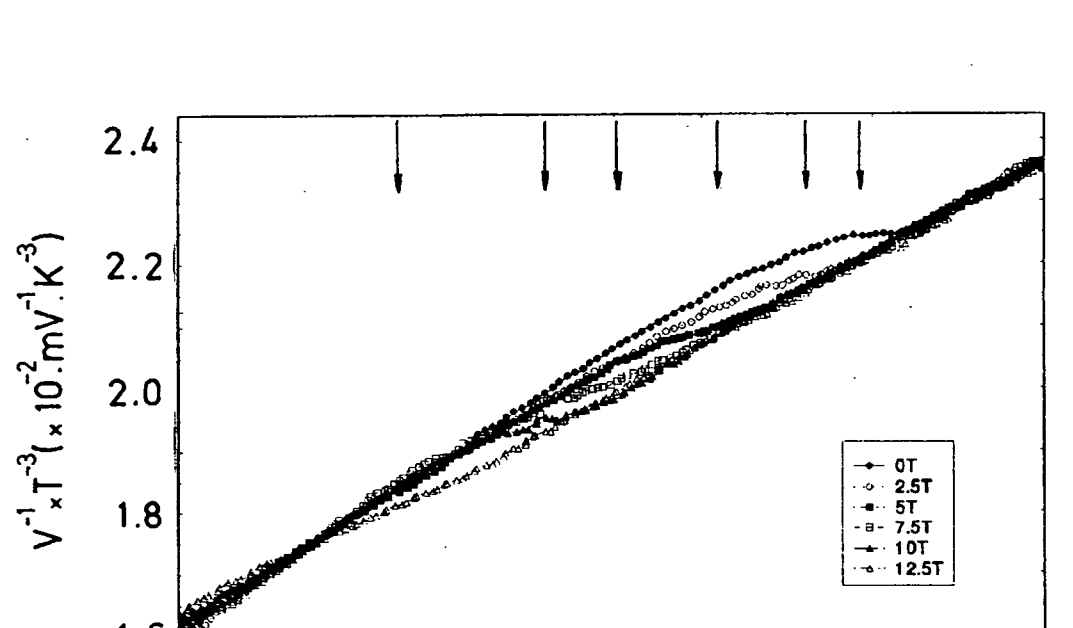

Fig. 9.7c). V^{-1}(rms)* T^{-3} as a function of temperature, in magnetic fields of the interval 0, 2.5, 5.0, 7.5, 10.0, and 12.5 T, to enhance the superconducting jump height, and to find the transition temperature T_C, for Gd-0.04 HIP'ed $Pb_{0.96}Gd_{0.04}Mo_6S_8$ (Gd-doping, x =0.04).

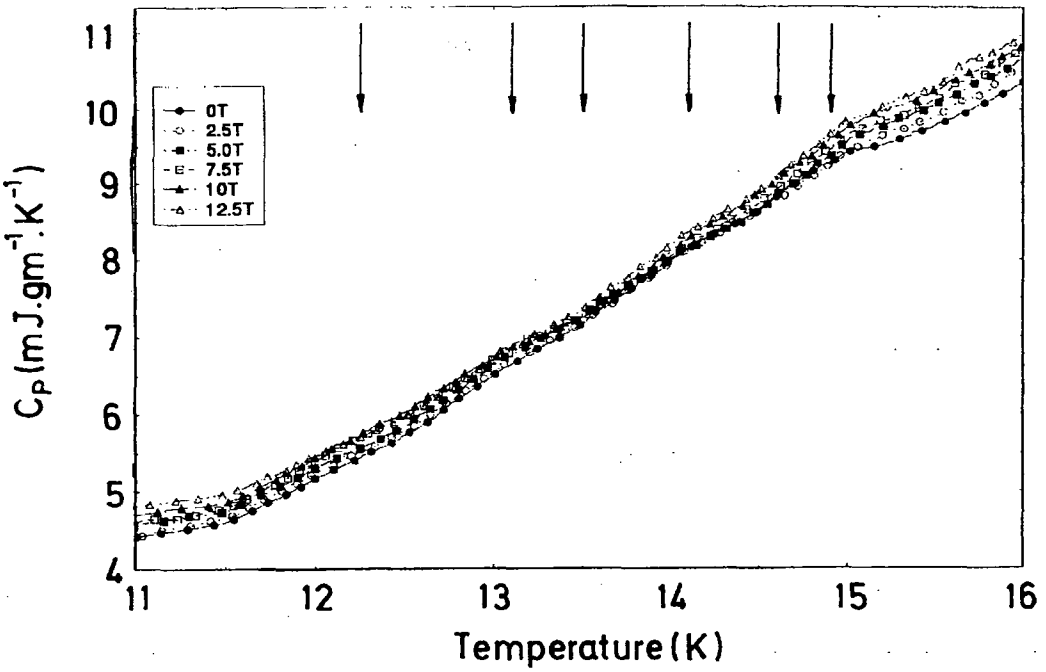

Fig. 9.8). Cp Vs. T in magnetic field in the interval of 0, 2.5, 5.0, 7.5 10.0 and 12.5 T for Gd-0.04 HIP'ed $Pb_{0.96}Gd_{0.04}Mo_6S_8$ (Gd-doping, x =0.04).

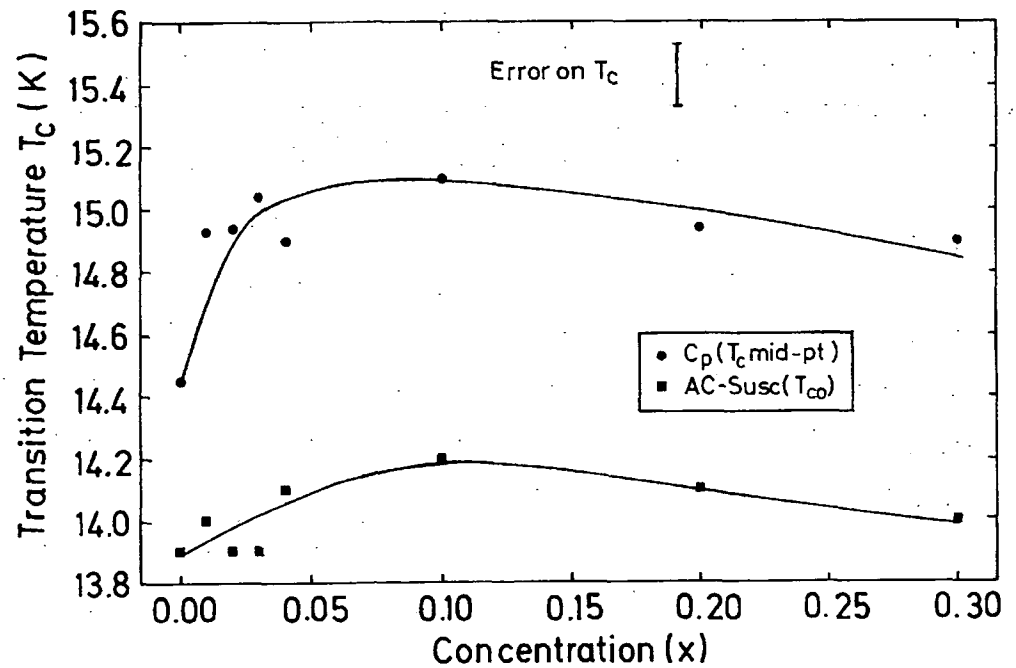

Fig.9.9). The effect of Gd-doping on the transition temperature Tc for $Pb_{1-x}Gd_xMo_6S_8$.

	Cp-Measurements	AC-Susceptibility	AC-Susceptibility
Gd-doping (x)	Trans. Temp. T_C* ±0.2 (K)	T_C*(onset) ±0.1 (K)	T_C*(mid-point) ±0.1 (K)
0	14.45	14.20	14.0
0.01	14.93	14.0	13.65
0.02	14.94	13.90	13.65
0.03	15.04	13.90	13.68
0.04	14.90	14.10	13.80
0.1	15.10	14.20	14.0
0.2	14.94	14.10	13.80
0.3	14.80	14.0	13.80
0.6**	3.20	-	-
1.0***	1.40	-	-

Table:9.2.The effect of Gd-doping (x) on the transition temperature of $Pb_{1-x}Gd_xMo_6S_8$.
*; To measure T_C in Cp-measurments has been explained in captions of Table 9.1.
**; From Φ. Fischer et. al.(1976) pp.181.[8].
***; From Ternary Compounds I, pp.4 [9].

9.4.2: Measuring Slope $dB/dT]_{T=Tc}$ and Upper Critical field $B_{C2}(T)$

The thermodynamic upper critical field $B_{C2}(T)$ vs. transition temperature T_C of low Gd-doped PMS samples for x= 0.02, and 0.04 is shown in Fig.9.10. We found a slope close to $T \approx T_C$ of -5.44 T/K and -5.26 T/K for Gd=0.02 and Gd=0.04 respectively as shown in Table 9.3.

Using WHH theory [10], [Eq.2.63], $B_{C2}(0)$ was calculated, assuming there is no paramagnetic limiting, and found to be 56.28 T and 54.35 T for Gd-0.02 and Gd-0.04 respectively. Although Gd-doping increased the T_C of the material, the slope dB/dT and $B_{C2}(0)$ is considerably lower than the slope and $B_{C2}(0)$ of pure PMS. This can be seen in Table 9.3.

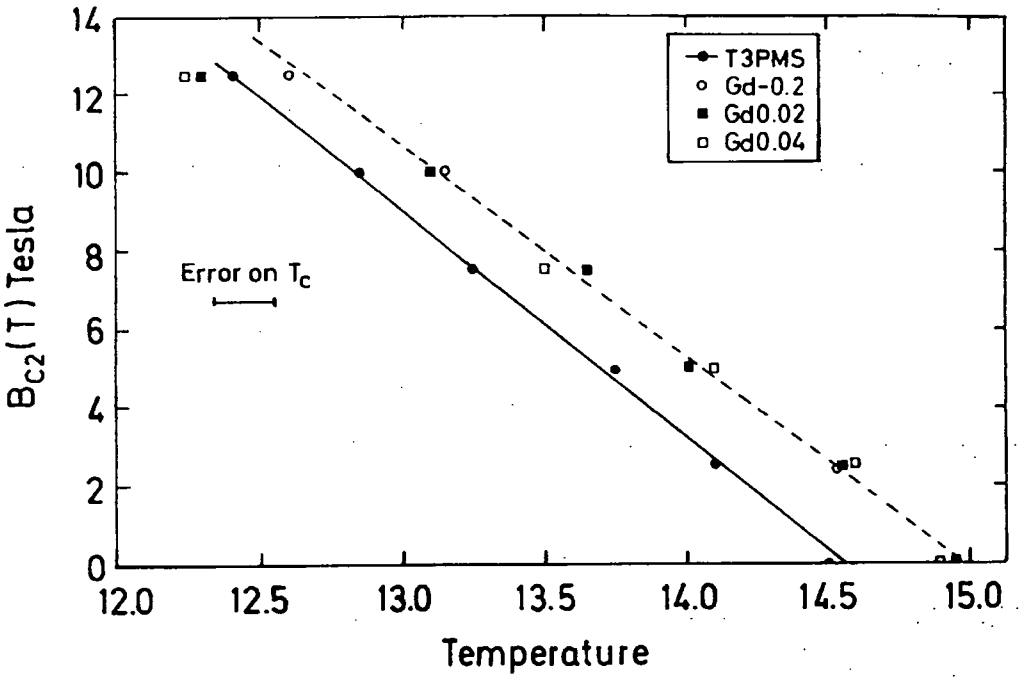

Fig.9.10). Upper Critical field $B_{C2}(T)$ as a function of superconducting transition temperature Tc for four HIP'ed $Pb_{1-x}Gd_xMo_6S_8$ samples, where x = 0, 0.2, 0.02 and 0.04. The drastic trend of bending toward the lower values at 12.5 T is obvious.

Material	T_C**± 0.2(K)	dB_{C2}/dT± 0.2 (T/K)	$B^*_{C2}(0)$ ±5 (T)	α ±0.03, [after Eq.7.3]	α ±0.03, [after Eq. 7.4]	λ_{SO}±0.02, [after Eq. 2.57]
T3PMS	14.4	-6.66	66.47	3.52	3.55	3.51
Gd-0.2	14.95	-5.21	53.97	2.75	2.77	2.18
Gd-0.02	14.94	-5.44	56.28	2.87	2.89	2.37
Gd-0.04	14.90	-5.26	54.35	2.78	2.80	2.25

Table 9.3: T_C, $(dB_{C2}/dT)_{T=Tc}$, $B^*_{C2}(0)$, α and λ_{SO} for pure $PbMo_6S_8$ (T3PMS), Gd=0.2 ($Pb_{0.8}Gd_{0.2}Mo_6S_8$), Gd-0.02($Pb_{0.98}Gd_{0.02}Mo_6S_8$) and Gd-0.04($Pb_{0.96}Gd_{0.04}Mo_6S_8$) samples. All the calculated parameters are after WHH theory [10].

9.4.3: Measuring α and λ_{SO}

The Maki [11] parameter has been calculated using Eqs. 7.3 and 7.4 for both samples, i.e., for Gd-0.02 and Gd-0.04, and was found to be 2.88±0.02, and 2.79± 0.02 respectively. The Spin-orbit scattering parameter λ_{SO} has also been calculated

using Eq. 2.57, viz. $B_{C2}(0)=1.33\ \sqrt{\lambda_{SO}}\ B_p$, where $B_{C2}(0)$ is the upper critical field assuming there is no PPL, and B_p is the Clogstan-Chandrashekher limiting field [12], which is found to be 2.369±0.02 and 2.252±0.02 for Gd-0.02 and Gd-0.04 respectively. All these results have been summarised in Table 9.3.

9.5. Discussion:

The superconducting transition jump height (anomaly) is usually present in superconducting materials, and represents a prominent parameter which shows the quality of the sample. It also plays an important role in finding out the transition temperature T_C. As explained in section 7.3.2, to enhance the jump height and find out the transition temperature correctly, instead of plotting Cp/T vs. T, we have plotted $V^{-1}(rms) * T^{-3}$ vs. T for all four of the Gd-doped PMS HIP samples. These are shown in Figs. 9.1b, 9.3c, 9.5b and 9.7c for Gd-0.01, Gd-0.02, Gd-0.03 and Gd-0.04 respectively. Cp vs. T for all four samples is displayed in Figs. 9.2, 9.4, 9.6 and 9.8 respectivly to check the proximity of the results. From the analysis of all these samples in the 0-field, our results were very close to the highest value of T_C as quoted in the literature for the Chevrel phase materials [1-7], i.e. 14.95±0.1 K, for all Gd-doped PMS, which can be seen in Table 9.3. The same results for different Gd-concentrations have been plotted in the Fig. 9.9, giving Tc vs Gd-concentration, to see the graphical form of these results. It is noted that all these values are within 14.95±0.1 K. The highest Tc value obtained may be due to the fact that Gd is a very good getter for oxygen [13]. It extracts the oxygen from the sample, resulting in an enhancement of the transition temperature T_C. So by reducing the amount of oxygen, and controlling other contamination during the process, the T_C can be enhanced to its maximum value obtained in Chevrel phase materials to date [1-7].

The magnetic transition phases at ~10.5 K or ~6.0 K which are present in the high doped Gd-samples, (See Chapter 8) were not observed in these less doped samples by our high resolution experimental set-up. The 1-4 % of Gd in the material is difficult to detect by X-rays diffraction, energy dispersive x-rays (EDX) or transmission electron microscopy (TEM) [14].

However, a very small and rounded jump in $V^{-1}_{rms} * T^{-3}$ vs. T of Figs. 9.1b, 9.3c, 9.5b, and 9.7c reveals possibly that, there is a Tc distribution throughout the

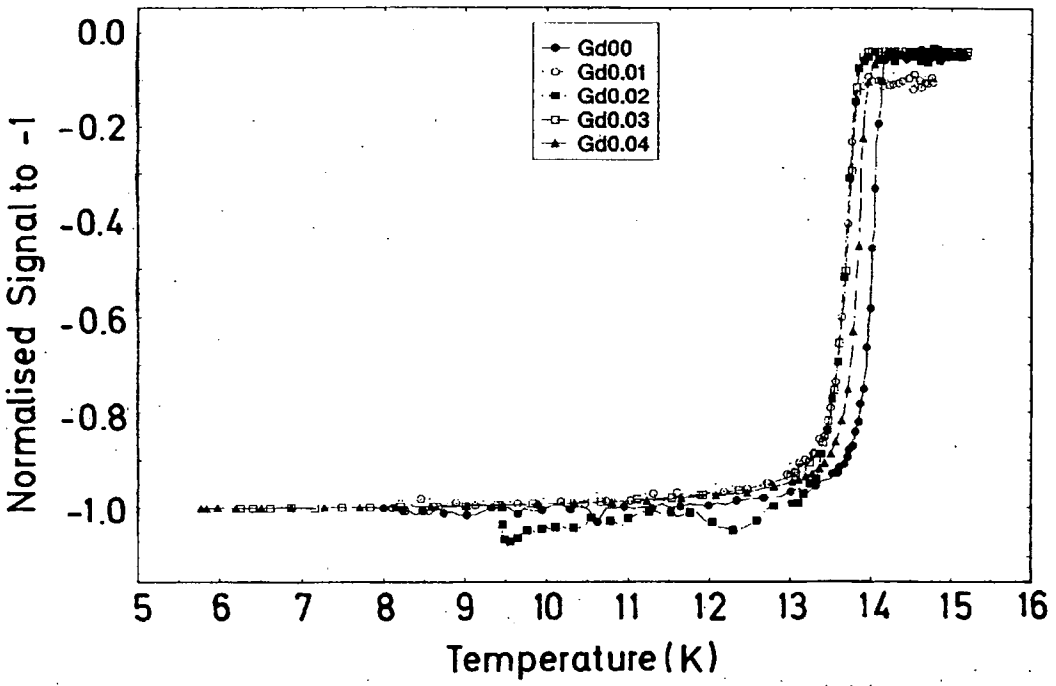

Fig.9.11). Normalised AC-Susceptibility data vs. temperature for $Pb_{1-x}Gd_xMo_6S_8$ samples, where x = 0, 0.01, 0.02, 0.03 and 0.04, for comparison with Cp data.

material, or a temperature gradient across the sample during the measurements or there is some small cracks in the material and the material is not pure in the sense that it is not an ideal PMS, due to the addition of Gd, which effect the structural as well as the magnetic properties of the material.

From ac-susceptibility measurements [15] in Fig.9.11 the materials are superconducting without showing any evidence for a magnetic phase transition. The Tc values obtained after the ac. susceptibility measurements are ~1 K lower than the Cp measurements. This can be seen in Table 9.2 and Fig. 9.9. This discrepancy may be due to the different thermometry used in both measurements, or due to inhomogeniety produced during the fabrication process. These measurement were made on different pieces of the same material. To eliminate this problem, the same sample should be used in both methods. However, Cattani et. al. [16] showed that different Tc obtained in susceptibility and Cp measurements is not an artifact of the measurement but is intrinsic. So more probably, the difference in Tc could be an intrinsic property.

The slope $dB/dT]_{T=Tc}$ of the Gd-0.02 and Gd-0.04 samples is less than the pure PMS (T3PMS), while it is higher than Gd-0.2 as can be seen in Table 9.3. This resulted in a slightly higher $B_{C2}(0)$ when compared with Gd-0.2. This $B_{C2}(0)$ has been

calculated from the specific heat data obtained in the magnetic field using the WHH theory. Although the T_C values have been increased after low Gd-doping to PMS by ~4.5% of the pure PMS (T3PMS), the $B_{C2}(0)$ has been decreased by 15.3% for Gd-0.02 and 18.2% for Gd-0.04. However, the low doping of Gd has increased the $B_{C2}(0)$ by 5% for Gd-0.02 and 2% for Gd-0.04 sample than Gd-0.2 (high Gd-doping x=0.2). These results are summarised in Table 9.3. The drop in the slope is partly compensated by higher Tc values. However, it has been concluded by Foner [13] that some oxygen contamination is necessary to make it more stable and to get higher $B_{C2}(T)$.

The Maki [11] parameter α has been calculated and found to be ~18.4% and ~21% lower than the pure PMS for Gd-0.02 and Gd-0.04 respectively and ~4% for Gd-0.02 and ~1% for Gd-0.04 higher than that of the Gd-0.2 as described in Chapter 8. This reveals that the strong paramagnetic limiting effect is present in the material and has strongly influenced the material when working in high fields. This can be seen in Fig. 9.10 and 9.12, (where the reduced upper critical field $b^*_{C2}(t)$ has been plotted against a reduced transition temperature t =T/Tc for α=3) where the low doping of the Gd samples show a dramatic decrease in the transition temperature at 12.5 T.

When calculating spin-orbit scattering parameter λ_{SO}, one finds that Gd-0.02 and Gd-0.04 are ~32.5% and ~36% lower than the pure PMS (T3PMS) respectively. While Gd-0.02 and Gd-0.04 are higher than the high doped Gd (x=0.2) by about ~9% and ~3.5%.

In addition to these Cp measurements, the group in Durham has completed an extensive series of transport and magnetic measurements. These complementary measurements allow us to address granularity in these materials since the Cp measurements provide bulk volumetric information whereas the transport measurements are strongly affected by the grain boundary properties.

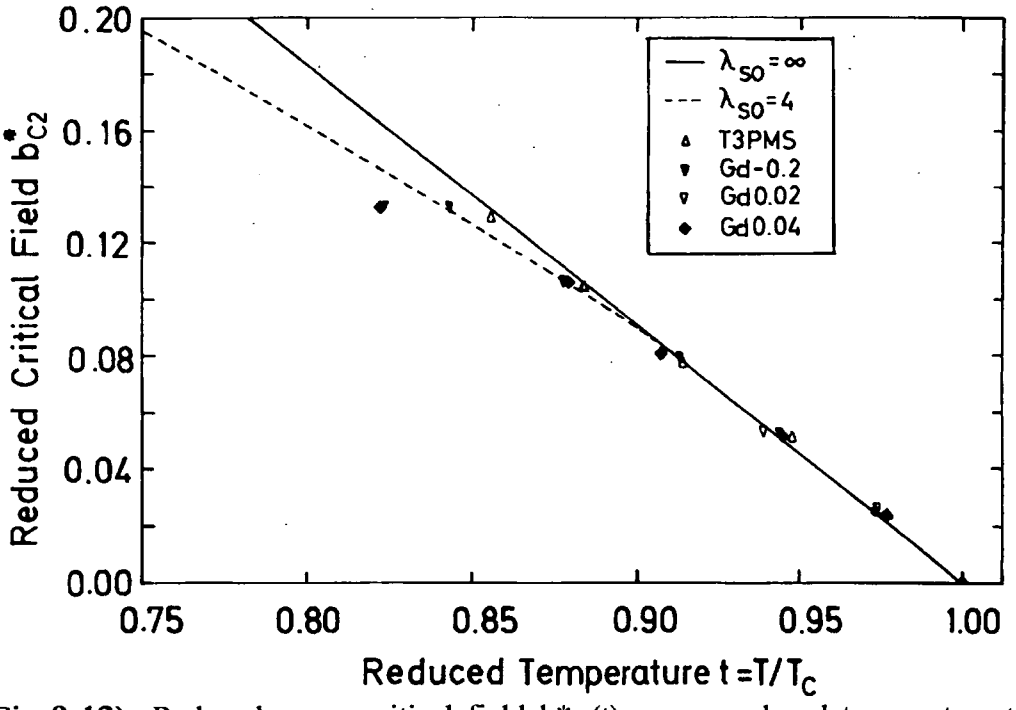

Fig.9.12). Reduced upper critical field $h^*_{c2}(t)$ versus reduced temperature t for different values of λ_{so} and $\alpha=3$, compared with the experimental values obtained for pure $PbMo_6S_8$ (Gd-0) and for $Pb_{1-x}Gd_xMo_6S_8$ for x = 0.2, 0.02 and 0.04 samples.

9.6. Conclusion

Low-doping of Gd in the $Pb_{1-x}Gd_xMo_6S_8$ materials may have increased the transition temperature 14.95±0.2K, to its maximum value as quoted in the literature so far, giving the optimum concentration x as 0.03. This may be due to the reason that Gd is a good getter for oxygen and there is no chance of contamination of other materials due to the controlled environment during the fabrication process. The Gd has extracted the oxygen, resulting in a relatively pure material. Although, this trend is different in ac. susceptibility measurements, where Tc values decreases with low doping. The possible reason for this may be due to inhomogeniety produced during the fabrication process, as different pieces of the same material were taken for measurements or different Tc obtained after different methods is an intrinsic property of the material. The absence of the magnetic transition phase in the materials is probably because the Gd concentration is too low to detect with the existing techniques. Although, the transition temperature Tc has been raised to about 4% in the Gd-0.03 sample, the low Gd-doping has reduced the $B_{C2}(0)$ by 15.3% in Gd-0.02

and by 18.2% in Gd-0.04 when compared with the T3PMS. However, low doping of Gd may have raised the $B_{C2}(0)$ by 5% and 2% for Gd-0.02 and Gd-0.04 materials respectively when compared with the high doping of Gd, i.e. Gd-0.2. On the other hand, the Gd-doping makes the material unsuitable when working in very high fields, i.e. beyond the 10 T, where a drastic depression in the curve has been observed. From the measurements in this chapter, it can be concluded that the low doping of Gd is a very suitable method for enhancing Tc and the $B_{C2}(0)$ in $PbMo_6S_8$.

References to Chap. 9:

1). Marezio, M., P. D. Dernier, J. P. Remeika, E. Corenzwit, B. T. Matthias: Mat. Res. Bull. 8 (1973) 657.

2). Fischer, Φ., H. Jones, G. Bongi, M. Sergent, and R. Chevrel, J.Phys. C: Solid State Phys. 7 (1974) L450-53.

3). Fischer, Φ. Appl. Phys. 16 (1978) 1 - 28.

4). Decroux, M., and B. Seeber, in Concise Encyclopedia of Magnetic & Superconducting Materials, edited by J. Evetts, Pergamon Press Ltd., Oxford, 1992, pp. 61-67

5). Yamasaki, H., and Y. Kimura, Solid State Comm. 61 (1987) 807-812.

6). Selvam, P., J. Cors, M. Decroux, and Φ. Fischer, Appl. Phys. A., 60 (1995) 459 - 465.

7). Selvam, P., D. Cattani, J. Cors, M. Decroux, Ph. Niedermann, S. Ritter, Φ. Fischer, P. Rabiller, R. Chevrel, L. Burel and M. Sergent, Mat. Res. Bull. 26 (1991) 1151-1165.

8). Fischer, Φ., M. Decroux, R. Chevrel, and M. Sergent; in Superconductivity in d- and f- Band Metals. Edited by D.H. Douglass, Plenum Press. New York and London (1976), pp.175-187.

9). Fischer, Φ., and M. B. Maple, in Superconductivity in Ternary Compounds I, 1982, Topics in Current Physics 32, eds. Φ. Fischer and M.B. Maple; Springer-Verlag, Berlin) p.4.

10). Werthamer, N.R., E. Helfand and P.C. Hohenberg, Phys. Rev., 147 (1966)295.

11). Maki, K., Phys. Rev., 139 (1965) A702-A705.

12). Clogston, A.M. Phys. Rev. Lett. 9 (1962) 266-67; B.S. Ckandrasekhar, App. Phys. Lett. 1 (1962) 7-8.

13). Foner, S., E. J. McNiff, Jr.,and D. G. Hinks, Phys. Rev. B., 31 (1985) 6108-11.

14). Zheng D.N, D.P Hampshire, (unpublished results)

15). Eastell, C., University of Oxford, Private Comminication, 1996.

16). Cattani, D., J. Cors, M. Decroux, B. Seeber, and Φ. Fischer, Physica C., 153-155 (1988) 461-462.

CHAPTER 10

Conclusion

10.1: Introduction

Specific heat measurements give unique information about the lattice and electronic properties of the material, transition temperature Tc, and thermodynamic critical fields. As specific heat is a bulk measurement, it can be used to check whether the transition is bulk or due to some other minority phase present in the material. The quality of the material can be checked on the basis of the shape of the anomaly. The adiabatic stability of the material depends on the Cp, since higher specific heat lead towards a more stable system.

The main emphasis in this work has been on lead Chevrel phase materials. They have transition temperature Tc ≈ 15 K, intermediate coherence length (ξ ≈30 Å), upper critical field $B_{C2}(0)$ ≈ 60 T, and Jc ≈ 2 x 10^8 A-m^{-2} in a magnetic field of 20 T, which make them a potential candidate to produce high magnetic fields beyond 20 T for the next generation.

In this thesis we have given a brief overview of the superconductivity. The related theory of the specific heat of normal, superconductors, and magnetic materials has been also addressed. A review of different techniques has been given for comparison. This was followed by the description of the design, construction and use of the probe designed in Durham to measure specific heat using different methods.

The measurements have been done on a high thermal conductivity material (Cu), and extended to NbTi in field and low thermal conductivity materials as PMS. The comparison between HIP'ed and unHIP'ed materials has been made. To investigate the effect of Gd-doping in PMS, we have made a thorough study of high- and low- Gd doping in $Pb_{1-x}Gd_xMo_6S_6$. Their properties extracted from the Cp measurements has been measured. The potential of Gd-doped PMS to be used in production of the high magnetic fields has been discussed.

10.2: Summary

To measure specific heat of superconductors, a probe was designed which

can be used to measure the specific heat in high magnetic fields using heat pulse method and a.c. technique. We have used a tiny, robust, almost magnetic field independent, high sensitive and fast characteristic thermal response time, Cernox thermometer. With this thermometer, there is no need for a bulky gas thermometer or non-reproducible capacitance thermometer to control the background temperature. The diameter of the probe has been reduced to Φ-20 mm, which is quite suitable for our ϕ-40 mm bore of 17 T d.c. magnetic field generated by superconductor. The computer programmes have been written to acquire the data using heat pulse method or a.c. technique. To make measurements fully computer controlled, different programs were developed. To find the optimum operating conditions, the pressure inside the probe, the frequency, time constant, input power, ramp rate, and excitation current to Cernox thermometer have been extensively investigated. Cu and NbTi which have well established literature values, are used to test the validity of the probe. In this way we achieved an accuracy of ±0.2 K in temperature in 0- as well as high magnetic fields, ≈ 10% a typical accuracy in the Cp measurements, and we have detected temperature oscillations of the order of 10^{-6} K .

A computer program has been developed to analyse the raw data obtained from the high thermal conductivity material and then extended to low thermal conductivity materials like PMS. A first order correction using the phase shift has been included in the analysis to find the accurate Cp. The results of Cu, NbTi, and PMS are compared with the literature values and found consistent within experimental errors. The results obtained are about ~10 % in agreement with the literature (based on Cu-values).

We have used a Hot Isostatic Press (HIP) to get high quality and dense samples, and to have better connectivity between the grains. After HIP processing, Tc as well as $B_{C2}(0)$ have improved. Further increase in Tc and $B_{C2}(0)$ has been obtained after minimising the oxygen contamination during the fabrication process in the PMS and after doping Gd to extract the oxygen in the controlled environment. We have found that by plotting $V^{-1}_{rms}*T^{-3}$ vs T we have enhanced the jump.

High Gd-doping increased the transition temperature to its maximum value of 15.10 ± 0.1 K which is amongst the best reported value in the literature for any Chevrel phase superconductor. We obtained this optimum value for Gd concentration

of ~0.1. However, the $B_{C2}(0)$ values obtained are less than the pure PMS. Complementary transport measurements have also made. The material shows magnetic transition at about 10 K which is probably due to the unreacted antiferromagnetic Gd_2S_3 material during the fabrication process due to low reaction temperature.

To obtain the optimum value of Tc and $B_{C2}(0)$ low Gd-doping in PMS has been tried. The Tc we have obtained is of the same order as high Gd-doped material but $B_{C2}(0)$ is slightly improved.

Future Recommendation

The above mentioned probe can be used at higher temperatures (> 77 K). To test it, we have made some preliminary measurements on YBCO successfully using this probe with a very slow ramp rate. Now we give recommendations to improve the probe performance;

When measuring Cp using a.c. technique, the input power to the sample heater needs to be varied, depending on the temperature and the sample thickness. Use of a frequency as low as possible by the LIA is recommended so that it can locked-in properly.

Use the D.C. filter for the measurements, if one is using very low frequency ($\approx$ 0.5 Hz).

The excitation current to CX-1030 thermometer needs to be always kept 100 uA.

There should be a compromise in choosing the ramp-rate (not very slow, time consuming and big oscillations in the sample temperature as well as background temperature, not very fast to miss the superconducting transition temperature).

Use a sample heater other than strain gauge (say, Carbon coating on one side of the sample) or using chopped light to reduce the addenda.

Calibrate the CX-1030 regularly (depending on the number of cycles it is used).

Explicitly fabricate precursor materials like Gd_2S_3 etc. to check the properties of Gd-doped PMS, if it is un-reacted.

Fabricate materials at higher temperature (above 1500 ^{0}C) for Pb sites to be replaced by Gd.

Study the effects of oxygen in Chevrel phase materials.

Appendix

A1: Computer Programming

All the data has been acquired and analysed using interactive, real-time graphical software ASYST (A Scientific System) V.4 by Keithley Instruments, such that all data is stored digitally in Lotus 1-2-3 file. Communication between the computer and instruments is via IEEE interface except for the d.c. magnet power supply that uses the RS-232 bus. The default ASYST system has been modified according to the requirements. To acquire the data, system overlays, file sharing, graphics and memory information are saved in NEW.Q and to analyse the data, these all with different set-up are stored in TEST.COM and TEST.OVL. NEW.Q automatically loads a file called DEVICES.PRO. This files contains all the IEEE address settings, initialisation sequences, serial polling and set-up sub-routines for all of the instruments used in the measurements.

The data has been acquired using SWITCH.PRO if using Heat Pulse Method and FAST.PRO if using Long-Duration Heat Pulse Method. To acquire the data using Alternating Current Technique, another program RUNB.PRO, which consists of seven other programmes, named: DEVICES.PRO, B.VAR, B1.PRO, B2.PRO, B3.PRO, B4.PRO and BGO.PRO, has been used.

The data has been analysed including first order theta correction, using RUNALI.PRO, which consists of two other programmes, ALI2.VAR and ALI.PRO.

A2: Cp-Measurements

All of the Cp-measurements are computer controlled. To measure specific heat in 0- and magnetic fields three programs as stated above were used. The Heat Pulse measurements were made keeping the background temperature as stable as possible and fixing the magnetic field. Long-duration Heat Pulse measurements were also made keeping the background temperature and magnetic field fixed but using the fast buffer of the voltmeters to record the data, eliminating the dwell time of the instruments. Measurements were made using a.c. technique keeping the magnetic field fixed and ramping the background temperature. All the variables are saved in the file B.VAR. The rest of the program is split into five other files. The following table A1 and A2 enlists the programming blocks in each file in which they were executed.

SWITCH.PRO (FAST.PRO)
save.sample
setupa
setupb
setup
vertical.axis
labels
plot.sample
(bufferh)
record.switch
chkstop
plot.temperature
readT
plot.switch
plot.it
go2
go

Table A1: Various blocks of the programms SWITCH.PRO and FAST.PRO, used in heat pulse method and long duration heat pulse method respectively

B1.PRO	B2.PRO	B3.PRO	B4.PRO	BGO.PRO
left	choicent	timing	sencase	setup
bottom	tcontrol	PID	chktemp	go1
pol	temprang	saveit	settemp	go2
pol1	temprate	stopHeat	plotscreen	go3
pol11	temprecap	chkstop	labels	go
response	totalrecap	chkspeedsuper	time	
reply	tconvert	stopDC	dataplot1	
ninput	choicepc	setDCfield	dataplot2	
look			dataplot3	
RHFE2			takedata	
RHFE22			finish	
setupA			totalfinish	
setupB			totalrecall1	
setupC			totalrecall2	
setupE				
switch				

Table A2: The various blocks of the program RUNB.PRO used to acquire the data in A.C. Technique.

A3: Data Analysis

A program called RUNALI.PRO was used to analyse the data which includes ALI2.VAR and ALI.PRO. This program is capable to analyse the data acquired by RUNB.PRO in 0- and high-magnetic fields. It read voltage from the lotus file and convert it into temperature after interpolation between two points. It is also converting V^{-1}rms into corresponding Cp, using a first order theta correction.

All the variables were saved in the file called ALI2.VAR. The various blocks and routines are shown in Table A2.

ALI.PRO
ninput
words
read
setup
interpol1
interpol2
getting
calculating
write
go

Table A3. The various blocks of the program RUNALI.PRO used in analysis of the Cp data acquired with RUNB.PRO.